VACUUM PHOTOTRIODES FOR ELECTROMAGNETIC CALORIMETER APPLICATIONS

A thesis submitted to **Brunel University London** for the degree of Doctor of Philosophy (Ph.D)

By

Sema Zahid

Supervised by

Prof. Peter Hobson

Department of
Electronic and Computer Engineering

July, 2018

Abstract

Vacuum Phototriodes (VPTs) are fast, sensitive and radiation-hard photodetectors. They provide internal gain in a high magnetic field. They are used in a number of High Energy Physics experiments one of which, the Compact Muon Solenoid (CMS) detector at the CERN Large Hadron Collider (LHC), is discussed here.

The COMSOL Multiphysics simulation environment has been used to model the VPT. A segment that captures the characteristics of the thin anode mesh, a critical component within the VPT, has been accurately modelled in COMSOL. The electron trajectories, backscatter and induced currents on the anode are simulated using the electrostatics and charged particle tracing modules within COMSOL. This provides an insight on how an initial photoelectron and subsequent secondary electrons, behave as they travel within the VPT. Additional simulations were carried out to model the effects of the magnetic environment that the VPT experiences inside the CMS detector.

When CMS was under construction extra VPTs were produced and stored in nitrogen purged refrigerators. These VPTs have been re-characterised to be used in a beam test at CERN, for a concept called double side readout. This re-characterisation process was carried out to ensure there was no severe degradation of the stored VPTs. The outcome shows there was minimal degradation with an average deviation of 6.6% from the initially measured gain during manufacture. The double-sided readout concept is discussed and its effect on reducing the effect of the non-uniformity of light produced in radiation damaged lead tungstate crystals is presented.

One option to upgrade the endcap electromagnetic calorimeter of CMS for the forthcoming High Luminosity Large Hadron Collider (HL-LHC) was to replace the existing VPTs with a four-fold segmented device within the same external glass vacuum envelope. This VPT contains a 4-fold segmented anode. Two possible upgrade options are discussed. One of which would use this segmented VPT in a shashlik configuration with optical fibres, the second option being a high granularity silicon-tungsten calorimeter. The prototype Hamamatsu VPT for the first option provides a solution for space restricted environments by providing 4 independent channels. Experimental characterisation of the performance of this new VPT is presented. The photocathode uniformity response was measured along with the crosstalk that occurs between

the segments as the illumination is precisely positioned along the faceplate. A COMSOL model was created for the segmented anode VPT prototype. The simulation included determining the induced signal as a function of time and the cross-talk in adjacent quadrants.

Declaration

I hereby declare that this thesis is entirely my work, and except where otherwise indicated, describes my research or publications. No part of this thesis has been previously submitted to this or any other university as part of the requirement for a higher degree.

Sema Zahid

Acknowledgements

This research would not be possible if it wasn't for the support and guidance provided by my supervisor Prof. Peter Hobson. Thank you for keeping me going with advice and encouragement whenever I needed it. Also, to Christopher Shelby, who has helped me with any technical support needed, and Alexander Metcalf for providing the SEM pictures of VPT anode mesh.

To my husband Dr. Asim Jan, who has supported me endlessly and given me the motivation to keep going. For building a support system for our experiences and hardships of our PhDs together. I am truly thankful for having you in my life. To my parents, brother and sister who have continually believed in my ability to succeed in my endeavours. Thank you for providing everything I needed to get me where I am today. To my in-laws who have joined the support team to keep me going and believing in me. To my friends Martina, Stephen and Uthay who have helped me get through the hard times with laughter and reassurance.

A huge thanks to all of the CERN staff that helped and assisted me, especially David Cockerill, David Petyt and Ken Bell. I would like to thank the Science & Technology Facilities Council for funding my studentship and making this research possible.

List of Abbreviations

- ADC – Analogue to Digital Converter
- APD – Avalanche Photodiode
- BH – Backing Hadron Calorimeter
- CMS – Compact Muon Solenoid
- CPT – Charged Particle Tracing
- DRO – Double-Side Readout
- ECAL – Electromagnetic calorimeter
- EE – Endcaps
- FE – Front End
- FEA – Finite Element Analysis
- FEM – Finite Element Mesh
- FH – Forward Hadronic
- FWHM – Full-Width Half Maximum
- HCAL – Hadronic calorimeter
- HG-CAL – High Granularity Calorimeter
- HL-LHC – High Luminosity Large Hadron Collider
- HPD – Hybrid Photodiode
- LHC – Large Hadron Collider
- MGPA – Multi Gain Pre-Amplifier
- OC – Orientation Correction
- PE – Photoelectron
- PMT – Photomultiplier Tube
- PT – Particle Tracing
- SE – Secondary Emission
- Si-PM – Silicon Photomultiplier
- TDR – Technical Design Report
- VFE – Very Front End
- VPT – Vacuum Phototriode
- WLS – Wavelength shifting

Contents

List of Figures

Table of Tables

Chapter 1. Introduction

The Large Hadron Collider (LHC) at CERN plays host to the world biggest experiments to try and recreate the same conditions as when the universe began. Collisions between high energy particles occur within the LHC, at 4 large detectors called ATLAS, CMS, LHCb and ALICE. The CMS detector is, with ATLAS, one of the two general-purpose detectors. It hosts a group of various sub-systems which are used to detect and measure high energy particles and photons from the collisions that occur within the LHC. Vacuum Phototriodes (VPT) are a single stage photomultiplier. They are key photodetectors within part of the CMS electromagnetic calorimeter, that convert the light produced when high energy electrons or photons interact with a dense scintillator into electrical pulses which are amplified and digitised. The VPTs must operate in a high magnetic field and survive very high radiation environments for more than 10 years. Thorough testing has been carried out to ensure that VPTs can operate within this high radiation environment and is a proven technology that is used in numerous physics experiments such as OPAL and DELPHI. This will most likely continue to feature as a vital component in future calorimeters. Further enhancements or upgrades of the VPT always in mind as a better understanding is achieved through the use of simulations and the analysis of its performance undergoing in current experiments. These enhancements can improve its robustness in harsh environments such as that in CMS.

1.1 Aim & Objectives

The aim of this thesis is to improve the modelling and understanding of existing VPTs, as well as developing a prototype VPT as a potential upgrade option. This incurs the following objectives:

- To develop a 3D model of the existing VPT used in CMS into a Multiphysics simulation package called COMSOL.
- Evaluating the performance of the VPT in magnetic fields up to 4 T.
- Extending on the previous works by Yaselli by introducing backscatter into the simulations and using the correct thickness of the anode mesh.,
- Evaluating a prototype segmented VPT that can be used for a Shashlik type calorimeter.
- Build a 3D model of the segmented VPT prototype in COMSOL.

- Investigate crosstalk between segments for the physical prototype and simulated model of the segmented VPT.

1.2 Thesis Outline

Chapter 2 discusses the operation of the major sub-systems of the CMS detector. The detector is discussed at sub-detector level with the greatest focus on the Electromagnetic Calorimeter (ECAL) as this is where the VPT is used in CMS

Chapter 3 describes VPTs in detail, specifically those used in the CMS detector. The structure of the VPT is described, along with its functionality in the detector environment. The degradation of the VPT is also mentioned, which occurs due to radiation damage and helium ingress.

Chapter 4 introduces COMSOL, the Multiphysics simulation software that is used in this thesis to model the VPT used in CMS. The VPT model presented in this thesis is an improvement upon that previously published [1][2] studies, by using simulation software that can model the VPT as realistically as desired with advanced three-dimensional meshing [3].

Chapter 5 discusses potential upgrade options for the endcap electromagnetic calorimeter of CMS that were motivated by the future High Luminosity LHC (HL-LHC). Options that were under discussion during the period covered by this thesis are a “Shashlik” configuration” of new scintillators with wavelength shifting fibres, a “High Granularity” sampling calorimeter using fast silicon sensors, and an alternative solution using a double-ended readout system which retained the existing VPTs and the scintillating crystals. Working with a group based at CERN, the “double end readout” concept was investigated as a possible way to upgrade CMS ECAL using its existing structure along with additional VPT sensors remaining in storage from the original construction of CMS. A concept of placing an additional VPT on the input of the lead tungstate crystals was agreed upon for further testing. A beam test was carried out to test the concept, the stored VPTs were re-characterised A description of the beam test and conclusions about the potential of the double end readout has been published [4][5].

Chapter 6 discusses a prototype VPT that contains a segmented anode which can be used for the Shashlik configuration. Measurements have been carried out on the prototype VPT including measurement of its performance in axial and non-axial magnetic fields up to 4 T, as well as measuring its position sensitivity [6]. The prototype VPT has also been modelled in COMSOL as close as possible using the provided information by the manufacturer. The

simulations are run to understand the behaviour under set conditions, and initial results were published [7].

Chapter 7 presents the conclusions and discusses possible further improvements through future work.

Some of the work discussed in greater detail in this thesis has already been published by the author alone [3] and the author in conjunction with collaborators [4]–[7]. The SPICE simulation in Chapter 4 (section 4.7.7) was provided by Professor Peter Hobson.

Chapter 2. The CMS Experiment

2.1 LHC and CMS detector

The Large Hadron Collider (LHC) first started in September in 2008 and is the largest and latest addition to the CERN's accelerator complex. The LHC consists of a 27 km ring of superconducting magnets, up to 175 m underground. At four positions around the LHC ring, there are four large detectors: ATLAS, CMS, ALICE and LHCb which are shown in Figure 2-1. The two bigger general-purpose detectors are ATLAS and CMS which are used to investigate a wide range of physics. They work independently which works as a confirmation process for each other, with the Higgs boson being the most famous discovery until now. Within the LHC tunnel, two proton beams travel in opposing directions and are then brought to focus and collide within the detectors. The detectors capture the outcome of the collisions to find information that can help understand what occurred when the universe started.

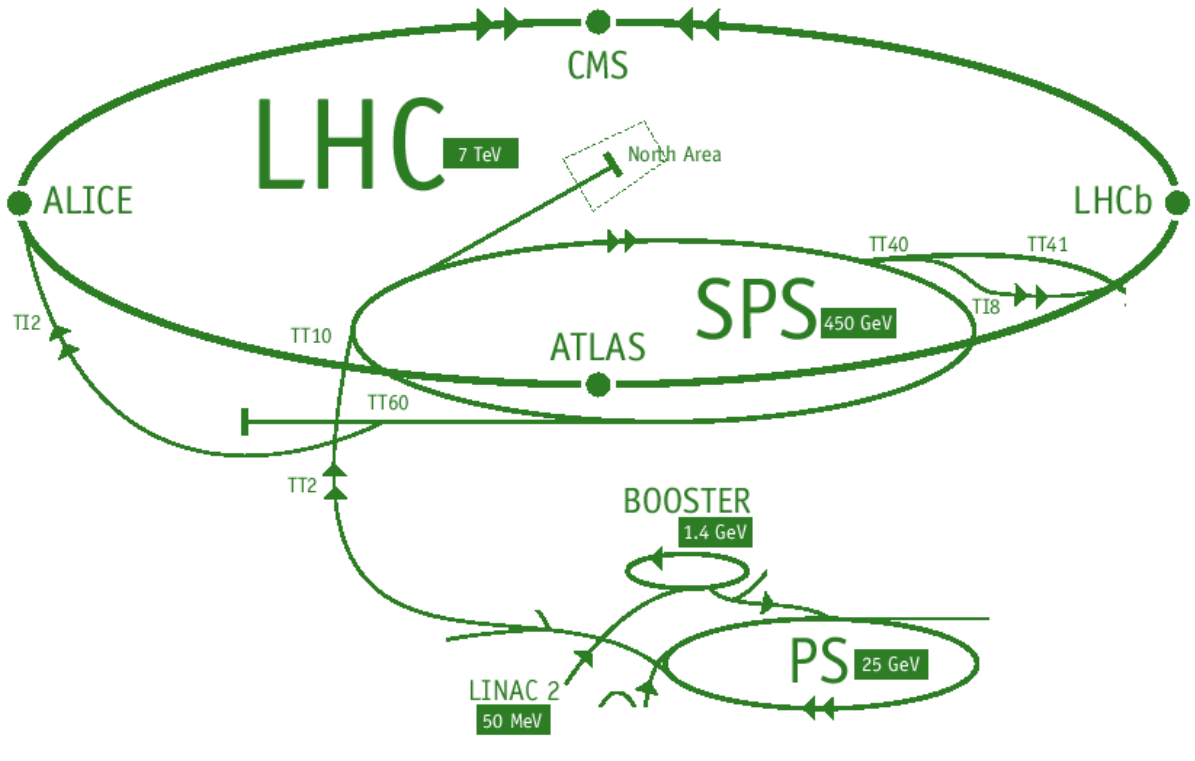

Figure 2-1 – The LHC accelerator with the four main detectors: ATLAS, CMS, ALICE and LHCb. [8]

During the operation for run 1 between years 2010 and 2013, the LHC delivered approximately 6.1 fb^{-1} integrated luminosity of proton-proton collision data at 7 TeV and about 23.3 fb^{-1} at 8 TeV. The CMS detector had in total recorded 93 % of the data [9]. The peak instantaneous luminosity of the LHC reached levels of $7.7\times10^{-2}s^{-1}$ in late 2012 with bunch spacing of 50 ns. Whilst operating at high instantaneous luminosity multiple proton-proton collisions take place, which is known as pile-up. The average pile-up in 2012 was 21 simultaneous proton-proton collisions, and half of all events had pile-up between 21 and 40 [10].

There was a long shutdown period between 2013-2014, where the upgrade was carried out across various point through the detector. After this, the phase run 2, which was between 2015-2018, operated at 13 TeV with the instantaneous luminosity reaching 2×10^{34} $cm^{-2}s^{-1}$, with 50 interactions per bunch crossing, with bunch spacing of 25 ns [11]. During the 2015 run 2 period phase, the integrated luminosity delivered by LHC was 4.2 fb^{-1} and CMS recorded 3.8 fb^{-1}, with 2.8 fb^{-1} also taken at 3.8 T. The response of the detector has been measured at above 97% with the working channels [12]. The integrated luminosities per year of the LHC running are shown in Figure 2-2.

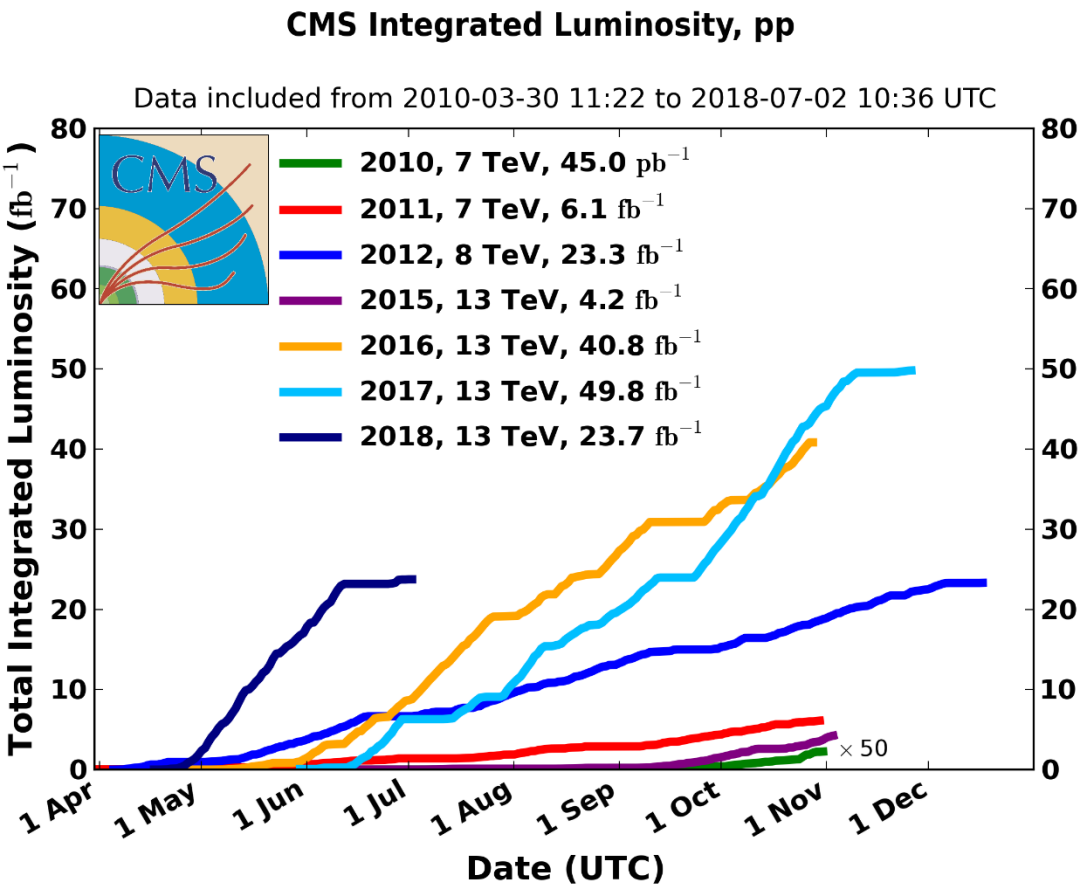

Figure 2-2 The CMS integrated luminosity delivered to CMS during stable beams in p-p collisions as a function of time over the period of 2010 – 2018 [9].

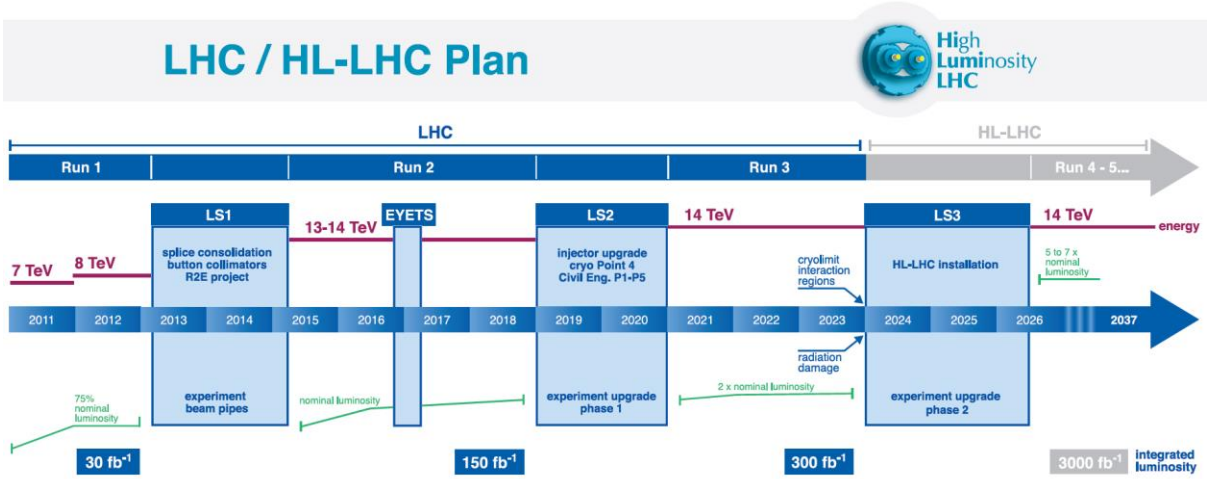

Figure 2-3 – The timeline of the LHC running, with the total integrated luminosity and energy [13].

The timeline of the LHC runs and shutdowns are shown in Figure 2-3, there is a long shutdown planned to take place at the end of 2018. Run 3 will be running at the start of 2021-2023, which leads onto a major upgrade, which will be the High-Luminosity LHC. For this phase of the experiment, the integrated luminosity is expected to reach 10 times by the end of run 3.

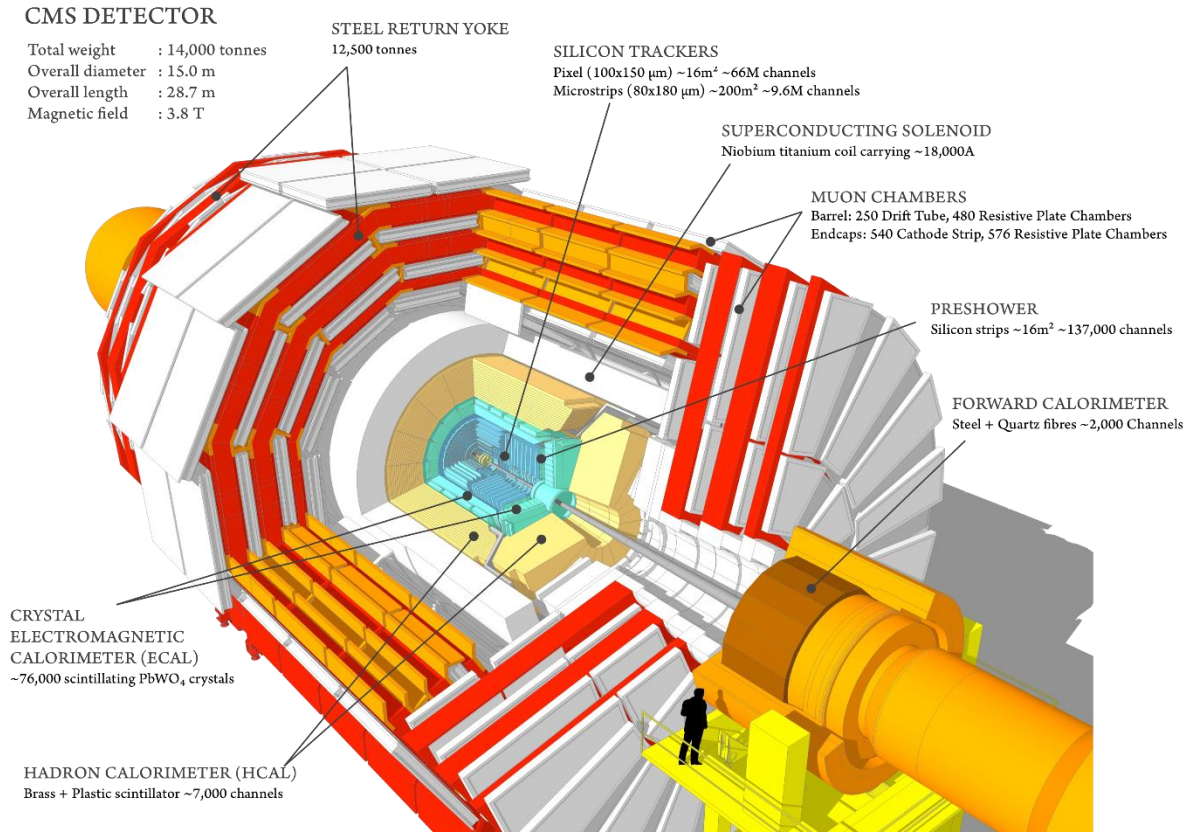

Figure 2-4 – The subdetectors of the CMS are visualised, detailing the structure of each subdetector [14].

The CMS detector is one of two general purpose detectors within the LHC, a visual representation of the CMS detector and its subdetectors is shown in Figure 2-4. The CMS detector has a total weight of 14,000 tonnes with an overall diameter of 15 m and length of 12.5 m [15]. The CMS experiment is designed around a superconducting 4 T solenoid magnet (operated at 3.8T), within which electromagnetic and hadronic calorimeters and the silicon tracker are placed. Outside of the solenoid is the massive iron return yoke of the magnet which is segmented to provide a number of instrumented layers with which the momenta of muons can be determined. The outline of the CMS detector with the typical interaction that occurs in each subdetector is shown is shown in Figure 2-5.

The total integrated luminosity accumulated over the runtime of 10 years is expected to be 500 fb^{-1}. This is the original runtime for phase 1 of the experiment. The experiment will now continue beyond this at a higher Lumosity: High Luminosity – Large Hadron Collider (HL-LHC).

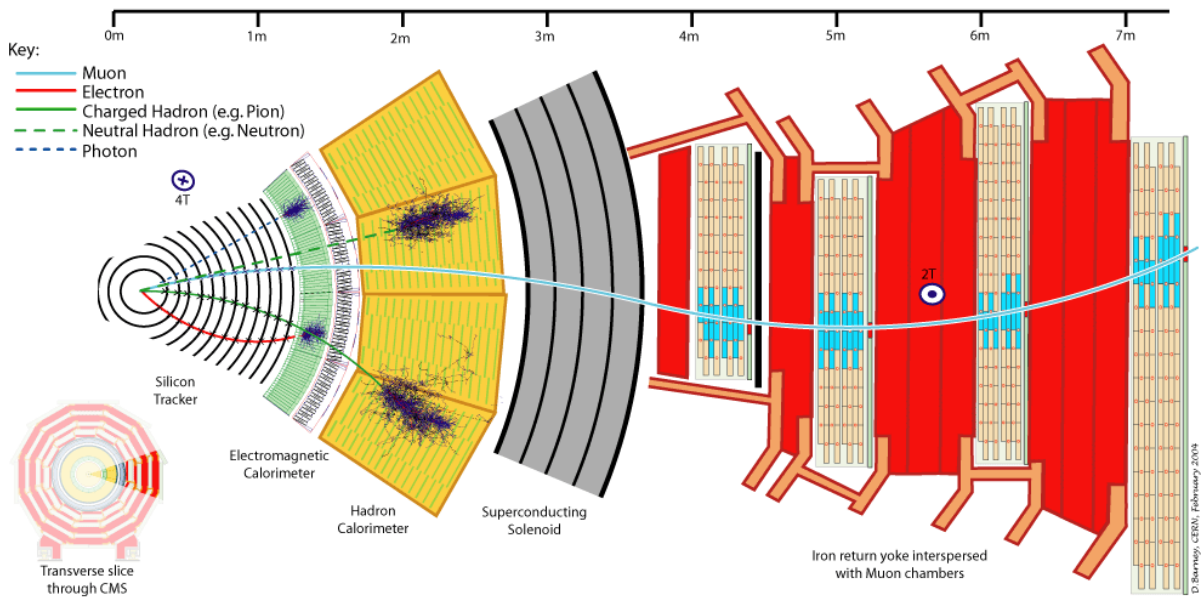

Figure 2-5 – Transverse slice through CMS, showing the components CMS is composed of. The typical interactions each of elementary particles with each subdetector is also shown (see key) [16].

2.2 Tracker

The tracker is the innermost part of the detector, receiving the highest number of particles and therefore, a large amount of radiation-induced from the particle fluence. Tracking the momentum of particles produced within the heart of CMS is crucial to understand what is really happening when the collisions occur within the detector. This is achieved by tracking the path of charged particles (high energy muons, electrons, hadrons and decay of very short-lived particles) within the magnetic field of CMS a number of layers, with accuracies to 10 µm in the transverse plane, 25 µm along the beam axis and 20 µm in the radial direction [17]. The silicon tracker has two components: the pixel layers and the strip detectors and is placed within the CMS superconducting magnet. The entire detector is constructed from 66 million silicon pixels covering an area of 1 m^2 and 10 million microstrips covering an area of 200 m^2 [18]. These are placed in concentric cylinders around the interaction region of the LHC beams [18].

The tracker occupies the region between 4 cm to 110 cm in radius and up to 280 cm either side of the collision point. For the tracker the best efficiency for the tracking is based in the barrel region of $|\eta| < 0.9$ with a rate of 94%, the region between $0.9<|\eta|<2.5$ has a efficiency of 85% [19]. The position of the primary interaction and secondary decay vertices are determined by the charged particle tracks. The tracker can keep up with the high rate collisions of the LHC at

a rate of 40 MHz, with temporal and spatial resolution measurements. The tracker is composed of two sub-detectors each with independent cooling, powering and read out. The inner pixel detector has a surface area of 1.1 m^2. The barrel of the tracker has three layers at 4.3 cm, 7.2 cm and 11 cm [20].

2.3 Electromagnetic Calorimeter

The electromagnetic calorimeter (ECAL) is hermetic and homogeneous and consists of scintillating lead tungstate crystals ($PbWO_4$) readout with avalanche photodiodes (APD) in the barrel and VPTs in the endcaps. The ECAL is fast and highly spatially granular, and radiation hard. It designed to withstand doses up to 4 kGy and $4x10^{13}$ n/cm^2 in the barrel region, and up to 25 times this within the endcaps. These doses will accumulate over the initial 10 year run of the detector which corresponds to an integrated luminosity of 500 fb^{-1} [21]. The estimated doses for the endcaps and particle fluences for 10 years of LHC operation are 0.5 kGy and $5x10^{13}$ n/cm^2 at the outer circumference of the endcaps. The inner region of the endcaps will experience an even higher dose at 20 kGy and $7x10^{14}$ n/cm^2 at $|\eta| = 2.6$ [15].

The high density of the $PbWO_4$ allows for a compact detector within the CMS. The region of space within the CMS detector is described by pseudorapidity η, this correlates with the angle of the particle relative to the beam axis to a spatial coordinate system. It is described as $\eta = -\ln[\tan\left(\frac{\theta}{2}\right)]$. The barrel region of the ECAL covers the pseudorapidity region up to $|\eta| = 1.48$, with the endcaps increasing this range till $|\eta|=3.0$ and with excellent energy and position resolution up to $|\eta|<2.5$, which matches the tracker coverage [22].

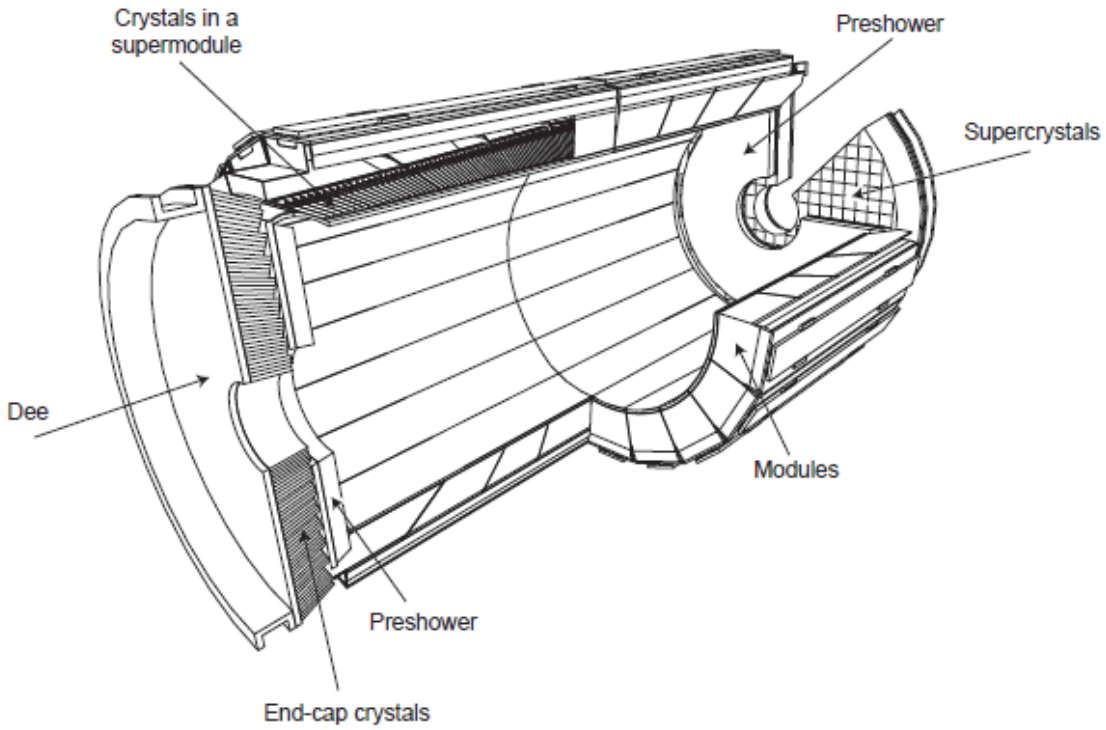

Figure 2-6 – This shows the layout of the CMS ECAL showing the positions of crystal modules, supermodules and endcaps, with the pre-shower in front [15].

The energy is measured by the ECAL through the scintillation process arising from electromagnetic showers in the lead tungstate crystals. The intensity of the light emitted from the crystals is linearly proportional to the energy of the shower from the initial electron or photon and is detected by one of the two types of photodetectors within the ECAL. The barrel region has 61,200, each crystal has a dimension of 22×22×230 mm^3. This covers a range of pseudorapidity $|\eta|<1.48$. With respect to the beam axis, it covers between 25.6° – 154.4° [23]. The two endcap regions contain a total of 14,648 crystals, each with a dimension of 30×30×220 mm^3. The endcaps cover a range of pseudorapidity $1.48<|\eta|<3.0$. With respect to the beam axis, it covers between 25.6° – 5.7° and 154.4° – 174.3° [23].

The VPTs developed that are currently being used in the CMS ECAL endcaps, were designed to withstand high radiation environments for more than 10 years. The ECAL barrel will experience an integrated gamma dose of up to 4 kGy during 10 years of operation. However, the endcaps will experience a integrated dose of several tens of kGy in the most central regions of the endcaps at 200 kGy [24]. Fast hadrons (mostly pions) will provide the bulk of the damage to the ECAL, which is due to the interactions which take place within the ECAL itself [25]. Additionally, the electromagnetic showers inside the crystals also produce a significant dose

[25]. Key requirements when designing the VPT were to provide a significant gain in a 4 T magnetic field, be ionising radiation tolerant, and be compact [23].

2.3.1 Lead Tungstate Crystals

. Within CMS there is more than 11m^3 of lead tungstate. The crystals in the Endcap ECAL are glued onto the ends of the VPTs. The scintillating light is 'guided' to the photocathode of the VPT by a mixture of direct and reflected visible photons. These properties of lead tungstate crystals make it a good choice for the ECAL – it has short radiation length (X_0) of 0.89 cm, is radiation tolerant and has a fast scintillation time at room temperature, 80% of the light emitted is within 20 ns [23]. The crystals chosen for this application must be fast, to be compatible with the LHC beam crossing that occur every 25 ns. Consequently, the ECAL readout had to be designed to operate within a sampling frequency of 40 MHz [23].

The photon yield per GeV of the deposited energy of the crystals must be high enough to keep the stochastic contribution to the energy resolution small [25]. Additionally the response longitudinally should be uniform to avoid a large constant term within the energy resolution for high energy particles [25].

In the barrel, the shape is slightly tapered with a crystal length of 230 mm. A thin-walled (0.1 mm) alveolar structure called a submodule is used to contain the crystals. These submodules contain 400 or 500 crystals depending on their position in η. Four modules are put together to form a supermodule containing 1,700 crystals [15].

The endcaps are cylindrical caps at the ends of the barrel of the ECAL. It also consists of a similar layout of crystals, with 5×5 crystals grouped together (supercrystals) within an alveoli structure made of carbon fibre. Each endcap is split in half, comprising 2 Dees, with each Dee holding 3,622 crystals. The crystals have a rear face cross section 30.0×30.0mm^2, a front face cross section 28.6×28.6mm^2 and a length of 220 mm (24.7 X_0) [15].

Figure 2-7 – An endcap Dee, showing the supercrystals and individual lead tungstate crystals within each supercrystal [15].

The crystals are optically clear, fast and radiation hard, with a high density of 8.28g/cm^3, a short radiation length of 0.89 cm and small Moliere radius of 2.2 cm [25]. The scintillation light emitted from the crystals is mainly between 420 – 430 nm (violet-blue) [15]. The radio-luminescence of the crystals is shown in Figure 2-8, along with the longitudinal optical transmission.

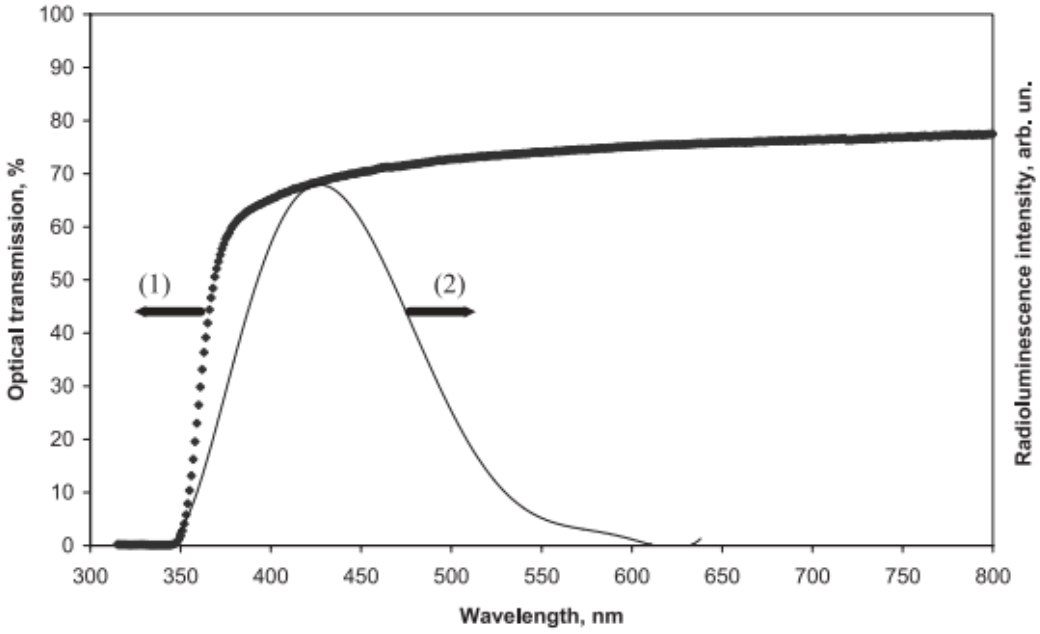

Figure 2-8 - Room temperature longitudinal optical transmission (1) and radio-luminescence (2) at steady state ^{57}Co excitation (122 keV) of PWO_4 CMS scintillation element [26].

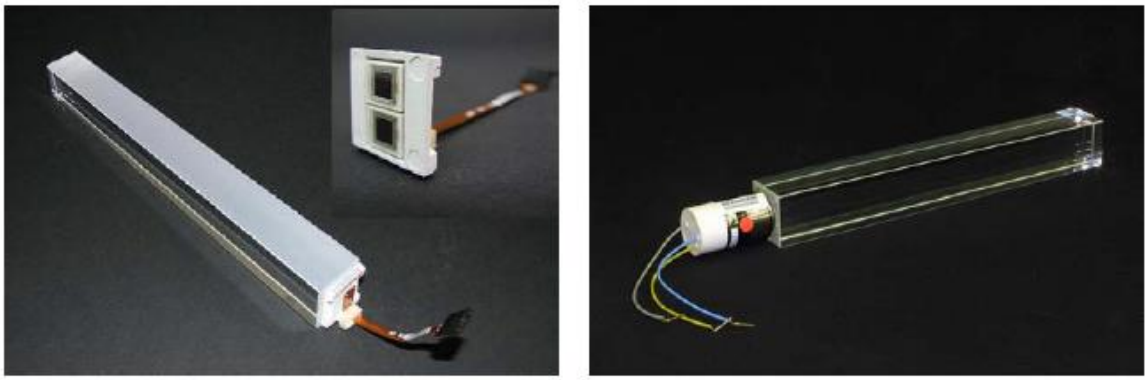

Figure 2-9 - Left: $PbWO_4$ crystal with an APD attached to the end. This is used within the ECAL barrel. Right: $PbWO_4$ crystal with a VPT attached to the end. This is used for the ECAL endcaps [15].

High levels of radiation and particle fluxes are expected throughout the runtime of the experiment, the crystals must be able to withstand a very harsh environment. Decolouration occurs from the high radiation level, the crystals have been present in. The ionising radiation produces absorption bands due to oxygen vacancies and impurities within the lattice [25]. This decolouration reduces the light transmission. This is monitored and corrected with a laser light that is injected and monitored to calibrate for the losses through the crystals. The transparency of the crystals is monitored every 40 minutes [27]. The laser system operated at 100 Hz during approximately 1% of the LHC beam abort gaps, with a period of 3 μs at the end of each beam cycle [28]. Running at this rate allows for the continued response of the crystals to be monitored without interfering with normal data taking of the LHC. To ensure redundancy is present within the system, more than one laser can be operated at different wavelengths to probe the transparency of the crystal [28]. From the permanent loss of transparency, the light will be collected at a higher rate when the emitting point is closer to the photodetectors [29]. This ultimately leads non-uniformity of the light collection, caused by the transparency loss of the crystal and consequently signal to noise ratio and the stochastic terms of energy both increase [30].

Since CMS has started running in 2011 the relative response to laser light has changed from 440 nm in 2011 to 447 nm from 2012 onwards, has been injected into the ECAL crystals which is measured by the laser monitoring system that is averaged over all the crystals in bins of pseudorapidity (η). The change of response in the ECAL channels for the running between 2011 – 2018 data taking shows a 10% change in the barrel which reaches up to 50% at $|\eta|=2.5$. The response closest to the beam pipe varies up to 90 % in response [31].

There are two types of damage to can occur to the lead tungstate crystals, these are:

1. Electromagnetic radiation – this type of radiation does not affect the scintillation process but does create a deficiency in the crystal light transmission through the crystal due to the development of colour centres. The transparency of the crystal can be reversed through temperature annealing at room.
2. Hadron irradiation damage – this damage is cumulative, and the loss of response does not anneal at room temperature like electromagnetic radiation. The transmission is seriously attenuated with the band edge of the transmission spectrum is shifted to higher wavelengths.

The water cooling system is a vital component within the ECAL and must maintain the temperature to a high precision. The crystals and PMTs must be kept within ±0.5 °C to maintain the energy resolution [15]. Temperature fluctuations in the system have a direct correlation to the light yield of the crystals, approximately at -2% per °C [32]. As the number of scintillation photons emitted by the crystals and the amplification of the APDs has a negative temperature dependent, the variation of the signal with temperature is -2.3%/°C [33]. The VPTs in the endcaps dependence on temperature sensitivity of the crystal light yield is negligible, with approximately about 0.1% /°C is assumed [32].

2.3.2 Photodetectors

2.3.2.1 Barrel: Avalanche Photodiodes

For the CMS barrel APDs have been used, which were specially developed for the experiment by Hamamatsu (type S8148). They have a reverse structure – the bulk n-type silicon is behind the p-n junction) [15]. The APDs have an active area of 5×5 mm^2 and they are mounted to each crystal in pairs. Both APDs are read out in parallel and are operated with an avalanche gain of 50. These devices are unaffected by the magnetic field and provide an acceptable signal to noise ratio, however, they are not sufficiently radiation hard to be used in the endcap region due to increased leakage currents.

2.3.2.2 Endcaps: Vacuum Phototriodes

The Vacuum phototriodes (type PMT188) used for the ECAL endcaps, were specially developed for CMS and manufactured by the National Research Institute Electron in St. Petersburg. VPTs have a single gain stage. Due to this, they have a very low gain compared to that of a PMT with high multi-stage gain. To match the overall response to the much higher quantum efficiency but a lower active area of the APDs in the ECAL barrel, the VPTs needed to have a minimum active diameter of 21 mm to provide the same signal from the lead tungstate

crystals compared to the 50 mm^2 active area from two APDs [34]. To be able to operate the devices within a 4 T magnetic field, they had been designed with a very fine anode mesh with a 10 μm pitch. This is to catch the tightly spiralling electrons affected by the magnetic field, with a fine mesh providing a better chance that a coarse mesh to catch those electrons that would be lost, or go on to hit the side of the tube [34]. The outer diameter of the chosen VPT for the endcaps is 26.5 mm. the effective photocathode diameter is 19 mm, with an active area of ~ 280 mm^2 and a typical quantum efficiency of 20% at 420 nm. The photocathode has a bialkali (SbKCs) composition, with a mean efficiency 22% at 430 nm and mean gain of the VPT is 10.2 at 0 T [24]. Within CMS the VPTs are in a 3.8 T magnetic field and the VPTs are at a varying range of 8° to 24° to the field direction. Due to the strong magnetic field, the VPTs response is slightly reduced - approximately ~ 90% compared to at 0 T [15].

2.4 Hadron Calorimeter

After the ECAL, the next sub-detector as one moves out radially within CMS is the Hadron Calorimeter (HCAL), this measures the energy of hadrons – which are particles composed of quarks and gluons (for example protons, neutrons, pions and kaons) [35]. The HCAL is a brass/scintillator sampling calorimeter, meaning the particles position, energy and arrival time is determined from showers generated in the brass absorber and detected in the alternating layers of the scintillator. Wavelength shifting fibres are used to translate and transport the scintillation light to the photodetectors, which in this case are hybrid photodiodes. The HCAL is composed of four sections: Barrel, Endcap, Outer and Forward.

The barrel region covers |η| from 0 to 1.4, the barrel and endcap share the region |η| range from 1.3 to 1.4, and the endcaps cover the |η| region of 1.3 to 3.0. The barrel region is built of 18 wedges each covering a 20-degree region in ∅, which is further divided into four 5-degree sections. Due to the space limitations within the magnet, the barrel thickness has been limited to 5.8 hadronic interaction lengths at η=0 which increases to 10 interaction lengths at |η|=1.2. The outer region of the HCAL is outside the solenoid cryostat, which approximately 5% of all hadrons above 100 GeV deposit energy in [36]. The front-end electronics of the HCAL are located within the muon detectors at various locations. Each of the barrel and endcaps tower has 17 scintillator layers, read out by an embedded wavelength shifting fibre and the signals are added optically. The optical signals are detected by a hybrid photodiode (HPD) within the barrel, endcaps and outer region. The forward region is detected by eight-stage PMTs with a borosilicate glass window. These register the Cherenkov light produced by the charged shower

particles in the quartz fibres [36]. To ensure the system is operating as expected and to calibrate it as it is gets damaged through the high radiation fluences, the system uses laser and LEDs similarly to the ECAL.

2.5 The Superconducting Magnet

The CMS magnet is a superconducting solenoid which has a uniform 3.8 T magnetic field. It has a 6 m diameter and is 12.5 m in length, with the capability of storing up to 2.6 GJ with a weight of 10,000 tonnes of the return yoke [37]. The magnet is an integral part of the CMS experiment as all the other subdetectors will be supported by it. The return yoke is a 12-sided structure which is further divided into three main components: the barrel yoke and the two endcaps. The barrel yoke is split into five-barrel rings each with a mass of 1,200 tons and can move in the axial direction on air pads which give access to the barrel muon stations. The endcap yoke is built from three independent disks which again can be moved on air pads to provide access to the forward muon stations and the inner subdetectors [37].

The magnetic field enables the momentum of charged particles that are produced in the primary collisions to be determined. The magnetic field within the detector causes the charged particles to move in helical trajectories. One of the most important aspects of the magnet are the parameters that were chosen during the setup of the magnet for the muon momenta. It was essential to get good momentum resolution without taking space from the muon chambers. The inner coil radius of the magnet is large enough to fit the tracker, electromagnetic calorimeter and hadron calorimeter are placed within the magnet coil. The magnet flux is returned through a 1.5 m thick saturated iron yoke instrumented with four stations of muon chambers [38].

2.6 The Muon Detectors

The Muon Detector is placed outside the solenoid magnet. Muons are charged particles which are 200 times heavier than electrons and positrons and they do not interact via the strong force. This property combined with the high mass, relative to the electron, allows muons to travel significantly further than the electrons and positrons given the same thickness of the material. By placing the detectors outside of the solenoid magnet and inside the magnetised return yoke, they mainly see only muons as other particles (other than neutrinos) have already interacted within the calorimeters. The muon detectors use three types of gaseous detectors: drift chambers on the barrel, cathode strip chambers on the endcaps, which have good spatial resolution and will ensure the precise position of the muon is measured and resistive plate

chambers which are placed in both the endcaps and barrel region. The latter provides a redundant and complementary trigger with a time resolution of a few nanoseconds [39]. The cathode strip chambers spatial resolution from the inner ranges from 52 μm to 145 μm for the outer chambers for the 2018 data [40]. With the resistive plate chambers resolution for the barrel ranging from 0.93 – 1.4 cm and the endcap ranging from 0.87 to 1.2 cm [40].

Chapter 3. Vacuum Phototriode

High energy physics experiments generally operate detectors within a magnetic field to enable momentum measurements to be performed on charged particles. Photosensors are used within these experiments to detect scintillation or Cerenkov light from a range of detectors, primarily calorimeters. Conventional multi-stage photomultiplier tubes cannot operate in high magnetic fields and many silicon photosensors suffer from hadron induced radiation damage which causes high leakage currents. VPTs are a single gain-stage device that is able to operate within a high magnetic field at angles up to 40° in axial [41]. Most PMTs are unable to produce a gain within a magnetic field, due to the electrostatic focusing, though some PMTs with a transmissive mesh dynode can provide a reasonable gain up to ~ 1 T [41].

An example of a PMT device is shown in Figure 3-1. For this type of device, the incoming photon hits the photocathode and photoelectrons are released through the device; in the first step, the photoelectrons are focussed through an electrode which these are then accelerated towards a series of dynodes where at each stage an increased number of secondary particles are created; the final step the signal is read-out through the anode. When a magnetic field is present the electrons within the tube follow these field lines whilst spiralling around these field lines. This can have an adverse effect on the output gain of the tube. The cascading secondary emission (SE) through the multi-stage dynodes does not occur or is not effective enough to produce a sufficient output. For these reasons, alternative devices have been used within CMS's ECAL.

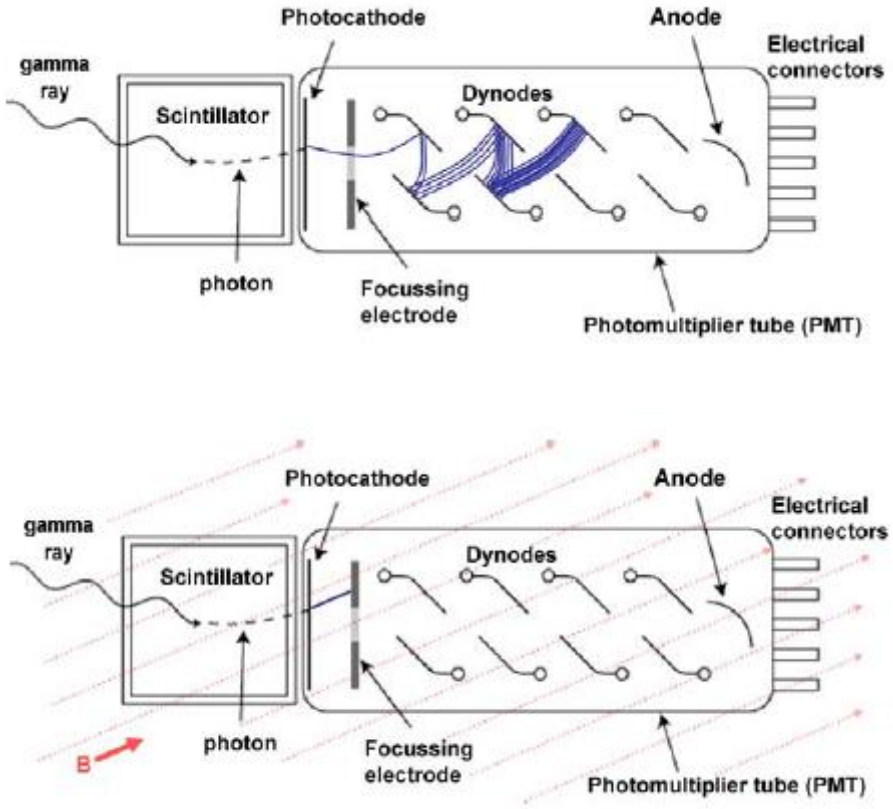

Figure 3-1 – Top image: a PMT at 0 T magnetic field. Bottom image: a PMT present within a magnetic field. The electrons within the VPT will following the magnetic field lines (red lines), resulting in minimal gain [1].

3.1 The principle of the VPT

VPTs are a single gain stage device that is used to convert a light source into a signal of amplified electrons that is proportional to the light magnitude. The VPT consists of a Cathode, Anode, Dynode electrode structure within a glass cylinder envelope under high vacuum.

A VPT contains three electrodes:

1. Photocathode – This is an electrode that has an emissive material placed inside a glass envelope, under high vacuum, which is used to convert light into photoelectrons.
2. Anode – Consisting of a fine metal mesh structure which is defined by its transparency and depth. The transparency is measured in lines per mm. It has the highest electric potential out of the 3 electrodes and is used to collect the signal.
3. Dynode – The dynode electrode provides gain. It is covered in a material that has a good secondary emission coefficient. As electrons hit the dynode, secondary electrons are created that are approximately proportional in number to the incident electron

energy. Thus, the VPT gain can be varied by altering the potentials on the anode and dynode.

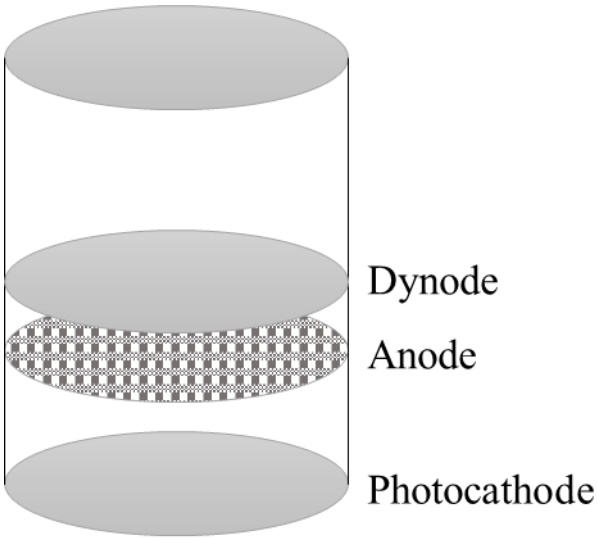

Figure 3-2 – Structure of a VPT, with the photocathode, anode grid and dynode.

VPTs are used in numerous experiments, some these are listed in Figure 3-3. With the types of scintillator used along with the VPTs, and some of the characteristics: the RMS noise and the cathode and anode.

Reported and estimated (denoted by 'a') characteristics of some experiments using VPTs.

Experiment	Scintillator	VPT Type	rms noise at the		Energy-equivalent noise, σ^{E}_{noise} [MeV]
			cathode, σ^{C}_{noise} [photoelectrons]	anode, σ^{A}_{noise} [electrons]	
CMS[a]	$PbWO_4$	RIE FEU 188	80[b]	1100[b]	140
DELPHI	Pb-Glass	Philips[c] XP1201/LF		270	
OPAl	Pb-Glass	RTC 1501/LF	14[b]	260	10.7
CMD-2	BGO	produced by BINP	34[b]	480[b]	0.6
KEDR	CsI	Hamamatsu R2184-01	20[b]	360[b]	0.02

[a] Results correspond to a 3 × 3 matrix of individual detectors.
[b] Estimated from reported numbers.
[c] Presently Photonis.

Figure 3-3 – Showing the characteristics of the VPTs used in some physics experiments, including CMS, DELPHI, OPAL, CMS-2 and KEDR [42].

3.2 Photocathodes

Photocathodes operate on Einstein's photoelectric effect. For photoemission to occur the energy of the incoming photon must be larger than the work function [43]. Looking at the window of the VPT at the photocathode, can give a good indication of the state of the device and if it is functional. The colour of the photocathode under white light can also reveal some of the basic properties. Bialkali photocathode appear yellow to the human eye, under white light [43]. The photocathode within the RIE-188 tube used in CMS is planar semi-transparent

and deposited on the inner surface of the glass faceplate. To match the spectral sensitivity to the emission spectrum of lead tungstate, a bialkali photocathode (SbKCs) was chosen.

The photoelectron energy spectra are available for commercially produced photocathodes; however, the details of their angular distribution is limited. Manufacturers generally assume there is an Lambertian angular distribution for any simulations they make [43].

3.3 Anode Mesh

The anode mesh is a metallic grid-like structure with inter-crossing vertical and horizontal lines. This is the second electrode in the VPT and this is where the signal is read out. The anode mesh has a transparency, which is the percentage of the area that is holes compared to the total area of the mesh [1]. For the RIE tube, the transparency is 50%, meaning that as the photoelectron is released from the photocathode they travel through the VPT, approximately 50% of the photoelectron will be absorbed by the anode mesh and the remaining photoelectrons will continue to travel through the VPT towards the dynode.

Ideally, the surface area of the photocathode and anode would be the same. However, this does not occur as the anode mesh is supported by a solid metal ring at its outer circumference [23]. Therefore, the active diameter of the anode is less than the photocathode and the diameter of the mesh is approximately 10% less than the diameter of the anode plate. This result reduced the gain slightly (20%) [23]. The gain of the tube is strongly dependent on the region of the photocathode which is illuminated, fewer photoelectrons are lost within the tube if the centre of the photocathode is illuminated rather than the edges.

The anode mesh casts a shadow on the dynode, therefore secondary electrons are only emitted in areas that are illuminated by incident photoelectrons. At 0 T the secondary emitted electrons have a distribution of an angle that is relative to the VPT axis. This smooths out the grid-like distribution of their spatial distribution by the time they reach the anode plane.

In a strong magnetic field, the travelling electrons move in tight spirals about the magnetic field lines. This cyclotron radii are only a few microns in a magnetic field of a few Tesla [23]. The cyclotron motion produced has a radius ρ that is shown in equation (3-1), with an invariant period τ given by equation (3-2) where v_T is the transverse velocity component, m is the secondary emission coefficient, e is the charge of the electron and B is the B-field.

$$\rho = mv_T/Be \tag{3-1}$$

$$\tau = 2\pi \mathrm{m}/\mathrm{B}e \qquad (3\text{-}2)$$

In the transverse plane, any v_T gives rise to a cyclotron motion in a circle of the radius with an invariant period [44].

One important factor on how the VPT will behave within a magnetic field is the physical size of each hole in the anode mesh, i.e. the overall transparency of the anode mesh. A finer mesh has a higher probability of capturing the electrons spiralling about the field lines. This gives an increased chance of the electrons colliding with the anode mesh. The probability that the electrons that will hit the mesh also increases if the field lines are angled to the axis of rotational symmetry of the VPT. However, for a phototriode configuration, it is required that some of the electrons travel through the anode mesh to go on and hit the dynode and produce SE. Not enough electrons hitting the dynode results in a smaller gain which results in excess noise [34].

The studies by Bajanov et al. [34] shows how different transparency meshes effects the gain of the VPT when placed in a magnetic field at different angles, in particular the effect of the gain for magnetic field strengths going from 0 T to 1.4 T, at a higher angle of 30°. The sizes of mesh are measured based on the number of lines per 1 mm. The sizes used were 30, 60 and 100 lines per mm. The VPTs were illuminated in the centre of the photocathode, with the 100 lines per mm showing the highest gain output from varying. This is most likely due to the high angle the photoelectrons are travelling through the VPT and therefore have an increased chance to hit the sides of anode mesh rather than directly front on for angles less than <30°. Also, as the VPTs were only illuminated at the centre, no electrons were lost by hitting the side of the tube whilst travelling through the VPT. This indicates the illumination of the photocathode position is also an important factor to consider when trying to maximise the gain of the VPT.

This anode mesh has a pitch of 10 μm, which is 100 lines per 1 mm. Photoelectrons will pass through the gaps of the anode mesh, but this also increases the probability that the secondary electron will pass through the same gap in the anode mesh as its incident photoelectron came through [23]. This will reduce the overall gain. For cases where the magnetic field is not parallel to the tube axis, the photoelectron can be directed to the outer wall of the VPT before it reaches the electrodes leading to a reduction in overall gain. Another effect to be aware of when placing VPTs in a magnetic field, at an angle to the field, is the thickness of the anode mesh. The electrons are travelling in a tight spiral and if they are not at the normal position to the anode electrode, the electrons could hit the inner mesh lining as it travels through the gaps [23]. This

effect can be seen in Figure 3-4, which shows the increase in the relative anode response as the angle varies from -90° to + 90°. The response is at its maximum at approximately ± 30° and decreases sharply for angles above +40° and below -40°.

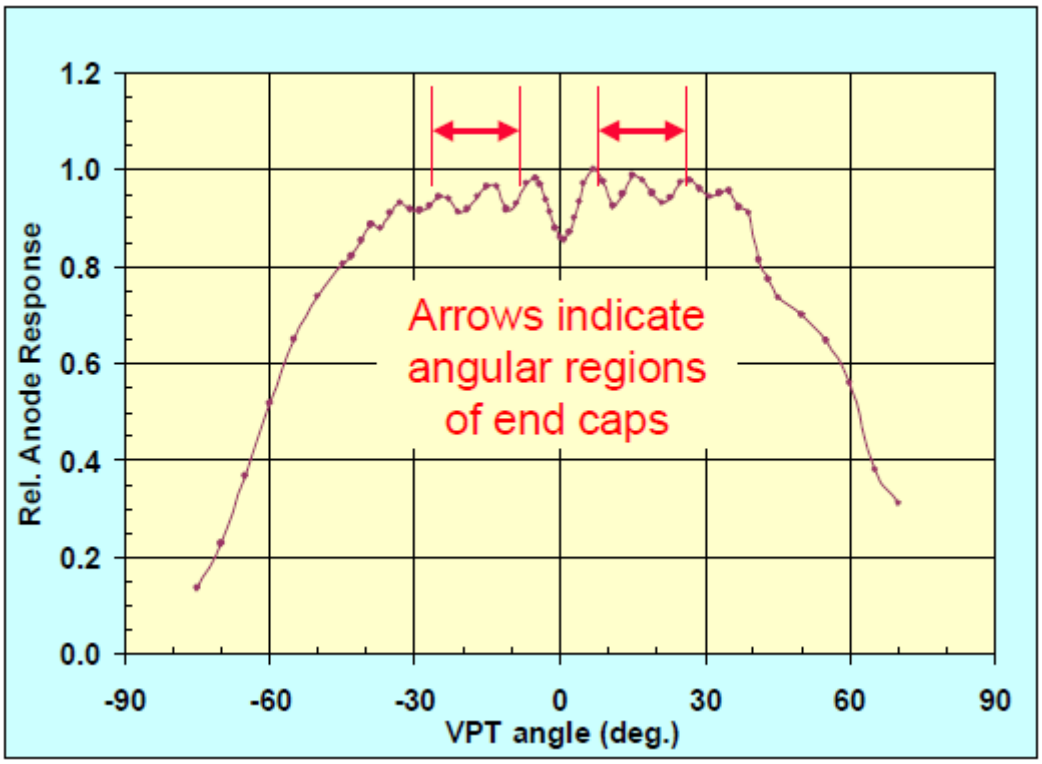

Figure 3-4 – The response of the RIE-188 VPT that is used within CMS endcaps, is placed in a 1.8 T magnetic field with varying the angle of the VPT to the magnetic field between -90° to + 90° [24].

3.4 Dynode Secondary Emission

The dynode is the third electrode within the VPT whose surface is coated with the same material as the photocathode (SbKCs). Photoelectrons hitting the dynode are absorbed, the kinetic energy of the electrons hitting the dynode is proportional to the cathode-dynode potential difference. Each photoelectron with an energy of 800 eV that hits the dynode produces on average 20 secondary electrons [23]. Ideally, SE should only occur from the dynode, and not any other internal structure.

Figure 3-5 shows 4 main scenarios, excluding backscatter, that can occur within a VPT. In the first scenario, there is a direct hit on the anode from the initial photoelectron. The second scenario is the photoelectron emitted from the photocathode passes through the anode mesh and directly hits the dynode, however it does not produce secondary electrons (due to insufficient kinetic energy). The third scenario is the same as the second scenario but there is sufficient energy to provide secondary electron emission, which goes on to be absorbed by the

anode mesh. Another scenario that can occur is the secondary electron emission can have some electrons (tertiary electrons), which as they are accelerated back towards the anode pass through the partially 50% transparent mesh. As they are attracted back towards the anode the electrons kinetic energy reduces to zero and are pulled back towards the anode (which has the greater electric potential) – this can cycle back and forth until it eventually hits the anode. It is assumed that the tertiary electrons will produce negligible amount quaternary electrons [23].

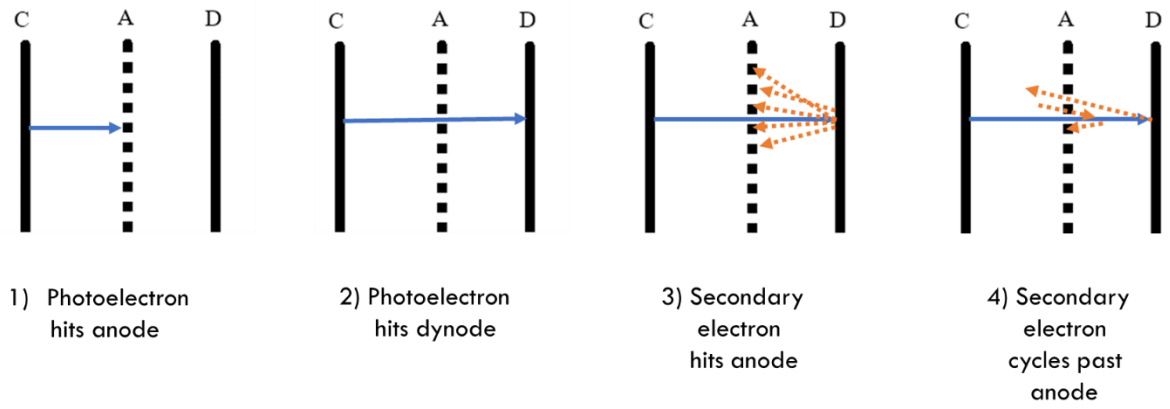

Figure 3-5 – Four main scenarios that are most likely to occur within the VPT. 1) the primary photoelectron hits the anode and gets absorbed. 2) The primary photoelectron goes through the anode mesh and gets absorbed by the dynode. 3) The primary photoelectron goes through the anode mesh and hits the dynode to produce secondary electrons that are directed back towards the anode mesh and get absorbed. 4) The primary photoelectron goes through the anode mesh and hits the dynode to produce secondary electrons that head back through the anode mesh.

During each of the collision stages, there is a chance that the electron will backscatter as it hits the anode or dynode electrode, instead of being absorbed and generating true secondary electrons. The many scenarios which could occur are shown in Figure 3-6.

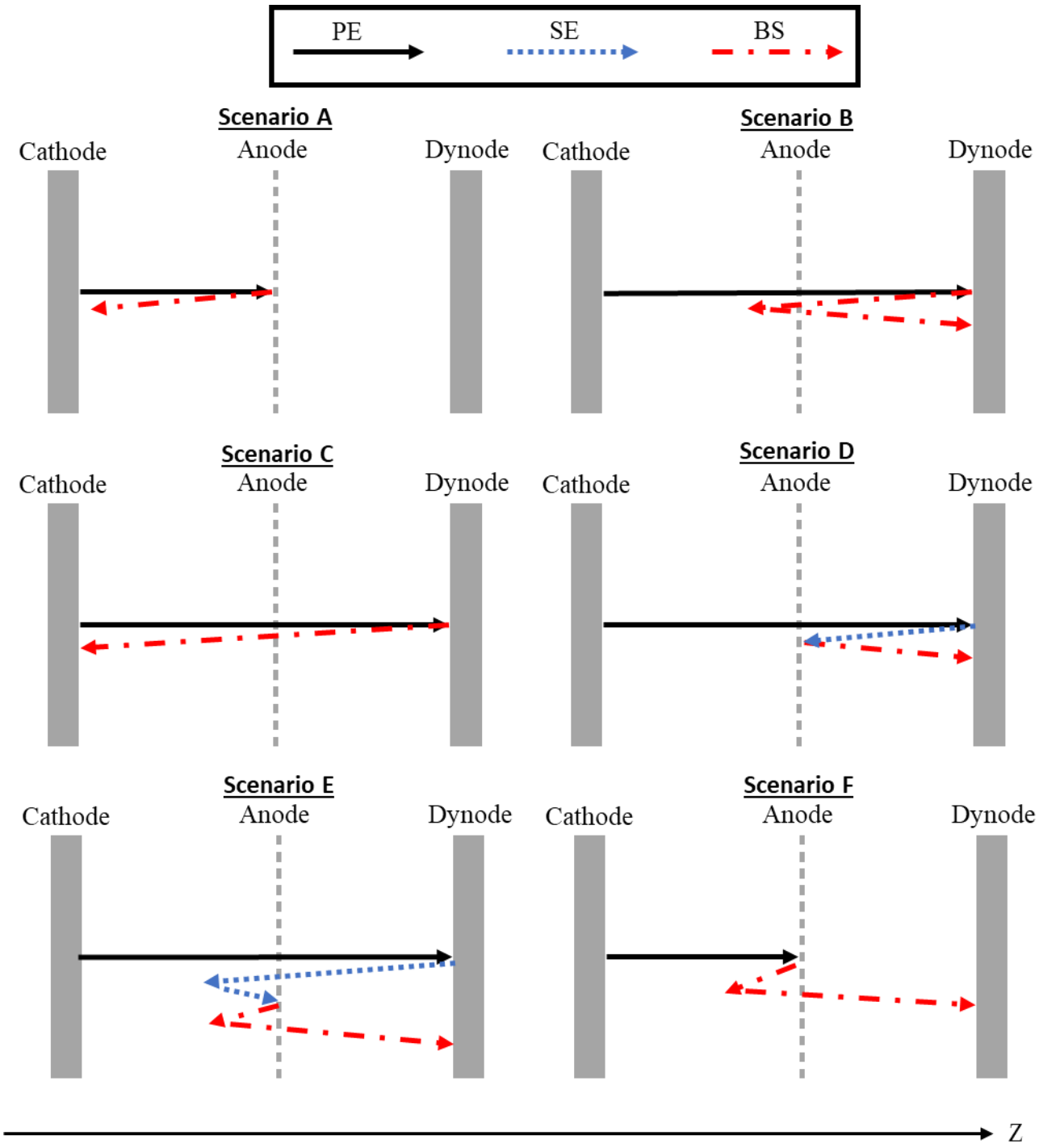

Figure 3-6 – Examples of backscatter scenarios labelled A-F.

Figure 3-6 illustrates the different scenarios that can occur when electron backscatter is considered. Scenario A is when backscatter is produced when the primary photoelectron hits the anode mesh and causes backscatter to go back towards the cathode, the probability of this (or scenario F) occurring is 20% for the VPT used in CMS. Scenario B occurs when an electron hits the dynode and backscatter is sent towards the anode mesh, which it goes through and cycles back through the anode mesh to go and hit the dynode. Scenario C is when an electron

hits the dynode and the backscatter heads through the anode mesh and hits the cathode. The probability of either scenario B and C occurring is 10%.

Scenario D occurs after secondary electrons are produced at the dynode which go on to hit the anode, from which backscatter is produced that heads back towards the dynode. Scenario E occurs when secondary electrons produced from the dynode go through the anode mesh and then hit the anode mesh when cycling back, where backscatter is produced from this collision. The backscatter heads towards the cathode but cycles back to go through the anode and hit the dynode. The probability of scenario D or E occurring is 50%, due to the 50 transparency of the anode mesh. Finally, scenario F occurs when the primary photoelectron hits the anode mesh, and backscatter is produced that heads towards the cathode but cycles back and goes through the anode mesh to go on and hit the dynode.

3.5 The Response in a Magnetic Field

The response of the VPT can be affected by the uniformity of the illumination of the photocathode in a magnetic field. How the photocathode is deposited within the VPT under consideration here, means that it covers the complete inside of the faceplate of the VPT and some of the outer walls as well. At 0 T the electrons travel along the electric field line and travel efficiently to the dynode and anode, using the full surface area of the photocathode [23].

When the magnetic field is parallel to the axis of the tube, due to the nature of how the electrons spiral along the magnetic field, the photoelectron released from the edges of the photocathode are likely to miss the anode and dynode (as the diameter is smaller). Reducing the effect of the loss of response by increasing the magnetic field is only effective if the illumination is focussed towards the centre of the photocathode [23].

The gaps between the photocathode and the anode/dynode is also an important factor to consider when operating in a magnetic field with an angle. To reduce the number of electrons hitting the sides of the outer walls of the tube rather than the electrodes, the gaps between the electrodes have been chosen to be proximity focused. The gap between the photocathode/anode is 3.5 mm and anode/dynode are 2 mm.

Overall, the probability that an electron will pass through the anode mesh depends on several factors: the radius of the trajectory relative to the mesh size, the pitch of the helix, the thickness of the mesh and the angle between the axis of the helix and the plane of the mesh [23].

When the magnetic field is 0 T the gain of the VPT is determined by the secondary emission of the dynode and the transparency of the anode mesh. The back scattering in this case has a negative effect on the gain of the VPT. At magnetic fields of below 0.5 T, Bateman discusses the dip in the gain of VPTs. He states that in this region of B field the focus condition guarantees that a photoelectron passing the anode mesh hole at position y,z produced SE at the dynode at the same y,z position and refocussed back onto the same y,z position in the anode plane. Therefore, guaranteeing that the electrons will miss the anode mesh. The focussing effect depends on the precision of the structure and the uniformity of the magnetic field [44].

3.6 Radiation Effects

The VPTs used within CMS are placed in a very harsh radiation environment. Ionising radiation of the VPTs, over time, darkens the outer glass shell. Most of the VPT response loss occurs from the faceplate transparency loss and VPT conditioning, which are predicted to occur from residual gasses from inside the tube which can be ionised whilst being operated within the experiment and is accelerated to the photocathode causing loss of QE from the impact [45]. It is predicted that all conditioning will have occurred within the tubes by the end of Run 1 in 2012 for regions $2.7<\eta<3.0$, for the regions $2.4<\eta<2.7$ by the end of 2016, the regions $2.1<\eta<2.4$ by mid-2018 (end of Run 2) and $1.8<\eta<2.1$ by the end of 2022, which is the end of Run 3 [45]. Figure 3-7 shows the response of the laser system when injected into the ECAL lead tungstate crystals for Run 1 and Run 2. The response change observed in the ECAL channels is up to 10% in the barrel, it reaches up to 50% at $\eta \sim 2.5$, the limit of the tracker acceptance, and is up to 90% in the region closest to the beam pipe. When there are no collisions within the LHC, there is some recovery in the crystal response. [46]

The chosen material had to survive in this environment for more than 10 years, whilst ensuring the loss in the response of the VPTs to scintillation light from the lead tungstate crystals was less than 10% for a received dose of 20 kGy. In the end, the material chosen was a borosilicate glass with enhanced UV transmission [23].

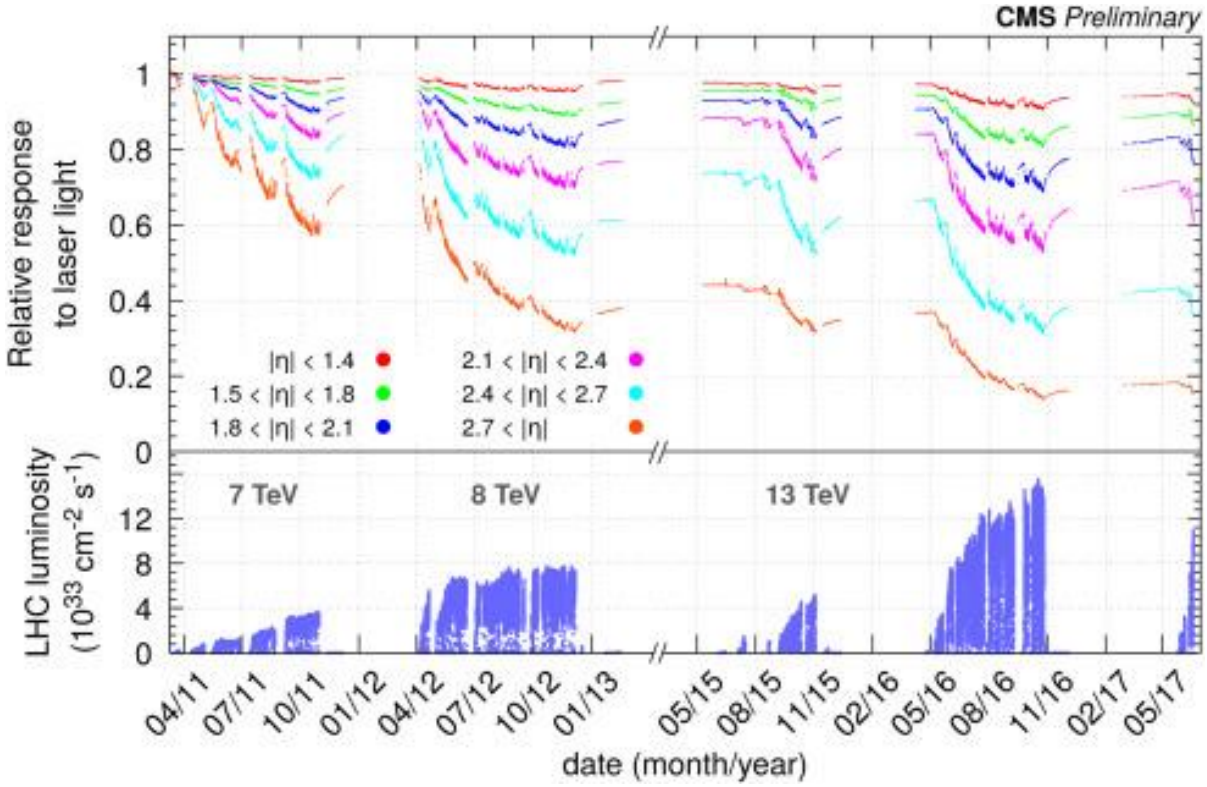

Figure 3-7 – The relative response to laser light injected in the ECAL crystals, averaged over all crystals in bins of pseudorapidity, for the LHC Run 1 and Run 2 data taking periods with the magnetic field at 3.8 T. The bottom plot shows the instantaneous LHC luminosity delivered during this time period. [46]

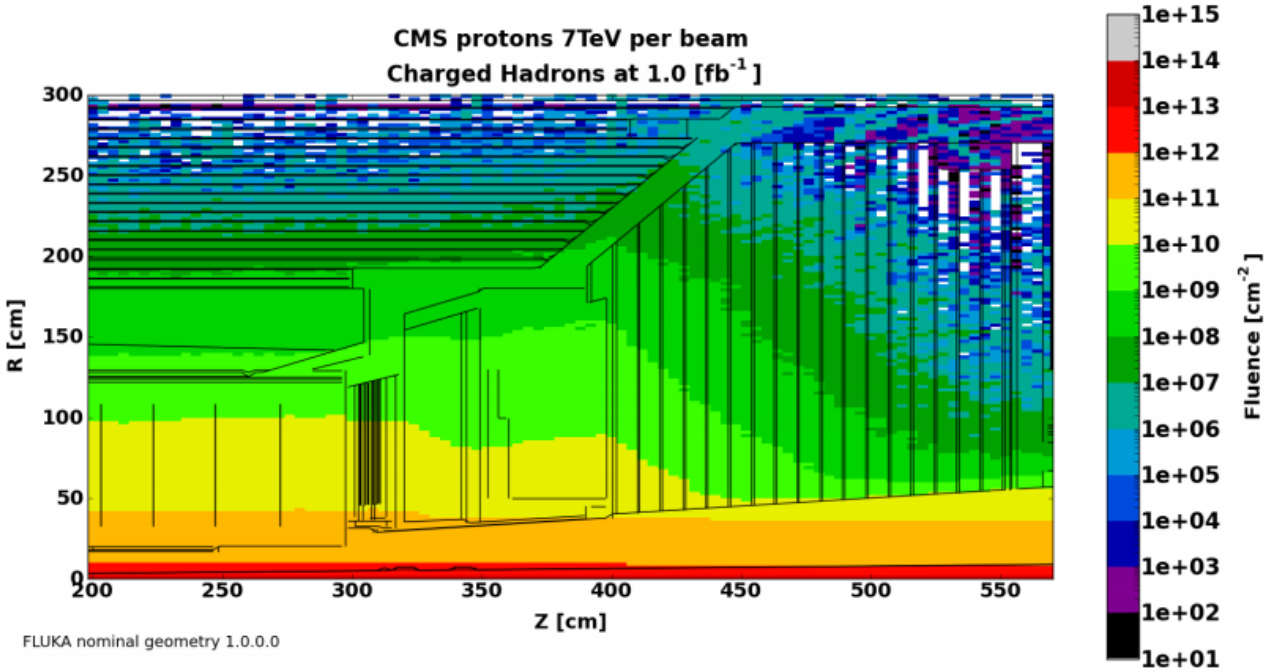

Figure 3-8 - The charged hadron fluence (cm^{-2}) for CMS using FLUKA [47]. The plot shows the charged hadron fluence in the calorimeters (ECAL and HCAL) for an integrated luminosity of 1.0 fb^{-1}. The ECAL endcaps and barrel are modelled as a single volume of lead tungstate. The HCAL endcaps and barrel are composed of brass and plastic scintillating layers.

By now it has been established that the environment within the CMS is a harsh radiation environment, the charged fluence for the tracker and ECAL is shown in Figure 3-8. However, it should be noted it is observed particles above a certain energy cause damage at a system level. As discussed in [25], neutrons below 20 MeV do not appear to cause significant damage to the crystals. If the crystals have a pre-existing point or structure defect when these are exposed to ionising radiation the defects can behave as traps or holes for the electrons. The creation of the colour centres is one of the main sources of optical damage and can go onto have major implications to the transmission of the scintillation light travelling through the crystals, as it creates discrete energy levels which absorbs some the light before it exits the crystal to the photodetector. Five possible colour centres have been discovered that are problematic within $PbWO_4$, they have the following absorption bands: 350-400, 470, 520, 620 and 715 nm [25].

One of the main points to remember regarding the signal loss in the endcaps, that are caused by the radiation damage to the lead tungstate crystals causing a reduced light output, is that the signal loss cannot be compensated for by increasing the gain of the VPT.

3.7 Helium Ingress

Most of the ageing caused to the VPTs is discussed in the previous section from the darkening of the faceplate from radiation and operation at high photocurrents. Another cause of damage degradation of performance is ingress of helium. Whilst the VPTs are operating, the helium can diffuse through the envelope of the tube. The helium pressure within the tube can rise, as the photocurrent ionises the helium this generates positive ions which are accelerated towards the photocathode [23]. This increase in pressure can cause secondary emission as additional electrons are generated from the photocathode, which increases the signal on the anode. The natural pressure of helium in the atmosphere is 0.7 Pa. When this pressure reaches 1 Pa, electrical breakdown starts to occur. The VPTs can be exposed to the natural helium in the atmosphere for an average of 10 years [41]. It was predicted that the pressure within a VPT would rise to 2.6×10^{-2} Pa. To preserve the longevity of operation of the VPTs for as long as possible, the region in which they are used is pumped with nitrogen. This is needed, as the concentration of helium would be higher than the natural pressure, as the cryogenic system within the LHC and CMS use helium for cooling the superconducting solenoid magnet. This effect is mitigated by nitrogen purging of the space around the VPT [23].

Chapter 4. Simulating VPT using COMSOL

With a good understanding of the VPT device used in CMS, the next step is to model the VPT using a physics simulation package. The modelling of the VPT is required to get a better understanding of how it functions within a given environment. This can include the effect of the external wiring on the VPT response, and other factors such as magnetic field interference. COMSOL is a Multiphysics simulation software [48] that can model realistic entities using complex 3D geometries paired with a variety of static and dynamic physics models. Model simulations can run in a stationary or time-dependent manner, in which the depth of the simulations can go to the particle level.

COMSOL is a suitable choice to model the VPT as it provides fewer constraints compared to other packages like SIMION 7, which was used by Yaselli [1]. It allows model development in the 3D space with a very advanced and complex simulation strategy to produce accurate simulations. The package also allows applying various physics to the model and its simulation environment such as magnetic force, RF, particle tracing and many more. This provide the ability to do an accurate and thorough analysis on a given physics task.

A simulation requires has a set of required tasks to be successful. These are: the geometry of each component required for the simulation is designed and created. Materials are then assigned to each of them to define their properties, and physics modules are applied to the components to model their characteristics and behaviour. Once the components are defined, a Finite Element Mesh is created to allow techniques of Finite Element Analysis (FEA), which are known as “studies” in COMSOL. These studies can be static or dynamic, based on the objective. Further analysis can be achieved through data analysis within COMSOL or exported to be used in another analysis software environment such as MATLAB.

Here, COMSOL has been used to model the VPT as realistically as possible and to run a thorough simulation to analyse its characteristics and its behaviour under certain conditions. This was achieved by using the VPT used in CMS to create a model with the same shape and dimensions. Once the model is designed, experiments were conducted to obtain the characteristics and behaviour of the simulated model, so it can be compared to the real VPT.

Beyond this, further experiments and analysis are done to understand the VPT model in the simulated environment.

4.1 COMSOL Configuration and Module Details

For the COMSOL simulations conducted throughout this thesis, a workstation with the following specifications was used: A four-core (plus hyperthreading) Intel i7 processor @3.7GHz and 48 GB of RAM was used. Within COMSOL, several modules were adopted to model the VPT. Each module enables certain attributes to be applied. These modules are discussed in the following sections.

4.1.1 AC/DC Module

The AC/DC module provides a set of physics interfaces that can give a detailed analysis of electronic components. It's a primary tool for modelling any form of electronics and electromagnetic tasks. The following interfaces are included [49]:

- Electrostatics
- Electric currents in conductive media
- Magnetostatics
- Low-frequency electromagnetics

With regards to the simulation, the interface that was required for the analysis of the VPT is Electrostatics.

4.1.1.1 Electrostatics

Electrostatics is a physics module within the AC/DC branch in COMSOL that is used to simulate the electrical behaviour of a model. This physics interface was used to compute the electric field, electric displacement and potential distributions within the model [49]. The studies for electrostatics were applied and measured on a static 2D/3D geometry model, where there is no time dependency required. This is in the form of applying potentials to each of the electrodes and the VPT body.

There are many available nodes for the electrostatics that are applied to component walls to define their properties and behaviour. Some of the relevant nodes for modelling a VPT are: Charge Conservation; Distributed Capacitance; Electric Displacement Field; Electric Potential; Accumulation; Ground; Initial Values; Surface Charge Density; and Zero Charge (the default boundary condition).

4.1.1.2 Use Case Summary

For the VPT simulation, the AC/DC module provided the Electrostatics interface that played a major role in defining the potential across the electrodes, as well as the charge conservation of the remaining geometry. Each of the electrodes within the VPT have their potential set based on the maximum operating conditions of the actual device, where the anode mesh is at 1000 V; dynode is at 800 V and the cathode is at 0 V.

4.1.2 Particle Tracing Physics Module

The Particle Tracing (PT) module was designed to give users access to tools that allow tracing particle trajectories within an external field. For the simulation, charged particles are the focus and the toolset for this within the PT module is Charged Particle Tracing (CPT), which is the pairing of particle tracing with the AC/DC module. Further details can be found under the PT module in the COMSOL reference manual [50]. The CPT physics module allows the user to model the behaviour of charged particles present in an electromagnetic forces environment. The module supports time-dependent studies, in 2D and 3D domains. COMSOL has many predefined forces which were added to help make as realistic model as possible, including elastic collision force, the electric force and magnetic forces.

For the models that have been created for VPTs, all the simulations were modelled with particles travelling are high speeds. COMSOL has a prebuilt function for relativistic corrections, which takes the relativistic effects on the particle mass into account. The particle mass m_p is computed using:

$$\boldsymbol{m_p = \frac{m_r}{\sqrt{1 - v.v/c^2}}} \tag{4-1}$$

where $\boldsymbol{v}$ is the particle velocity and $\boldsymbol{c}$ is the speed of light.

4.1.2.1 Particle Properties

Each particle has a few attributes that define its current state. These are as follows:

1. **Particle mass** - This is a predefined constant for the electron mass $9.10938188 \cdot 10^{-31} kg$. This is selected when the Newtonian option is selected as the formulation.
2. **Charge Number** – The default for this is the charge number for an electron, -1. This is displayed when Newtonian is selected as the formulation.
3. **Particle Velocity** – a vector can be entered by the user for the particle velocity, V. This option is only displayed when Massless is selected as the formulation. *The Massless*

formulation means that the particles follow streamlines of the particle velocity expression [50].

4.1.2.2 Wall Nodes

The wall node was used within the CPT physics to determine what happens to a particle when it meets a boundary. Firstly, a boundary was selected to act as a wall, then specific conditions were applied to it. A summary of these are shown in Table 4-1:

Table 4-1 - List of wall conditions and their purposes [50].

Condition	**Objective**
Freeze - (default)	Fixes the particle position and velocity at the instant a wall is struck. So, the particle position no longer changes after contact with the wall and the particle velocity remains at the same value as when the particle struck the wall. This boundary condition is typically used to recover the velocity or energy distribution of charged particles at the instant contact was made with the wall.
Bounce	Specularly reflects from the wall such that the particle momentum is conserved. This option is typically used when tracing microscopic particles in a fluid.
Stick	Fixes the particle position at the instant the wall is struck. The particle velocity is set to zero. This can be used if the velocity or energy of the particles striking a wall is not of interest.
Disappear	The particle is not displayed once it has made contact with the wall. This option should be used if the display of the particle location after contact with the wall is not of interest.
Diffuse Scattering	Bounces particles off a wall according to Knudsen's cosine law. That is, the probability a particle bouncing off the surface in a given direction within a solid angle $d\omega$ is given by $\cos(\theta)d\omega$ where θ is the angle between the direction of the particle and the wall normal. The total particle momentum is conserved.
General reflection	Allows an arbitrary velocity to be specified after a particle makes contact with the wall. This can either be done in Cartesian coordinates (default) or, if the 'Specify tangential and normal velocity components' option is selected, in the tangent-normal coordinate

	system. The velocity components can be functions of the incident particle velocity, energy or any other quantity. Note that the total momentum of the particle does not necessarily have to be conserved with this option.

4.1.2.3 Electric Force

This node was used to define the electric part of the Lorentz force. The particles were accelerated in the same direction as the electric field. The force should be specified through the electric potential or electric field. For the case where the field is computed in the frequency domain, the force can be computed by multiplying the field by the phase angle [49]. Also, piecewise polynomial recovery can give a more accurate representation of the specified electric field.

The Electric force is defined as:

$$F = qE \tag{4-2}$$

where q is the particle charge and E is the electric field value. When an electric potential is used to specify the electric field:

$$E = -\nabla V \tag{4-3}$$

4.1.2.4 Magnetic Force

The magnetic force node was used to define the magnetic component of the Lorentz force. This will cause the particles to curve perpendicularly to the particle velocity and magnetic field. A particle would remain at its original energy if there are no other external forces present along with a magnetic force. The force is specified via a magnetic flux density.

$$\vec{F} = q\left(\vec{v} \times \vec{B}\right) \tag{4-4}$$

Where magnetic field density, $\vec{B}$ is computed in the frequency domain and is a complex value. Therefore, the field must be cast into a real value which depends on the angular frequency and the simulation time [50]:

$$\vec{B}(t) = \text{real}\,(\vec{B}e^{j\omega t}) \quad (4\text{-}5)$$

4.1.2.5 Particle Field Interaction

This node was used if space charge effects are important by adding two-way coupling between the particle and field. That means the field exerts a force on the particles and the particles exert a space charge on the field. To see this effect the particles and fields must be solved simultaneously.

4.1.2.6 Use Case Summary

The CPT module can be used to model the behaviour of particles within the VPT. This includes tracking their trajectories, the total charge level, number of particles that include primary, secondary and beyond. The particle behaviour can also be observed when effected by a magnetic field, which is required to replicate the VPT used within CMS. This module is vital to understand how the VPT will behave.

4.2 Creating VPT Model in COMSOL

The geometry of the VPT model was based on the physical VPT used in the CMS experiment, which is the RIE FEU-188. The VPT structure is detailed in the CMS TDR [21], which was used as a guideline for creating the simulated model.

4.2.1 RIE FEU-188 VPT Structure

The RIE FEU-188 VPT Structure consists of four main components. These are the internal electrodes (Cathode, Anode Mesh and Dynode), and an outer housing shell. The dimensions for these are as follows [1]:

- The overall length of the tube is 46.0 mm
- The external diameter is 26.5 ± 0.7 mm
- The cathode and anode gap is 3.5 mm
- The anode and dynode gap is 2 mm

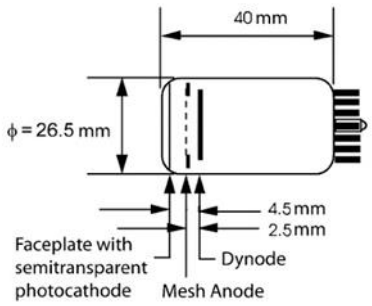

Figure 4-1 – Dimensions of the RIE FEU-188 VPT that is used in the CMS experiment.

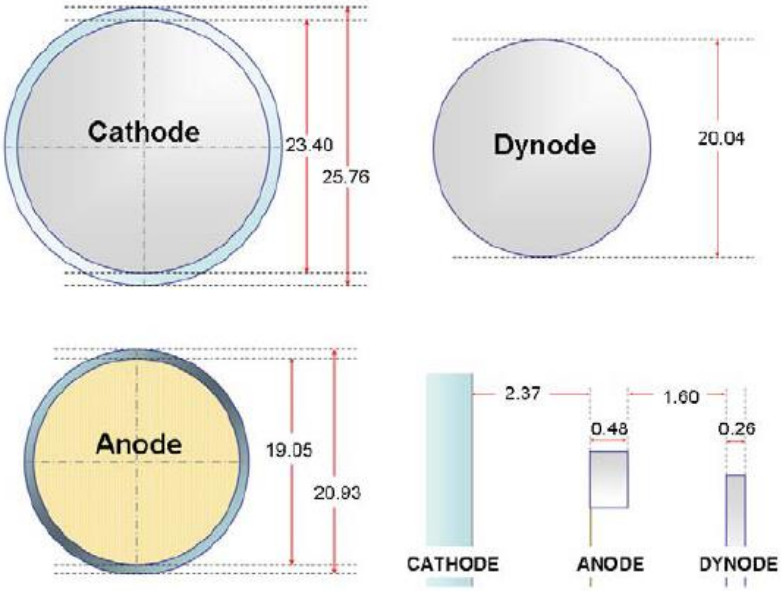

Figure 4-2 – The dimensions (mm) of the cathode, anode and dynode electrodes are shown, along with the distance between each electrode [1].

4.2.2 VPT Geometry Design

The geometry of the model was set up in a 3D space within COMSOL, using version 5.3. The 3D design for each component is a straightforward task in COMSOL, except for the anode mesh. This is explained further in the next section.

The VPT housing was created using a cylinder with the same diameter and length as the physical VPT. Within the housing, the dynode and cathode were also created using a cylinder shape with their respective dimensions. For the anode mesh, a different approach was taken to build its complex structure within COMSOL.

4.2.2.1 Anode Mesh Structure

Modelling the anode mesh was more challenging compared to the rest of the VPT, as it contained a fine mesh with a pitch of 10 µm (with a deviation of approximately ± 5.25%) and a depth of approximately 1.66 µm. Figure 4-3 shows the mesh from a dismantled FEU-188 VPT, showing the dimensions of the anode grid determined using an electron microscope. The anode mesh allows approximately 50% of the electrons to pass through, whilst the electrons are travelling through the VPT. This means the other 50% of the electrons are absorbed.

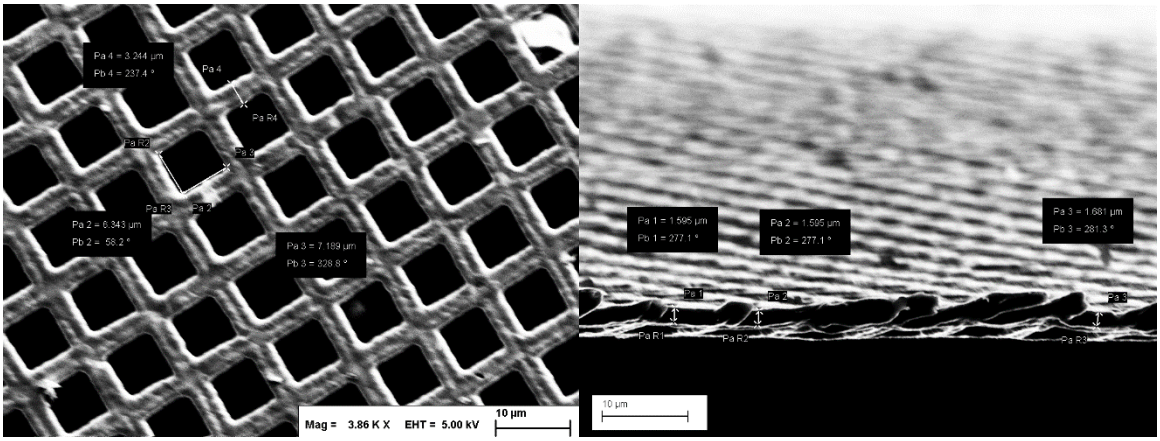

Figure 4-3 – Left: showing an electron microscope image of the anode mesh through showing the regular pattern of holes. Right: the anode mesh through the electron microscope showing the thickness of the anode mesh.

To achieve this in COMSOL, a 2D design was initially approached to get the face of the mesh created. Within the 2D design, a single cell (a single square hole and its edges) was created to provide 50% transparency. This cell was manipulated to produce arrays of cells in a square grid format. This allowed the user to create the grid size they want as a smaller grid means a significantly faster simulation runtime. Once the grid of cells was created in 2D, it was then extruded into a 3D grid that could represent the anode mesh.

4.3 Model Attributes

Once the geometry of the VPT was created, the next stage was to apply attributes to each of the components and define their behaviour. This section will describe the applied properties and conditions to each component within the VPT model.

4.3.1 Walls

In COMSOL, a Wall is a boundary/face of a component. Each wall of each component can have special properties assigned to them that includes its material, physics properties and how

it reacts with particles. Each wall can have multiple characteristics from different physics modules. If they are assigned properties twice from the same module, then the latest added property of that module overrides the previous one. E.g. if the dynode was initially set to 200 V electric potential, and then to 800 V, the 200 V will be overridden by the 800 V.

4.3.1.1 Materials

The COMSOL library supports a vast range of over 2,500 pre-defined materials that mimic their real-life attributes. They are supplied through a built-in database that can be accessed and applied to each component within the model. For the VPT model, the internal space was set to be a vacuum. The dynode material was set to Aluminium Gallium Arsenide, which was the alternative to the physical VPTs dynode material of KCsSb. The cathode material was set to Copper as it is only used to release particles. The material for the anode mesh was set to Beryllium Copper. The housing of the physical VPT was made from borosilicate glass, which was not available in COMSOL. Therefore, the closest match to this was to use the standard glass material within COMSOL.

4.3.2 Electrostatics for VPT Modelling

The simulated VPT model has electrostatic properties applied to each of its components. By default, each component starts off with Zero Charge, where everything was set to 0 V. Electric potential properties were added to each component to override the 0 V and become the desired potential.

4.3.2.1 Charge Conservation

The charge conservation node was used to add equations for charge conservation according to Gauss' Law for the electric displacement field [49]. The material type was defined under this node (solid, non-solid and from the material). This allowed the module to decide how the material should behave and how the meshing interprets the material properties. By default, the zero-charge node was added to all components within the geometry. The initial value node defaults all components to 0 V. These are later overwritten by other nodes where appropriate when defining the VPT properties.

4.3.2.2 Electric Potential

This Electric potential node applies a user-specified electric potential to selected walls of the components within the model. This will overwrite all the default values the model creates

initially. The anode mesh was set to 1000 V, dynode was 800 V. The rest of the components remain at 0V.

4.3.3 Charged Particle Tracing for VPT Modelling

The VPT requires a lot of nodes from the CPT module to run the simulations where the VPT was under different conditions, such as having a magnetic force applied at different strengths and angles.

4.3.3.1 Inlets

The Inlet represents a source of charged particles, of which their properties can be pre-defined. This included their position density, quantity, release times and velocity. They can have different conditions to release charged particles and different moments within the simulation. For the VPT model, the cathode wall was set as an Inlet, where the initial particles were released. The particles produced by Inlets are classed as primary particles. To release particles with different energies, multiple Inlets were added to the same wall with different parameter settings.

4.3.3.2 Electric & Magnetic Force

The requirement for Electric Force to be applied was to simply select between electric field or electric potential for the components that require its calculation. In the case of the VPT, an electric field was needed and was selected across the whole geometry.

The Magnetic force was used in certain simulations when the VPT is supposedly placed inside a magnetic field like the physical VPTs used in CMS. There were two factors that were varied throughout each simulation. The first was the strength of the magnetic field, which varied from 0 T; 1 T; and 4 T. This included testing the CMS condition at 4 T, as well as other strengths to see how the performance differed. The other factor was the degree to which the magnetic force was applied, ranging from 0 degrees and 15 degrees which is in the middle of the range of angles which the VPTs are placed in CMS. Both factors were also combined giving a thorough analysis of every case.

4.3.3.3 Secondary Emission

The Secondary Emission node assigns the possibility to produce additional charged particles based on a collision with a primary particle against the wall. The parameters for this wall include the number of secondary particles released and their initial velocity. Conditions could be set to activate the secondary emissions, as well as a probability or evaluation expression of

their release. In the simulation, the secondary emission node was applied to the dynode wall, with the purpose of producing electrons when a primary electron collided with it. Once an electron collided with the dynode, it gets absorbed to produce the secondary electrons. This also enabled secondary electrons to collide with the dynode and produce tertiary electrons and so on.

4.3.4 Probes

Once the model and its properties were set, probes were used to monitor the behaviour at any desired location. They can be useful for running analysis in real-time where the user can specify their desired function.

There are many uses for the probes in the simulation to help analyse the simulation outcome. For example:

- Detect number of particle collisions on selected walls throughout the simulation, using a probe as an accumulator
- The accumulators are also used as counters to see how many particles collided with other electrodes or with the VPT housing

These probes also work live during the simulation, as the particle trajectories are being simulated. An advantage of this was for giving an early insight into whether the simulation was working as expected. This was very helpful for situations where simulation runtime was for many hours, as the probes can show unusual signs as they happened, and the simulation could be cancelled and rerun with the required changes.

4.3.5 Particle Release overview

For simulating the particle flow through the VPT, a range of energies were defined to be released from the inlet wall of the photocathode. The particles are released from t=0 in the simulation, with an initial release of 2 eV with a Lambertian distribution [44]. The particles were then forced to travel through the VPT due to the acceleration caused by the electric field lines. When there was a magnetic field, the electrons were forced to travel in a helix. The dynode plate had the wall condition set to ‘disappear’ as the particles hit the plate. The SE was attached to this plate and the emission occurred in the same general direction as the incoming particles. [44]. The secondary particles were released from the same exact location the initial particle collided, they were released in a random emission of a cone of ±10° from the centre point of emission.

The number of secondary electrons released was based on the energy of the incident electron. For the model, the dynode was set to 800 V. The number of secondary electrons produced can be calculated with the following:

$$N_S = \frac{KE_P}{m} \tag{4-6}$$

where N_S is the total number of secondary electrons, KE_P is the kinetic energy of the primary incident electron and m is the minimum energy required to create a secondary electron. The minimum energy can be defined as a ratio of the SE coefficient, $m = \frac{\delta max}{\delta}$. The number of secondary electrons produced from a 1000 eV incident electron produced 20 secondary electrons based on data by Brunel, which would require $m = 40$. However, within COMSOL, the parameter for the number of secondary electrons was set by the user. Therefore, an incident primary electron of 1000 eV had been set to produce 20 secondary electrons by dividing the electron energy by $m = 40$. The energies above and below 1000 eV are also divided by $m = 40$ to give the equivalent number of secondaries for that energy. The energy distribution of the secondary electrons was centred at 5 eV based on Figure 4-6 and from Bateman [44].

The secondary electrons were attracted to the anode plate due to the greater potential. Once they hit the plate the particles were once again set to 'disappear' from the model. COMSOL stores a wide range of computations that are predefined to commute when the simulation is run, from these a whole range of plots, figures and tables can be produced in the results section of the model. Alongside this COMSOL also runs any parameters set by the user, and in this case, the inbuilt function for global probe had been used to calculate the induced current using the Shockley–Ramo theorem equation defined in section 4.5 [51].

4.4 COMSOL Mesh

COMSOL meshing is a process that makes it possible to analyse small areas of a geometry to create a detailed analysis of the simulation. A Finite Element Mesh (FEM) was created across all the components in the geometry before the physics analysis starts, through a process called a Finite Element Analysis (FEA).

FEA is used to create computational models of real-world scenarios. The first step of using FEA is creating a computer-aided design (CAD) model, this model contains the physical dimensions, along with additional information on the material properties [52].

The FEM within COMSOL breaks the geometry of the model into a large number of small elements. These elements are dependent on whether it is 1D, 2D or 3D geometry. For 2D geometries, the geometry is fragmented into triangular or quadrilateral mesh elements. For curved boundaries, the elements are represented as an approximation of the original geometry. The sides of the element triangles or quadrilaterals are called mesh edges and the corners are mesh vertices. For 3D geometries, the geometry is fragmented into tetrahedral, hexahedral, prism or pyramid mesh elements. For both 2D and 3D, the geometry vertices are represented by vertex elements [49].

4.4.1 Parameters Used

Figure 4-3 shows the dimensions of a real VPT anode mesh. According to specifications there would be over 3.2 million equivalent square holes in the in the COMSOL model geometry. Simulating this within COMSOL has been problematic. To allow for the simulations to compute, the mesh model has been reduced to 100×100 grid of square holes. This was the maximum number of holes that could be simulated on the PC used, without producing meshing errors or running out of memory. One of the most important factors that needed to be simulated realistically was the thickness of the anode mesh, this has been replicated to match the real thickness of 1.66 µm. The particle trajectories were simulated within a magnetic field along with different angles for particle release. The path that the particles travelled through the VPT made the depth of the mesh important.

A tetrahedral mesh has been applied to the VPT model, by using two separate meshes defined within the model. The first mesh was computed on the entire VPT apart from the anode mesh. It was necessary to compute the mesh for the anode mesh separately because of its small edges when compared to the remainder of the VPT. If it is not computed separately, numerous errors were produced that include running out of memory and failing to join the mesh of small edges to the VPT body.

Initially, the anode mesh was scaled up by a factor of 2-3 the real dimensions, so the mesh would compute without running out of memory. However, simulating the real dimensions was important and would have impacted all the results obtained from simulations negatively if the correct dimensions were not used. To help make the simulation easier to compute, a second mesh was defined and was applied to the edges and corners of the anode mesh. This second definition allowed the model to compute a smaller mesh (the realistic mesh size). The finer

mesh with smaller elements, ran without any out of memory errors and computed quicker than if this finer element mesh had been applied to the whole VPT.

4.4.2 COMSOL Parameters

The main parameters that have been set up within the COMSOL model are summarised in Table 4-2. Screenshots showing some of these parameters within the COMSOL model environment are shown in Appendix A. These listed parameters are the same for all simulations completed, the only factor that changes is the magnetic field, where the three options are listed in Table 4-2.

Table 4-2 - COMSOL parameters used within COMSOL

COMSOL Parameter	**Parameter Value**
VPT Dimensions	
Length of tube	46.0 mm
External diameter of tube	26.5 mm
Cathode diameter	25.76 mm
Anode diameter	20.04 mm
Dynode diameter	20.93 mm
Cathode and anode gap	3.5 mm
Anode and dynode gap	2.0 mm
Cathode and dynode depth	250 µm
Anode electrode depth	1.66 µm
Anode mesh size	100 × 100 array
Anode cell size	10 µm x 10 µm
Electrostatics	
Cathode voltage	0 V
Anode voltage	1000 V
Dynode voltage	800 V
Particle parameters	
Initial PE release from cathode	100 PE
PE release energy	2 eV, with a Lambertian distribution
Backscatter at anode	20% with any collision at the anode

Backscatter at dynode	10% with any collision at the anode
Secondary emission	Number of secondary particle dependent on incoming particle energy. Released with ± 10° cone
Magnetic field	Testing carried out at 0 T, 4 T and 4 T at 15°
VPT Materials	
Internal space	Vacuum
Cathode material	Copper
Anode mesh material	Beryllium copper
Dynode material	Aluminium Gallium Arsenide
Physical housing of VPT	Glass

4.4.3 Meshing Difficulties

Figure 4-4 shows a screenshot of the FEM that was applied to the anode mesh electrode model within the COMSOL model. The COMSOL mesh was problematic to compute due to the ratio between the anode mesh and the rest of the geometry. The mesh can fail when converging on the corners of the anode mesh. As the meshing process gets closer to the anode mesh from the outer vacuum walls, the rate of production of meshing must decrease or increase (if looking at it from the opposite direction). The outer walls of the VPT were ~4.5 mm and the internal components of the anode mesh were 1.6 µm, which is almost 3000 times smaller.

The meshing components of the model that was used for the simulations contained 4,611,133 domain elements, 769,569 boundary elements, and 230,119 edge elements. Out of this, the anode mesh itself consists of 2,265,221 (49.12%) domain elements, 386,802 (50.26%) boundary elements, and 25,168 (10.93%) edge elements.

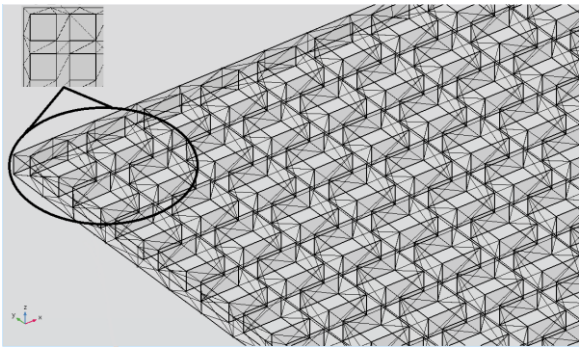

Figure 4-4 – Implementation of the anode mesh within COMSOL. The FEM of COMSOL can be seen applied to the anode mesh.

4.5 Signal Generation

In order to simulate the electrical signal, there were certain laws to consider and that should be obeyed when setting parameter values. Each of these is detailed below:

4.5.1 Shockley-Ramo Theorem

The signal formed within the VPT was created by the electrons travelling through the VPT, by generating an induced current through the instantaneous changes of electrostatic flux. The induced current within the VPT can be calculated from:

$$i = -q \cdot \vec{v} \cdot \overrightarrow{F_k} \tag{4-7}$$

Where q is the charge of the photoelectron and $\vec{v} = [v_x v_y v_z]$ is its instantaneous velocity. The weighting field $\overrightarrow{F_k}$, is determined by setting the cathode and dynode to zero potential and the anode to unit potential. This is not the same as the electric field which was used to determine the electron trajectories.

4.5.2 Weighting Field

To calculate the induced current within COMSOL, a global probe was applied to the model that specifically calculated the total induced current within the VPT for every time step of the simulation. The induced current values were calculated and stored as a user-defined parameter. The weighting field of the VPT was calculated using the Laplace Equations physics node in a separate cloned model. Within the model, the anode mesh electrode was set to unit potential and the cathode and dynode were set to zero potential. The weighting field was calculated for the x, y and z domain and stored in a table under 3 parameters ux, uy, and uz. These

parameters were imported into the original model and this was then used within the probe to calculate the induced current for each time step.

4.5.3 Secondary Emission

There were three main processes that occur when an electron hits a surface, each of these being mutually exclusive: the first is as the incoming electron this the surface it is backscattered elastically (I_e) whilst the rest of the incoming electrons were absorbed by the surface. The second scenario is called 're-diffused' electrons (I_r) this is when some of the electrons which are absorbed by the surface are scattered from one or more atoms within the material and are reflected out of the material. The backscattered and re-diffused electron both only produce single electrons in these scenarios. For simulation purposes, there was no fundamental distinction between backscattered and diffused electrons [53]. Third and most common being 'true secondary electrons' (I_{ts}), these are emitted from the surface of the material within a small range of angles and energies. For true SE any number of electrons can be emitted, depending on the incoming primary electron energy and the material of the dynode. The events between backscattered/re-diffused electrons versus secondary electron creation are mutually exclusive.

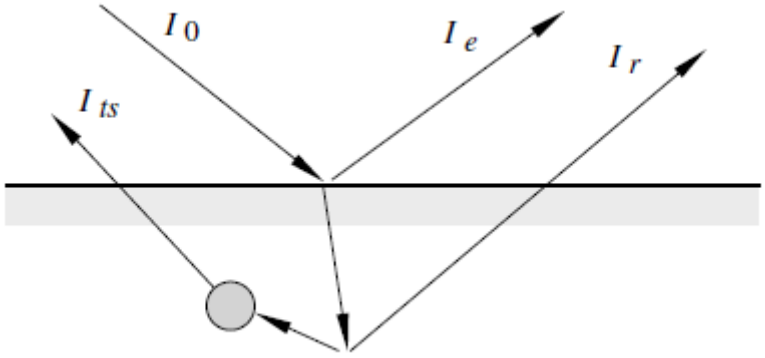

Figure 4-5 – I_0 is the incoming electron which has the possibility to create three mutually exclusive events: I_e being elastic backscatter, I_r being re-diffused electrons and I_{ts} being true SE, which could be more than one electron [53].

Figure 4-6 shows the real energy spectrum of photoelectrons of energy 300 eV hitting a sample of stainless steel. The secondary electron emission spectrum was composed of three main components: true secondaries (about 57%) with an average emission energy of 5 eV, re-diffused secondaries (about 36%) which is the approximately flat energy spectrum from 50 eV to almost 300 eV and lastly the backscattered electrons (about 5%) which are elastically backscattered at the incoming energy of 300 eV [53].

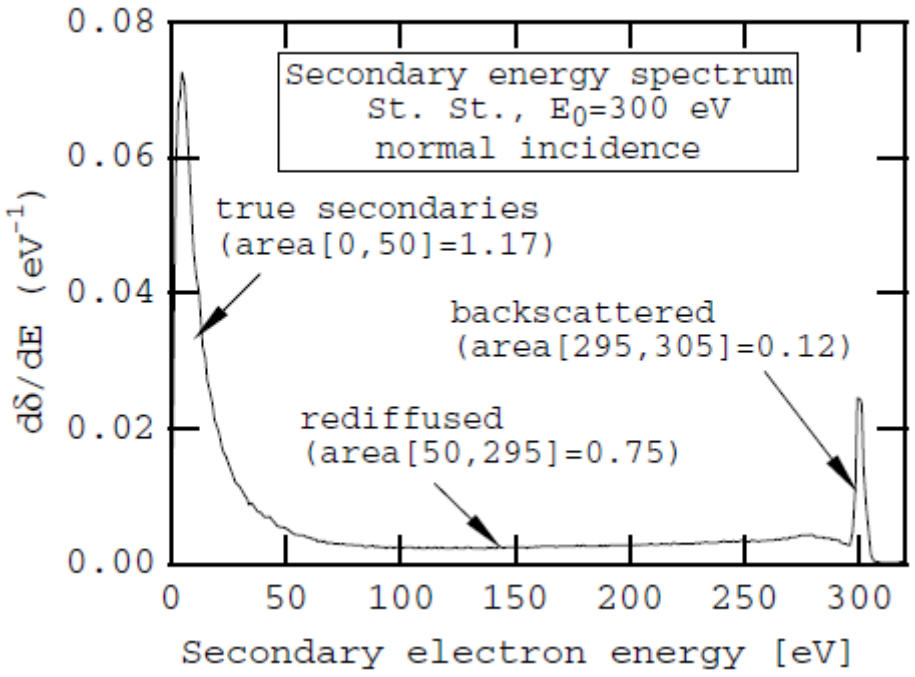

Figure 4-6 – Energy spectrum measured of a sample of unconditioned stainless steel. The photoelectrons hit the sample at energies of 300 eV with normal incidence [53].

To simplify the computation of the simulation in this thesis, each true secondary electron produced by an incident electron had a fixed energy of 5 eV, which is the average value for them [53]. There is no impact in particle behaviour when fixing the true secondary electrons to 5 eV rather than a range from 1 eV to 5 eV because the electric force immediately increased the energy of them.

The mesh transparency can have a very different effect on the output signal. For example, a low transparency mesh of 35%, the electron cascade finishes quickly, with 1% contributing to tertiary electrons [44]. On the other hand, a high transparency mesh of 70%, there is nearly 10% contribution to tertiary electrons. The signal produced is very fast of under 1 ns, the electron movement across the gaps between the cathode, anode and dynode vary between 0.2 – 0.5 ns [44].

When a photoelectron collides with the dynode with enough energy to provide SE, the emission of these secondaries was spread over a circle of a few hundred microns, heading back towards the anode plate [44]. As the particles travel through the VPT and go through anode mesh, they experienced a weak attractive field around the mesh wires. This was crucial factor to consider when the VPT was placed within the high magnetic field. The photoelectrons must travel within a mean secondary cyclotron radius of a few microns for fields above 1 T, so they may pass the

anode mesh and hit the dynode to generate SE [44]. If the axial magnetic field is applied in parallel to the electric field the motion of the particles along the electric field is unaffected by the B-field.

The light emission from lead tungstate has a spectral maximum of photon energy of about 2.6 eV. The cathode, CsSb photoelectron spectrum has an exponential distribution with a mean energy of 0.75 eV with spatial distribution about cos θ [44]. When the photoelectron hits the dynode, it has the energy of 200 eV ($V_{cathode} - V_{dynode}$ = 800 – 1000 eV), whereas the photoelectrons arrive at the anode with 1000 eV.

4.5.4 Orientation Correction

There are two factors that determine the polarity of the induced current. These are the position of the electron with respect to the anode, and the direction it is heading towards. Figure 4-7 shows two regions in which orientation correction (OC) changes the polarity. OC is +1 when the speeds V_A & V_Z are either both greater than 0, or less than 0, and when the particle is in-between the cathode and anode. Where V_A is the speed at which the electron approaches the anode and V_Z is the speed of the electron on the axis of the VPT. V_A changes sign as the electron crosses the anode however $V_Z$does not. This indicates that no significant change is required to the induced current as it is in the cathode-anode region. When the particle is in the anode-dynode region, the induced current polarity is reversed.

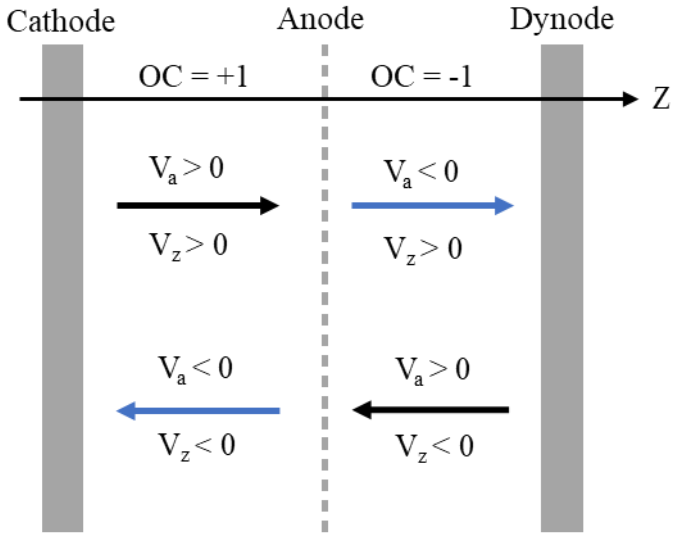

Figure 4-7 – Diagram of how the polarity for a particle is changed depending on its location and direction.

4.5.5 Backscattering

Backscattering is dependent on the primary electron energy and the atomic number of the material, according to Dressler [54]. There are two types of backscattering scenarios that are described in the previous section 4.5.3 of elastically backscattered and re-diffused electrons. Throughout the simulations, there has been no clear separation between finding backscattered or re-diffused electrons. Therefore, both re-diffused and backscattered electrons will be referred solely as backscatter.

The spectrum of secondary electrons has a peak at a few eV. This spectrum is continuous up to the energy of the primary electron, where the elastic backscattering can occur. The inelastically backscattered primary electrons are found in the mid-energy range of around 500 eV. Some of the primary electrons that are released to become inelastic backscattered primary electrons [44]. Approximately 30% of the photoelectrons are backscattered with a mean energy of 70% of the incident photoelectron with a $\cos\theta$ spatial distribution to the incoming direction of the photoelectron [44].

Backscattering also occurs on the anode mesh, depending on its material. Assuming that the anode mesh material is similar to either Ni or Cu and has some coating of Sb and Cs, the backscattering is approximately 20% [44]. The backscattered electrons travel through the VPT until they are absorbed by the anode, or the dynode, or hit the sides of the tube. Backscattering reduces the overall gain of the VPT.

4.5.6 Magnetic Fields

Once a magnetic field was applied to the VPT, the electrons within the tube will follow the magnetic field lines rather than the electric field. The anode mesh was made from Nickel, which will attract the field lines. Therefore, the electrons travel through the material up until the point a magnetic field of at least 0.5 T was applied to the VPT tube. This leads to some loss of signal as the electron movement is dominated by the magnetic field which guides the secondary electrons to the centre of the anode mesh gaps, and therefore, cannot hit the anode which produces an output signal loss [55]. Another loss of signal source was from the magnetic materials that are used to support the mesh and other components within the VPT. These also altered the B-field near the edges of the active area of the mesh [44].

Overall, Bateman [44] predicts a VPT with a finer anode mesh outperforms a VPT with a coarser mesh within a B-field. With the primary use of the tubes within CMS operated at a high magnetic field of 3.8T, fine mesh VPTs were chosen.

4.6 Simulation Optimisation

Some simulation optimisation has been carried out to reduce the run time of the simulations. Two areas that can be optimised to significantly reduce the simulation runtime are the size of the anode mesh array, and the sampling rate to evaluate the model. Both were investigated to find the optimal solution.

4.6.1 Time Step Optimisation

The step size of the sampling of the COMSOL simulations must be considered carefully. Ideally, the time steps should be as short as possible or allowed within COMSOL. If the time step is too big, the vital behaviour could be missed. However, running the simulation smoothly without errors using a very fine sampling rate can cause memory errors or result in 24+ hours simulation runtime. Along with running the simulation, the plotting and post-processing of the data within COMSOL also have challenges due to many data points.

To decide which time step was appropriate without introducing significant systematic errors, simulations were carried out starting with the finest time step feasible (without producing a memory error) of 0.1 ps, up to a time step of 10 ps. The objective was to determine how the change in sampling effects the accuracy of the simulation. The duration of the simulation was from the initial release of primary electrons until they reached the anode mesh which was 226 ps. 100 particles were released from the cathode and the total charge was measured across the 226 ps. The ideal result would have a charge of $100 \times e$ at the anode mesh.

Table 4-3 shows the total charge accumulated when using six different time steps of 0.1 ps, 0.5 ps, 1 ps, 2 ps, 5 ps and 10 ps. The finest time step of 0.1 ps has produced the closest to the ideal result, with 99.07 particles remaining. As the sampling time increases, so do the inaccuracy of the output data with the worst performance only retaining 64.63 particles. Therefore, it can be concluded that the finest time step is more accurate for the simulation, with the drawback of requiring more computational resources and time to execute. The optimal solution that has been chosen, is using the 0.5 ps, as this produced fewer datapoints without losing out much on accuracy. This will result in faster simulation runtime and faster analysis on the data such as producing plots.

Table 4-3 – Simulation results of total charge inside VPT when using various time steps. The simulation results are compared to the actual particle charge expected (100 electrons), and the loss for each time step is calculated.

Time step (ps)	Charge (C)	Derived number of particles	Percentage loss
0.1	-1.59E-17	99.07	0.93%
0.5	-1.58E-17	98.61	1.39%
1	-1.57E-17	98.21	1.79%
2	-1.56E-17	97.41	2.59%
5	-1.48E-17	92.31	7.69%
10	-1.04E-17	64.63	35.37%

4.6.2 Anode Mesh Optimisation

The anode mesh optimisation is another task that can significantly improve the overall performance of the simulation. This is achieved by setting the array size of the mesh. The anode mesh is a complex component in the VPT because of the size of the holes it contains when compared to the size of the other components. There was a size factor of nearly 150 times when comparing the smallest edge in the anode mesh with the smallest edge in the dynode and cathode, and a staggering 27,710 ratio when comparing the depth of the anode mesh and the depth of the VPT housing.

These large scaling factors cause problems with running the geometry meshing within COMSOL. Joining the mesh from both components becomes very intricate and having too many areas to join can lead to meshing errors. The objective for this optimisation was to determine how big the array size can be before it causes geometry meshing errors. Having a smaller amount will speed up simulation runtime as well as reduce the overall model file size. However, this can potentially reduce the reliability of the simulated model when compared to the physical device. Therefore, it would be best to keep the highest array count possible without causing errors. Another issue with having a large array is the file size it produced.

A 100×100 array for the anode mesh produced an average of 25 GB size files. An array size of 150×150 was produced without any errors but only by increasing the depth of the anode mesh from 1.66 µm to 2.5 µm. However, this was later rejected as it would affect the transparency of the anode mesh. The maximum array size produced using the correct mesh

thickness of 1.66 µm without any errors was 100×100, which was used for the remaining simulations.

4.7 Results

The following section presents the simulations results achieved within COMSOL version 5.3 [48] for the VPT model under varying magnetic field strengths and angle.

4.7.1 Electrostatics Results

The following Figure 4-8 shows the electric potentials of the VPT model within COMSOL. The outer shell of the VPT and anode were set to 0 V, the cathode at +1000 V and dynode at +800 V. These are the maximum operating potentials of the VPTs within CMS. The coloured bar represents the electric potential in volts. In Figure 4-8 the space above the electrodes appears to be empty. However, this space was reserved for the internal connections from the base of the VPT to the electrodes, for possible future simulations.

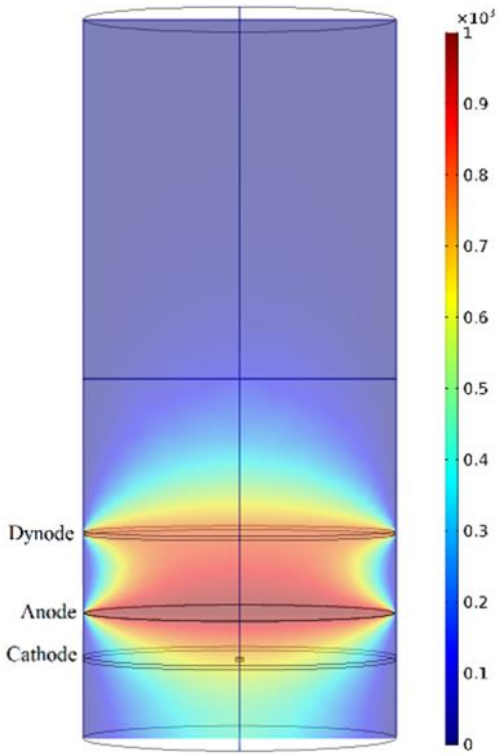

Figure 4-8 – Plot showing the electric field within the VPT. The coloured legend shows the potential in volts.

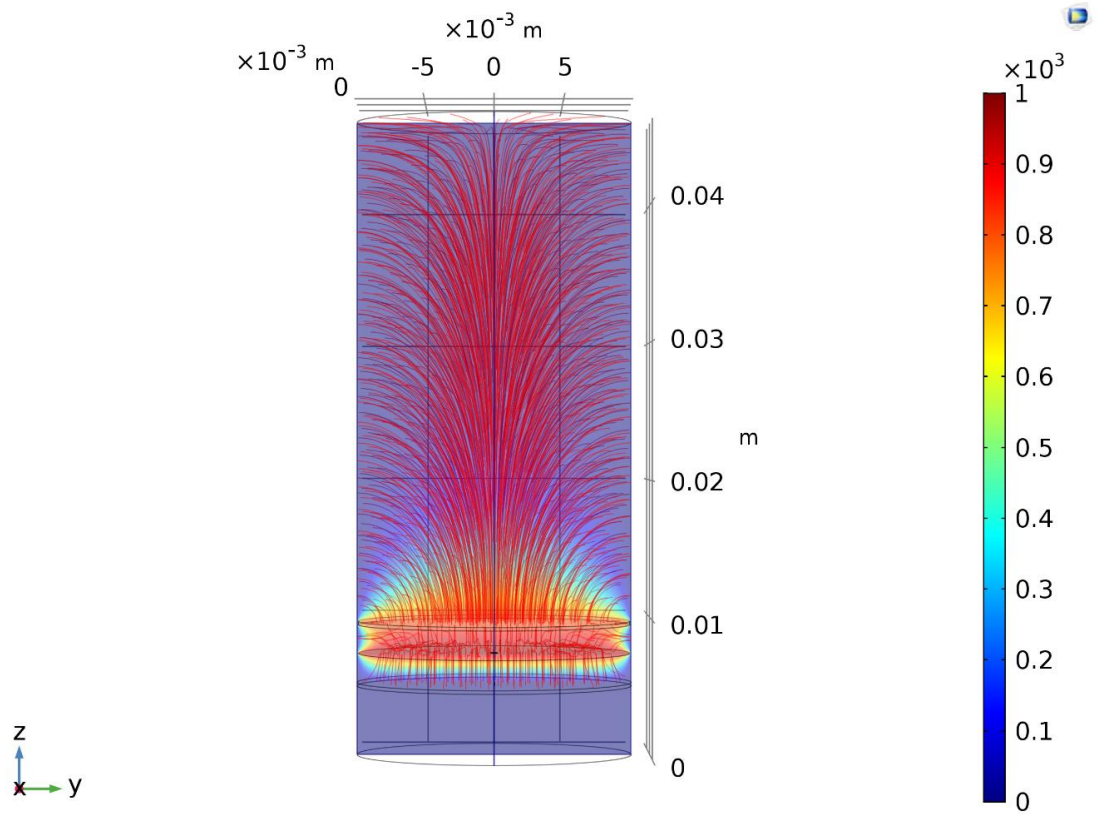

Figure 4-9 - Image showing the electric field line density within the VPT, with the colour legend showing the electric potentials in volts.

4.7.2 Induced Current Plots

The induced current for each particle within COMSOL was calculated using the Shockley-Ramo Theorem. This was to analyse the instantaneous changes of electrostatic flux [51]. To demonstrate some of the scenarios that were likely to occur within the VPT, Figure 4-10 and Figure 4-11 shows two sets of scenarios. The first set represents the initial photoelectrons and the SE emission produced as these electrons hit the dynode is shown in Figure 4-10. Set 2 represents the scenarios in which backscatter was likely to occur. Please note it is unlikely that all the possible sets of scenarios would occur within a single simulation. The following result in Figure 4-11 was chosen where most of the backscattered scenarios occur.

In the first set of scenarios, electrons have been shifted in time to show each scenario with visual clarity when the induced current is plotted. This was achieved by releasing a bunch of electrons from the cathode at different time steps of 0 ns and 0.1 ns. This ensured that the electrons reached the anode mesh and dynode at different times.

Figure 4-10 shows the induced current produced of set 1, each point labelled A-E on the figure represents: A - represents a photoelectron that was released from the cathode and traveled

through the VPT directly hitting the anode mesh. B - represents a single photoelectron that was released from the cathode and was accelerated towards the anode, passed through the anode and directly hit the dynode. C - The dashed red blue line represents a single secondary electron emitted from the initial photoelectron. This emitted secondary was accelerated towards the anode mesh, but in this case, the particle passed through the mesh. The kinetic energy was reduced to zero as the potential pull of the anode acts upon the particle and then was accelerated back towards the anode mesh but passed through and continued to travel until it hit the dynode. This cycling can happen until a particle eventually hits the anode mesh. D – represents a single secondary electron that was emitted from the dynode, was accelerated towards the anode mesh and passed through the mesh. The kinetic energy was reduced to zero again and then attracted back towards the anode where it collided with the mesh. E - represents a single secondary emitted electron from the dynode, which was accelerated back towards the anode due to the greater potential and directly hit the mesh.

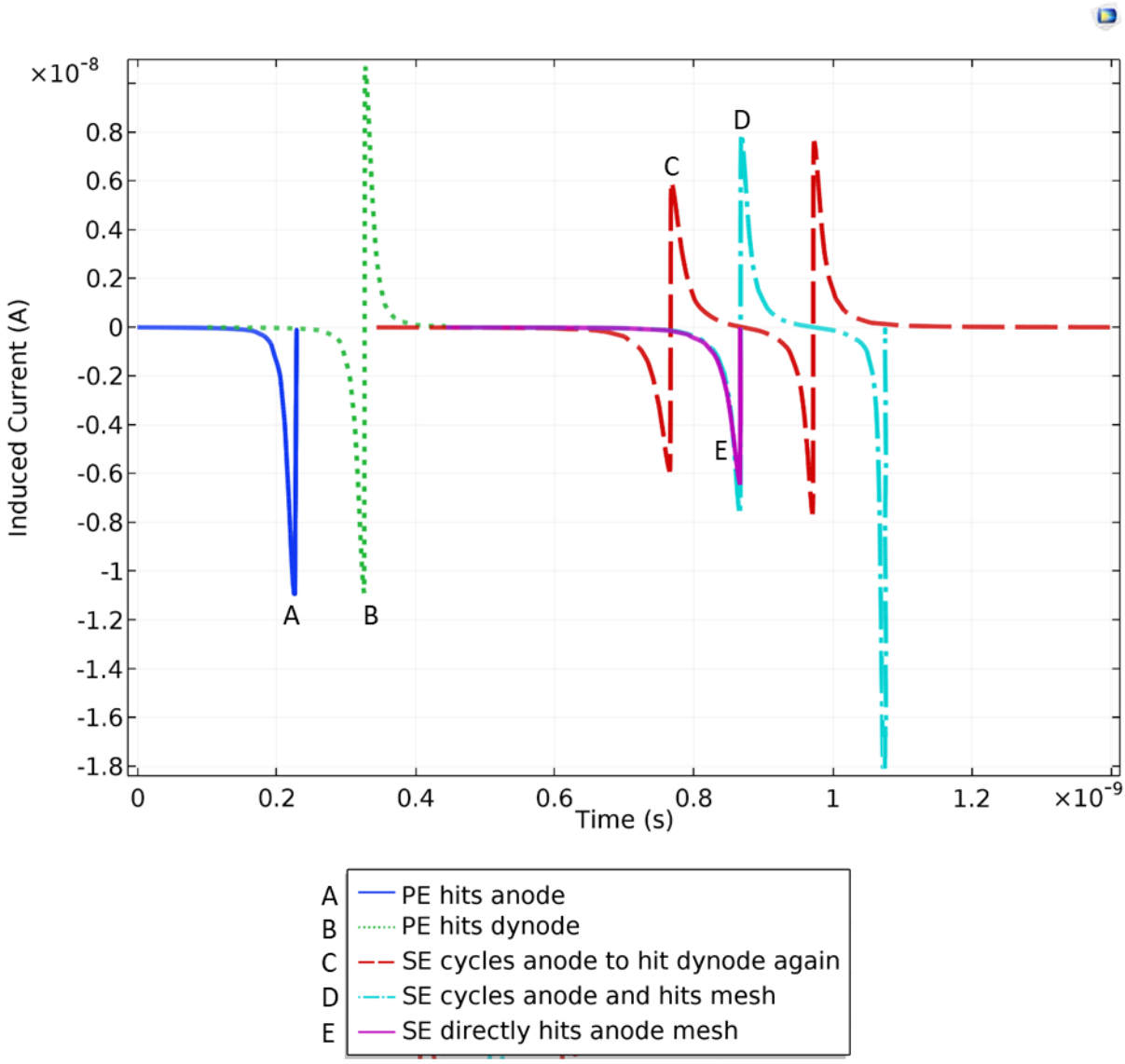

Figure 4-10 – Set 1: photoelectron and SE scenarios (A-E) showing the induced current due to a single electron within the RIE-188 tube at 0 T. Scenarios A and B have electrons released at different times for visual clarity, with A released at 0 ns and B at 0.1 ns

Different scenarios possible with backscatter within the VPT are show in Figure 3-6, which will be used to demonstrate different scenarios possible with backscatter in set 2 which is presented in Figure 4-11. A - represents a photoelectron that was released from the cathode, which directly hit the anode as it travelled through the VPT and a backscatter particle was generated heading towards the cathode. B represents a photoelectron which travelled past the anode mesh and collided with the dynode, and from this backscatter occurred which was directed back towards the anode mesh. The backscattered particle travelled through the mesh, where the potential pull of the anode drops the kinetic energy to zero and was attracted back towards the anode. In this case, it missed the anode mesh again and went on to collide with the

dynode. C represents a photoelectron that travelled through the anode mesh and hit the dynode, to generate a backscattered electron which travelled back through the VPT towards the cathode and either collided with the cathode or hit the VPT tube. D represents a photoelectron which hit the dynode to generate SE, which was accelerated towards the anode mesh and collided, this goes on to generate a backscattered electron that was directed towards the dynode. E represents a photoelectron which hit the dynode, generating a SE which travelled past the anode mesh. It slowed to zero kinetic and goes back towards the anode mesh where it collided and generated backscattered electron travelling towards the cathode. Again, its K.E is reduced to zero and its trajectory was directed back towards the anode mesh where it goes through the mesh holes and hit the dynode. E represents a photoelectron that hit the anode mesh and generated a backscattered electron in the -Z direction, and its trajectory was reduced to zero and then was accelerated towards the anode going through the mesh hole and hit the dynode. These scenarios are present for case 2 of the induced current examples shown in Figure 4-11. For this simulation run, there was no scenario F present.

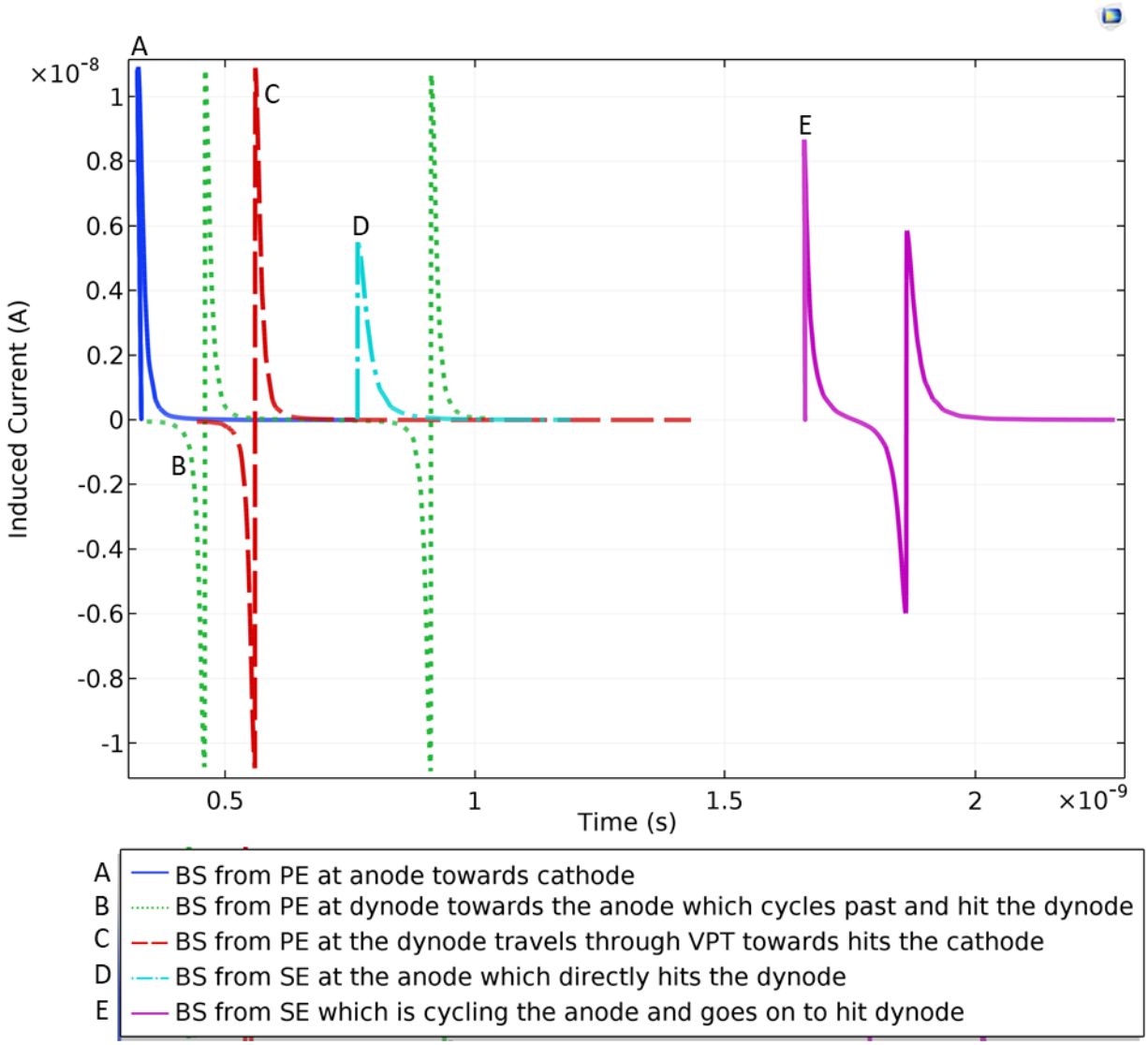

Figure 4-11 - Case 2: backscatter scenarios (A-E) showing the induced current due to a single electron within the RIE-188 tube at 0 T.

4.7.2.1 Charge Conservation Test

One of the checks to see how ideal the simulated environment was with particle tracking and the total charge, was to have a single electron go from the cathode through the anode mesh and hit the dynode. In theory, this should result in the total charge with respect to the anode mesh integrating to 0.

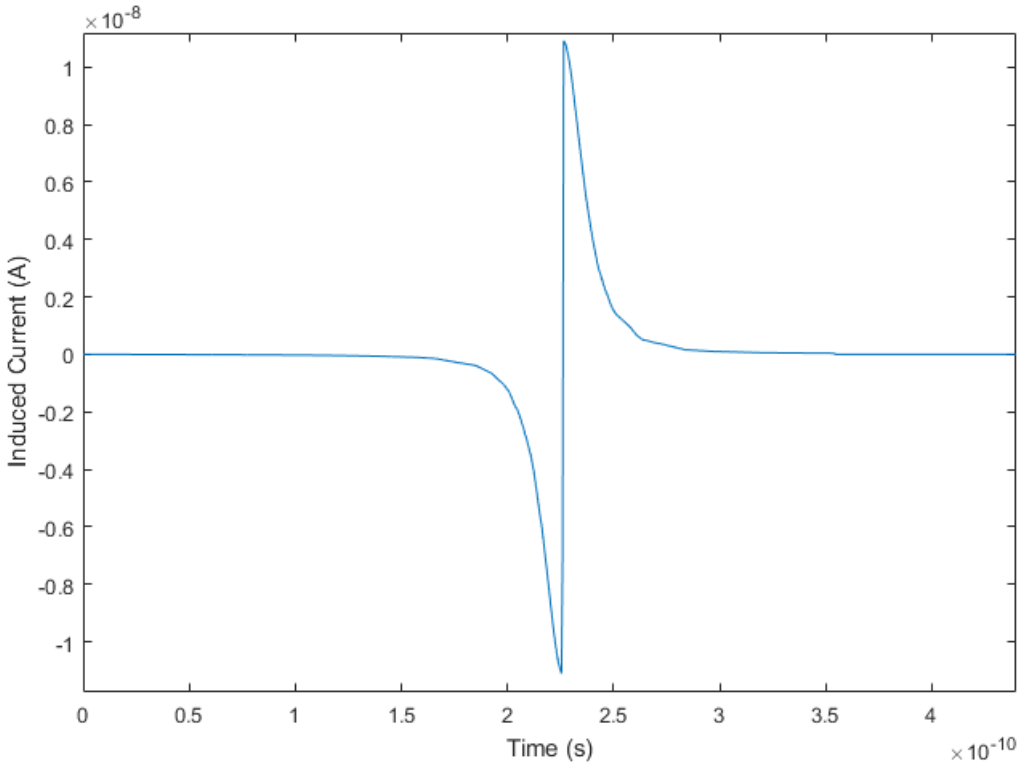

Figure 4-12 – Plot showing the induced current of a single particle released from the cathode, going through the anode mesh and hitting the dynode.

Figure 4-12 demonstrates the induced current behaviour with respect to the anode mesh, of a single particle released at the cathode, making its way through the anode mesh and hitting the dynode. To calculate the total charge, the area under the curve was integrated. The expected charge should be 0 C. However, the simulation produced 2.06^{-21} C which represents 0.38% charge of a single electron, which is close to the ideal value of zero. This gives an idea of the systematic error that can occur with the simulations. These errors can only be fully removed if there was an infinite time sampling rate, which is not possible.

4.7.3 Simulation with at 0 T

For the following section, the number of particles being released at by cathode has been increased to 100. The particles were released with a Lambertian distribution. This releases the particles initial direction based on Lambert's cosine law, which states that the probability of a ray being released through a differential solid angle element with polar angle θ is proportional to cos θ [56]. SE occurs at the dynode respective to the incoming energy. It is released with an angle of ± 10° that is randomly distributed. Within the model, there was a 20% chance of backscatter at the anode and 10% at the dynode as mentioned in 4.5.5. Figure 4-13 shows the particle trajectories through the VPT.

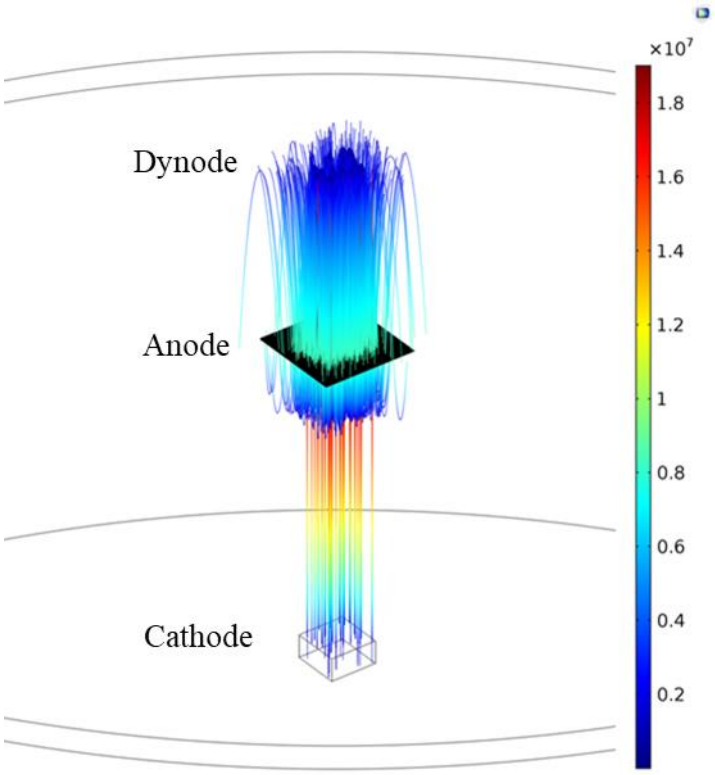

Figure 4-13 - Particle trajectories within the VPT at 0 T. The electrons are released from a square region on the cathode. The potentials are as follows: cathode 0 V, anode +1000 V and dynode 800 V. The coloured scale shows the speed of the particles in m/s.

The current induced by these particles within the VPT, as seen by the anode is shown in Figure 4-14. Stage 1 in the plot shows the initial 100 photoelectrons that were released from the cathode and travel towards the anode mesh. Approximately 50% of these initial 100 photoelectrons hit the anode and the remaining 50 % continues to travel towards the dynode. This is caused by the 50% transparency mesh.

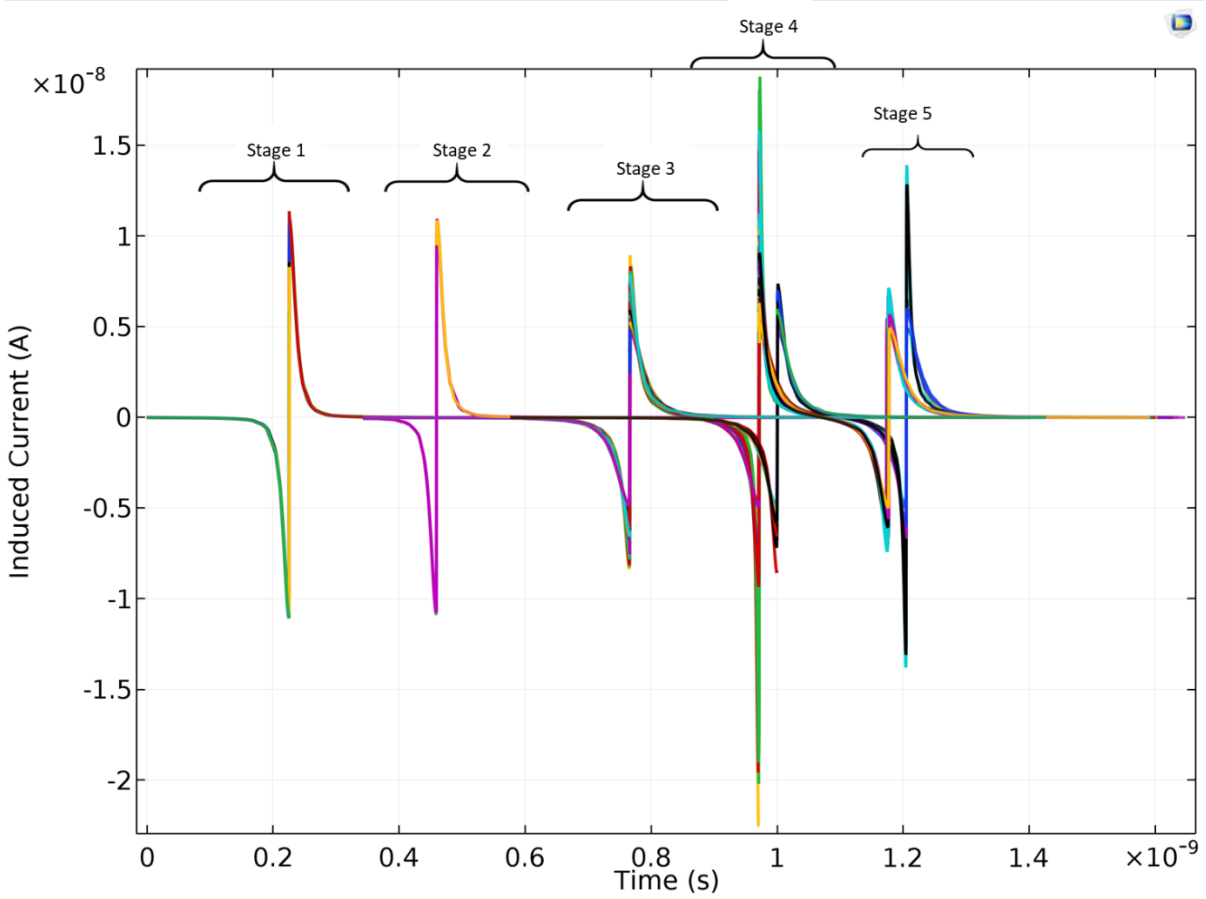

Figure 4-14 – The induced currents are shown for all the particles individually within the VPT at 0 T. The induced currents are split up into 3 stages, to help explain the different scenarios which occur. Stage 1 is the induced current from photoelectron being released and travelling towards the anode and dynode. Stage 2 is the induced current due to SE and stage 3 is the induced current from stray particles and backscatter. Stage 4 is the induced current of the SE that go on to hit the dynode, and stage 5 is the induced current of the SE produced by the backscatter from stage 2 that goes on to hit the dynode.

The beginning of stage 2 was the start of the SE from the dynode. The induced current signal is reduced with each oscillation stage until eventually, the signal dies down. It can be seen there are many overlapping particles in stage 2, that all have a slight varying trajectory due to the emission angle. Stage 3 shows the leftover particle within the VPT which are mainly from the backscatter or further oscillating particles which have not hit the anode mesh after a few iterations of going back and forth. Stage 4 is the induced current of the SE that go on to hit the dynode, and stage 5 is the induced current of the SE produced by the backscatter from stage 2 that goes on to hit the dynode. The actual output from stage 2 and 5 as the sum of the signals is insignificant when compared to stage 1 and 3, this can be seen more clearly by the sum of induced currents in Figure 4-18.

Figure 4-15 shows the particle position of the particles through the VPT in the Z domain (depth of the VPT). The cathode, anode mesh and dynode have been labelled on the plot. The anode

and dynode backscatter are labelled on the plot. There are several cases pointed out on the plot to show a few of the significant outcomes: A – corresponds to the initial photoelectron hitting the anode and produced several backscattered electrons, as these travel back towards the anode mesh, some were stopped but two electrons missed the mesh and traveled further towards the cathode. This was where one particle essentially was lost within the VPT tube as it hits the shell or cathode and the other was attracted back towards the anode mesh. Yet again it missed the mesh and finally hits the dynode, however not producing any SE. The backscattered electrons were generated to be released at the same energy as the incoming photoelectron. Point B – was the SE produced from the initial photoelectron hitting the dynode producing SE and some particles being backscattered at the anode back towards the dynode and this was where the SE occurs. Point C – was the initial SE that has cycled past the anode and hits the dynode again to cause SE.

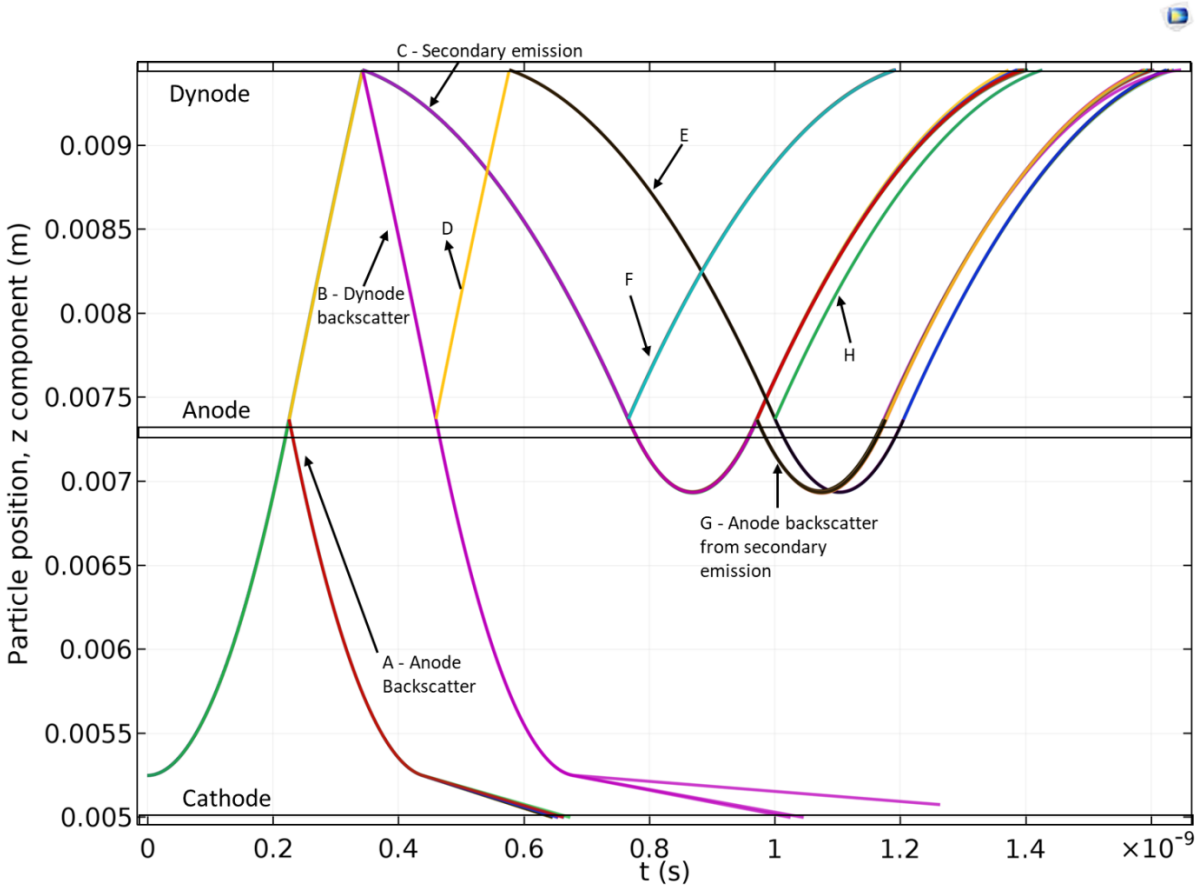

Figure 4-15 – Particle position is shown in the VPT along the z domain of the VPT model. The cathode, anode and dynode are labelled respectively to where they are in the COMSOL model. The backscatter events are labelled on the plot.

Point D – is the anode backscatter from point B, which leads on to produce another backscatter (point E). Point E – is the continued response from the backscatter point D. This was most

likely a few secondary particles that were being released as the backscattered electron hits the dynode. Point F – is backscatter from the SE of point C. Point H was a backscattered electron from point E, which was directed back towards the dynode when produced and the anode mesh (from of the electrons carry on through the anode mesh). Point G – is the anode backscatter directed from secondary emission (point C), this towards the cathode which does on to loop the mesh and collide with the dynode.

The energy of the particles is shown in Figure 4-16, the release of the photoelectron started at 0 eV and grows to a maximum of 1000 eV, due to the anode which has a potential of +1000 V in the model. The photoelectron that reached the anode mesh reaches a maximum of 1000 eV, the photoelectron that gets past the anode mesh and hit the dynode were deaccelerated to 800 eV. Secondary electrons reach a maximum of 200 eV between the dynode and the anode. The backscattered electrons are the curves which tend from 1000 to 800 eV when they go from the dynode to the anode (B), anode to anode (G) and anode to dynode (F), as they are essentially sent back with almost the same energy as they came in with. The backscatter that goes from the anode to the cathode (A) tend to have an energy of 0 eV.

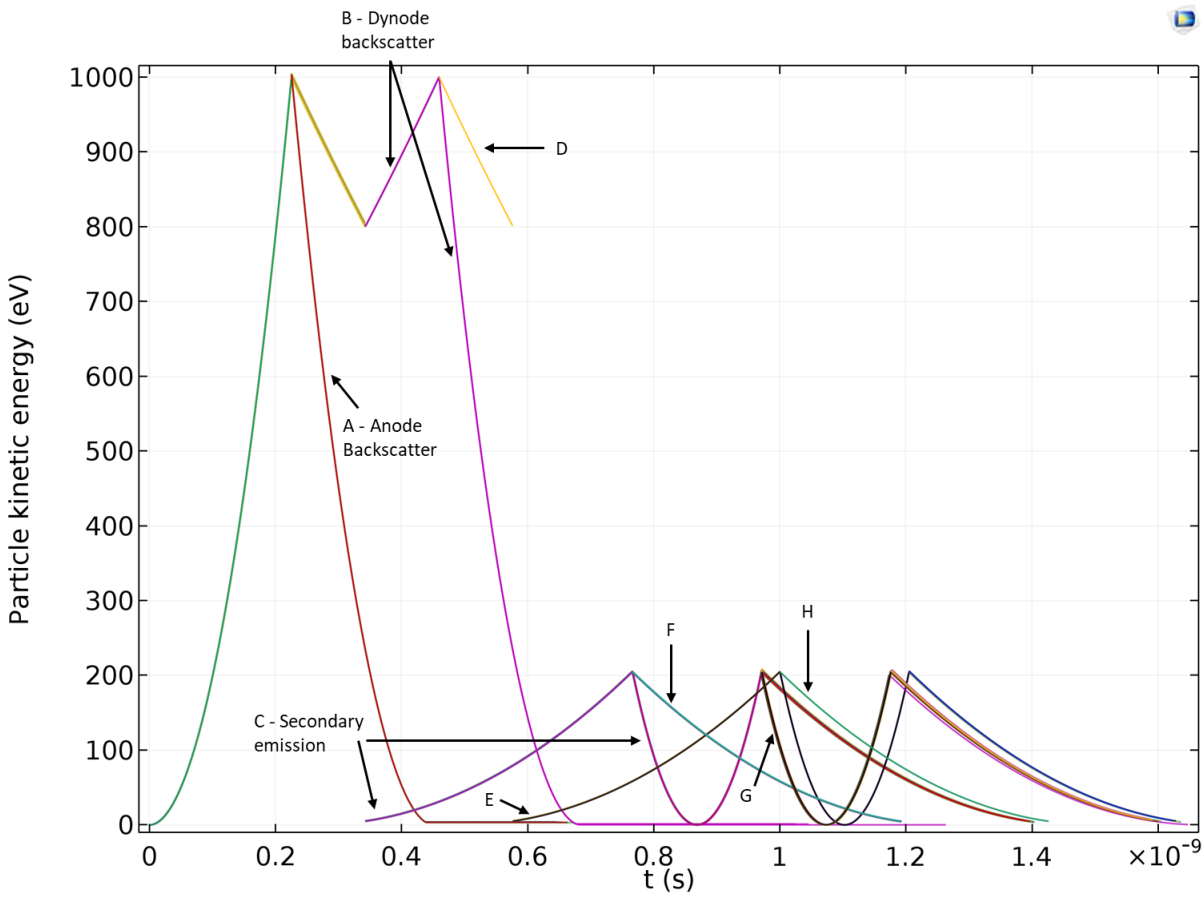

Figure 4-16 – The energy of the particles is displayed in eV. The anode mesh and dynode are labelled on the plot. The dynode is held at + 800 V, anode mesh at + 1000 V and cathode at 0 V.

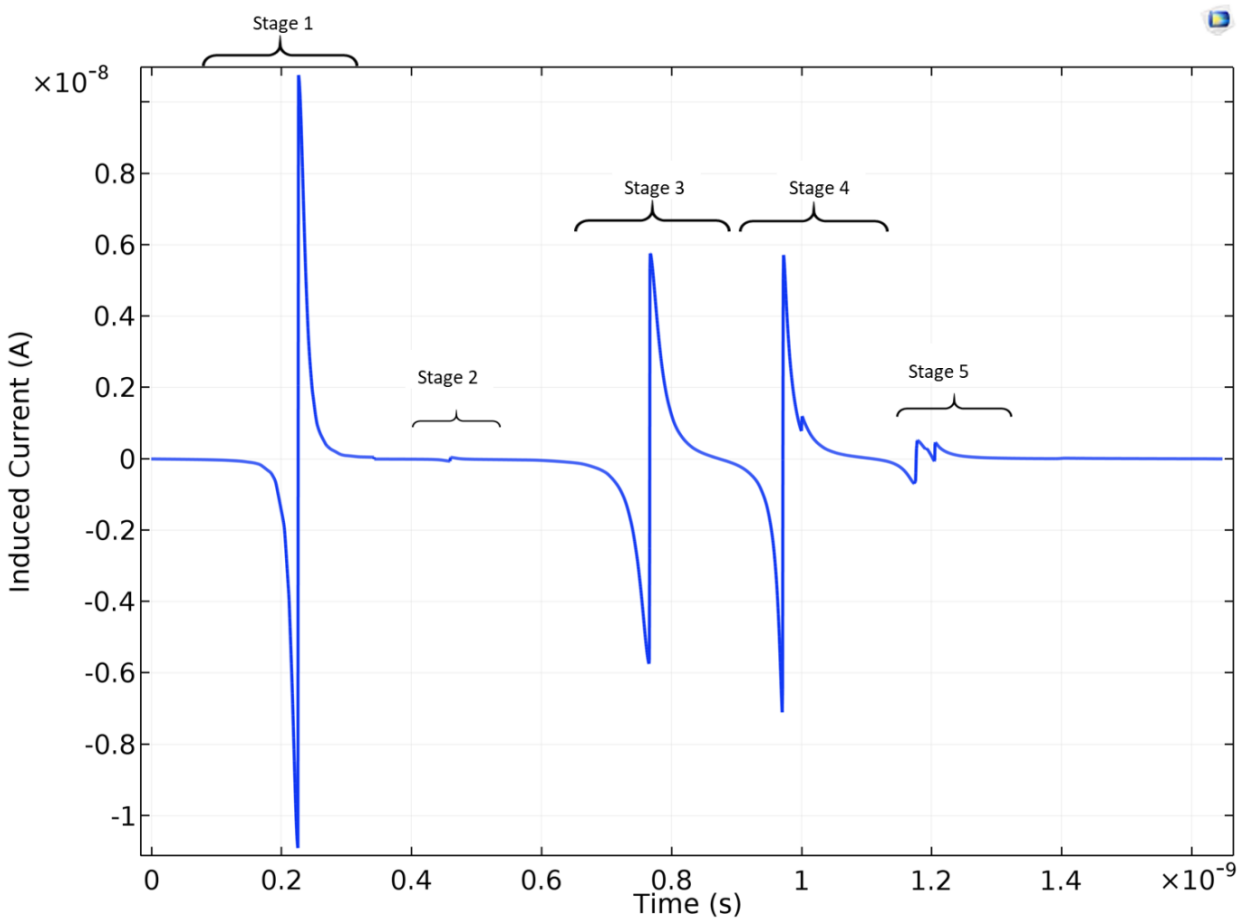

Figure 4-17 – The average induced current on the anode of the VPT.

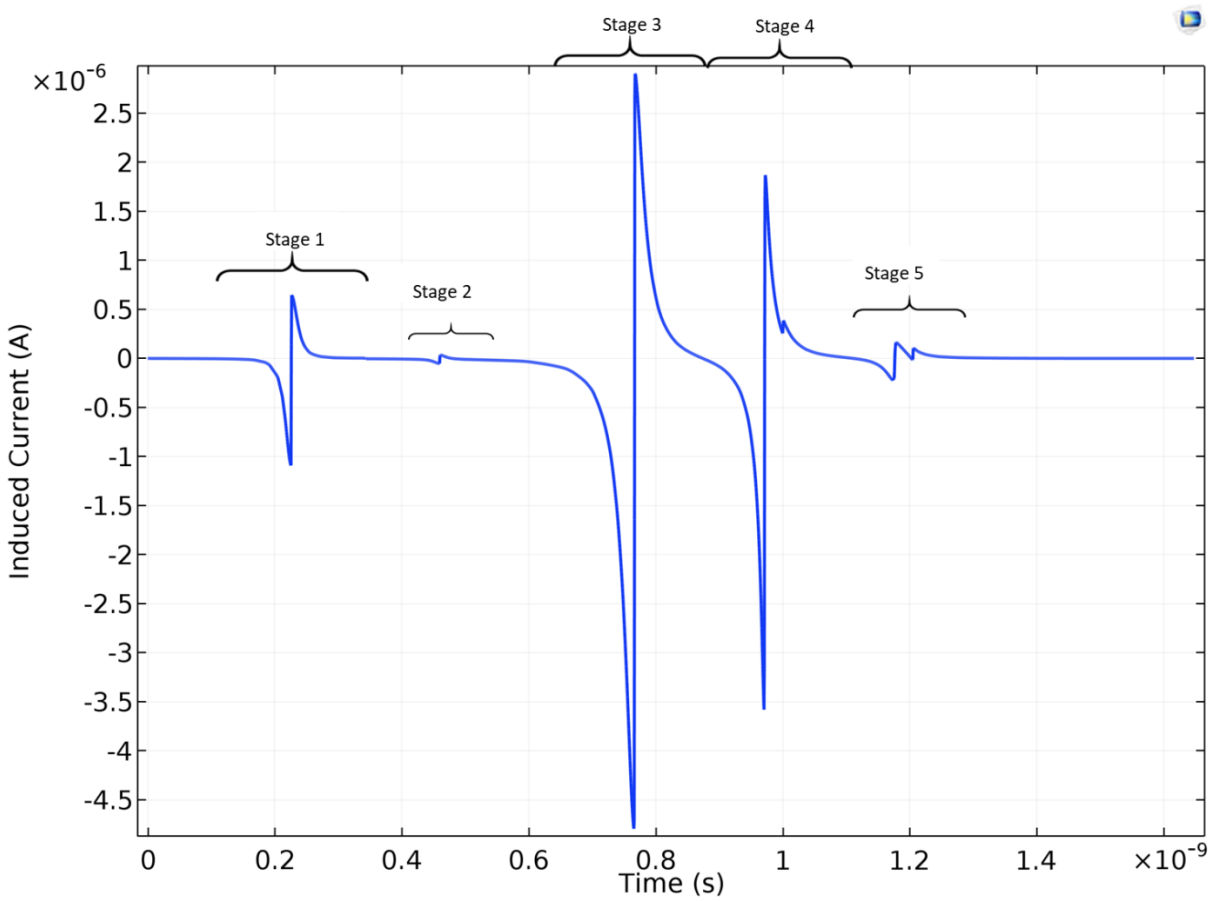

Figure 4-18 – The sum of the induced currents on the anode of the VPT.

The induced current as the sum of all the induced current in Figure 4-14, is considered the final output of the VPT and is shown in Figure 4-18. Here it is easier to see the bulk of the induced current occurs from the initial photoelectrons and the SE (stage 1 and stage 3). Although stage 5 seems significant enough in Figure 4-14, you can easily see here that the contribution to the signal is insignificant (~1.2 ns). This result was used in a SPICE simulation to show the realistic output from the device, using the inter-capacitances and inductances of the device in a later section in 4.7.7.

4.7.4 Simulation with a 4 T field at 0°

This section describes the simulation with the VPT model in a 4 T magnetic field. To make it easier to explain what was happening inside the VPT model in terms of the induced currents, the process is split into four stages.

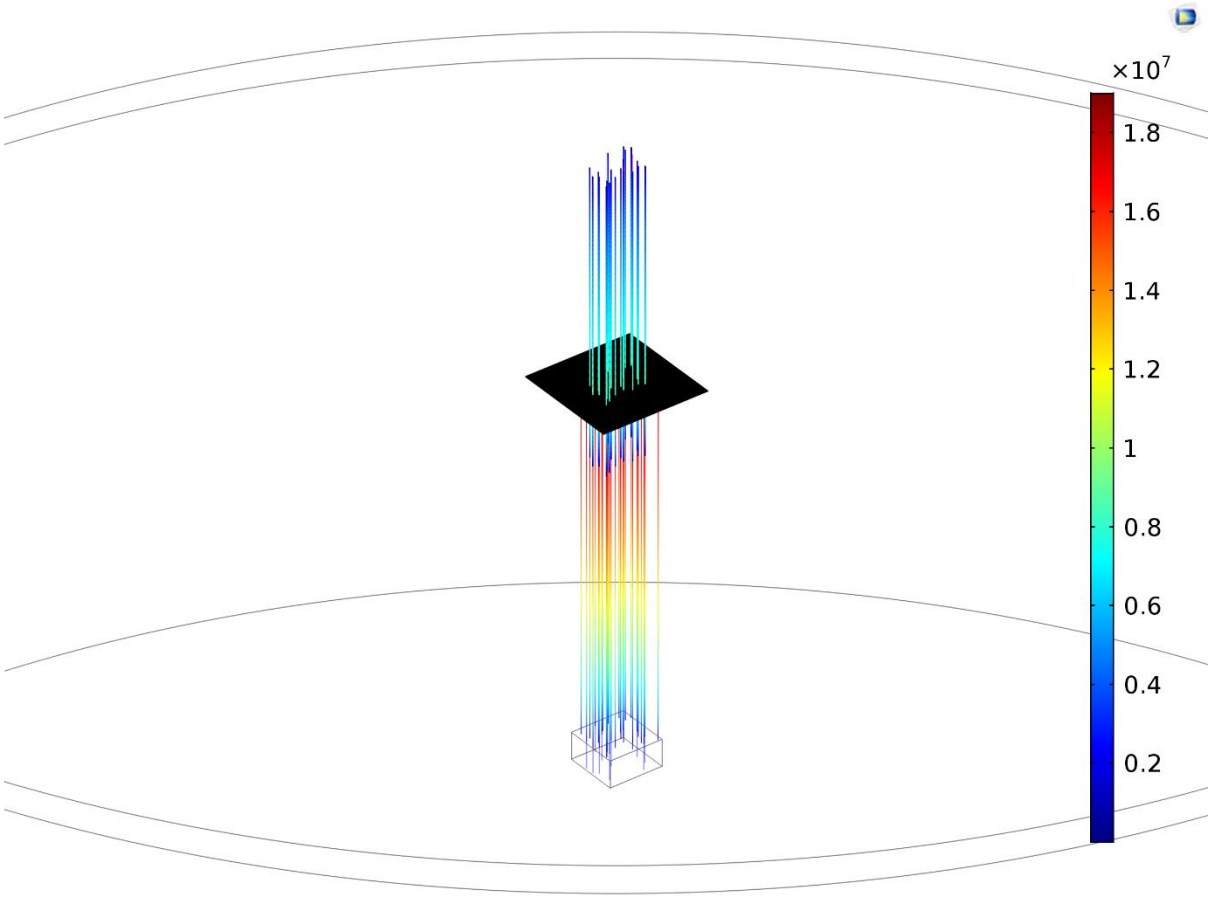

Figure 4-19 - Particle trajectories within the VPT at 4 T. The photoelectrons are released from a square region on the cathode. The potentials are cathode 0 V, anode +1000 V and dynode +800 V. the coloured scale shows the speed of the particles in m/s.

The first stage - stage 1: 100 primary photoelectrons were released from the cathode with various energies. 43 of these primary photoelectrons collided with the anode mesh, with the remaining 57 going past the anode before 0.3 ns reaching peak currents of approximately 10 nA. At the end of stage 1 and between the end of stage 2, backscatter on the anode occurred, as the initial photoelectron were released and some of these hit the anode mesh. This is pointed out in Figure 4-22, this is difficult to see on the induced current plot without a colour scheme, this has been highlighted in Figure 4-21. As this electron hits the cathode it was set to absorbed by the electrode.

Stage 2 is where backscattered electrons were produced by the dynode and go through the anode mesh and hit the cathode. Stage 3 is the SE that occurred at the dynode. At this stage the SE electron can cycle back and forth around the anode – this was shown by the current changing sign. Towards the end of stage 2 again, the predominately red curves show the backscattered particles at the anode. At this stage, the particles released range between 3-25 eV in energy. Stage 3 at 4 T was predominantly from a few secondary electrons which have to go through

the anode and cycle back and go through the anode again and go on further to hit the dynode again releasing a wave of tertiary of particle. These secondary electrons are seen in the middle of stage 3 (dense block of colours overlapped), with a few stray backscattered particles inducing a current on the anode on either side of (yellow, black and blue). Stage 4 is the induced current the backscattered electrons and the SE heading back towards the dynode.

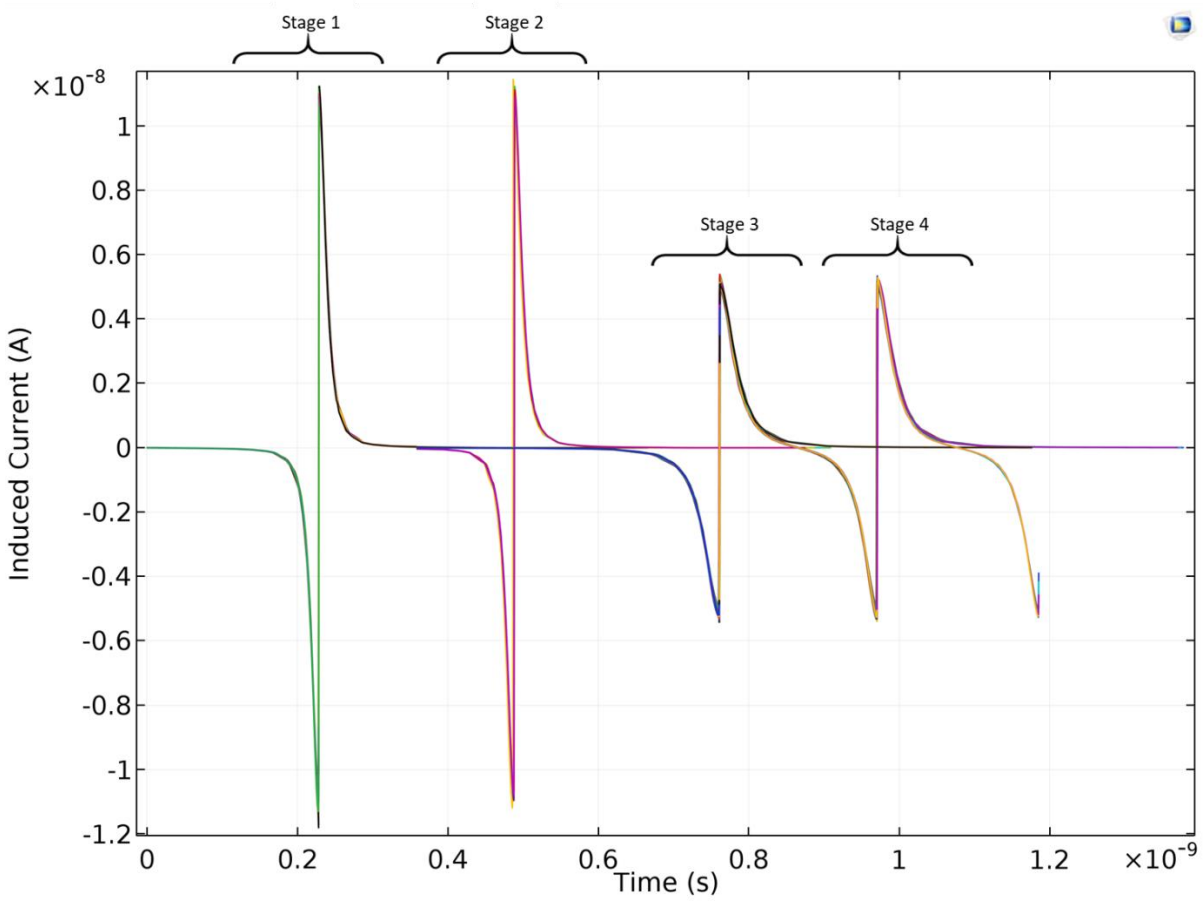

Figure 4-20 – The induced currents are shown for all the particles within the VPT at 4 T. The induced currents are split up into 4 stages, to help explain the different scenarios which occur. Stage 1 is the induced current from photoelectron being released and travelling towards the anode and dynode. Stage 2 is the induced current for the backscattered photoelectron. Stage 3 is the induced current due to SE and stage 4 is the induced current the backscattered electrons and the SE heading back towards the dynode.

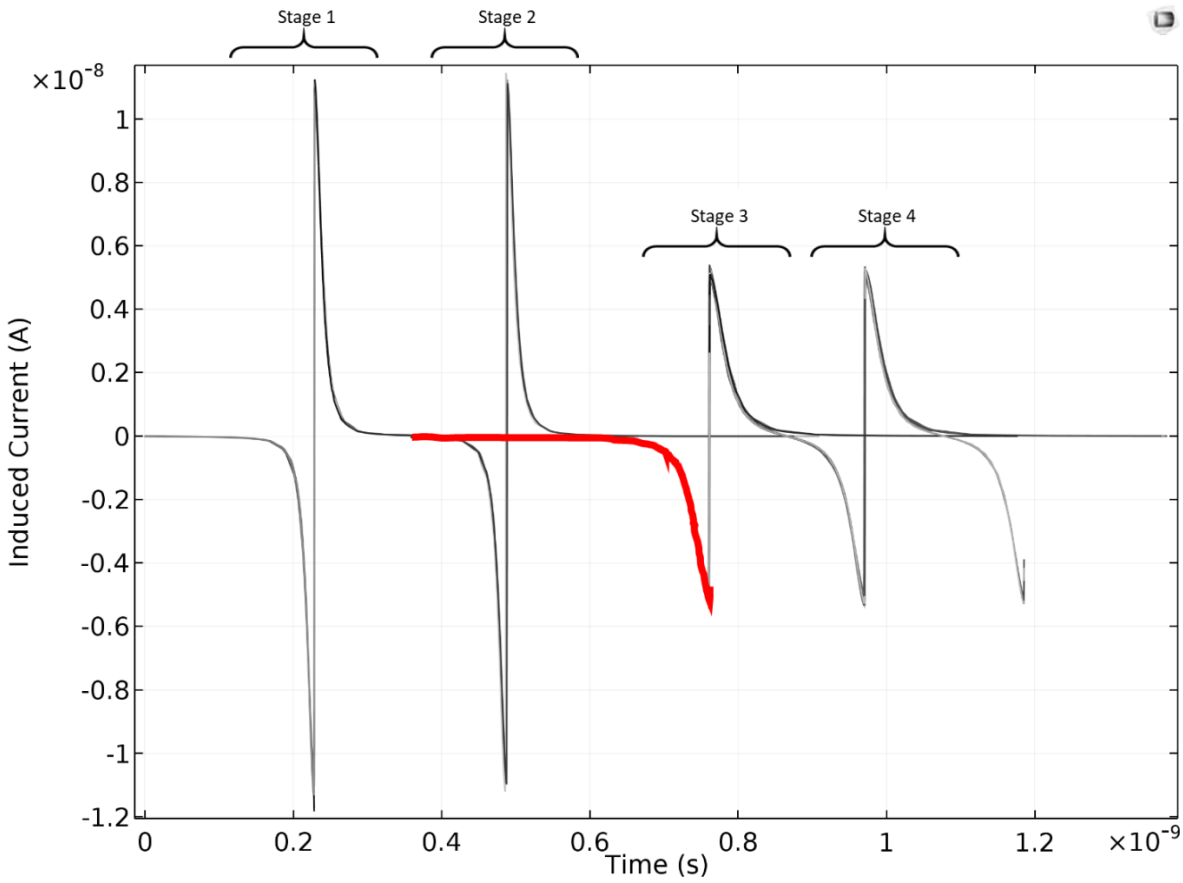

Figure 4-21 – This plot is the induced currents within the VPT, with the special case of the backscattered electron at the anode highlighted.

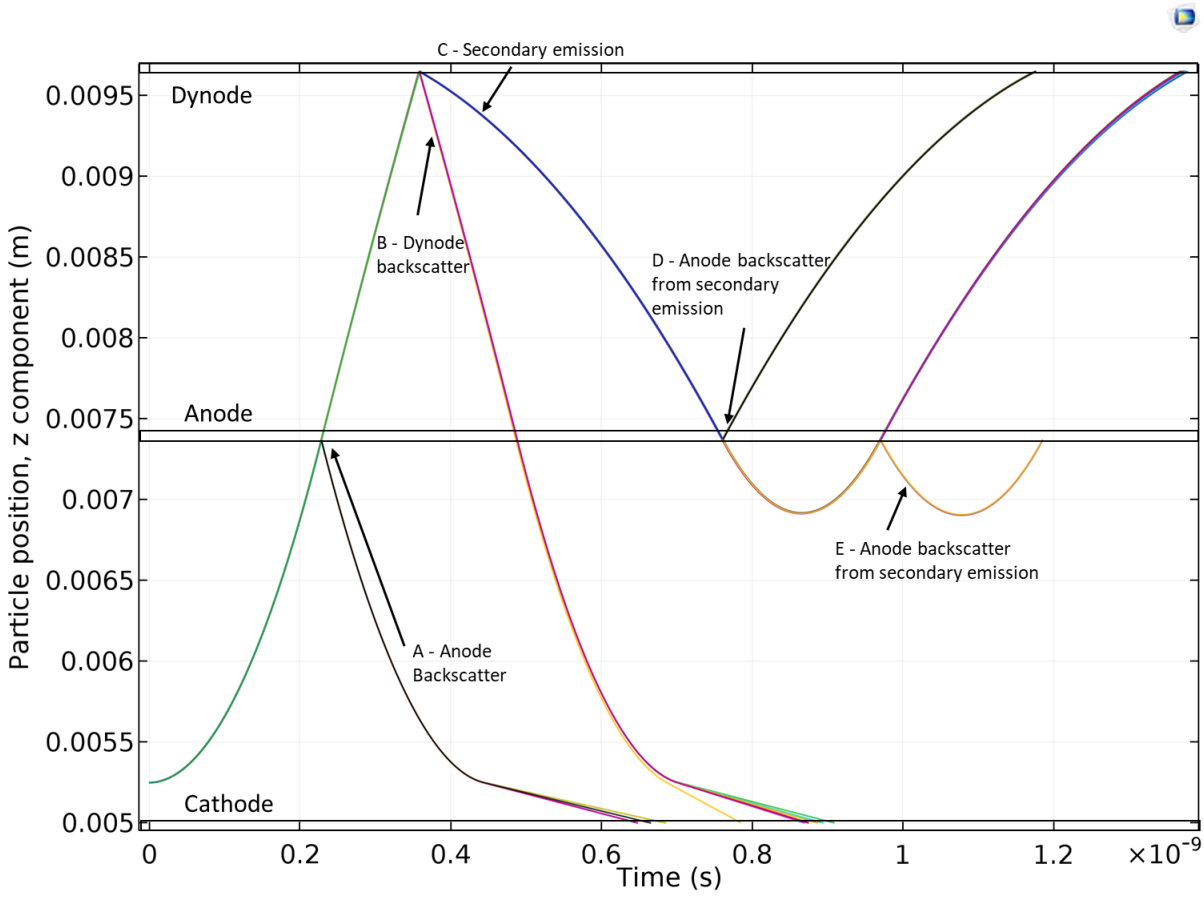

Figure 4-22 – Particle position is shown in the VPT along the z domain of the VPT model. The cathode, anode and dynode are labelled respectively to where they are in the COMSOL model. The backscatter events are labelled on the plot.

The particle positions for each of the particles in the induced current plot is shown in Figure 4-22. The anode and dynode backscatter have been labelled on the plot. The point labelled A is a backscattered particle from the initial SE from the incoming photoelectron, that travelled back towards the dynode. Point B was the backscatter at the dynode from the incoming photoelectron. Point C was the SE as the initial photoelectron hit the dynode. As they travelled back towards the anode, approximately 50% of the electrons miss the anode and continue to on travel towards the cathode. Eventually, the K.E is reduced to zero and the electrons are attracted back towards the anode, where again there was a 50% of the remaining particles being stopped, this is highlighted in Figure 4-23. As most of the particle's curves are overlapping, it is difficult to see visually. Point D was the anode backscatter from the secondary emission which was directed back towards the dynode. As the SE emission loops the anode mesh at 0.9 ns and the secondary electrons were directed back towards the dynode, as they go past the anode mesh with approximately 50 % of those electrons colliding. From this collision an electron was

backscattered towards the direction of the cathode and was attracted towards the anode mesh and was directly captured, this is the final point E.

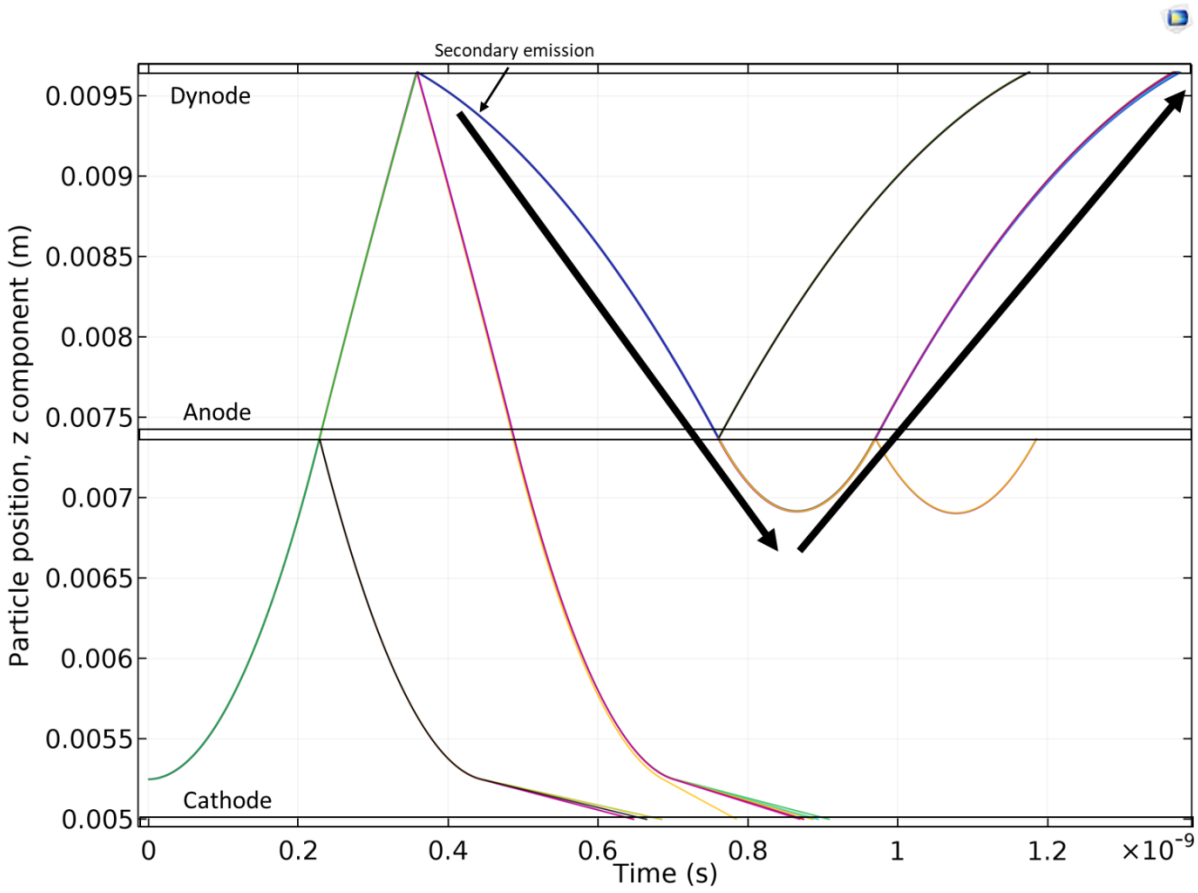

Figure 4-23 – The lines representing the SE is highlighted with black arrows.

The energy of the particles is shown in Figure 4-24. The initial photoelectrons were released at a few eV and they increase in energy as they went towards the anode which it hit at 1000 eV. The SE electrons are then travelling towards the anode which experienced a potential difference of 200 eV between the anode and dynode.

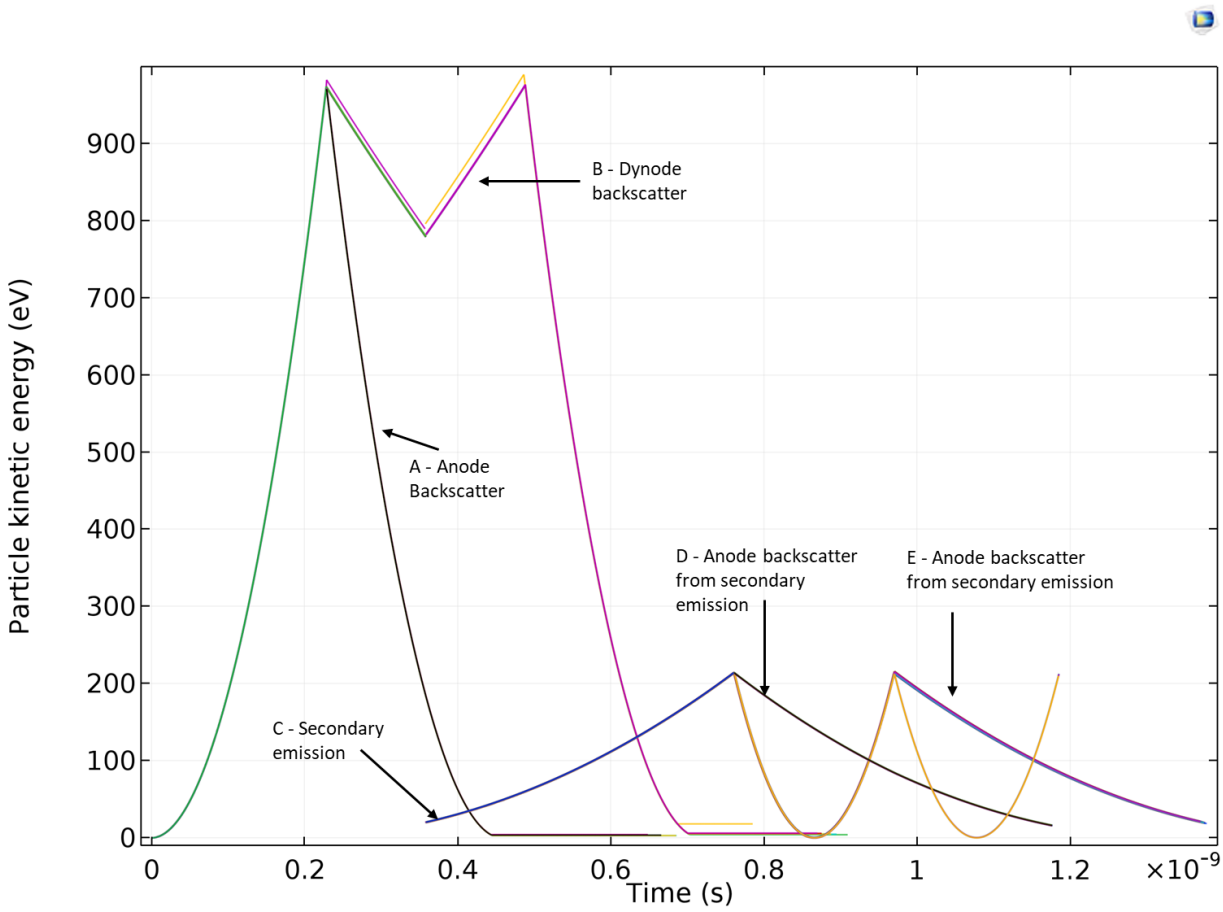

Figure 4-24 – Particle energy in eV for all the particles within the VPT. Each coloured curve represents an electron within the VPT.

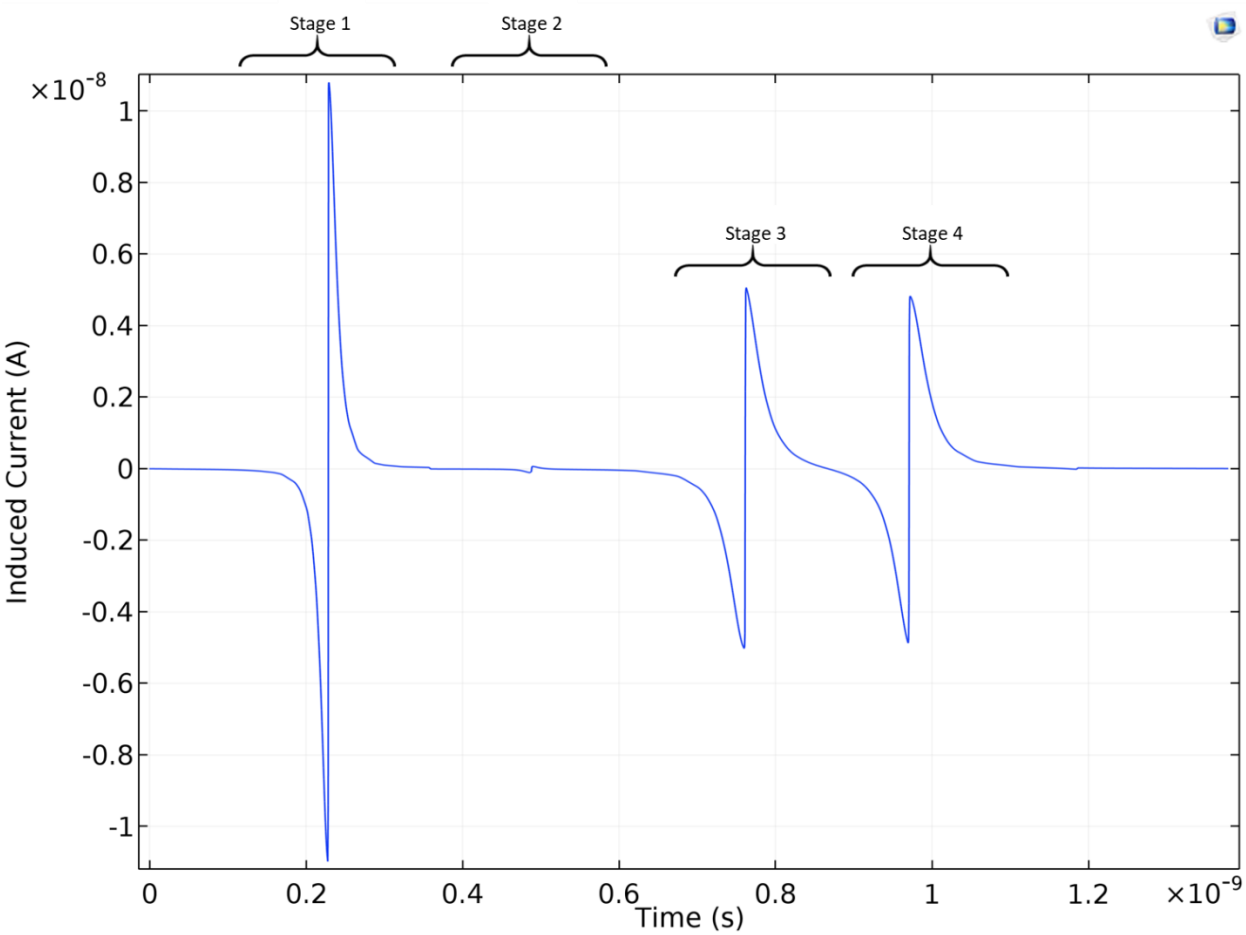

Figure 4-25 – The induced current shown as an average of all the particles.

Looking at the average signal of the VPT produced in Figure 4-25. The SE on average had a lower induced current than the initial photoelectron, due to the 200 V difference between the anode and dynode compared to the 800 V gap between the cathode and dynode.

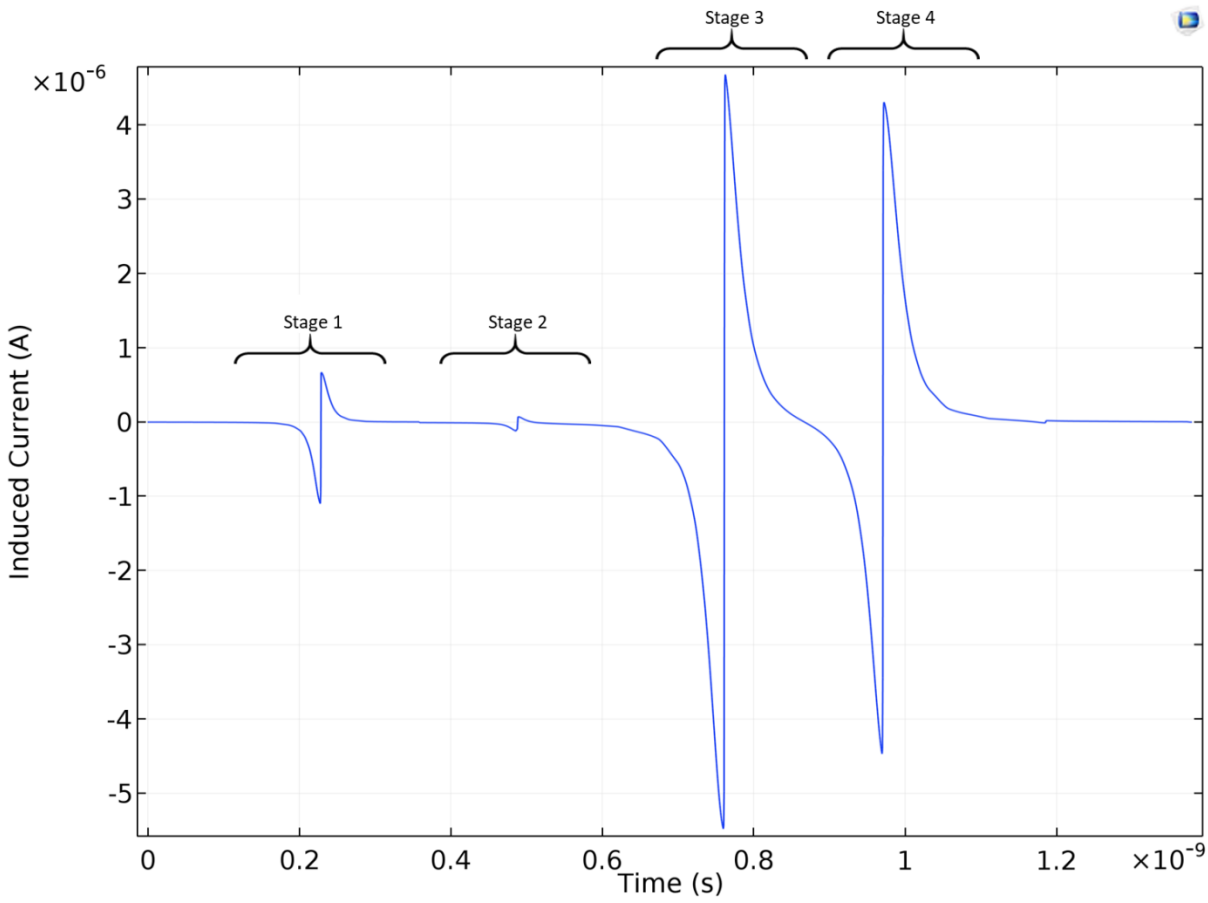

Figure 4-26 - The sum of the induced current seen on the anode by the VPT with a magnetic field of 4 T.

4.7.5 Simulation with a 4 T field at 15°

The following results are COMSOL simulations with the same release specifications as the previous sections (4.7.3 and 4.7.4), however with a magnetic field at 15° degree field applied to the VPT. The particle trajectories of the electrons within the VPT follow the magnetic field lines, which are at 15° to a 4 T magnetic field. The trajectory path of the particles can be seen in Figure 4-27. The electrons were released from the cathode towards the anode mesh where 52 electrons were absorbed and 48 go onto to hit the dynode to produce SE.

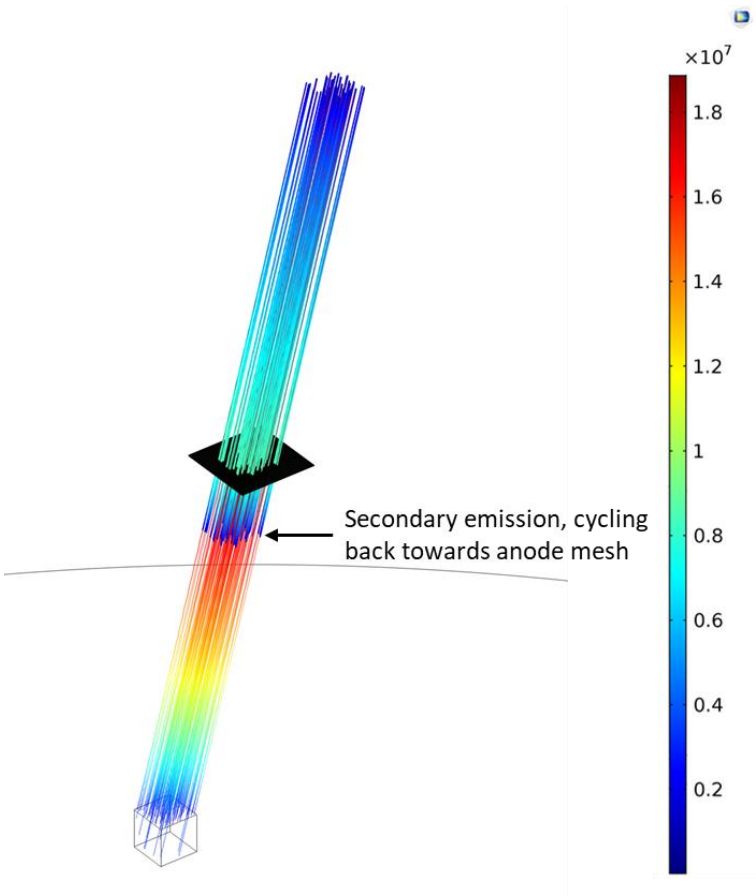

Figure 4-27 - Particle trajectories within the VPT at 15°, the colour scale shows the particle speed in m/s.

The SE that goes past the anode and cycles back has been labelled. Most of the electrons are consistently attracted back towards the mesh at roughly the same point.

Stage 1 in Figure 4-28 is the induced current seen the anode mesh from the initial photoelectrons released from the cathode. There was a small number of anode backscatter (stage 2), which corresponds to the anode backscatter that starts to occur at ~ 0.45 ns and ends just before 0.6 ns. The SE occurred at the start of stage 3 between 0.75 ns and 1.5 ns,

contributing to the signal output as the sum of the induced currents in Figure 4-32. Stage 4-6 were the induced currents caused by different backscatter scenarios.

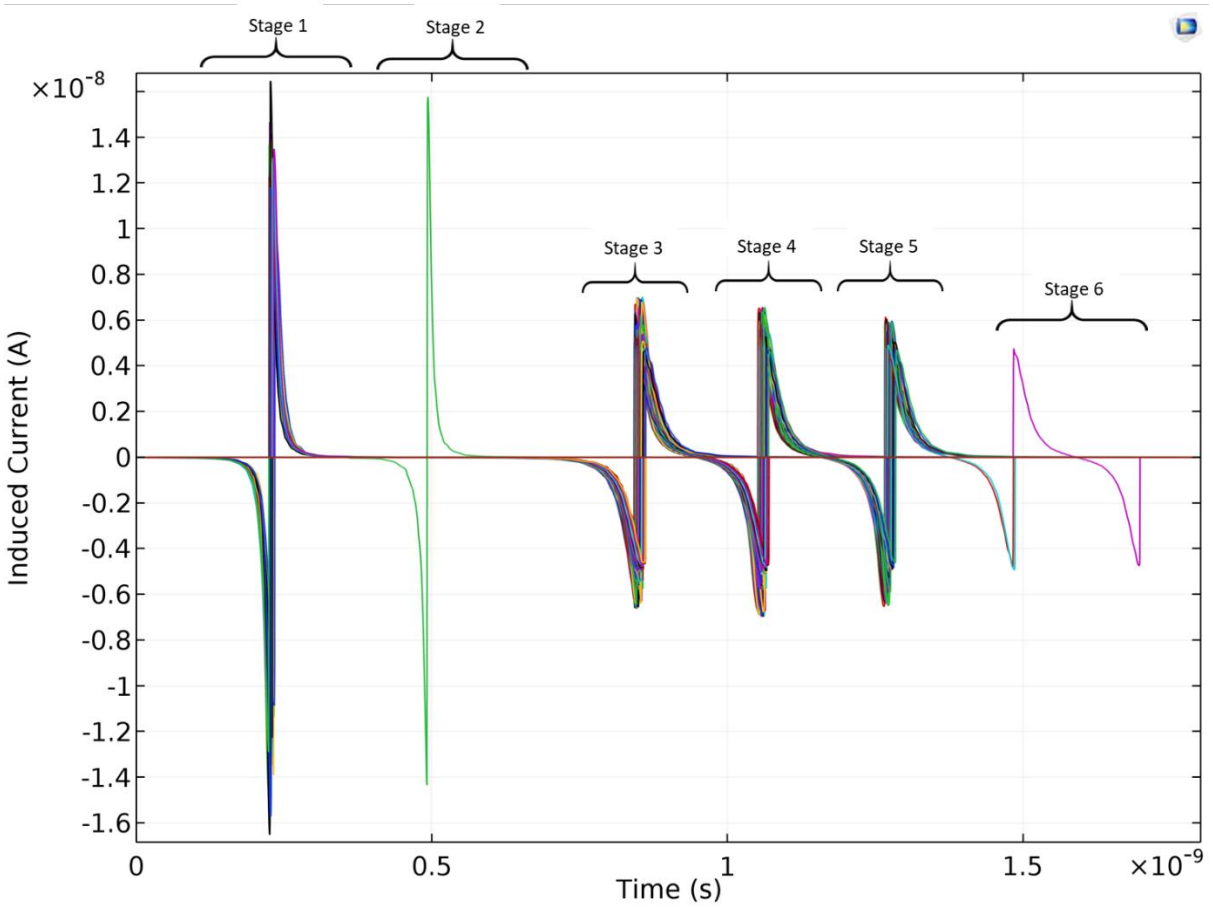

Figure 4-28 – The induced currents for all the particles within the VPT, with a magnetic field of 4 T at 15° degrees. Stage 1 of the plot is the induced current on the anode by the release of the photoelectron from the cathode. Stage 2 is the induced current from the backscatter at the anode as the initial photoelectron reach the anode. Stage 3 is induced a current from the SE. Stage 4 represents anode backscatter at the anode from SE. stage 5 is the induced current from SE that is cycling the anode and as hits the anode mesh there is backscatter which goes on to hit the dynode. Stage 6 is the anode backscatter which is a result of anode backscatter as well.

The particle position is shown in Figure 4-29 of the particles within the VPT along the z-axis. The cathode, anode and dynode electrodes have been annotated on the plot to show where they reside in the VPT tube along the z-axis. Points labelled A-D are some of the more notable behaviours of the trajectories of the particles. Point A shows the backscatter from the initial photoelectron release from the cathode and as it hit the anode there are some particles which were backscattered. Point B shows as the photoelectrons hit the dynode and a single particle was backscattered towards the cathode, which travelled through the VPT and hit the cathode. Point C shows the SE which was released by the dynode and travelled towards the anode. As these SE particles approach the anode mesh the particles split in two ways: the first - some of

these SE particles were backscattered towards the dynode and second the SE particles travelled through the mesh and cycle around back towards the anode. Here, again there were three options the particles have (at 1.1 ns): first, the ~ 50% of SE particles carried on through the mesh, the other ~50% were stopped by the anode mesh and third some of these particles hit the anode mesh and cause backscatter. At point E, the backscatter was directed towards the cathode (- z-direction) and as its K.E was reduced to zero and was directed back towards the anode mesh hitting the mesh (at ~1.25 ns) some of these particles were stopped by the mesh and caused some backscatter (point F). The other ~ 50% of the particles which were not stopped by the mesh go onto collide with the dynode, where the signal stops.

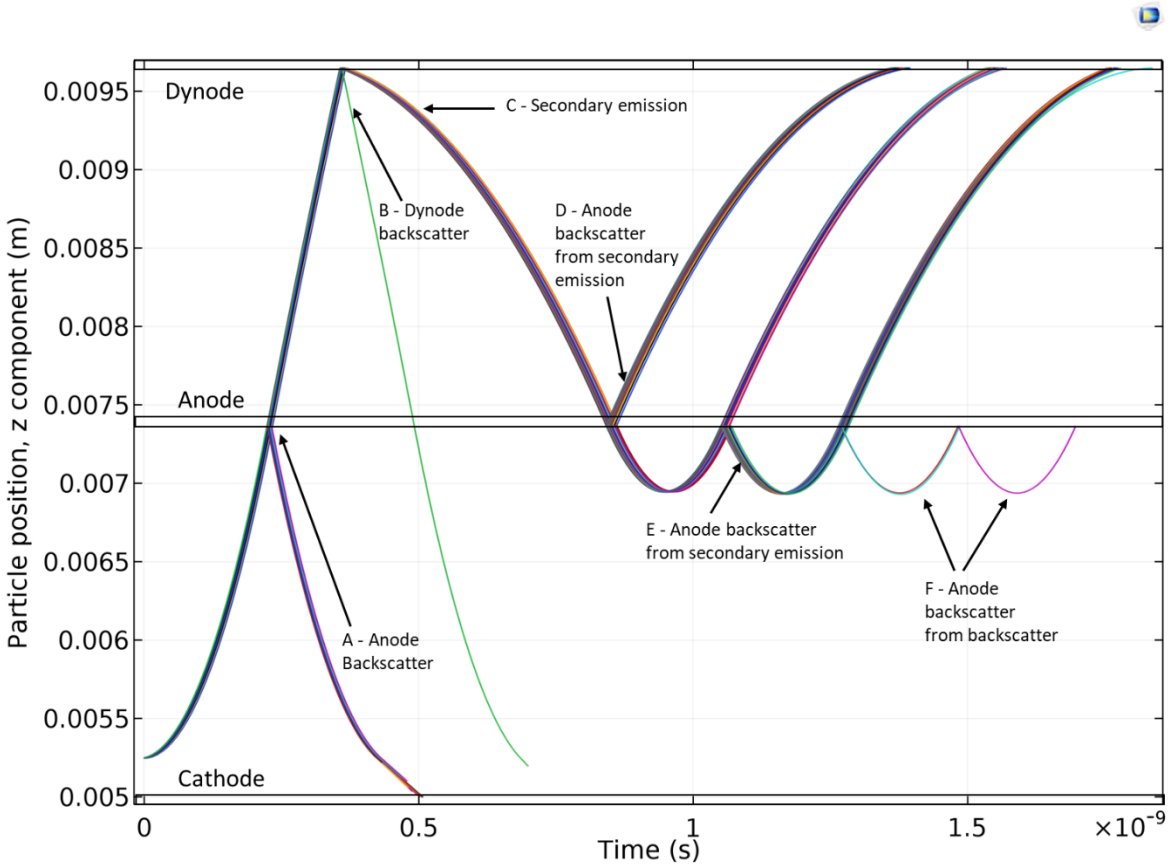

Figure 4-29 – The particle position of each particle within the VPT along the z-axis. Points A – F are highlighted as the important behaviour within the VPT.

The electron energy is presented in Figure 4-30 in eV. The same highlighted points have been shown on this plot to match the particle position in Figure 4-29 to show how the particles that's travelled through the VPT experience different energies. As the anode was set to +1000 V the initial photoelectron approaches the anode mesh with 1000 eV energy and as they go past the anode mesh and approach the dynode their energy was decreased to 800 eV as the dynode was

set to + 800 V. The potential between the anode and dynode was 200 V, therefore SE emission reach a peak of 200 eV.

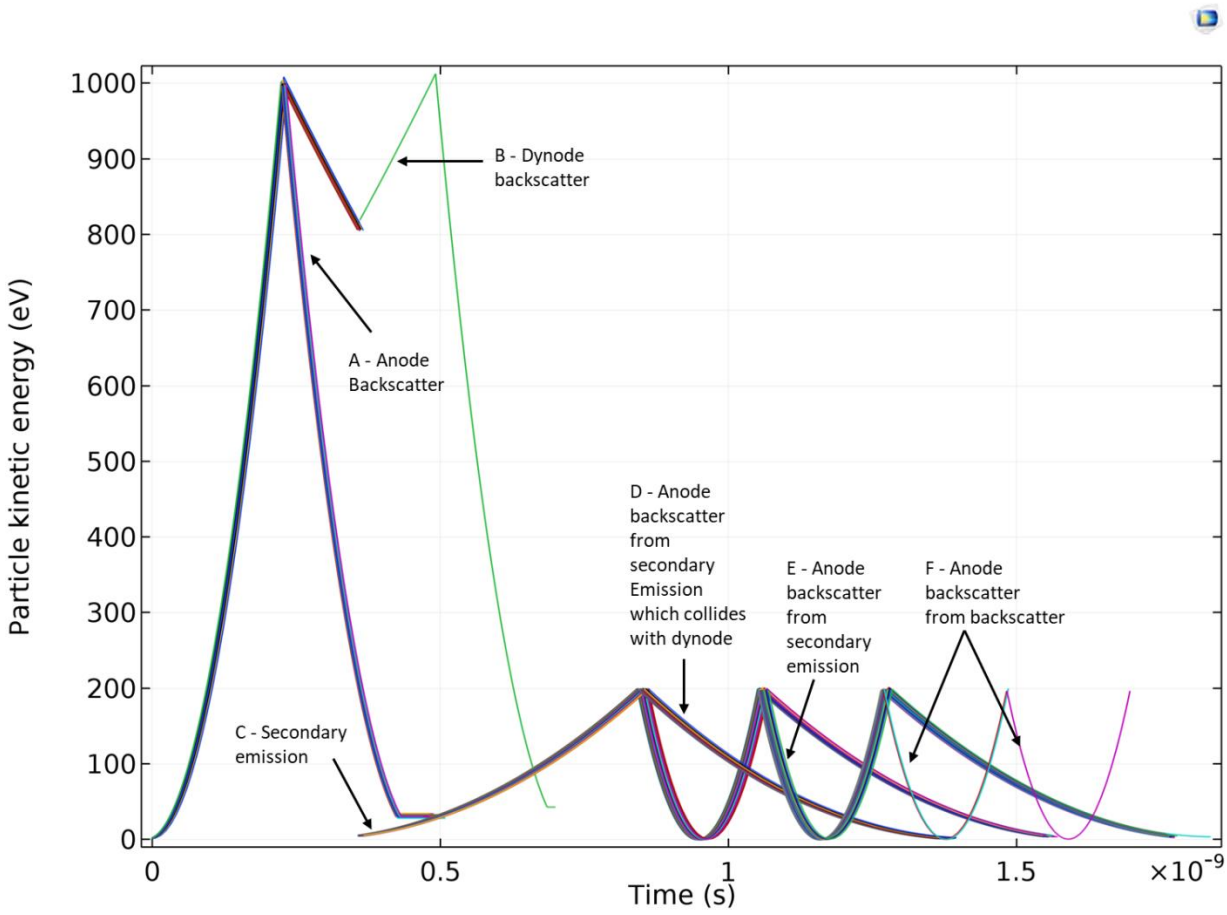

Figure 4-30 – Energy of each particle within the VPT in eV.

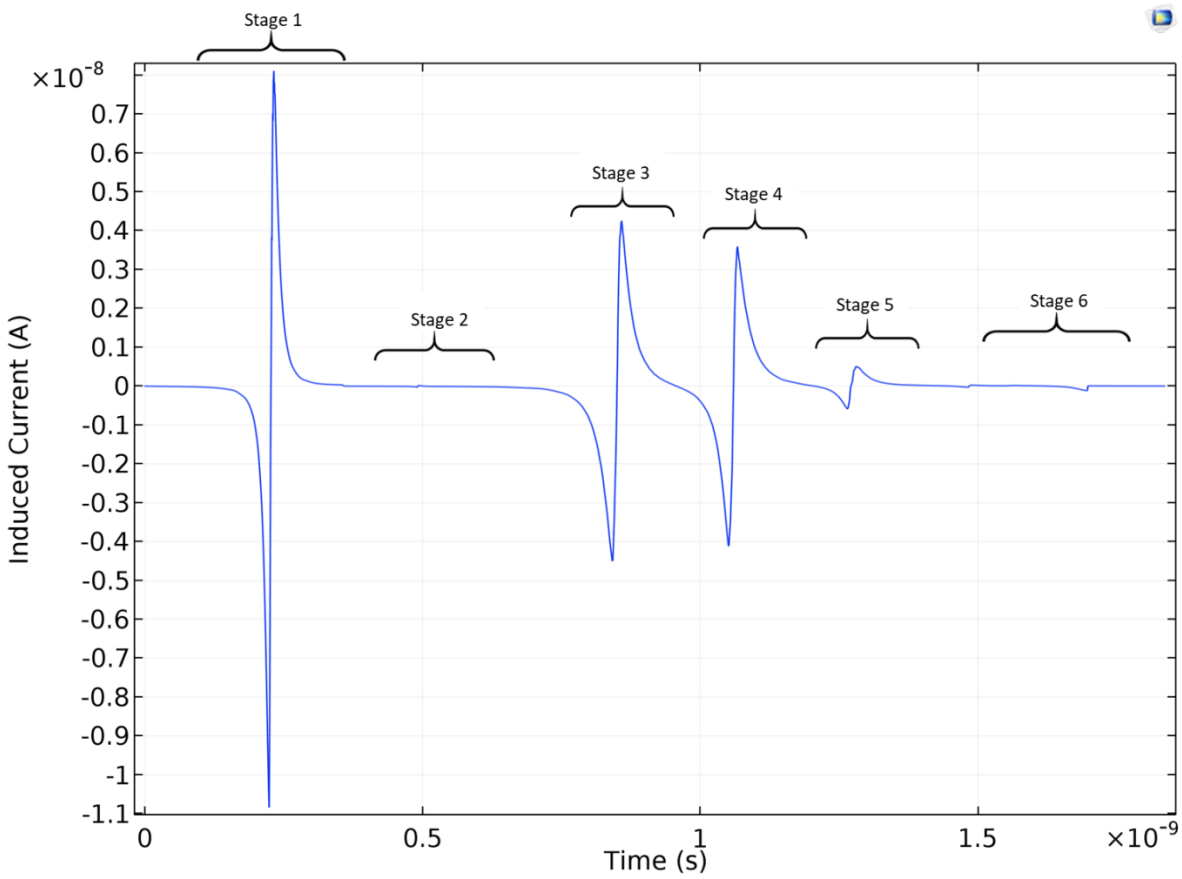

Figure 4-31 – Average of all the induced currents in the VPT.

Looking at the sum of the signal in Figure 4-32, most of the signal occurs between 0 – 1.3 ns. The number of actual particles after 1 ns in the VPT is a fraction of the initial particles and the SE, the remainder particles are from the backscatter at the anode and dynode (stage 5 and 6). This is more clearly visible in Figure 4-32, which shows the sum of the induced currents.

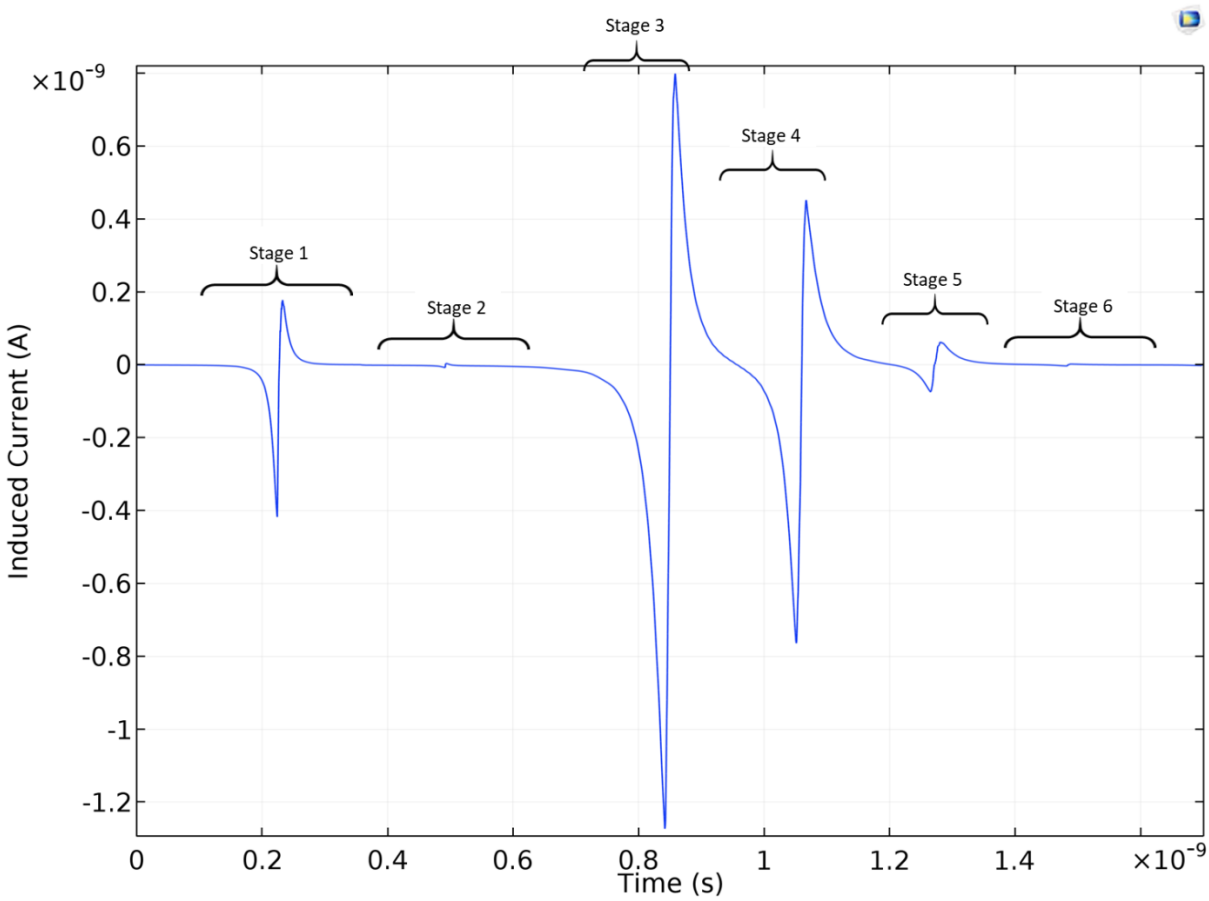

Figure 4-32 – The sum of the induced currents within the VPT.

4.7.6 Model Comparison

For the simulation of the VPT, the model designed in COMSOL has a higher accuracy in design than those made by Bateman [55] and Ignacio [1]. Bateman used a square approximation for the plates with an edge dimension of 20 mm. He also used 5000 photoelectrons for their simulation which was based on 2D geometry. This simulation is very limited in model design, which with recent advanced software can be made more accurate for better simulation results.

The main complicated component of the VPT is the anode mesh. Ignacio attempted to replicate the anode mesh using SIMION7. At the time of his works, he was unable to model the exact dimensions of the anode mesh, using a depth of 5μm. His simulations also did not include detailed information such as backscatter.

The simulations done in COMSOL have managed to achieve the accurate dimensions of the anode mesh (up to a 100×100 array) along with the full 3D model simulated with the right physics and backscattering included. However, the model was still incomplete in using the full anode mesh, along with using large quantities of primary electrons at the same time. These

were caused by hardware limitations which means it is still possible to achieve the full model creation in COMSOL.

To understand the role backscatter can play within the VPT model, simulations have been carried out to demonstrate the impact to the overall induced current with and without backscatter. To make the comparison fair, the environment and the simulation conditions have been set to be the same, which includes using the same random seed to produce the exact same particle trajectories.

The top graph of Figure 4-32 shows the sum of the induced current for the simulation that has no backscatter, with the bottom graph showing with backscatter. There are a few noticeable differences between the two plots. The first is the spike that it visible at times 0.48 ns and 1.18 ns. They are caused by the backscattered electrons that cycle the anode mesh.

The second noticeable difference is the total induced current at the top peaks when the secondary electrons cycle the anode mesh. There is a total increase in induced current of about ~12% which is cause by the backscatter that remains between the anode and the dynode.

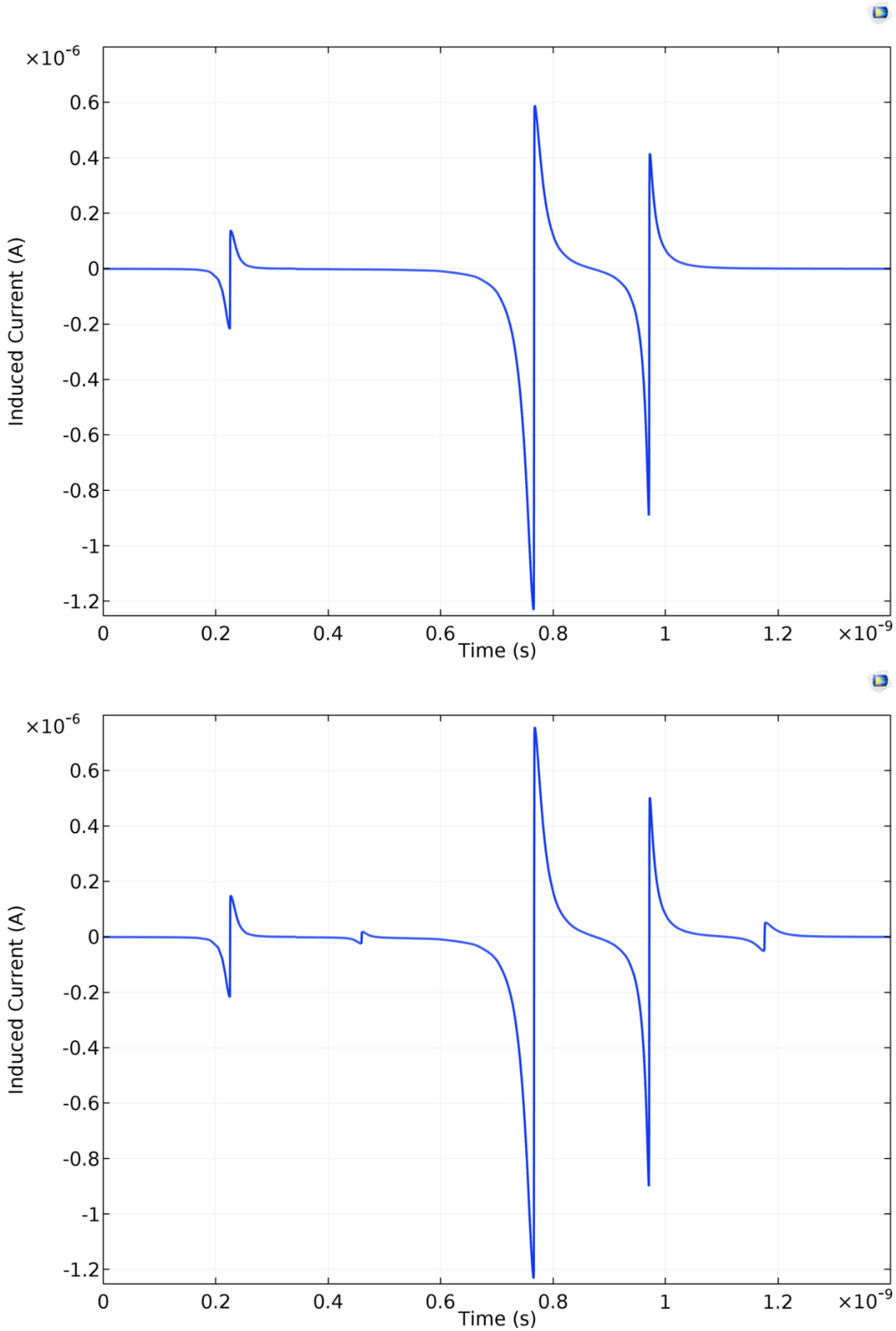

Figure 4-33 – The top plot shows the sum of the induced current within the VPT at 0 T. The bottom plot shows the sum of the induced current within the VPT at 0 T with backscatter at the anode mesh and the dynode occurring at 0.48 ns and 1.18 ns.

4.7.7 Effect of internal wiring in the VPT

The real VPT has wires connecting the internal electrodes to the external pins in the base. To investigate the effect these have on the output, a SPICE simulation, provided by Prof Peter Hobson, is included here. The output from Figure 4-18 in section 4.7.3, which is the sum of the induced current of the COMSOL simulation running at 0 T, was used in an LTspice IV [57] simulation with a maximum timestep of 1 ps. This simulation was used to investigate the effect of using the physical VPT, by modelling the inductance of the VPT internal wiring, the anode-cathode capacitance and the inter-pin capacitance of the VPT base. The circuit diagram to represent the VPT internal model is shown in Figure 4-34 and is that used previously [2].

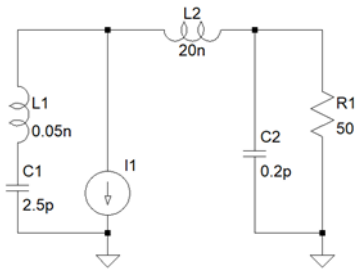

Figure 4-34 - Circuit used in simulation, I1 represents the induced anode current, C1 represents the anode-cathode capacitance and L1 and L2 represent inductance arising from internal wiring. C2 is the interelectrode capacitance at the base of the VPT

The output from the COMSOL simulation of the sum of induced current was the input source for I1 in Figure 4-34. A Piece-wise linear approximation of the COMSOL output is shown in Figure 4-35. This is the output from current generator I1 and the output current flows through R1 and is shown in Figure 4-36.

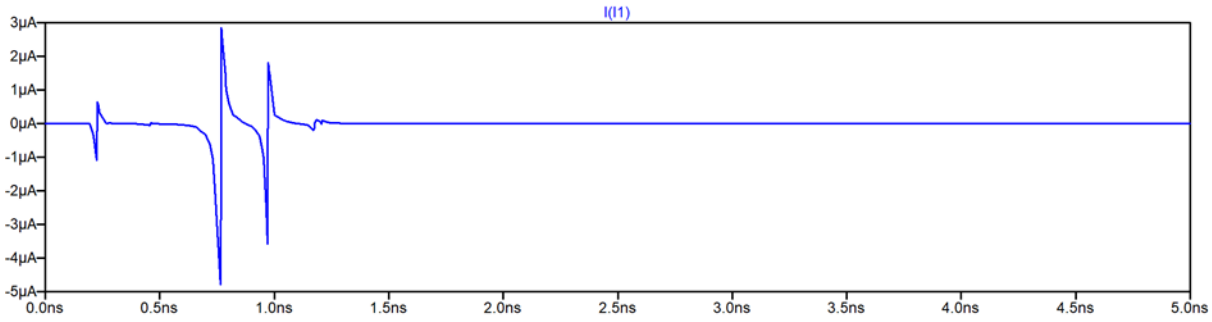

Figure 4-35 - Induced anode current, derived from COMSOL simulation as a Piece-wise linear approximation.

The output can be broken down into 3 parts. The initial spike; the first batch of secondary emission; and finally, the looping secondary emission with some backscatter. The first part produces a slight increase in current at the output at timestep 0.25 ns. The negative charge cycle

occurs later in the output signal, at 1.75 ns. The second part shows a gradual increase in current hitting a peak of ~260 nA at 1 ns on the output. The third part hits its peak at 2.5 ns of approximately 50 nA and slowly decreasing to 0 nA.

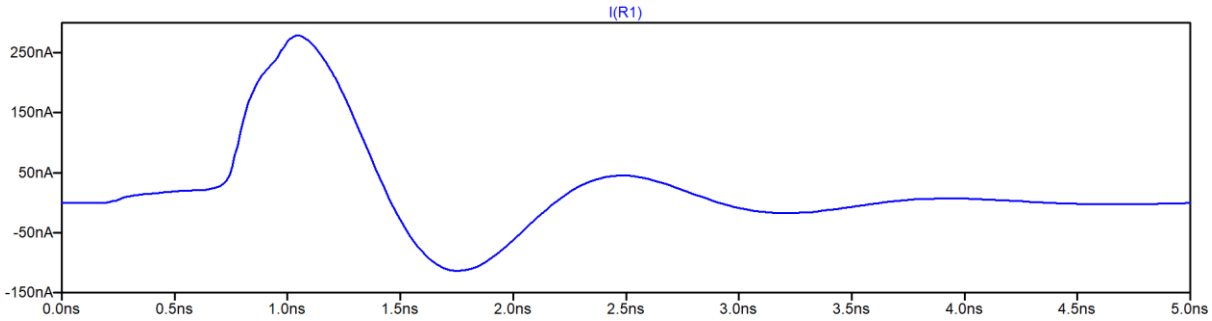

Figure 4-36 - SPICE simulation, using LTspice IV [57], of current at the output anode pin of the VPT.

4.7.8 Model Simplifications in COMSOL

The VPT model in COMSOL has been simplified in certain ways to decrease the computational resource requirement for the simulations. The simplifications have been applied based on assumptions that they will not cause the simulation results to deviate much from the results without. Some of these simplifications include:

- The size of the anode mesh is reduced to 100×100 array of single cell, from an approximate size of 1800×1800. The anode mesh size has a really big impact on the computational resources required as there are a lot of edges and vertices produced. This also significantly impacts the model construction and meshing stages within COMSOL. To ensure that the simulation is not affected by this, the source photoelectrons are released from a smaller area within the cathode. The placement of this release is designed so that the photoelectrons meet the reduced anode mesh. Overall the transparency of the anode mesh is still 50 % and the depth of the anode mesh of 1.6 µm which is the real depth of the anode mesh, this is one of the most important factors when trying to determine the particle trajectories. With all the simulations that were carried out, the highest array that could be simulated was 150×150. This was reduced to 100×100 due to computation time of the simulation and the RAM used by the model being at almost 100%, which made created running of the of the workstation extremely slow and unusable.
- The photoelectrons are released from the cathode at the same time to give the ideal scenario. This may not occur in the CMS experiment as the photoelectrons can enter the VPT nanoseconds apart, causing peaks that may occur at different offsets. In the

simulations, all the peaks from similar particle trajectories occur at the same time. This allows a clearer understanding of the various particle trajectory scenarios that can occur within the VPT. However, for some application involving fast laser pulses the photon arrival can occur very fast and can all almost be at the same time.

- The anode mesh is first created as a perfect square cell and replicated to create the 100 × 100 array. However, in Figure 4-3, there are visible imperfections on the edges that are not consistent and are difficult to replicate in the 3D model. It would also be challenging to create the COMSOL mesh on this. The impact of not simulating the imperfections should be minimal as the transparency is still near 50%.
- The angular distribution of the backscatter uses the simplest approach of the electrons being released in the same direction of the incoming electron had been applied to the model.

4.8 Summary

For the results of the previous 3 sections, the output of the VPT is taken up until 2 ns, this was due to where the bulk of the output occurs. After this point there maybe 1-2 stray particles within the VPT, which eventually will also disappear by hitting the side of the VPT shell or another structure within the VPT. The total surface area of the mesh that was simulated is 1 mm×1mm, this is approximately 1.3% of the surface area of the anode. The gain of the tube was calculated to be 7 and the collision probability that occurred in the simulations varied from 42-50%, in terms of the particles collected on the anode versus the particles not hitting. Ideally, the collision probability should be 50%, due to the transparency of the physical anode mesh being 50%. However, the cathode release area was smaller than the anode mesh, to prevent collisions occurring beyond the anode mesh. This could be one of the factors for the decreased collision rate.

To look at the full behaviour of the particles within the VPT, the same information has to be seen in multiple ways to understand the finer detail. For example, looking at the results for 4 T at 15° angle magnetic field, when initially looking at the induced current plot (Figure 4-28) stage 4 it appears to look as if there are the same number of particles as in stage 3. However, when looking at the sum of the induced currents it is clear the actual number of particles is significantly less. The induced current at stage 2, which is caused by backscatter at the dynode seems to look big compared to the SE at stage 3, but the actual impact of that in the overall signal is insignificant, resulting in a signal of 1 pA. A SPICE simulation has been carried out

to show the impact of the inter-capacitances and inductance of the VPT on the output of the COMSOL simulation.

The standard deviation σ is calculated for PEs hitting the anode mesh based on 5 simulations. The setting for the simulation is based on section 4.7.3, using 0 T. The number of anode mesh hits are as follows, in order of simulation: 48; 49; 48; 46; 48.

This chapter has provided the following contributions:

- Creating an accurate 3D model of the VPT with properties that are exactly or similar to that of the physical device. The anode mesh has been carefully designed to match the physical device dimensions up to a 100×100 grid.
- Developing the environment that matches the magnetic strength found in the CMS detector, and varying the range from 0 T to 4 T, at 0° and 15°.
- Improvements have been made on the work by Yaselli [1] with regards to the limitations in model and simulation capabilities:
    - Improved quantity of total particles at a given time
    - Accurate dimensions for the anode mesh
    - Additional functionality captured such as backscattering
    - Simulation is based on 3D modelling, not 2D
    - Material properties are better characterised in COMSOL compared to SIMION 7
- Backscatter has been simulated at the anode and dynode that is reflective of Batemans work.
- Simulations provided in-depth details such as the induced current and particle trajectories within the varying conditions.

Chapter 5. Upgrading ECAL Calorimetry in CMS

The CMS detector is going to be upgraded for the HL-LHC for collisions at higher luminosity. This requires the detector to be upgraded to accommodate the data to be gathered from the higher collision rate. It has also been damaged by radiation via previous experiments and would require replacing or upgrading components.

There are two options have been chosen as possible upgrade options for the ECAL, which are the ECAL Shashlik and the High Granularity Calorimeter (HG-CAL). Both upgrade options are being reviewed by the upgrade board at CERN. Another option called the Double End Readout (DRO) is also discussed internally that uses the current ECAL architecture. The focus of this chapter is on the double side readout concept, which is an alternative solution that is faster and cheaper as it uses the existing ECAL setup but adds an additional photosensor to each crystal to help mitigate the side effects of the radiation damage on the current photosensors and crystals. Not only this, but there are already many of the RIE-188 photosensors available to use if this concept is needed.

This research contributes towards testing 23 VPTs that were held in storage to see how stable they are compared to when they were manufactured in the early 2000s. They were also tested in the DRO beam test at H4, North Area, CERN.

5.1 CMS ECAL Upgrade

Initially, at the start of CERN experiment, the CMS detector itself was designed for an overall operating period of 10 years with a total integrated luminosity of 500 fb^{-1} and a possible maximum instantaneous luminosity of 1×10^{34} $cm^{-2}s^{-1}$ [45]. As the end of run 2 is approaching the total instantaneous luminosity that the detector has encounter within the period of run 2 the detector will hit instantaneous luminosity of up to 2×10^{34} $cm^{-2}s^{-1}$ or higher [58]. The experiment will continue past this planned for an extended time period of up to 25 years of total operation. It will operate within a much harsher radiation environment, at higher instantaneous luminosity for 10 years. This phase of the experiment will be called HL-LHC, it will result in 200 collisions per bunch crossing and will experience an expected integrated luminosity of 3000 fb^{-1} [59]. For comparison, the current CMS detectors are designed for operation at 25 collisions per bunch crossing and integrated luminosity up to 500 fb^{-1} [59]. The instantaneous luminosity is expected

to be 5×10^{34} cm^{-2} s^{-1} with 250 fb^{-1} integrated per year and 3000 fb^{-1} in total [29]. The charged hadron fluence within ECAL at $|\eta|=2.6$ is predicted to be $2x10^{14}$ particle/cm^2, with an absorbed dose of 300 kGy and an expected dose rate of 30 Gy/h [60]. For this next phase which will begin in 2026, the calorimeter must be upgraded to meet the needs of the harsh environment. This higher luminosity provides up to six times more data, which allows in-depth analysis and to give a view beyond the standard model analysis [29]. However, at these increased rates there would also be six times more radiation damage and five times more pile-up than the current rate [29]. At these increased radiation rates, there would be a substantial loss of light transmission within the crystals in the endcap, resulting in unacceptable performance degradation, therefore multiple CMS subdetectors must be upgraded including the ECAL to ensure these effects are mitigated and operate as the same performance as phase 1 [21] [45]. One the most important and restricting factors of upgrading the detector is ensuring the upgraded detector occupies the same amount of physical space, as only certain aspects of the detector will be upgraded due to degradation of components from the radiation damage. It is also essential that any upgraded components function harmoniously with the existing detector.

The bunch crossing is expected to reach 140 – 200 bunches per second, which is a huge increase from the current running of the LHC of approximately 20. The increase in a pileup is likely to cause confusion in the reconstruction of particles from the hard scatter interaction with those produced in different pileup interactions. The ability to differentiate between jets (especially of vector boson fusion processes) that are produced in events of interest and jets produced by pileup interactions will degrade [61].

It is necessary that the performance of the detector in terms of electron and photon reconstruction efficiency, energy resolution, identification of jets and missing transverse energy for the hadronic part, are all important features for the detector and must be must perform at high efficiencies. To tackle damage that has already occurred, certain aspects of the CMS detector will have to be upgraded in order to prevent rapid deterioration at HL-LHC. One of the most difficult regions to plan and design for is the ECAL endcaps. The radiation levels here can vary strongly with η – for example, it can differ by a factor of 100 between $|\eta| = 1.48$ and $|\eta|=3.00$. It is also predicted the radiation dose will be 100 times higher in the ECAL endcaps versus the ECAL barrel [46].

Defects in the semiconductor lattice can be created as highly energetic particles hit the sensors and have the ability to trapping of charge carriers, an increase of leakage current, change of the

effective doping concentration and of the electric field in silicon sensors. Especially running at HL-LHC and experiencing the increased fluences, the sensors that will be used must be able to withstand these defects which would cause a significant deterioration of the detector performance. The RD50 collaboration is using the latest techniques to fully understand the materials that will be used in the upgrade. These include thermally stimulated current and deep level transient spectroscopy, to identify the defects induced by radiation and measure their electrical properties [62].

5.2 ECAL Barrel Upgrade

Compared to the challenges of the endcap region the radiation damage in the ECAL barrel is easier to deal with. However, this region will still need some upgrading to meet the needs of the higher pile-up and the increased APD noise consequential of the anticipated instantaneous luminosity of 5×10^{34} $cm^{-2}s^{-1}$. The APD is operated at a gain of 50 and at a temperature of 18˚C. Due to their silicon construction, they are sensitive to gamma and hadron damage. Gamma radiation causes a decrease in the quantum efficiency and increases the surface leakage current. For operation at HL-LHC where neutrons dominate the hadron spectrum behind the ECAL crystals, the damage caused by these are of more concern. Defects in the silicon bulk are caused by the hadrons, which increase the dark current within the detector and ultimately the electronic noise. These effects can be seen in Figure 5-1, during the technical stops and winter shutdown the APDs defects anneal slightly and as a result, the current is reduced. According to FLUKA simulations presented in [25] the dark current for a pair of APDs at gain 50 at η=1.45 is expected to between 200-250 μA, if you only consider the permanent bulk damage. The dark current increases linearly with the neutron fluence and is expected to increase by a factor of 10 - ~400 MeV/channel [46]. Another possible damage due to neutron damage at a high fluence is the reduction of quantum efficiency and the shift of the bias voltage which would be required to obtain a gain of 50. The noise of the preamplifier is expected to increase 9-10 ADC counts for a dark current of 200-250 μA, with one ADC count equalling to ~ 40 MeV. The APD dark current is highly correlated to the operating temperature. It is planned during the upgrade the ECAL operating temperature will be reduced from 18˚C to 8˚C, this reduction in temperature will result in a 35% decrease in noise and a 2.5-factor reduction in dark current.

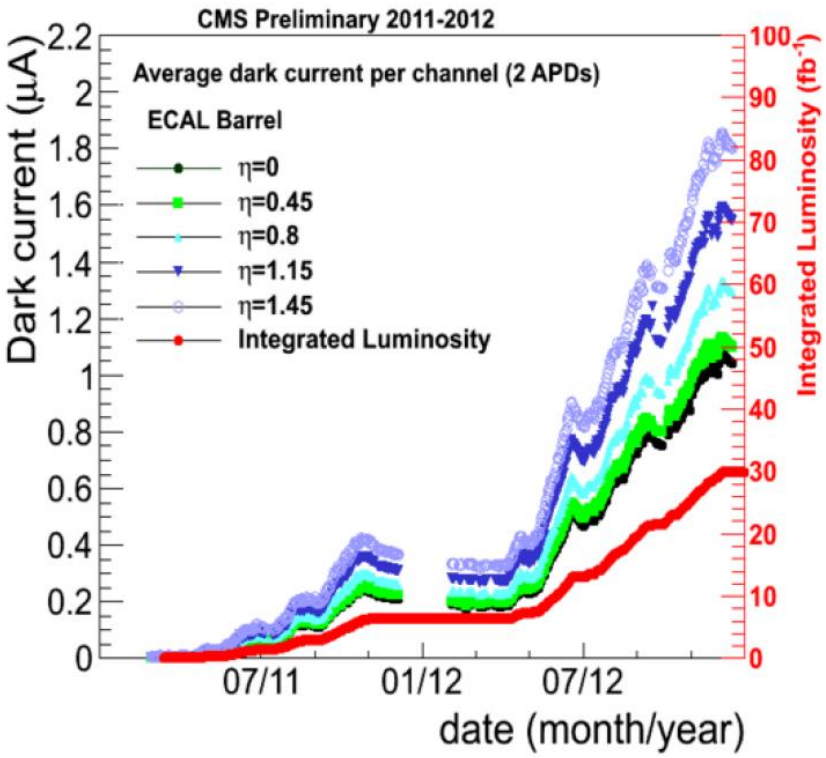

Figure 5-1 – Dark current is shown in the ECALs APDs. The different coloured key represents the pseudorapidity during the LHC Run1. The red y-axis and line represent the delivered LHC luminosity as a function of time. A partial reduction is current if observed after the winter shutdown and technical stops [60].

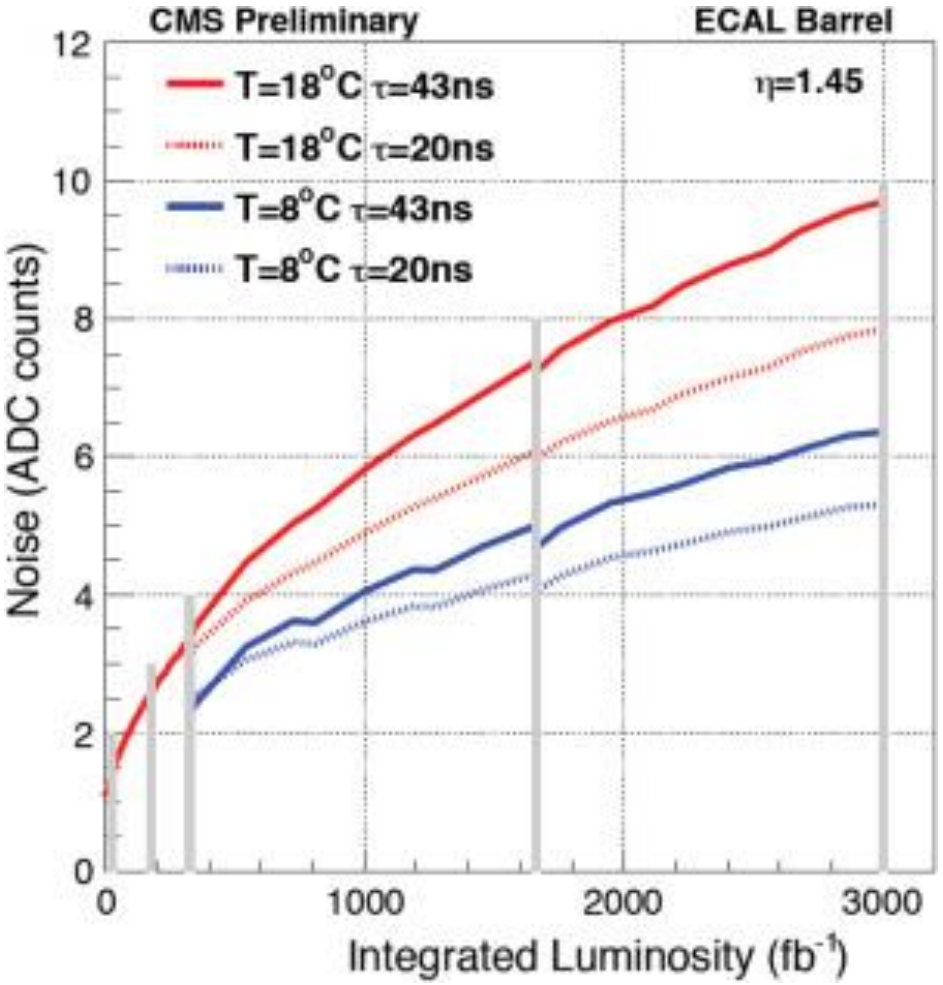

Figure 5-2 – The expected noise is shown for the centre of the barrel η=0 and the edge of the barrel η=1.45, as a function of the LHC integrated luminosity. Two cases are presented for the temperature of the detector: one at the current which is 18˚ and the new proposed ECAL operating temperature of 8˚. With τ presenting the signal shaping time [46].

The layout of the current barrel electronics connects the APDs to a passive motherboard (MB) – this distributes the high and low voltage and connects the APDs to the very-front-end (VFE) cards, which has five readout channels with a multi-gain-pre-amplifier (MGPA). The MGPA has a shaping time of 43 ns and a 12-bit analogue-to-digital converter (ADC), these digitised signals are fed to the Front-End (FE) card. The FE card has a 5×5 crystal array which has a digital latency buffer and primary event buffer [60]. The barrel electronics for the upgrade will need to be upgraded to meet the new trigger requirements, which would have an increase in latency up to 20 μs and increase in bandwidth to 1 MHz. To be able to meet these requirements and ensure operation at HL-LHC is possible the VFE and FE cards will be replaced. Additionally, the low voltage distribution and optical links will also need to be changed. However, neither the APDs and not the crystals need to be changed [60].

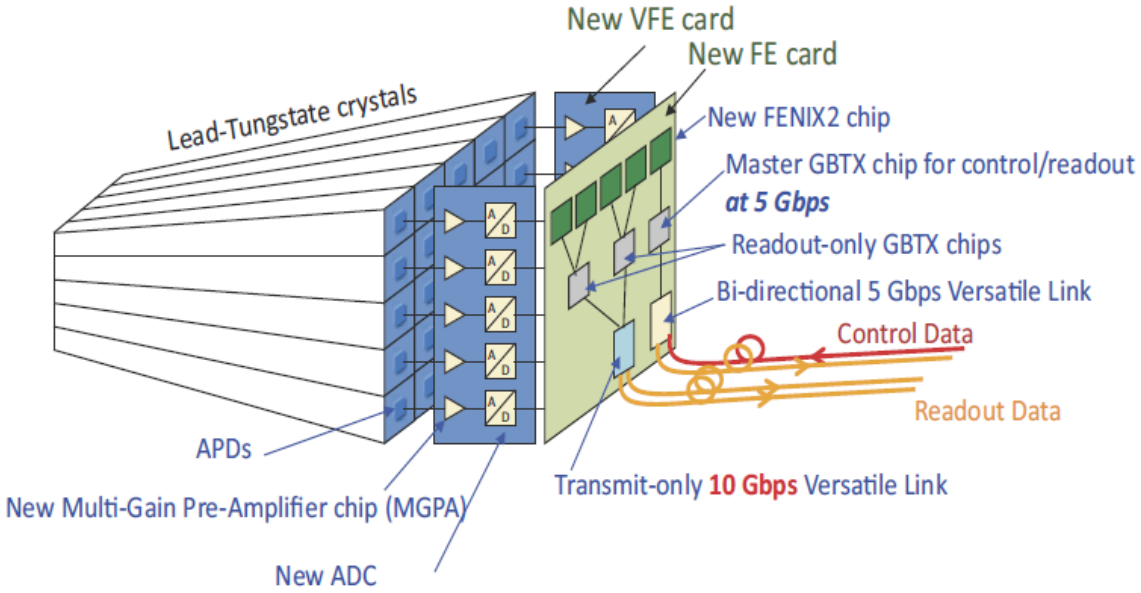

Figure 5-3 – The upgraded readout architecture for the ECAL barrel [60].

5.3 ECAL Endcap Upgrade Options

Due to the high level of radiation experienced during the lifetime of the experiment, mainly to the forward region of the CMS, the ECAL endcaps will need to be upgraded before the start of HL-LHC operation. The endcaps regions will endure very high integrated fluences of up to 1 MGy and 10^{16} neutron/cm^2, this is shown in Figure 5-4. You can see the endcaps (EE) consisting of 28 layers will suffer the most, followed by the forward-hadronic (FH) consisting of 12 layers and the backing hadron calorimeter (BH) consisting of 12 layers [63].

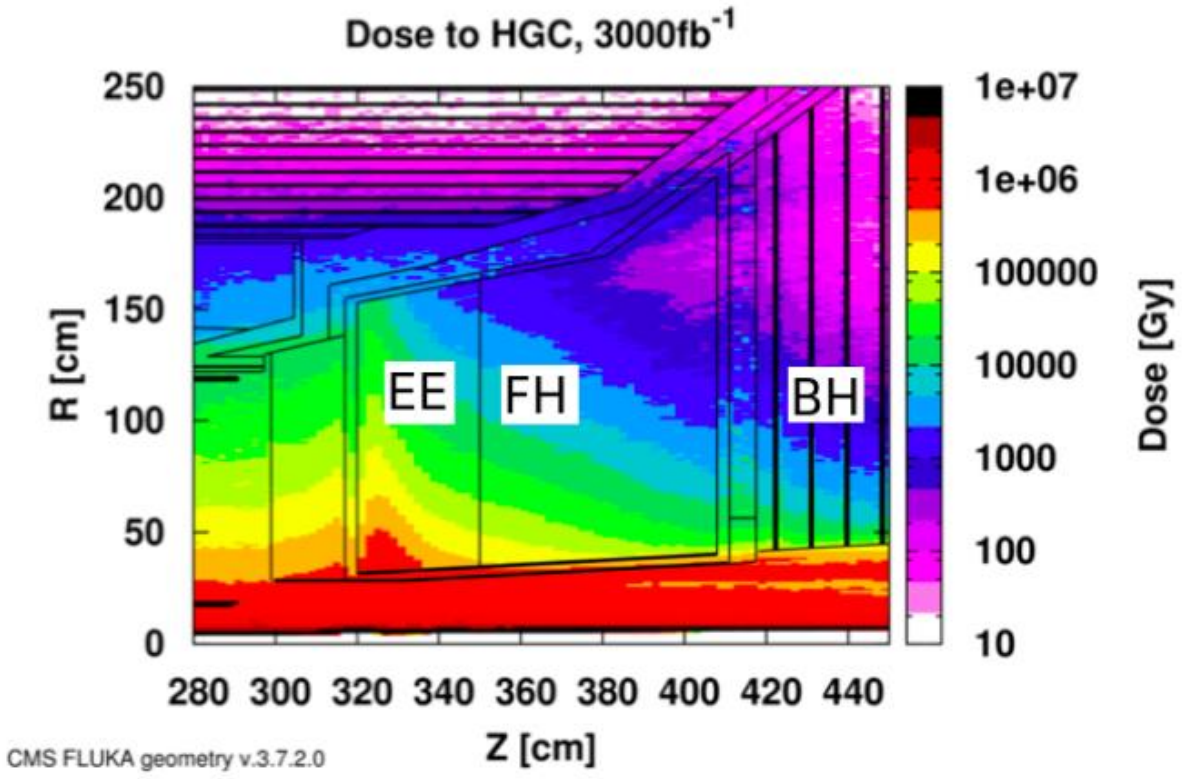

Figure 5-4 – Integrated doses expected as a function of the distance to the collision point along the beam axis z, by the end of the high-luminosity LHC program (3000 fb^{-1} of integrated luminosity) [63]. A quarter slice of the inner region of the CMS detector is shown.

5.3.1 ECAL endcap Shashlik configuration

For the ECAL calorimeter endcaps, there were two possible upgrades under discussion. The first design proposed is shown in Figure 5-5, this was a new sampling ECAL endcaps with tungsten/LYSO: Ce^{3+} which would provide the best energy resolution, dimensional compactness and highest light yield for ECAL in the endcaps and forward region according to simulations [60]. This would provide an energy resolution of approximately 10%/ √E and with would be optimised for small Moliere radius (about 14 mm for the W/LYSO combination versus 21 mm of lead tungstate) to prevent the effects of a pile-up and have a high radiation tolerance. This new combination would provide a comparable emission wavelength and decay to lead tungstate. The structure design is very dense, with a radiation length of 5.1 mm versus the current 8.9 mm for lead tungstate (it would make it more compact compared to the current ECAL endcap) with alternating layers of the dense absorber and scintillating crystal tiles.

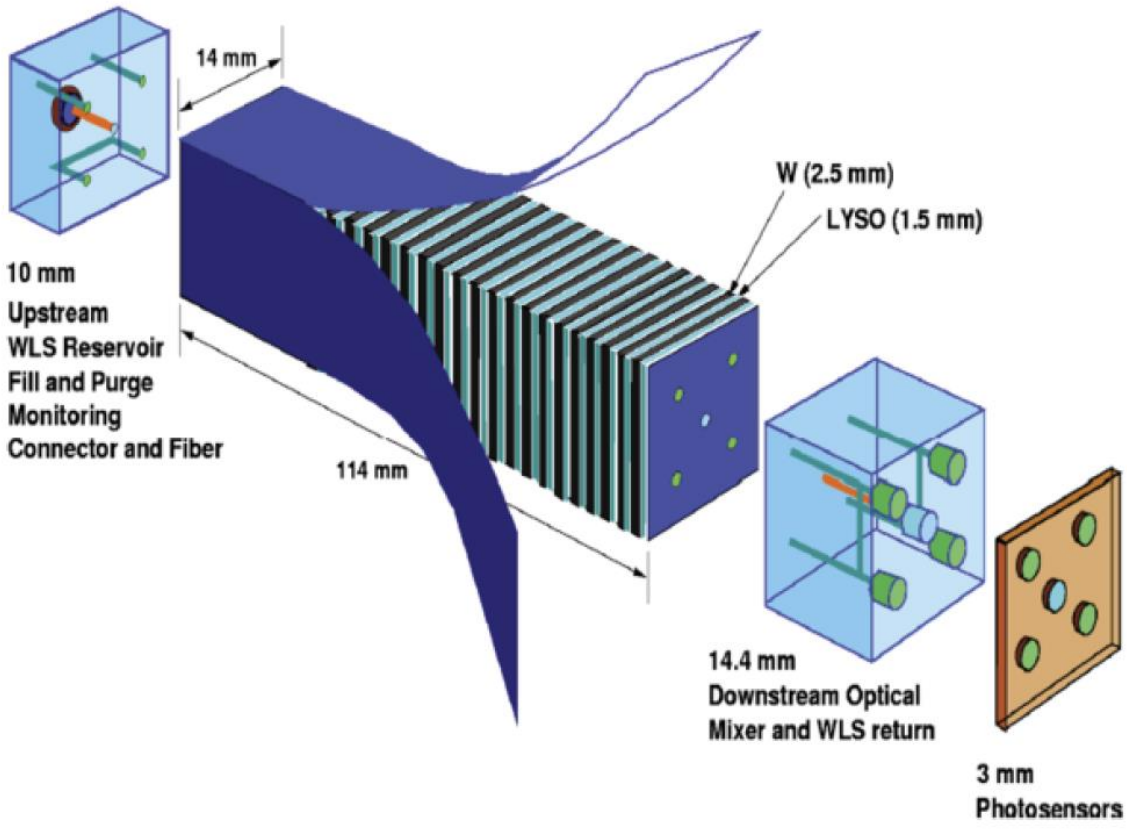

Figure 5-5 – Proposed design showing the ECAL endcap Shashlik configuration. The module consists of twenty-nine LYSO crystals of thickness 1.5 mm which are interwoven between twenty-eight W plates of thickness 2.5 mm. The module has four wavelength shifting quartz capillaries which lead out the scintillation light leading to a photosensor. Running through the centre of the module is also a calibration fibre which is used for monitoring proposes, this is the same sampling structure and thickness but is replaced with CeF_3 instead of LYSO [60].

5.3.2 High Granularity Calorimeter

The second design for the ECAL upgrade is a dense High Granularity Calorimeter (HG-CAL). This design like the first would perform well in a high pile-up environment if the forward endcap regions, with high precision detection of single particles and jets. The dense structure means there is only a small gap between the electromagnetic and hadron calorimeters which improves the jet measurements [59]. Which when used alongside the particle flow technique it would future improve the resolution. The design would consist of an electromagnetic part and two hadronic parts: Front Hadronic calorimeter (FH) and Back Hadronic calorimeter (BH) [59], the expected layout is shown in Figure 5-6.

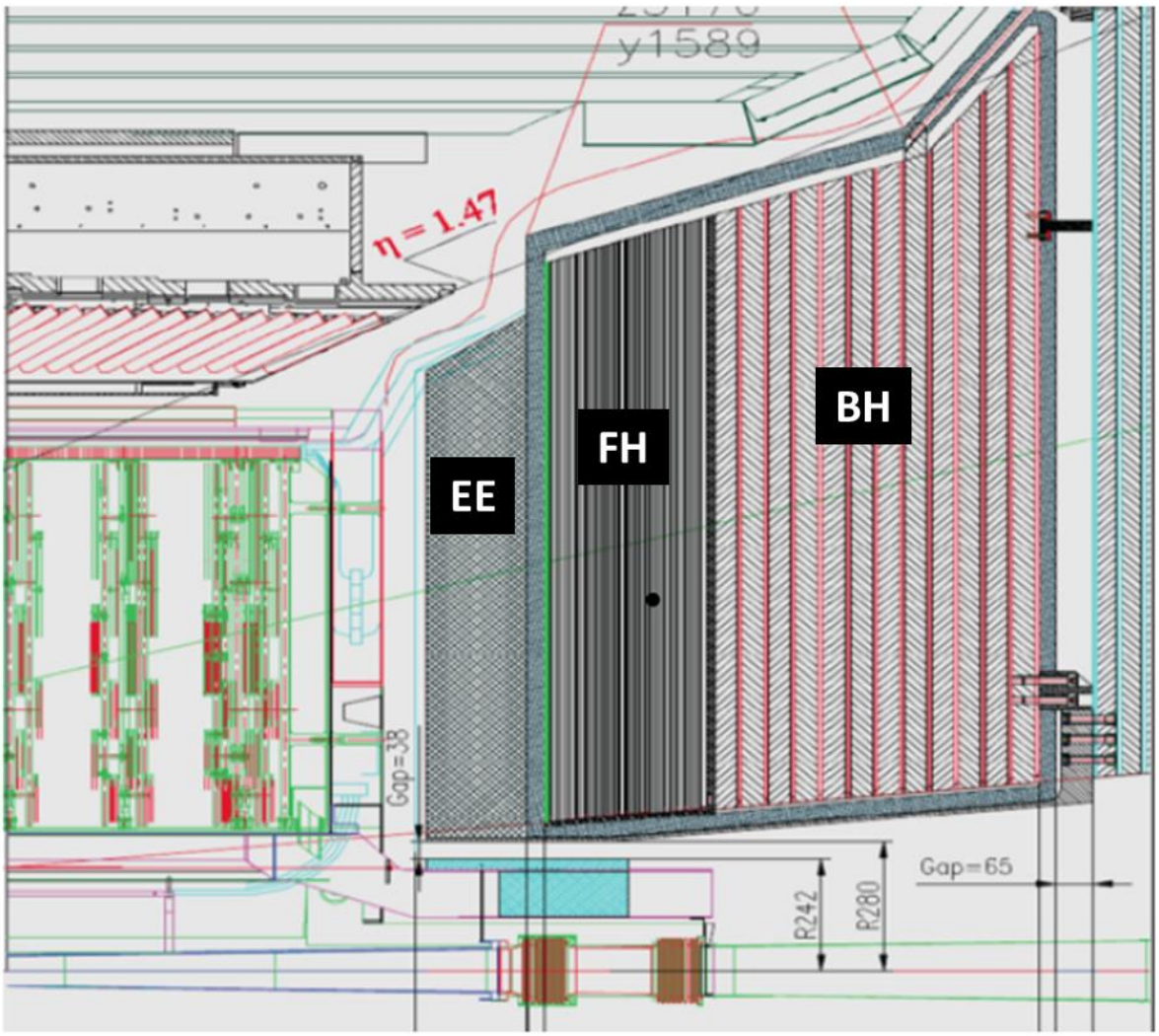

Figure 5-6 – The diagram shows the possible structure of the HG-CAL. This would be located in the space contained by the current EE. The HL-LHC electromagnetic calorimeter would be located behind the brass-silicon hadron calorimeter which has a wavelength of 3.6. Directly behind the brass-silicon hadron calorimeter is a brass-scintillator sampling backing calorimeter of wavelength 5.5 [60].

The innermost region around the interaction region starts with tungstate/lead-silicon sampling electromagnetic [34] calorimeter, would have a depth of 25 X_0 and ~1 wavelength, consisting of 28 layers of silicon pad sensors as the active material and lead in a stainless steel envelope as the absorber [59].

Surrounding the electromagnetic calorimeter would be a brass-silicon FH, of 3.5 wavelengths deep, which is followed by a 5.5 wavelength brass-scintillator sampling BH. This brings the total calorimeter depth to 8.5 wavelengths with 24 layers and steel absorbers [59]. In the regions of higher radiation of electromagnetic calorimeter and FH, planes of silicon would be used as the active medium. For regions with lower radiation levels of the BH, several options could be used: plastic scintillator, GEM or Micromegas gas chambers. [60] states testing the system with

525 micron-thick silicon sensor gives an energy resolution of approximately 16%/ $\sqrt{E}$ with a linear energy response [64].

The active elements of the system have been chosen to ensure the detector performance can be its best. For the silicon active elements, it is been shown that thinner sensors whilst operating at an increases bias voltage experience less signal loss due to irritation [45] [65] [66]. To mitigate the increased leakage current from the increased bias voltage, the EE and both hadronic calorimeter will be kept at -30°C, using CO_2 cooling. This will limit the leakage current for the silicon sensors, which will improve the efficiency and accuracy of the system [59].

The sensors within the HG-CAL will be exposed to hadron fluences up to $2\times10^{14} – 10^{16}$ 1 MeV neutron equivalent per cm^3 (neq/cm^2). These fluences are similar to the tracker for the HL-LHC, with fluence dominated from charged hadrons. Experimentation is underway to test the performance of the sensors within the HG-CAL is affected differently due to neutrons [65].

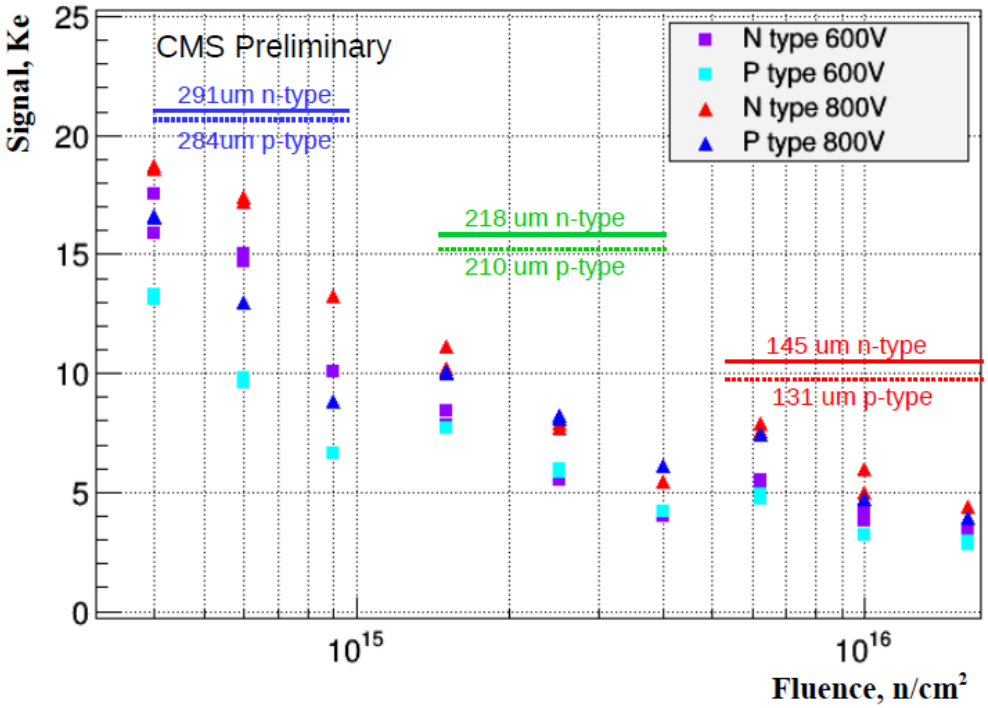

(a)

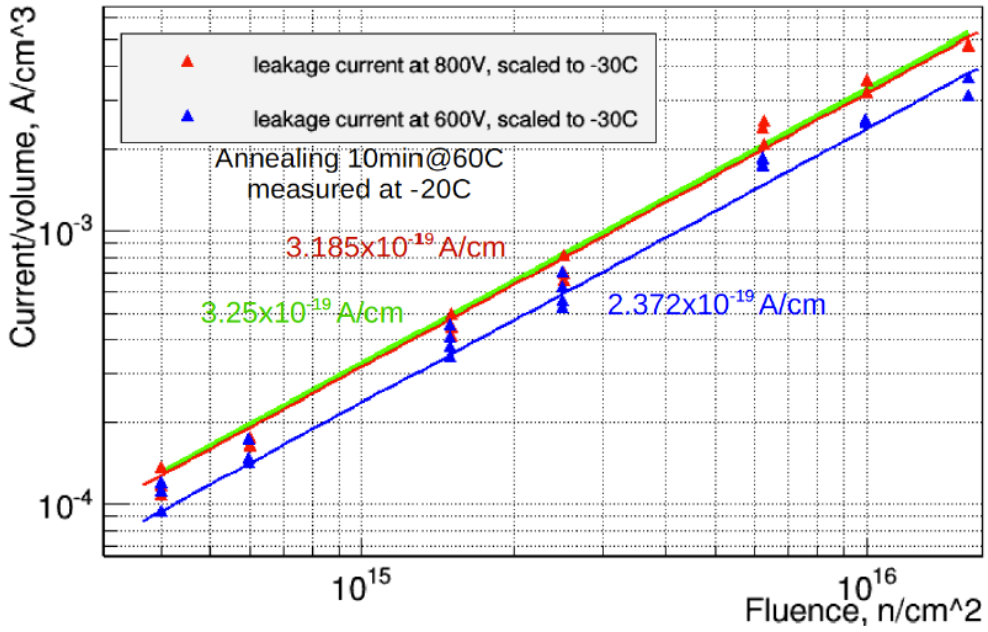

(b)

Figure 5-7 – Three different depths of the active material, with the mean signal in the silicon diodes versus the neutron fluences shown in (a). To mitigate the signal loss, thinner sensors are shown and operated at a higher voltage. In (b) the scaled leakage current versus the active detector volume and neutron fluence up to 1.6 $\times 10^{16}$ neq/cm^2 is shown. This shows the noise contribution scales with the square root of the leakage current [59].

5.3.3 Summary

For the planned operation at HL-LHC starting in 2026, the instantaneous luminosity will be 10 times higher compared to the LHC [65]. To mitigate the effects of this increased radiation dose that will affect the subdetector hardware two upgrade options had been presented for the CMS ECAL, the HG-CAL and a Shashlik configuration.

During the initial stages of this research, it was understood that the decision for the upgrade of CMs was undecided. One of the options discussed in 5.3 is the proposed Shashlik configuration which contains four wavelength shifting fibres that carry the light from the module to a photosensor. Keeping this in mind, a prototype VPT had been created with a 4-fold segmented anode with independent readout functionality. Each segment anode would match the four wavelength shifting fibres. The VPT has been created to put the current dimensions of the CMS and existing hardware within CMS. Out of the two options presented in 5.3, the HG-LHC was chosen in mid-2017.

The selected option for the CMS upgrade is the high-granularity sampling calorimeter design, which features hexagonal silicon sensors of cell size 0.5 – 1 cm^2 for the ECAL and majority of HCAL and the remainder of the HCAL with highly segmented scintillators with SiPM readout. The endcap calorimeters will be exposed to the highest radiation levels with the inner regions expected to withstand 150 MRad [59]. With these conditions the current EE would degrade quickly and for this reason as of mid-2017 it has been decided that CMS will go ahead with HG-CAL for the replacement of the current ECAL. The design of the detector has been chosen to help mitigate the high radiation doses, through choosing silicon in the high η regions as the active material and for the lower η regions, scintillating tiles with SiPMs have been chosen [59]. The detector will allow high granularity in transverse and longitudinal direction for particle flow analysis.

5.4 Double-Side Readout Concept

The ECAL Endcap crystals are ageing due to the extremely high radiation environment they are based in. This is leading to a spatial non-uniformity of the light collection efficiency from the lead tungstate crystals, leading to an increase in the constant term of energy resolution. The performance of majority of calorimeters is based on the scintillators active material non-uniformity of light collection efficiency [5]. Ideally, the collection efficiency of the scintillation light should be the same across different points of the calorimetric cell. However, after damage this is no longer the case and the energy resolution of the electromagnetic showers is degraded

from the non-uniform light collection [5]. For the particular case of CMS ECAL this has been studied in detail and the high fluences of hadrons create stable defects inside the volume of the $PbWO_4$ [67] [68]. This ultimately leads to the degradation of its energy resolution for the electromagnetic showers due to the change in light collection efficiency [5]. This leads to an increased stochastic term and equivalent noise. For this reason, the crystals need to be replaced to mitigate the degradation of the constant term and the loss of light observed by the crystals [29].

For the upgrade of the CMS detector, a potential concept was tested which could use a lot of the existing infrastructure and components of the ECAL. To deal with the damage from the large hadron fluences to the lead tungstate crystals, a technique which would keep the current set-up in the ECAL but add an additional photodetector to the front of the crystal whilst retaining the existing photodetector at the back [5], is called the DRO technique. In the original format which is based on the CMS detector, there is a photodetector based at the end of the crystals; APDS are used in the ECAL barrel and VPTs in the endcaps. Adding an additional photodetector as shown in Figure 5-8, allows for simultaneous detection of the scintillation light at both ends of the crystal [5].

5.4.1 Double-Side Readout Technique

The DRO technique allows for additional information to be collected from an additional photodetector which is attached to the front face of the crystal, as shown in Figure 5-8. As each electron hits the crystal, a shower of lower energy electrons and photons are produced within the volume of the crystal. The shower's average maximum production of scintillation photons (t_{max}) is directly linked to the energy of the incoming particle, $t_{max} \propto \ln(E)$, which for electrons of 50 GeV is 6.5 cm and for 200 GeV is 7.5 cm from the front face of the $PbWO_4$ crystal [5]. However, due to the stochastic nature of the shower development t_{max} can vary for each event, this directly changes the average light path of the scintillation photons that travels through the crystal to the photodetector. This leads to the light being attenuated depending on where t_{max} is within the crystal, which for the original configuration of a single photodetector can cause signal degradation of the energy resolution within damaged crystals caused by the non-uniform light collection efficiency [4]. This is where the DRO concept can help mitigate these fluctuations caused by hadron damage, the simultaneous readout of the front and rear face signals allow for the position of t_{max} to be calculated and corrected for each event.

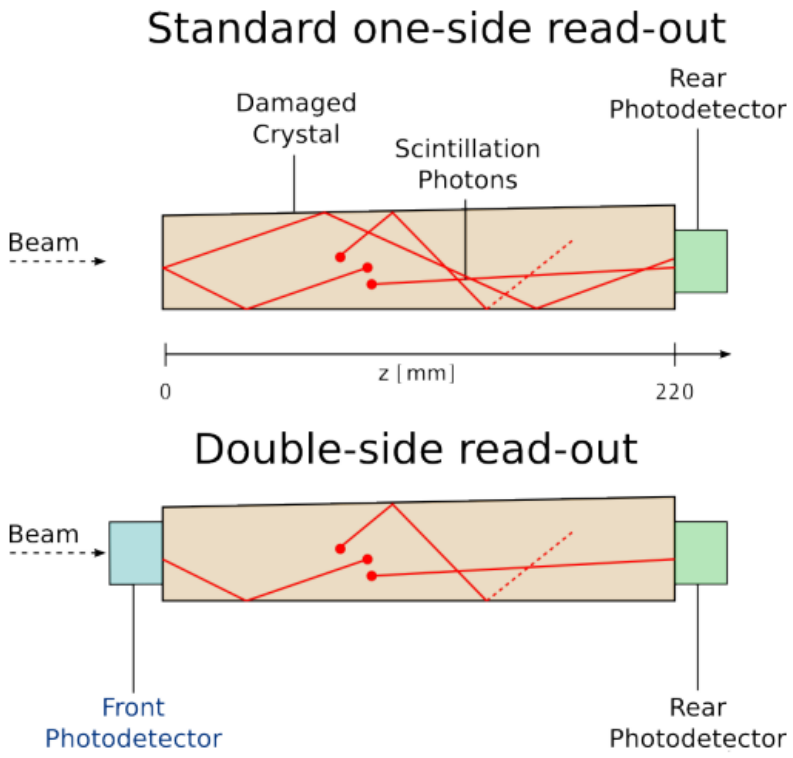

Figure 5-8 – The current standard one-side read-out that is used within CMS currently is displayed (top image) top. This has a single photodetector attached to the rear of the crystal. Double-side readout concept is shown (bottom image). This concept adds an additional photodetector at the front of the crystal as well as the current one present at the rear of the crystal [5]. The beam hits the crystals at the front end (in this configuration, the left narrow end of the crystal).

A simulation had been created as explained in *GEANT4 collaboration* by *S. Agostinelli* [69] to simulate the effects of shower fluctuations. The GEANT4 is a toolkit which was created for simulating the passage of particles through matter. It is a reliable tool with many physics processes which can be used to the user's needs, including electromagnetic, hadronic and optical processes with a whole variety of particles, material and element over energy ranges from 250 eV to TeV range [69]. The toolkit was used to investigate how the shower maximum fluctuations affect the light detected on the two ends of the crystals, that have undergone radiation damage. To ensure the simulation is accurate, the tapered geometry and the scintillation properties have been taken into account [21]. A range of levels of light absorption ranging from $\mu_{ind} = 0$ to $\mu_{ind} = 20$ m^{-1} have been simulated. Figure 5-9 shows an example of the light collection efficiency curves ε_{LC}, with the probability for the scintillation light produced at a given position in the crystal is to be collected at the photodetector with $\mu_{ind} = 10$ m^{-1} [5]. The example shows a maximum shower is closer to the front photodetector when the showers are from 50-200 GeV electrons. As the light reaches the rear crystal the light is more attenuated with respect to the light detected at the front face. Therefore, the front photodetector results in

a worse energy resolution than the rear, as t_{max} fluctuates in a region where ε_f is steeper than ε_r which causes a larger variation of the response [5].

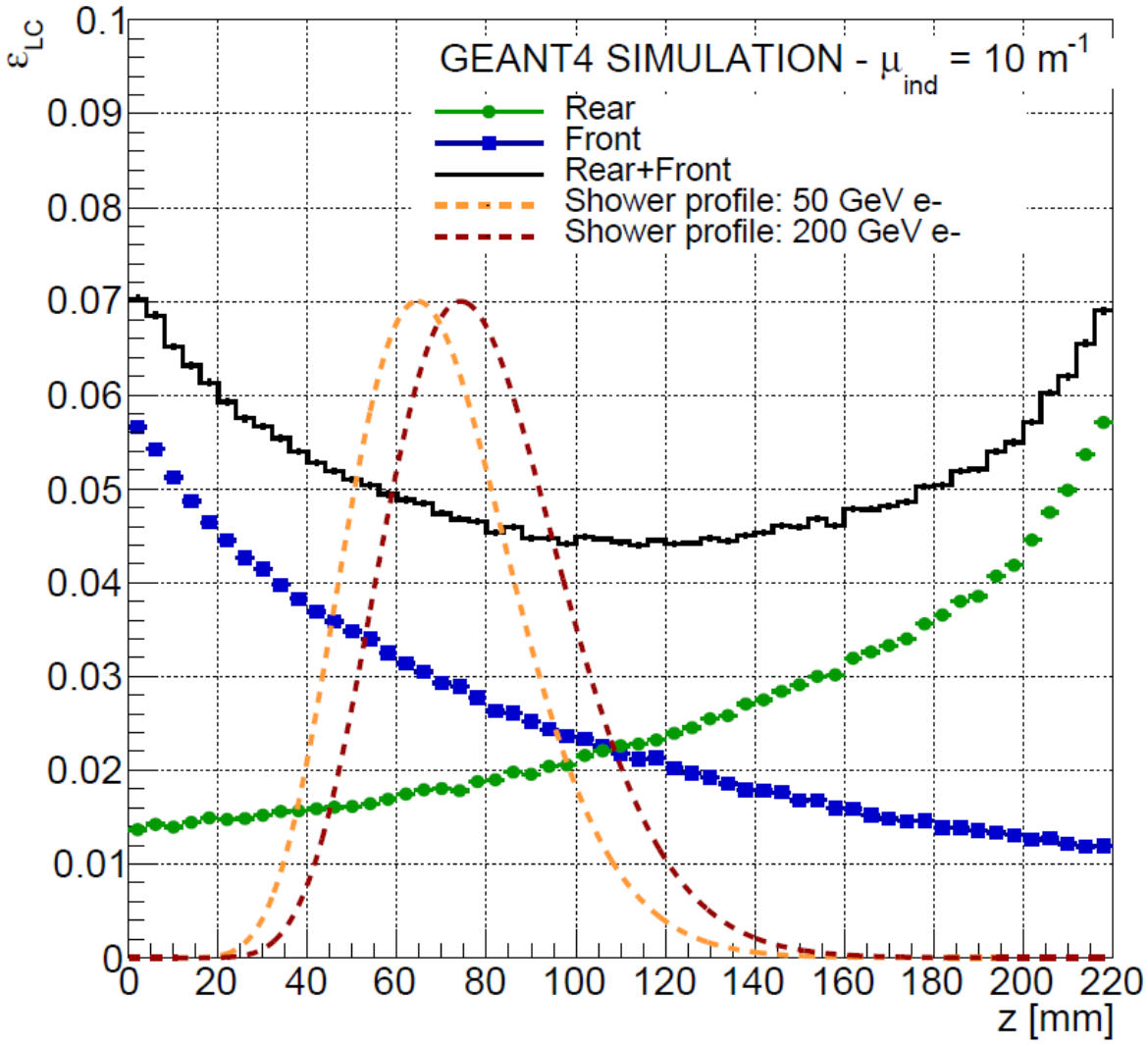

Figure 5-9 - Geant4 simulation curves of light collection efficiency for the front, rear and double read-out, for a crystal with μ_{ind} = 10 m^{-1}. Average shower profile of electrons with an energy of 50–200 GeV is also shown. [5]

Signals detected at the front (F_{sh}) photodetector and rear (R_{sh}) photodetector, which are of electron of energy E developing a shower in a crystal with absorption coefficient μ can be written as:

$$F_{sh} = K_f \int E_{dep}(E,z)\varepsilon_f(\mu,z)dz \tag{5-1}$$

$$R_{sh} = K_r \int E_{dep}(E,z)\varepsilon_r(\mu,z)dz \tag{5-2}$$

where ε_f light efficiency curves for the front photodetector and ε_r for the rear photodetectors, and K_f, K_r are calibration coefficients which take into account the photodetectors quantum efficiency and gain [5].

Using intercalibration the front and rear detector signals can be combined using:

$$S_{\text{sum}} = \frac{K_r \cdot F_{sh} + K_f \cdot R_{sh}}{K_f K_r} = \int E_{dep}(E, z)\, \varepsilon_{\text{dro}}(\mu, z) dz \tag{5-3}$$

In this case, the slope of the resulting light collection efficiency curve $\varepsilon_{dro} = \varepsilon_f + \varepsilon_r$ results in a less steep curve versus the individual curves $\varepsilon_f, \varepsilon_r$. As a result of the DRO configuration, the overall response of electrons is less affected by the light collection degradation, leading to a reduced energy degradation when compared to a single readout configuration [5].

When using equation (5-3) the reconstructed signal improves the energy resolution due to the more uniform slope of ε_{dro}. However, it is still affected by longitudinal shower fluctuations. To ensure the DRO technique is used to its maximum capability, the ratio of front and rear photodetector signals should be used to estimate the average position of the shower on the z-axis and correction can be applied on an event by event basis [5].

$$S_{\text{dro}} = F \cdot e^{\mu z} + R \cdot e^{-\mu(z - \frac{L}{2})} \tag{5-4}$$

Since both μ and z are unknown variables, the following relation can be used:

$$\sqrt{\frac{R}{F}} = e^{\mu(z - \frac{L}{2})} \tag{5-5}$$

in (5-4) to obtain:

$$S_{\text{dro}} = k_\mu \left[\sqrt{\frac{R}{F}} + R \cdot \sqrt{\frac{F}{R}} \right] = 2k_\mu \sqrt{FR} \tag{5-6}$$

where $k_\mu = e^{\mu L/2}$ is a constant for the overall calibration and the ratio of the front and rear signals providing the event-by-event correction. The fluctuations that are caused by the longitudinal shower development, with respect to equation (5-3), are reduced by the reconstructed signal using equation (5-6). The beam test provides the experimental light collection efficiency for the front and rear photodetectors ($\varepsilon_f, \varepsilon_r$) and provides proof of concept for the DRO concept.

5.5 Experimental setup

To test this concept a test beam was carried out at CERN, SPS North Area. The results of this experiment were able to provide an improved understanding of the effects of radiation damage in the $PbWO_4$ crystals. The facility was provided with a stable beam using electrons in the energy range of 50-200GeV. The calorimetric module used for the experiment consisted of a range of different crystals which had incurred a range of hadron damage, these lead to differently induced light absorption coefficients μ_{ind} between 0 to 20 m^{-1} [5].

5.5.1 Calorimetric Module

For the test beam, a calorimetric module was created to mimic the CMS ECAL endcaps. The module consisted of a 3×3 array with $PbWO_4$ tapered crystals that are 3×3×22 cm^3 [21]. A range of damaged crystals were used, 2 out of the 9 crystals were irradiated by placing them in the forward region of the CMS detector for a few months [5]. 6 crystals were irradiated with 24 GeV protons at the CERN PS facility [5], with last crystal having no irradiation being used as a reference. To mimic the levels of the influence the CMS endcaps would experience by the of High Luminosity LHC operations, a range of fluences were used between 2.1×10^{13} and 1.3×10^{14} cm^{-2} [5].

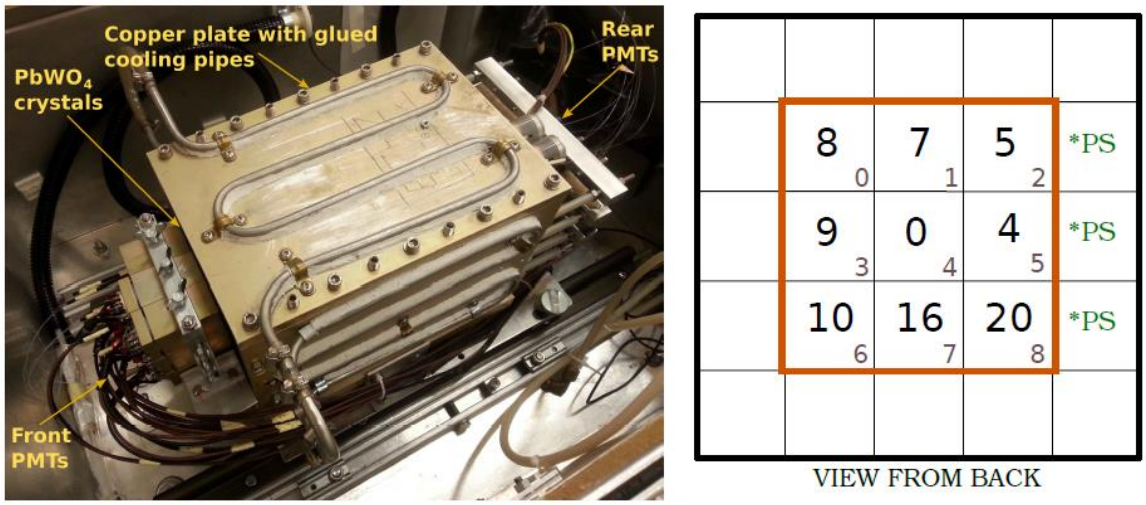

Figure 5-10 - Left - picture of the experiment box, containing 9 crystals. Right - Arrangement of irradiated crystals inside the alveolar structure of the calorimetric module. The bold numbers show the corresponding μ_{ind} for the crystal in that position, the grey numbers in the bottom right corners show the position channel number [5].

The grid casing in which the $PbWO_4$ crystals were held in, had to be thermally stable for the running of the experiment. The casing was surrounded by 1 cm thick copper plates with pipes for water circulation to allow for thermal stabilisation within 0.2 ˚C [5]. To optimise the light

extraction from the crystal, an optical coolant with a refractive index of 1.45 had been used between the PMT and the crystal.

Hamamatsu Photonics R5380 PMTs with bialkali photocathodes and borosilicate glass windows of 20 mm diameter were used to read out the light from both sides of each crystal [70].

The whole experimental setup, including the cooling and light monitoring system, was mounted inside a light-tight aluminium box providing thermal isolation. The box was installed on a remotely controlled $x - y$ table with a positioning precision of ~1 mm and displacement range of ±30 cm [6].

5.5.2 The Beam Line

The location for this experiment was at the CERN SPS North Area H4. This location was chosen as it can provide an adequate quality of the electron beam in the 50 GeV – 200 GeV range with hadron and muon contamination below 0.2%. Four scintillator counters were used to trigger the data acquisition from the incoming beam particles [5]. To detect the impact of the beam particles on the crystal matrix two sets of beam hodoscopes were used (for x and y directions), with a nominal resolution better than 200 μm [5]. Both of these contained two planes of 64 scintillating fibres of square cross-section 0.5×0.5 mm^2 and were read out by a multi-anode PMT [5]. A 12-bit ADC was used to digitise the signals from the PMTs, beam counters and the hodoscopes, with an integration time of 300 ns. This ensured there was enough time to accommodate the PMT pulse length and channel to channel transition time variation in a long coaxial cable connecting the PMT output and ADC input [5].

5.5.3 Experimental procedure

The experimental procedure was set up in the following steps:

- The initial point for the beam incidence was set to the central crystal, using 100 GeV electrons.
- Determine the position of each crystal by its response from the shower transverse leakage captured as a function of impact point that is measured by the rear PMTs.
- Adjust the voltage of the PMT so that the peak from a 100 GeV shower produces ~ 1200 ADC counts for each crystal. This allowed having the same PMT gain for the whole energy scan in the 50-200 GeV range.

- Once the PMTs were set, the energy scans were tested with the beam incident central to each crystal using 50, 100, 150 and 200 GeV electrons.
- After the energy scans, the whole calorimetric module was rotated 90 degrees anti-clockwise. This is to have the beam hitting the lateral side of the crystals, to determine their response along the z-axis and as a direct measurement of the light collection efficiency.

5.5.4 Lead Tungstate Crystals

The $PbWO_4$ crystals have a high density of 8.28 g/cm^3, a short radiation length of 0.89 cm and small Molière radius of 2.2 cm [6]. The characteristics of the $PbWO_4$ crystals – optically clear, fast and radiation hard, make it a suitable choice for the CMS detector, which allows for a fine granularity and compact calorimeter.

5.6 DRO Results

5.6.1 Shower fluctuations

Due to the stochastic processes involved in the shower development the shower maximum t_{max} fluctuates in position within the $PbWO_4$ crystal. For non-irradiated crystals, the response of the crystal was uniform along the longitudinal axis, therefore this fluctuation did not move the measured signal by the photodetector. In the cases for highly damaged crystals, which is the case for crystals which have been inside CMS for a number of years, which results in strongly non-uniform the light collection efficiency along the crystal axis. This caused a smearing of the detected signal related to the shower location [5].

The DRO technique is reliant on the basis of an assumption that the light signal shared amongst the front and rear photodetector is correlated to the longitudinal fluctuations of the shower development. In an ideal case where the crystals are non-irradiated, there is almost uniform efficiency of the light collection along the z-axis. The light detected on both the photodetectors would be identical, it does not matter where the shower maximum has occurred [5].

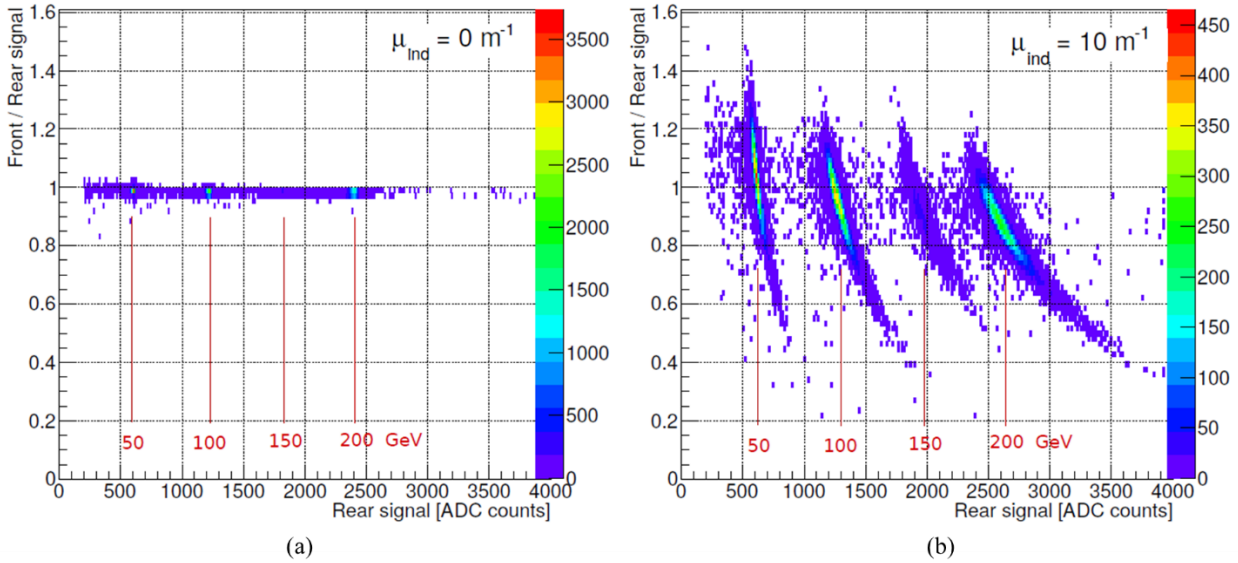

Figure 5-11 – For different energies (50, 100, 150 and 200 GeV) the correlation between the front and rear signal ratio and the signal measured is shown. (a) shows the ratio between the front and rear photodetector signals for non-irradiated crystals. (b) shows the ratio between front and rear photodetectors for damaged crystals with μ_{ind} = 10 m^{-1}. Large variations in the front and rear signal ratio are caused by the event-by-event fluctuations in the shower longitudinal development [5].

Figure 5-11 shows the comparison between non-irradiated and crystals with μ_{ind} = 10 m^{-1} damage and how this affected the ratio of the front and rear signal from the fluctuations caused in the shower maximum position when the crystal is damaged. When the μ_{ind} = 0 m^{-1} the front and rear ratio remains constant over the whole electron range and the event by event fluctuations were minimal. However, for the μ_{ind} = 10 m^{-1} damaged crystal the ratio between the two photodetectors was strongly affected by the event by event fluctuations for a fixed electron energy [5].

5.6.2 Energy reconstruction and linearity

For the following results, a beam spot of 4 × 4 mm^2 was positioned in the centre of each crystal and was used to minimise the effect of transverse shower leakage. Equation (2.6) was used after inter-calibration to show the comparison between the amplitude distributions of the front and rear photodetectors. Figure 5-12 shows the shape of the distribution of non-irradiated crystals and μ_{ind} = 10 m^{-1}. For the non-irradiation, there was no change of the distribution. However, for the damaged crystal, the energy distribution gained from the combined front and rear signal was narrower than the single read out. To ensure a more Gaussian-like distribution the non-gaussian tails have been removed. The distribution for the front photodetector signal was wider than the rear one, due to the slope of ε_f being steeper than ε_r around shower maximum position [5].

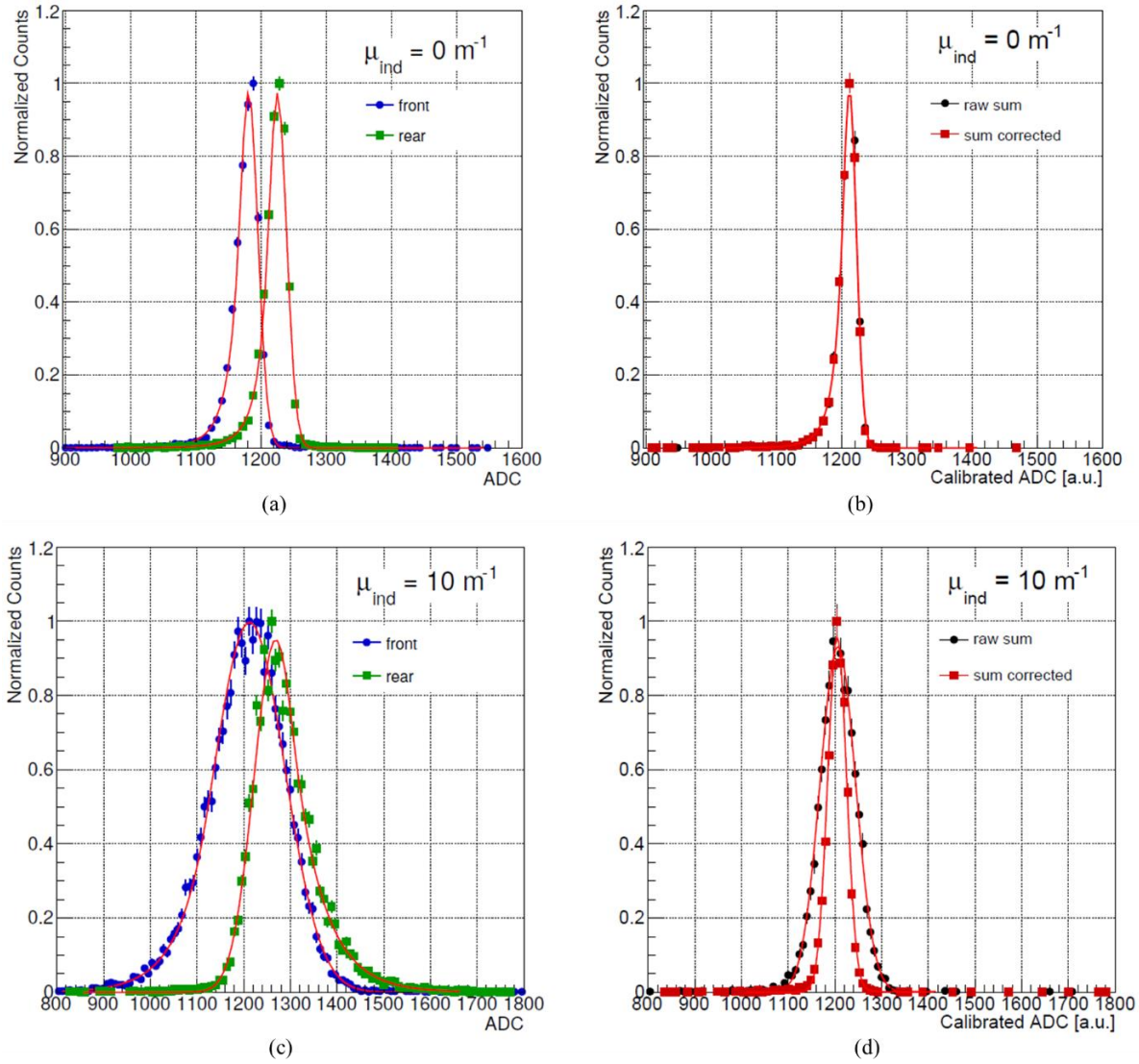

Figure 5-12 – The top two plots show the energy distribution of a non-irradiated crystal using 100 GeV electrons for a single readout configuration (a) and the combined DRO signal (b) using eq (5-3) (raw sum) and eq (5-6) (sum corrected). The bottom two plots show the energy distribution for a damaged crystal of μ_{ind} = 10 m^{-1} with 100 GeV electrons for single readout configuration (c) and the combined DRO (d) using eq (5-3) (raw sum) and eq (5-6) (sum corrected). [5]

To study the linearity of the system, the response from various crystals have been observed for electron energies of 50, 100, 150 and 200 GeV. A Crystal Ball [4] function has been used to fit the amplitude distributions. The Crystal Ball function is a continuously differentiable function, which is typically used to model lossy processes and can hit peaks that continue into the exponential tails [71]. This allows for the asymmetric tails to be taken into account and the most probable value was used as the estimator for the crystal response $S(E_b)$ at a given beam energy E_b. The linearity, $L(E_b)$ of the crystal response is written as:

$$L(E_b) = \frac{S(E_b)}{E_b} \cdot \frac{50}{S(50)} \tag{5-7}$$

Two examples of non-irradiated crystals and crystal with μ_{ind} = 10 m^{-1} are shown in Figure 5-13. Using the linearity curves, it was easy to spot the non-linearities of the response from the increase of μ_{ind} in each crystal with a single configuration (front or rear PMT) and the combined DRO sum. For the case of the μ_{ind} = 0, their linearity of the system is within ~1%. There was a slight decrease in the measure signals above 120 GeV, which is due to longitudinal shower leakage [5]. For the case of the damaged crystal (μ_{ind} = 10 m^{-1}), it was easy to spot the nonlinear behaviour which goes up to ~ 12%. This also confirms behaviour seen from a previous test beam [4].

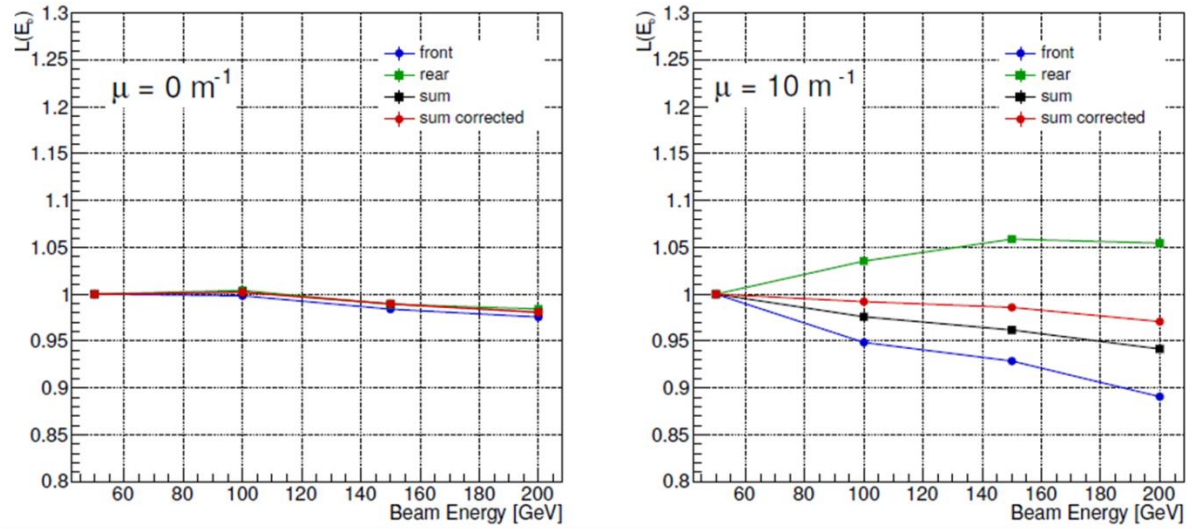

Figure 5-13 - Linearity curves normalized to 50 GeV for the non-irradiated crystal (left) and for a damaged crystal with μ_{ind} = 10 m^{-1}. Different read-out configuration is shown: front photodetector (blue squares), the rear photodetector (green dots), raw sum given by Eq. (5-3) (black) and corrected sum given by Eq. (5-6) (red). [5]

For (b) in Figure 5-13 the DRO response is noticeably more uniform and linear for the energy range 50 -200 GeV, and it is getting close to the non-irradiated crystal response.

5.7 Stored VPT characterisation

The VPTs were tested to determine if their characteristics changed whilst they were stored away for a long period in nitrogen purged refrigerators. 23 of the stored VPTs were sent to the UK from CERN to be re-characterised at a lab in Brunel University London. They were placed inside a 4 T magnetic field to emulate the CMS superconducting magnet, closely matching its magnetic field strength of 3.8 T. The measured gain of the VPTs was compared to the "passport

gain", provided by the manufacturer. These were manufactured between 2000 – 2004. The VPT was operated, under the same operating potentials as in the original "passport gain" classification, with a grounded photocathode, the dynode at 800V and the anode at 1000V.

Once they are characterised, they were sent back to CERN to be used in the DRO experiment. As discussed in 5.4, nine of the VPTs were attached to the 3×3 calorimetric module. The module was attached to a moving $x - y$ table where a beam stepping from 50 to 200 GeV in steps of 50 GeV was applied to each individual crystal that had various μ_{ind}.

5.7.1 VPT Characterisation

Calculating the DC measurements, the illumination source is a set of 4 blue LED plus diffuser illuminating via an aperture the central 10 mm diameter of the VPT. A large area (10×10 mm^2) unbiased pin photodiode picks up light emitted at an angle from the LED group to act as a normalising intensity reference if needed. The VPT is left in the dark environment for 30 minutes before measurements were made. The cathode and anode dark current are measured, with voltages across 1MΩ resistors. To ensure stable measurements the pulses LED was kept on for the duration of the experiment when the readings were taken.

The purpose of this test is to compare the performance of the VPTs after they had been stored away for a long period. The main performance metric is the gain of the VPT, and how it compares to the passport gain. Figure 5-14 shows the results of 23 VPTs tested comparing the original passport Gain vs the measured gain operating at 1000V/800V.

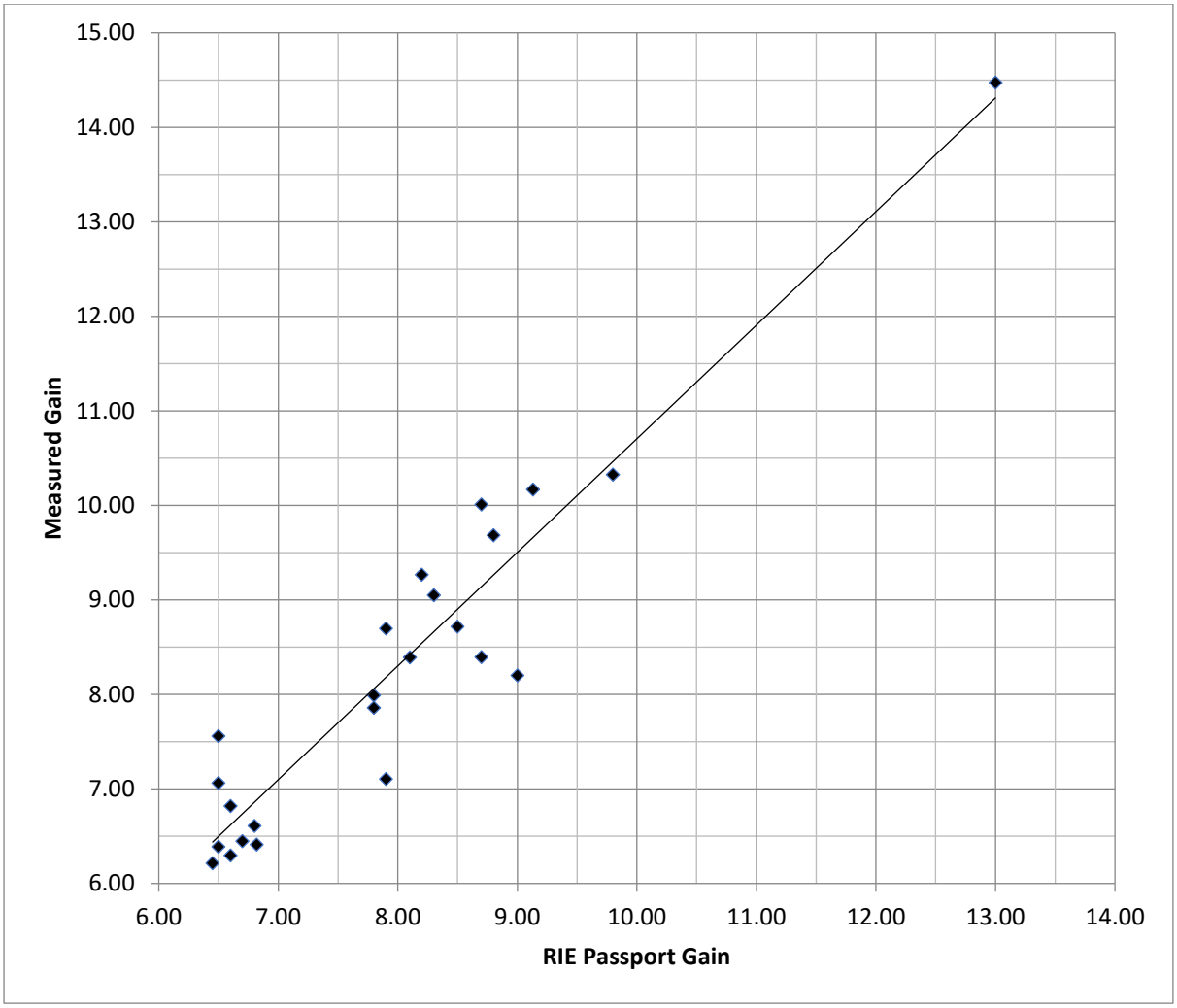

Figure 5-14 - Graph showing the DC gain at 1000V at the dynode and 800 V at the anode. The RIE passport gain vs the measured gain currently.

Visually, the VPTs gain follows a trend line that is close to 1:1 ratio. This demonstrates that there was not much deviation between the measured gain and the passport gain. There are six VPTs with a gain that varies beyond 10% of their respective passport gains. The highest gain change is up to 14.02%, with an average change of 6.62% and $\sigma = 3.83\%$.

5.7.2 Pulsed Measurements

The illumination source was a single blue LED coupled to an optical fibre and then illuminating the faceplate via reflections within a 2″ diameter integrating sphere made by Labsphere with a Spectralon® coating. This provides a Lambertian illumination of the central 20 mm diameter of the VPT photocathode. The LED was driven by a 50 ns wide 5V pulse. The VPT signal was recorded on a peak-voltage sensing ADC (model EG&G MAESTRO Type 916) after a pre-amplifier and an inverting amplifier (ORTEC 474 set to a nominal gain of 20). For the duration of the experiment and measurement taking the pulsed LED was kept on ensuring stability. After

each set of data was taken and the voltage was adjusted, the system was left to stabilise for 15 minutes.

Twenty-three of the VPTs that had been kept in storage were tested to determine their peak signal and their Full-Width Half Maximum (FWHM). The settings for the anode and dynode were 300 V and 100 V respectively, followed by 800 V and 600 V, and by 1000 V and 800 V. A ratio was calculated between the peak/FWHM which was used to determine whether a VPT has a good response relative to the noise level.

Table 6-4 shows the readings of VPT 16465 and VPT 16488 which were taken from the group of 23 VPTs. VPT 16465 shows the response of a good functioning VPT, which has high peak values with a small FWHM. VPT 16488 shows the opposite response where the peak is smaller and the FWHM is larger, which is considered a noisy VPT. The full set of results are shown in Appendix B.

Table 5-1 – An example of a what was classed as a good and as a bad VPT. The peak and FWHM is shown in ADC counts.

VPT 16465				
Va (V)	Vd (V)	Peak	FWHM	Peak/FWHM
300	100	93.62	2.16	43.34
800	600	213	3.61	59.00
1000	800	232.25	3.94	58.95
VPT 16488				
Va (V)	Vd (V)	Peak	FWHM	Peak/FWHM
300	100	59.24	2.14	27.68
800	600	179.22	4.6	38.96
1000	800	203.65	5.36	37.99

5.8 Summary

This chapter has discussed the two possible upgrades to the CMS detector, along with another approach that was designed to be a quicker and efficient solution to get running. Between the ECAL Shashlik and the HG-CAL approaches, the HG-CAL was chosen as the upgrade for CMS. The benefits of using HG-CAL are that it performs well in a high pile-up environment. It has a dense active scintillator structure, that primarily consists of silicon sensors. The small gap between the FH and the BH allows a higher quality particle flow technique to be applied.

The ECAL Shashlik option has not been chosen as the upgrade for CMS, but the details for the developed prototype of the segmented anode VPT and its experiments are discussed in the following chapter.

The DRO experiment investigates a new concept which adds a second photosensor to the existing $PbWO_4$ crystals. This technique helps mitigates the non-linearity from the irradiated crystals, which has shown promising results from the beam test when compared to using a single photosensor at either the front or rear of the crystal.

Testing 23 VPTs that have been kept in storage since the end of the CMS construction, to see if they had been deteriorated over time. Even though these VPTs were used in the experiment, the published results [5] were not included in the respective publication as SiPMs had been chosen instead because of their high gain and low noise.

This chapter has provided the following contributions:

- The whole double-side readout concept was a group effort led by Marco Lucchini.
- The experimental setup and DRO results were taken from the beam test [4], [5].
- The main contribution to the group effort has been the physical test and characterisation of the stored VPTs which occurred prior to the beam test, for the beam test.
- Analysing the outcome of the characterisation and identifying the most suitable VPTs for the physical experiment.
- Physical participation in the beam test experiment.

Chapter 6. Segmented Anode Prototype

A prototype of a novel VPT which has a four-fold segmented anode and a transmissive mesh dynode has been built for us by Hamamatsu. This seems to be the first of its kind, there have been other devices with similar layout: one of which contains a segmented dynode. This device discussed by H.Kume talks of a triode tube with a segmented reflection dynode that is split into four sections and has position sensitivity of the light incident on the area of photocathode [72].

Other position sensitive photosensor have been developed, most of them gaining their position sensitivity from having multiple anodes. M. Salomon [73], [74] discusses a 3-inch diameter PMT containing a 10-layered cross-wired multi-anode developed by Hamamatsu, modified from an existing model with a single anode (R1652). These were developed for application in a PET scanner. The position of the emission from the cathode can be determined with an accuracy of 1.3 mm. The timing response of the tube with the light coupled to the PMT using a 1 mm diameter optic fibre resulted in a rise time of 1 ns and 50 ns exponential decay [73], with a quantum efficiency of 20% and a gain of 10^6. H. Uchida [75] also discusses a position sensitive PMT with a 75 mm diameter using cross-wired anode with a 4 mm pitch. This is another option for a 2-D detector system for a possible positron CT application. The position of the electron is calculated by the charge division in X and Y direction independently, with the final of the multi dynodes used for energy and timing signal output.

Most of the literature available has either been for a medical application or high energy physics experiments. One of which discusses a PMT constructed with 88 multi-anodes with a spatial resolution of better than 2.6 mm. S. Suzuki [76] discusses a possibility of a new type of position sensitive PMT without the use if image rectifier due to their issues of real-time image construction and count rate limitations. Detecting single simultaneous incident light events with discrete multi anodes, with a rise time of 2.7 ns and can operate within a magnetic field with angle set parallel to the device. Without the use of the magnetic field, the device would have a very high crosstalk of 68% between adjacent segments. The use of a magnetic field tackles this issue by focussing the electrons around the field lines.

One of the main motivators for building a device with a 4-fold segmented anode results from the ECAL upgrade options discussed in Chapter 5.1. An option discussed for the ECAL endcaps was a Shashlik configuration with alternating layers of dense absorber and scintillating crystals tiles, with four wavelength shifting fibres which would be used as the readout. The

prototype presented in this chapter has a segmented anode into 4 quadrants, these quadrants would have matched each module and its four fibres for the readout. A single VPT can be used for the readout instead of 4 separate photosensors. This would reduce the number of individual photodetectors by a factor of four and improve the space utilisation.

6.1 Hamamatsu Prototype "Triode 4"

A prototype with a segmented VPT with a fine mesh, transmissive dynode and a four-fold segmented anode has been constructed by Hamamatsu (type "Triode4", serial number ZG6986). This device can be valuable for applications where space is limited. The active area of the VPT is maximised compared to using four separate independent devices in the same volume. This is achieved through the four nominally independent channels which share a common photocathode and single gain stage.

The prototype VPT has a length of 40 mm and an external diameter of 23 mm. The VPT has a planar photocathode, a transmissive fine-mesh dynode and a segmented anode. The segmented anode comprises a circular plate that is equally split into four quadrants as shown in Figure 6-1. Each of these electrically isolated quadrants has a 1 mm gap between their edges to separate them. The cathode used is a standard bialkali photocathode that has a quoted response of "about 60 μA/lm", which is lower than the typical PMT device that uses this photocathode [6].

Figure 6-1 shows the prototype model within COMSOL, the actual photocathode and the labelling scheme used in this thesis for the four anode segments. Approximate dimensions for the internal electrodes were provided by the manufacturer Hamamatsu in the form of a diagram. The diagrams are classified as commercially sensitive and have thus not been reproduced here, but a set of measurements have been calculated based on the diagram and physical measurements, which are estimated to be accurate within 0.5 mm. These are:

- The gap between the cathode and dynode: 4.0 mm
- The gap between the dynode and anode: 3.0 mm
- The length of the VPT is 40 mm, with an external diameter: 23 mm

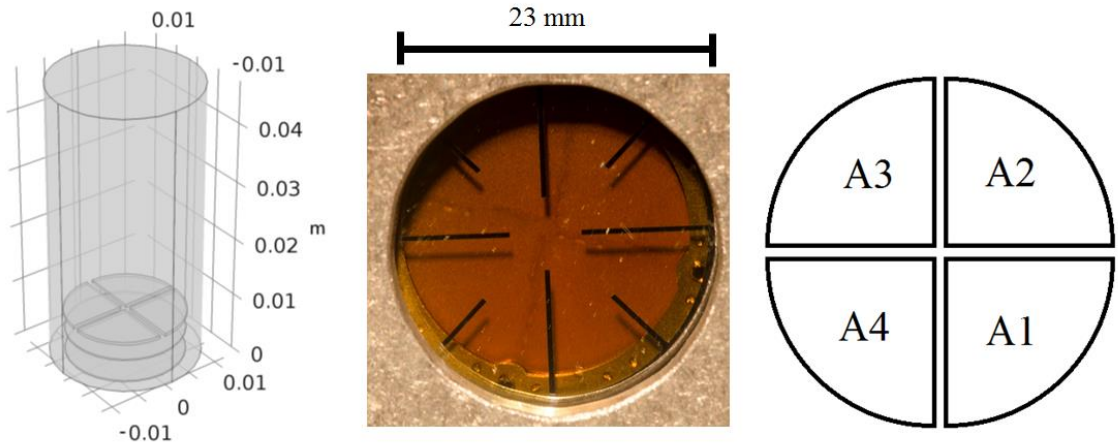

Figure 6-1 – Left: the model of the segmented anode prototype device within COMSOL. Middle: an image of the front faceplate of the device, you can see the slight outline of the segments. The segments are not aligned with the conductive lines on the photocathode. Right: the assigned labels for each segment [6].

6.2 Experimental Work

The following section discusses the experiments for the physical segmented anode VPT prototype. These include a faceplate scan to get a response of the photocathode uniformity; checks for crosstalk that may occur across segments; a fine faceplate scan that will get a detailed response that includes how the segmented anode performs when the source moves from one segment to another; the internal capacitances that occur across electrodes, including between each segmented anode; and finally, the segmented anode VPT operation within a quasi-axial magnetic fields up to 4 T is described.

Data created during this research is available from a data archive at http://dx.doi.org/10.17633/rd.brunel.5620561.

6.2.1 Full faceplate scan for relative photocathode response

A scan of the entire photocathode for each anode segment was carried out to test the DC response of the prototype. The potentials of the cathode, dynode and four anodes were -800 V, -200 V and 0 V respectively. The prototype was mounted on an X-Y-Z stage located in a dark optics lab. A motion controller (Newport ESP3000) was used to control the x-stage and the y-axis was manually controlled with a micrometre. A full scan was made across the VPT faceplate using 1.00 mm steps in both x and y directions.

The light source consisted of a blue LED (model Kingbright L-2523QBC-D), with a measured peak wavelength of 488 nm. To focus the LED a 500 µm pinhole was used, then to refocus the

light onto the photocathode a second biconvex lens was used. The resulting spot size was 0.54 mm which was used on the VPT faceplate. The FWHM of the focused spot was determined, using a CMOS pixel imaging device, to be 370 μm. The power at the focus was 106 nW. Each of the segments was read out individually using two separate current meters: Keithley 614 electrometer and 617 programmable electrometers.

Segment A2 showed some instability throughout the experiments. The results for this segment depending on the region of the segment illuminated tended to be on between 5 - 30 % higher compared to the other segments. The response of the segment also appeared to be less uniform compared to the other 3 anode segments. Figure 6-2 shows the currents on the anode for a step size of 1.00 mm×1.00 mm. The highest current readout was roughly in the middle of each segment, including segment A2 even though it is higher compared to the rest. The outline of the VPT can be seen quite clearly, as the current drops off quickly as the LED light was moved off the edge of the photocathode. The internal structure of the outline of the anode segments can also be seen, which is rotated with respect to the conductive lines on the photocathode. This can also be seen visually by eye on the VPT, you can see this faintly in Figure 6-1 middle image. The current also drops on average ~ 60 % as the focussed LED travels across the conductive lines going halfway into each segment. For example, at locations (5,5), (6,6), (7,7) in the anode segment A3. The physical gap between the segments results in a significant reduction of the current.

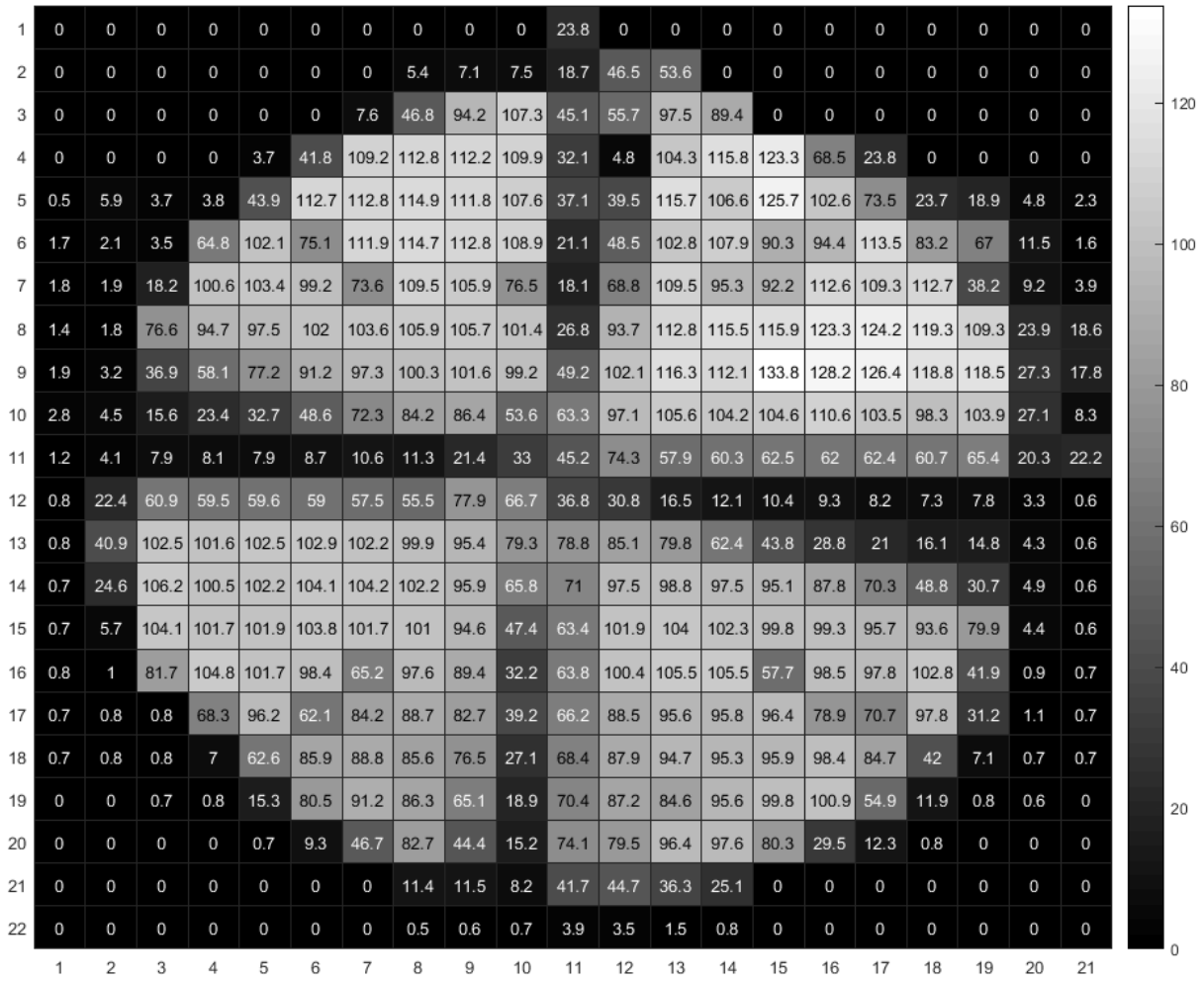

Figure 6-2 – Heatmap showing the current in nA, at each step of 1.00 mm×1.00 mm. The 0 values mean that no reading was taken at those positions.

Figure 6-3 shows a full front faceplate scan in 1.00 mm×1.00 mm steps of the peak current.

The heat map has been normalised to the peak current in each anode segment separately.

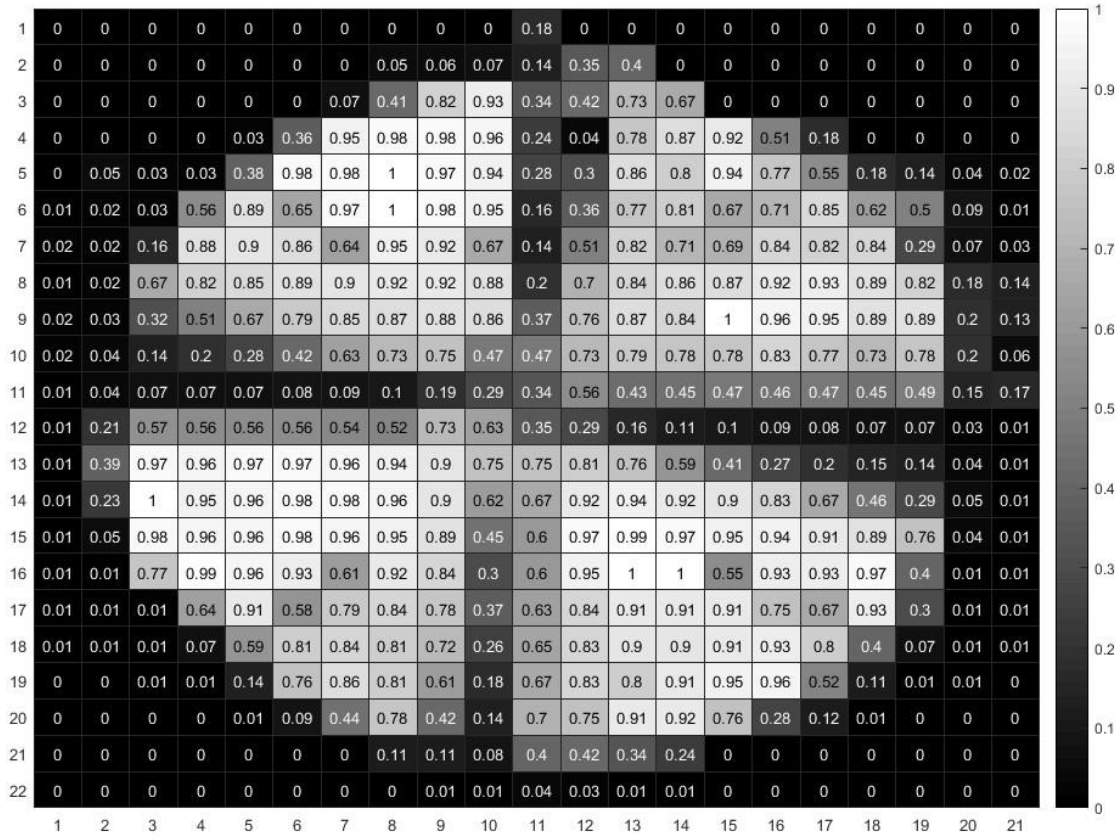

Figure 6-3 - Heatmap normalized to the peak current in each anode separately. The step size is 1.00 mm × 1.00 mm. The 0 values mean that no reading was taken at those positions.

The dark currents were measured after the device had been powered in the dark for at least 3 hours to stabilise. The device was stored in a dark room for weeks leading up to all the experiments carried out. The dark current in each anode were: A1: 0.18 nA, A2: 2.5 nA, A3: 0.59 nA and A4: 0.1 nA.

6.2.2 Crosstalk

The following Figure 6-4 shows the induced crosstalk as a percentage that was measured by anode A4 when the LED was focused on segment A1. Each square block in segment A1 shows the current in nA (a), the same block in segment A4 (b) that is percentage crosstalk normalised to segment A1. The crosstalk is between 2-3% for electrons that hit the centre of A1.

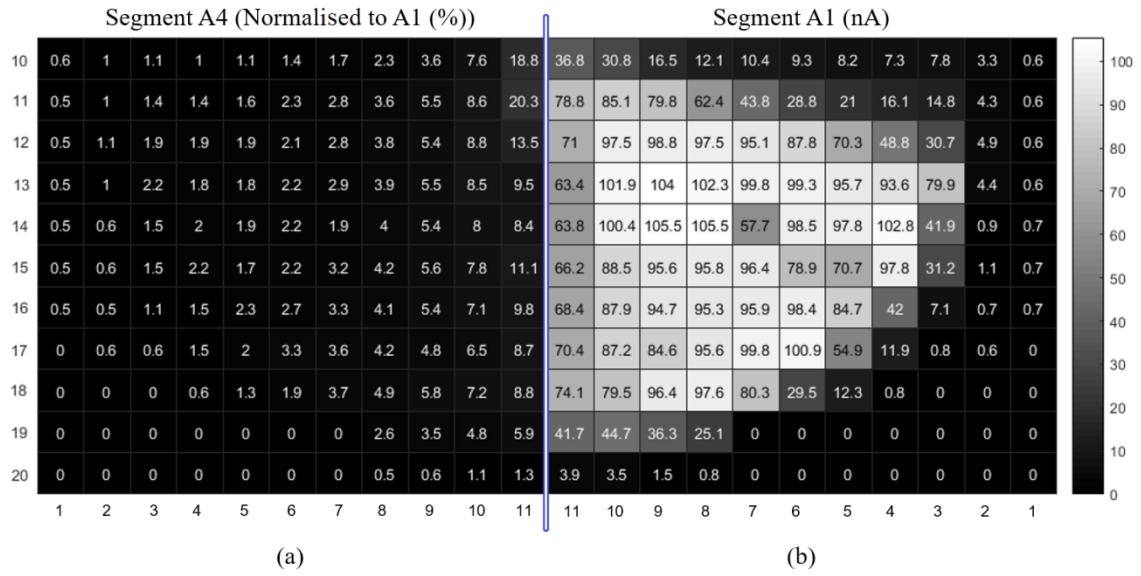

Figure 6-4 - Heatmap showing the percentage crosstalk measured on anode A4 when the LED is focused on the photocathode in the region above anode A1. Heatmap (b) shows the output current of the anode A1 in nA. The step size is 1.00 mm×1.00 mm

6.2.3 Fine Faceplate Scan

A fine scan in steps of 0.25 mm was carried out for a smaller region on the edge of the VPT for the selected anode segment as shown in Figure 6-5. This was smaller than the FWHM of the light spot, in order to obtain a detailed measurement of the transition that occurs between the anode and edge of the anode. Three horizontal lines were chosen towards the middle of the segment. At the y position of 13, 14 and 15 which also matches the same position as the heatmap in Figure 6-4. The current response indicates a generally uniform photocathode response.

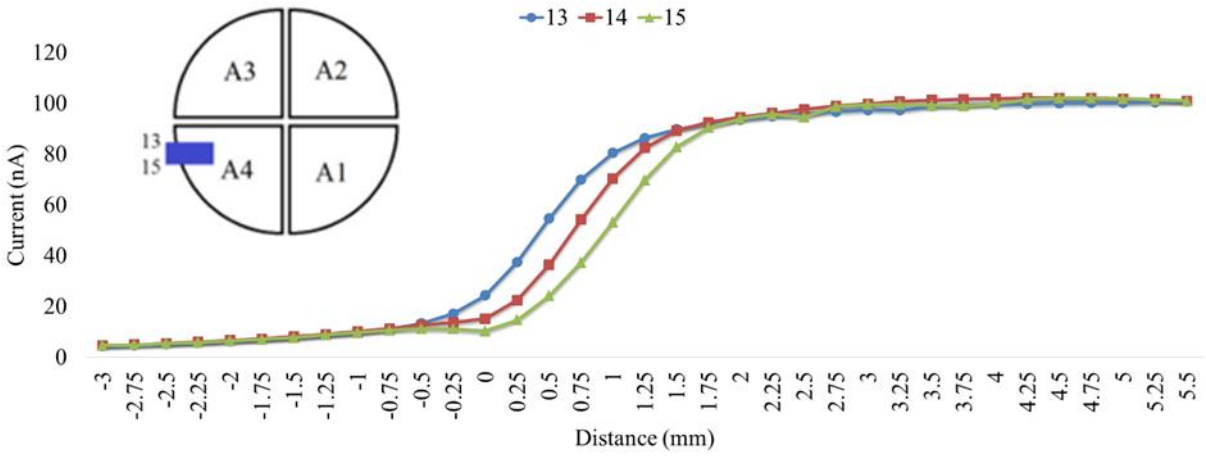

Figure 6-5 - Fine scan in steps of 0.25 mm steps in the horizontal axis. The curve legends correspond to the rows of the heatmap in Figure 6-3.

A separate, fine resolution, scan across the segments inner gaps had been carried out in steps of 0.25 mm to judge the photocathode response and the output current from each of the segments. The photocathode response was the current at the photocathode during each step of the fine scan.

The results shown in Figure 6-6 show the output current across each of the segments and the photocathode response. For the top result between segment A1 and A2, the photocathode response seems constant and consistent with the output current of each of segment. There was a slight drop in the gap between segments, however, the response does not drop to zero. For the bottom result between A3 and A4 the dips in the responses at distance -4 and 4 mm, are the conductive lines that are placed at an angle in the middle of the faceplate, the lower response was also seen on the photocathode.

There was a consistent dip in the current of the photocathode when the illumination source goes over the conductive lines that are on the faceplate. This was because some of the illumination sources were blocked from reaching the photocathode which caused the dip that propagates through to the anode segments.

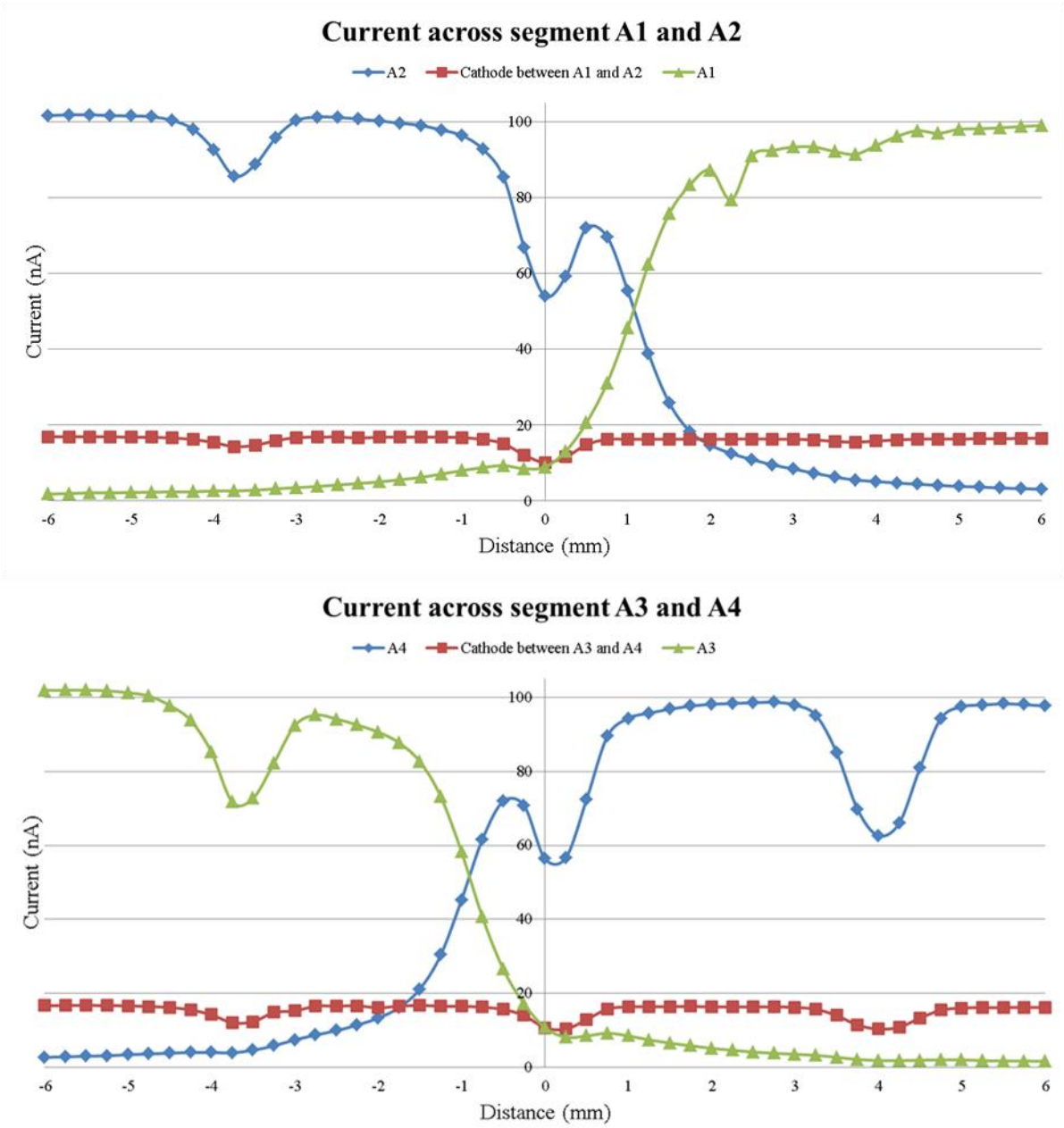

Figure 6-6 – The fine scan in steps of 0.25 mm results between the segment gaps of A1 and A2 and A3 and A4. The dips in the currents corresponding at points at approximately -4 and 4 mm are the conductive lines on the faceplate across the middle of the segment. The location 0 mm is the approximated middle point between the segments.

6.2.4 Internal Capacitances

The internal capacitances have been measured between cathode and dynode, and each of the segment within the prototype. These were measured using an HP, LF impedance analyser (4192A) [77] at a frequency of 100 kHz.

The results in Table 6-1 show the capacitance between each of the segments within the prototype VPT. The lowest capacitance is between segments A1 and A3.

The capacitance between the cathode and dynode is measured to be 5.46 pF.

Table 6-1 – The intercapacitance measured in pF between segments from the anode, labelled A1 to A4.

	A1	**A2**	**A3**
A2	1.49		
A3	1.18	1.41	
A4	1.46	1.31	1.44

Table 6-2 – The capacitance between the dynode and each anode segment.

Dynode Segment	Capacitance (pF)
A1	2.17
A2	2.00
A3	2.10
A4	1.97

The four segments were expected to have similar capacitance to each other, the mean capacitance between the segments and dynode is 2.06 pF with σ of 0.08 pF.

6.2.5 VPT Operation in a Magnetic Field

Due to the curvature of the ECAL, the photosensors are angled within the range of 8° to 24° non-axial. For testing purposes, the middle of the range has been chosen, which is a 15° angle. Initially, the CMS magnet had been designed to operate at 4 T. However, for the duration of the LHC running, it has been operated to produce a 3.8 T field.

The magnet that is set up at Brunel University London is based on an Oxford Instruments warm-bore superconducting magnet (model - Jeol JNM-FX200 Superconducting Magnet). This was configured to run at 4.00 T with an operating current of 31.25 A; to mimic the original CMS magnet operating specification was specified to run at 4.00 T. The Brunel magnet has no power supply making it electrically quiet. The schematic of the Brunel magnet is shown in Appendix C.

The following tests were carried out with the segmented anode VPT placed inside a cylindrical component called a torpedo with dimensions of 5.08 cm diameter and 36 cm height. The torpedo was designed to house the electrical circuitry for the VPT which is electrically shielded, and two Nichia NSPB 500S LED (peak wavelength 470 nm, FWHM of 30 nm) to illuminate the photocathode approximately uniformly. This torpedo is placed in the core of the 4 T magnet at Brunel.

A lock-in amplifier model: Stanford Research System model number SR810 [78] was used to detect the signal output from the VPT. The signal was phase locked to the input wave of the LED light, operated at 17 kHz with a sine wave. The lock-in amplifier was set to a time constant of 1 s, filter slope of 6 dB and "Normal" reserve.

6.2.5.1 VPT operation at 0 T at 0°, 4 T at 0°and 4 T at 15° for Varying Dynode Voltage

Figure 6-8, Figure 6-9 and Figure 6-10 show the responses of the segmented anodes when the dynode voltage varies from 0 V to 600 V and the magnetic field strength varies from 0 T at 0°, 4 T at 0° and 4 T at 15°. The response for 0 T at 0° shows a gradual increase for all segmented anodes, with a peak of ~ 20 nA. For the response of 4 T at 0° the current significantly decreased compared to the 0 T at 0° response, with an attenuation of ~ 6 times. This is most likely due the structure of the fine mesh dynode. The anode segments can be seen through the faceplate of the VPT, which gives the indication the dynode has a fine mesh, mostly likely a form of transmissive dynode structure. Unfortunately, the structure of the dynode mesh was not provided by Hamamatsu and could be determined without dismantling the device. The thickness of the transmissive dynode can range from 1 to 10 μm. The attraction to use transmissive dynodes stems from the benefit of their use for proximity focused imaging devices [43].

Adding a 15° angle to the photoelectrons as they were released from the cathode shows the response varying amongst the anode segments. This was most likely due to the electrons that were heading towards the A3 and A4 segments are now heading towards the A2 and A1 segments caused by the 15° shift. Therefore, the response will be higher than the 4 T at 0° response for the A2 and A1 segments, and lower than the 4 T at 0° response for the A1 and A2 segments.

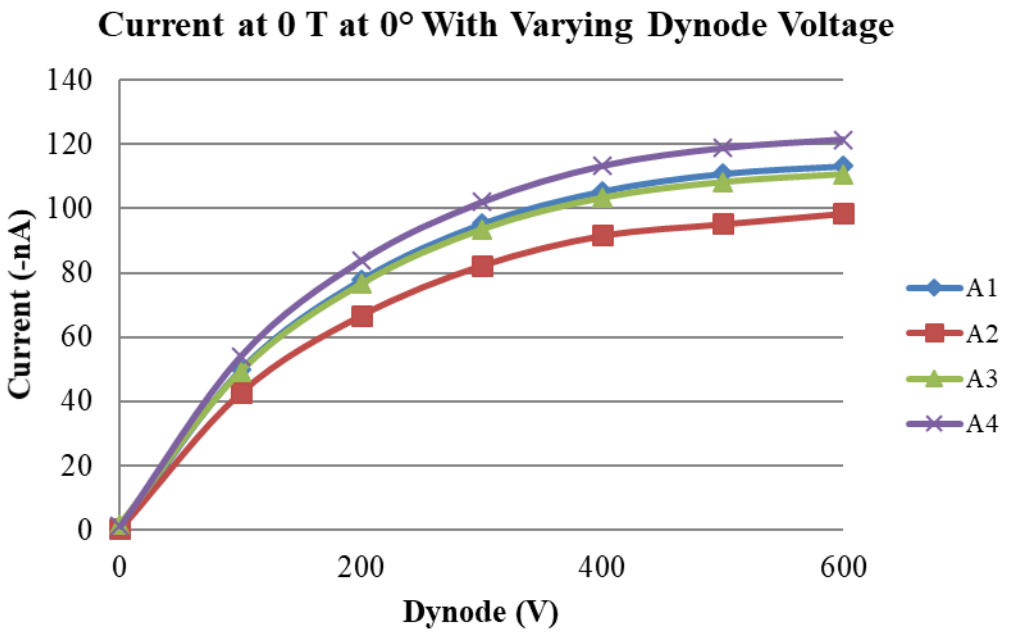

Figure 6-7 – Current produced at each segmented anode in a 0 T at 0° magnetic field. The anode voltage is fixed to 800 V and the dynode voltage varying from 0 V to 600 V in steps of 200 V.

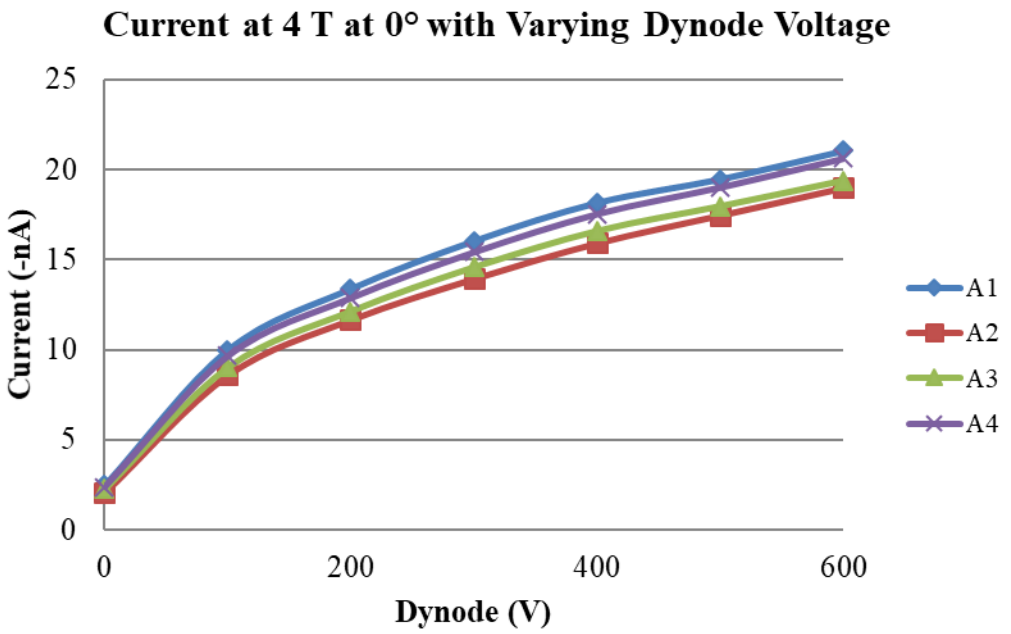

Figure 6-8 - Current produced at each segmented anode in a 4 T at 0° magnetic field. The Anode voltage is fixed to 800 V and the dynode voltage varying from 0 V to 600 V in steps of 200 V.

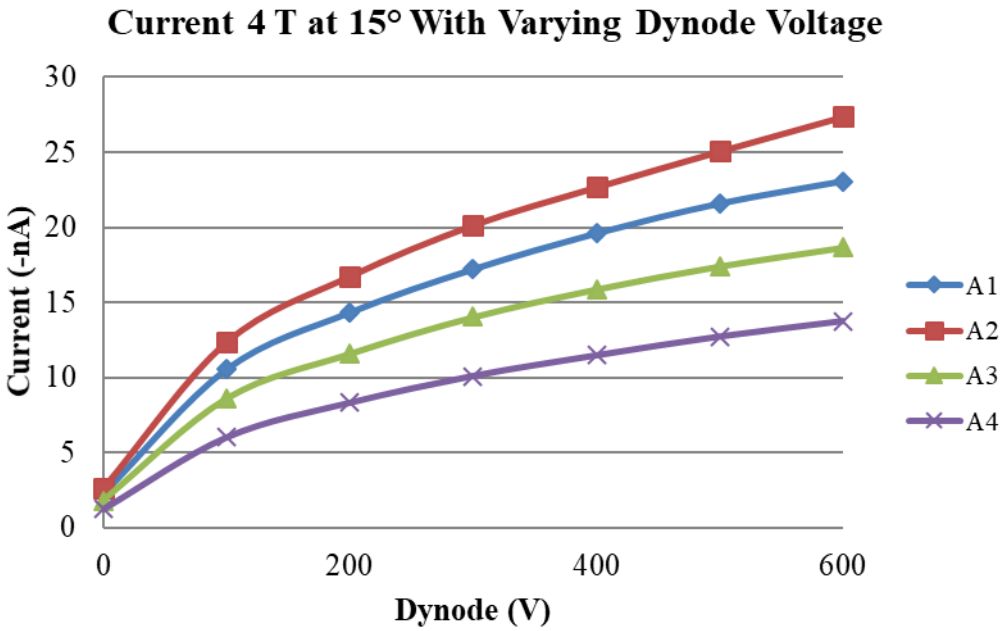

Figure 6-9 - Current produced at each segmented anode in a 4 T at 15° to the magnetic field. The Anode voltage is fixed to 800 V and the dynode voltage varying from 0 V to 600 V in steps of 200 V.

6.2.5.2 VPT operation at 0 T at 0°, 4 T at 0° and 4 T at 15° with fixed 200 V Difference Between Dynode and Anode

Figure 6-10, Figure 6-11 and Figure 6-12 show the response of the VPT when the anode voltage was fixed 200 V higher than the dynode voltage. The voltage was increased in steps of 200 V for both and the magnetic field strength was varied from 0 T at 0° to 4 T at 0° and 4 T at 15°. The response for all experiments follows a similar trend to those from 6.2.5.1. There was still an ~ 6 times attenuation when a 4 T at 0° magnetic field was applied. The segments also experience the same effect when there was a 15° angle applied to the illumination source, with A2 and A1 gaining current and A3 and A4 missing out on current when compared to 4 T at 0°.

When the voltage for the dynode and anode was set high, there was a higher induced current. The increase was slower after 400 V – 600 V dynode to anode ratio than during the initial jump from 0 V – 200 V to 200 V – 400 V.

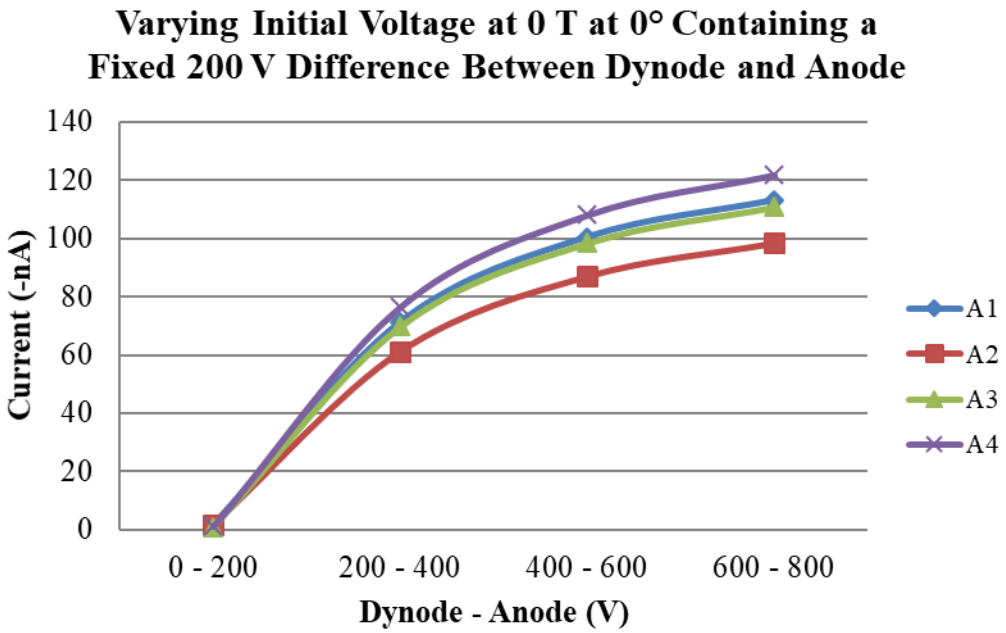

Figure 6-10 – Current produced at each segmented anode at 0 T at 0° magnetic field. The anode voltage varies with the dynode voltage, where the anode is always 200 V higher than the dynode.

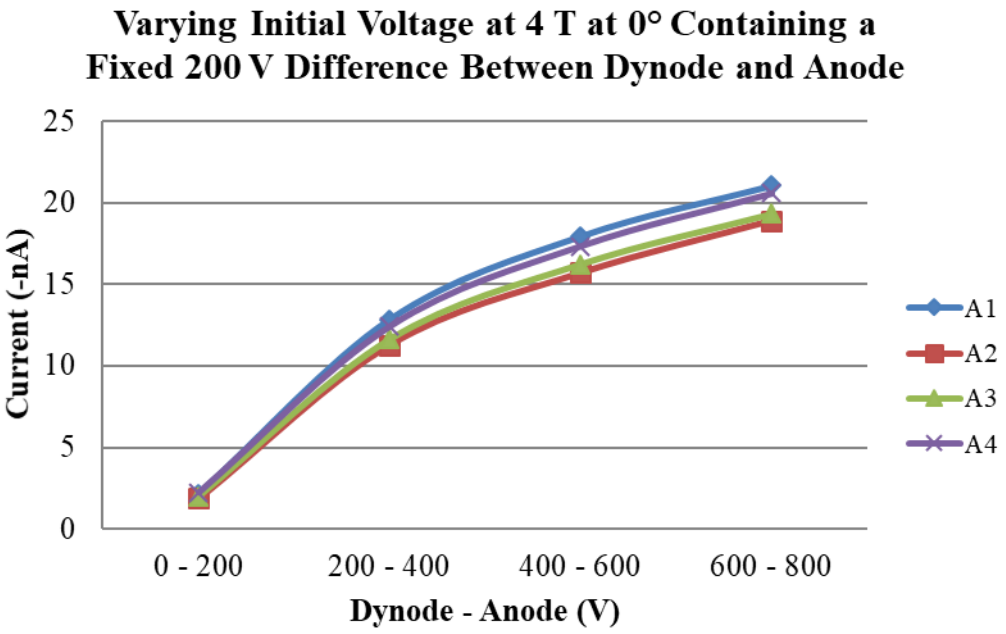

Figure 6-11 - Current produced at each segmented anode at 4 T at 0° magnetic field. The anode voltage varies with the dynode voltage, where the anode is always 200 V higher than the dynode.

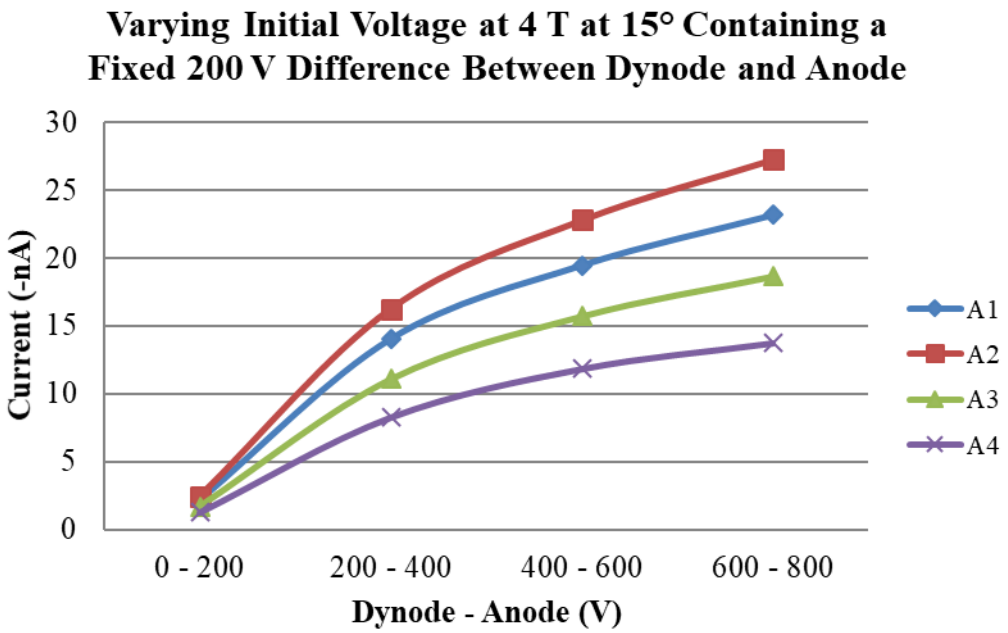

Figure 6-12 - Current produced at each segmented anode at 4 T at 15° to the magnetic field. The anode voltage varies with the dynode voltage, where the anode is always 200 V higher than the dynode.

6.2.5.3 Fringe Field

The VPT was placed in the solenoidal fringe field to make 1 T measurements. The axial component field varies from 0.97 T to 1.25 T over a distance of 10 mm along the VPT longitudinal axis in this region. The 0 T at 0° measurements were carried out with the same equipment but placed at a distance from the magnet. The current across the segments range from 101.75 – 125.79 nA when the axial field on the VPT is 0 T at 0° for both Figure 6-13 and Figure 6-14. The distance between the flange and the top of the magnet directly correlates to the strength of the magnetic field applied to the VPT (bigger the distance from the middle of the magnet provides a weaker magnetic field).

Figure 6-13 and Figure 6-14 shows how the bigger the distance between the VPT and the centre of the magnet (i.e. a weaker magnetic field), results in a higher current output from the VPT. With no magnetic field present at all or having a 15° angle in the magnetic field biased towards segments A2 and A1, produced a higher current as well. The VPT was shown to have a good response up till 3 T at 0°, where after this the response of the VPT drops sharply at 4 T at both a 0° and 15° tilt.

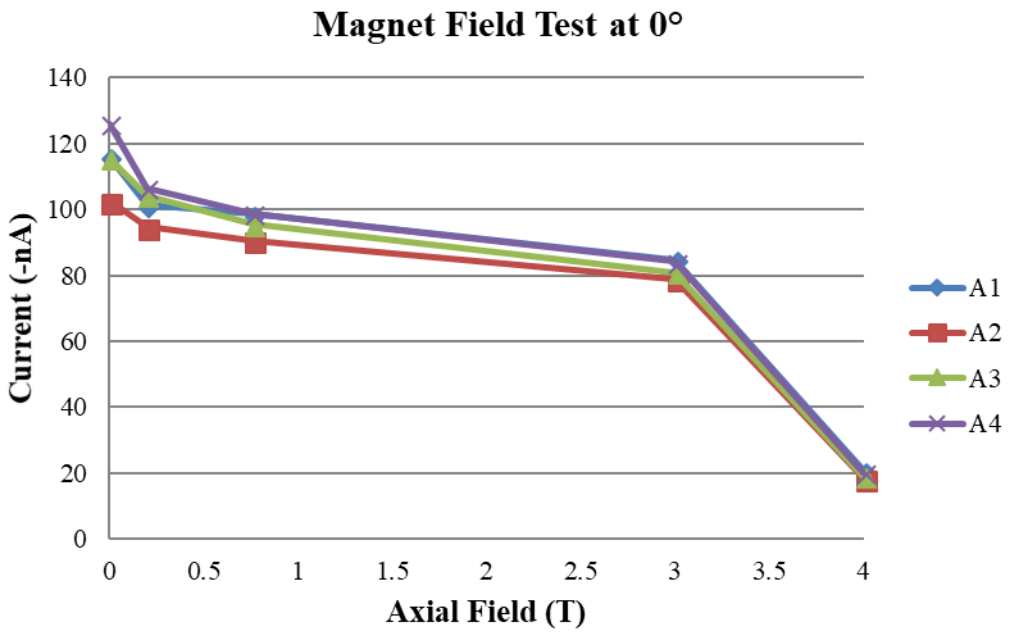

Figure 6-13 – Current produced by the VPT segments when the magnet is set to 4 T at 0°. The torpedo is placed at different depths within the magnet, which affects the magnetic strength on the VPT. The measurements are shown for 0 T, 0.8 T, 3 T and 4 T, all at 0°.

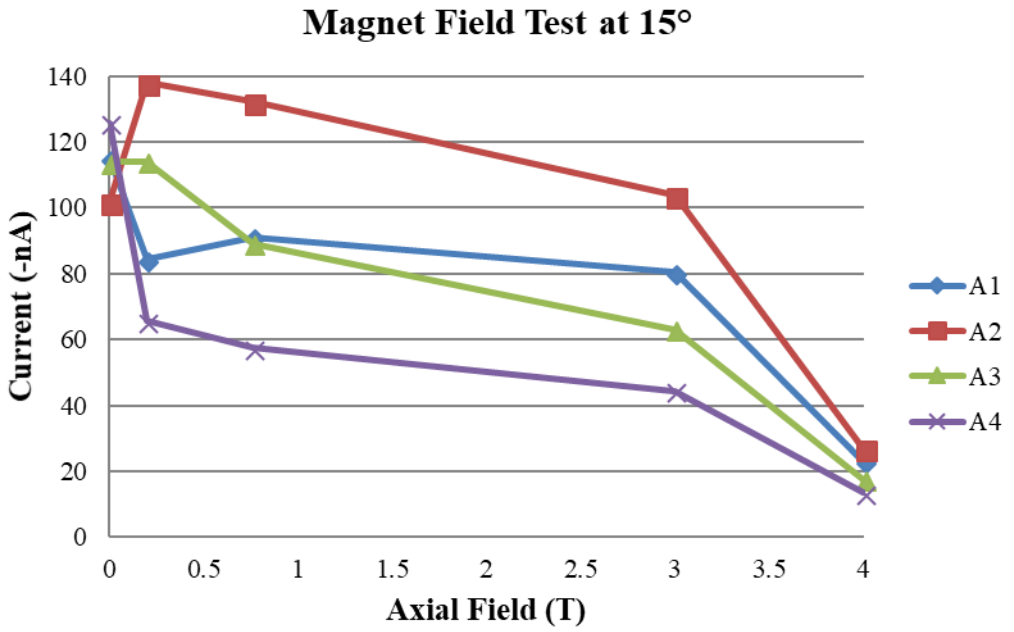

Figure 6-14 – Current produced by the VPT segments when the magnet is set to 4 T at 15°. The torpedo is placed at different depths within the magnet, which affects the magnetic strength on the VPT. The measurements are shown for 0 T, 0.8 T, 3 T and 4 T, all at 0°.

6.3 Simulations

The following section presents the results from a simulation using COMSOL. The design of the model was based on the RIE-188 VPT described in Chapter 4. The geometry incorporates the changed overall dimensions, the new four-fold anode design and in the absence of any information about the transmissive mesh-dynode, a simple planar disc was used for that component.

6.3.1 Segmented Anode Geometry

The geometry of the segmented anode VPT had been designed in COMSOL to closely match the physical prototype. The device was made into a cylinder shape, with the electrodes placed inside in their relevant positions as shown in the right image of Figure 6-15. The segmented anode was made by initially creating a circle, and then the gaps are taken from it to evenly separate each segment by 1 mm as shown in the left image in Figure 6-15. The segments were then extruded to give the depth of 250 µm. The distance between the anode segments and the dynode was 3 mm, and between the dynode and cathode was 4 mm. The dynode and cathode also have a depth of 250 µm. As no information is provided for the depths of the electrode plates, an approximation has been made to extrude the depths of the electrodes with a depth of 250 µm.

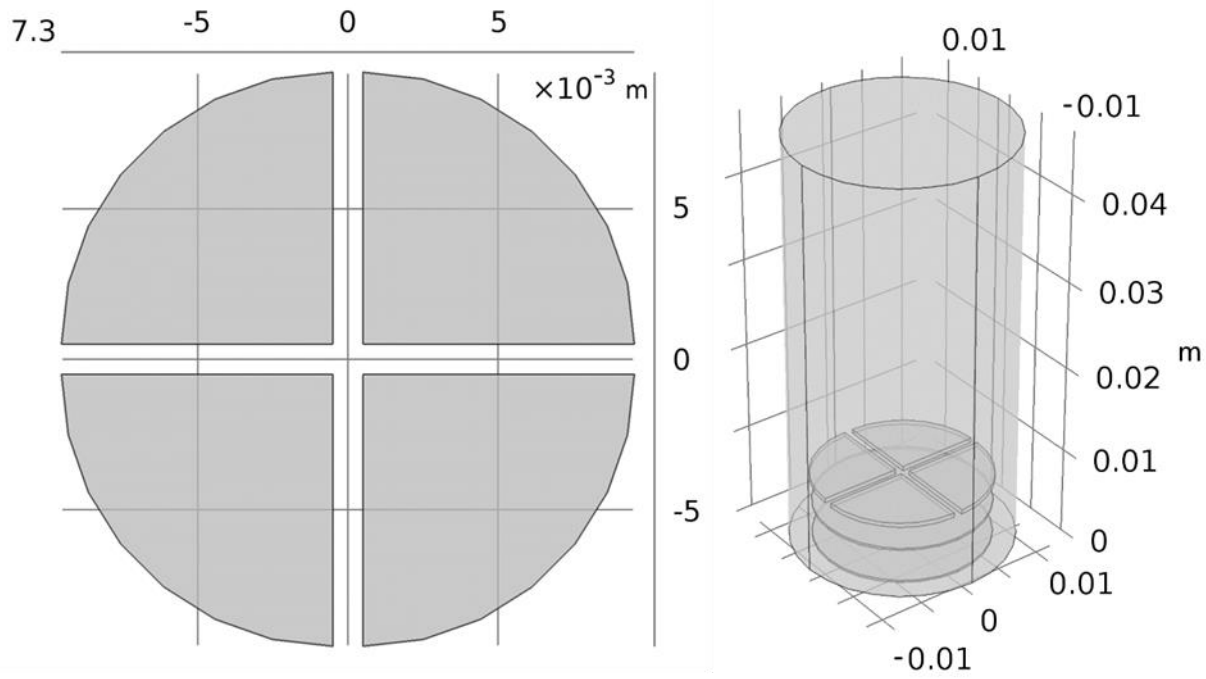

Figure 6-15 – The left image shows the segmented anodes with a 1 mm gap between them, within the COMSOL geometry. The right image shows the full geometry of the VPT within the COMSOL geometry.

6.3.2 Electrostatics

The electric field of the segmented anode prototype is shown in Figure 6-16. The outer shell and cathode are set to 0 V, dynode at +600 V and the 4-segment anode at +800 V.

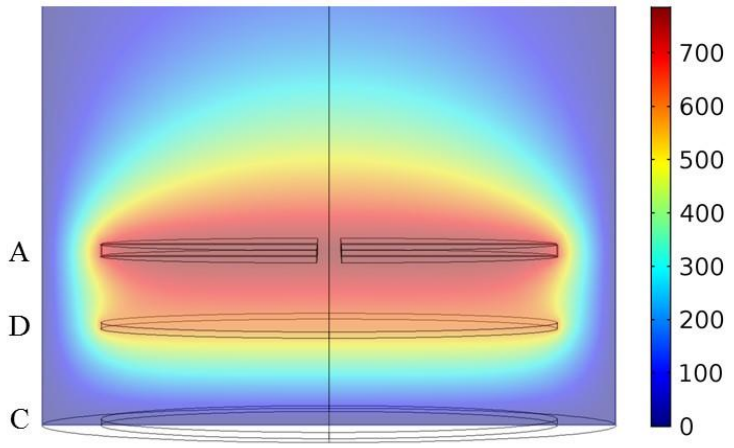

Figure 6-16 – The electric field within the segmented anode VPT. The coloured scale shows the potential in volts.

6.3.3 Electron Trajectories

The motion of electrons within the segmented anode prototype was simulated, the results are shown in Figure 6-17 for 0 T and Figure 6-18 for 15° to an axial 4 T field. For the 0 T particle trajectories, the particles experience a slight focusing effect towards the centre of the device.

Some of the electrons that experience a 15° shift from the 4 T axial field end up hitting the outer shell of the VPT. This contributes towards the loss of signal, with approximately 30 % of the electrons hitting the shell and not the segmented anodes.

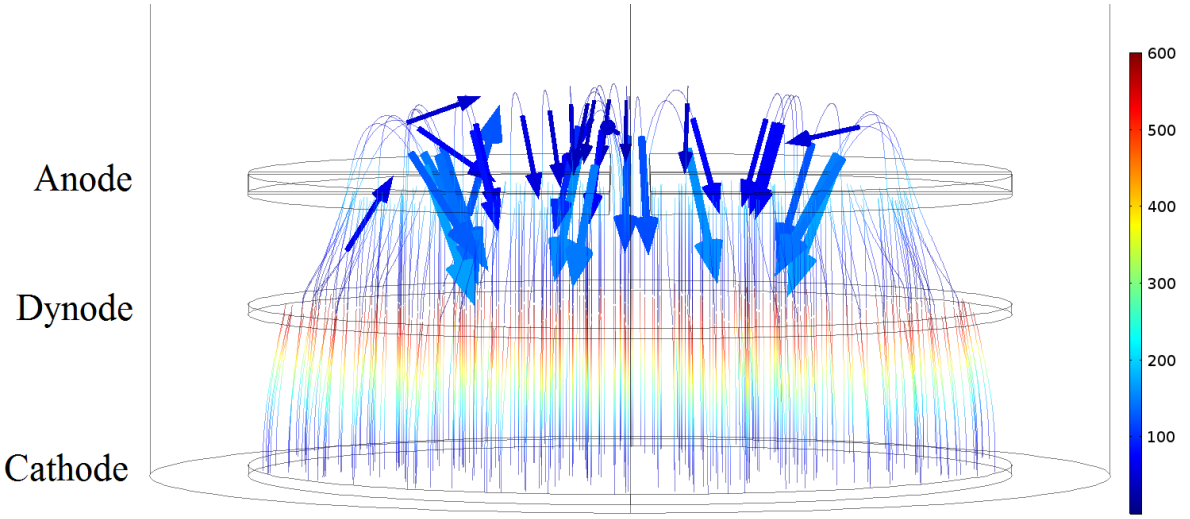

Figure 6-17 – The trajectories at 0 T for photoelectrons travelling from the photocathode via a transmissive dynode towards a segmented solid anode. The particles that pass through the segmented anode gap are attracted back towards the anode. The colour scale shows the electron energy in electron-volts [6].

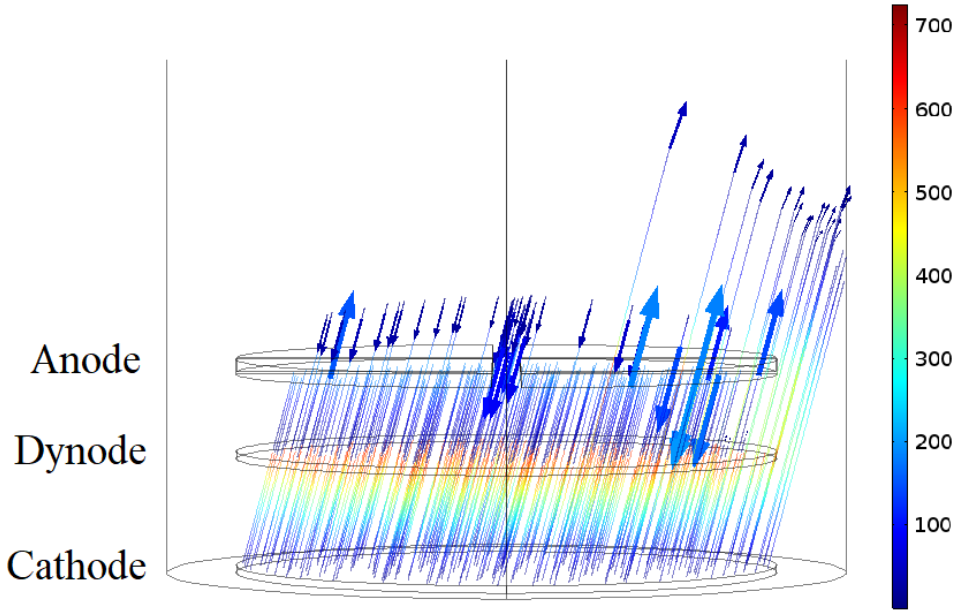

Figure 6-18 - Particle trajectories at 15° to an axial 4 T field. Approximately 8% of the photoelectrons initially released from the photo-cathode hit the VPT shell. From the SE, approximately 30% of the electrons do not hit the segmented anode. Instead, these electrons either hit the VPT shell or escape through the gaps in between the anode segments. The colour scale shows the electron energy in electron-volts [6].

6.3.4 Distribution of Particles on Segments with the Varying Magnetic Field.

In this section, simulations were run to analyse the segmented VPTs behaviour under varying conditions. Each segment was individually probed for collisions with electrons that were released in different quantities and under different magnetic field strengths.

The simulation on the RIE-188 modelled VPT that contained the anode mesh has a complex and realistic secondary emission and backscatter procedure. However, for the segmented anode VPT model, there was not enough time to get the same level of complexity implemented. Therefore, a simpler solution was implemented that should give a good understanding but is not as realistic as could be possible.

Table 6-3 shows the distribution of electrons on each segment where there was a 0 T magnetic field. The primary particles released vary from 10 to 15000, and each segment was probed for the number of electron collisions, along with the gap that was in-between each of the segments.

Table 6-3 - Distribution of particles on each segment at 0 T

Primary Particles	Gap	Segment 1	Segment 2	Segment 3	Segment 4
10	0	0	26	66	14
100	156	274	198	252	276
500	595	1189	1226	1269	1273
1000	1280	2477	2618	2414	2307
2000	2614	4916	5116	5066	4880
5000	6917	12385	12399	12643	12052
10000	14542	24922	24577	24212	24815
15000	21556	37105	37035	36509	37475

The gap determines how many electrons were lost whilst heading towards the anode segments. When compared to those that go on to collide with the anode, approximately 10% – 11% of the total electrons (including secondaries) were lost through the gap.

The results from tables Table 6-4, Table 6-5 and Table 6-6 show that for the 1 T condition, slightly more collisions occurred between the gaps of the anode when compared to 0 T. The range of total electrons that hit the gap increased to 11% - 13%. 4 T has further collisions in the gap, going to 12% - 13%. When a 15° release angle was applied, electrons start to hit the side walls of the VPT. This further increased the number of lost electrons and brings the range of total electrons lost to 11% - 13%.

Table 6-4 - Distribution of particles on each segment at 1 T

Primary Particles	Gap	Segment 1	Segment 2	Segment 3	Segment 4
10	0	0	26	66	14

100	144	238	174	216	252
500	644	1021	1082	1184	1105
1000	1329	2154	2414	2252	2055
2000	2701	4291	4708	4452	4412
5000	7046	10980	11310	11480	10868
10000	14921	22454	22147	21932	22468
15000	22470	33306	33069	32973	33669

Table 6-5 - Distribution of particles on each segment at 4 T

Primary Particles	Gap	Segment 1	Segment 2	Segment 3	Segment 4
10	0	0	26	66	14
100	144	238	174	216	252
500	656	1009	1082	1184	1105
1000	1330	2142	2414	2251	2067
2000	2714	4279	4708	4451	4412
5000	7094	10955	11310	11467	10858
10000	15010	22403	22109	21919	22480
15000	22583	33256	33033	32960	33656

Table 6-6 - Distribution of particles on each segment at 4 T 15 degree

Primary Particles	Gap	Side wall	Segment 1	Segment 2	Segment 3	Segment 4
10	0	1	0	26	54	13
100	117	12	260	171	224	264
500	590	54	968	973	1292	1182
1000	1283	102	1707	1873	2613	2370
2000	1482	213	1760	1958	2967	3157
5000	6659	519	9760	9879	12595	12328
10000	14032	1002	19430	19148	24131	25591
15000	21102	1559	28627	28603	36671	38189

6.3.5 Distribution of Electrons from Varying Release Angle

Another experiment that was considered is how the segmented anode VPT behaves when the axis of rotational symmetry of the VPT was placed at different angles to the magnetic field. The idea behind this simulation was to match the conditions in CMS where all the VPT are placed at varying angles to the 3.8 T field.

As the angle of the released electrons was increased, the electrons that go through the gap between the segments decreased. This was because the electrons that start to enter the gap have a better chance to hit the sides on the anode when the electron release angle was big. The downside to the bigger angle was that a lot of electrons also go on to collide with the side walls a lot easier, which would have a bigger impact on the total lost electrons. There was a big impact on loss of electrons when primary electrons were lost due to the large angle, as the potential to produce secondary electrons was lowered. The total loss of electrons increased significantly as the angle increased when compared to 0°, with a large jump when at 35° - 40°. However, even though a lot of electrons were lost at the largest angle, 82% of the electrons still collide with the dynode and produce secondary emission.

Table 6-7 - Different angles in the 4 T field with 1000 particles through the inlet

Angle	Gap	Side wall	Segment 1	Segment 2	Segment 3	Segment 4	Loss compared to 0°
5	1369	20	2041	2187	2324	2118	2%
10	1429	60	1810	2075	2470	2156	4%
11	1417	67	1805	2036	2495	2166	4%
12	1400	79	1815	1984	2531	2166	4%
13	1282	88	1839	1970	2577	2231	3%
14	1232	99	1772	1929	2613	2232	4%
15	1283	102	1707	1873	2613	2369	4%
20	1398	136	1568	1683	2686	2329	7%
25	1240	193	1438	1495	2723	2511	8%
30	1172	241	1171	1368	2880	2639	9%
35	1144	284	923	1014	2948	2826	13%
40	923	349	611	754	3062	2872	18%

6.3.6 Induced Current

The induced current is calculated in an identical manner to that discussed in Chapter 4.

6.3.6.1 Direct Hit and Crosstalk

Using the Shockley-Ramo theorem the induced current was calculated when a single secondary electron would hit the anode segment directly in the middle of the segment and the current was induced on the adjacent segment, at 0 T at 0° and 4 T at 15° axial field.

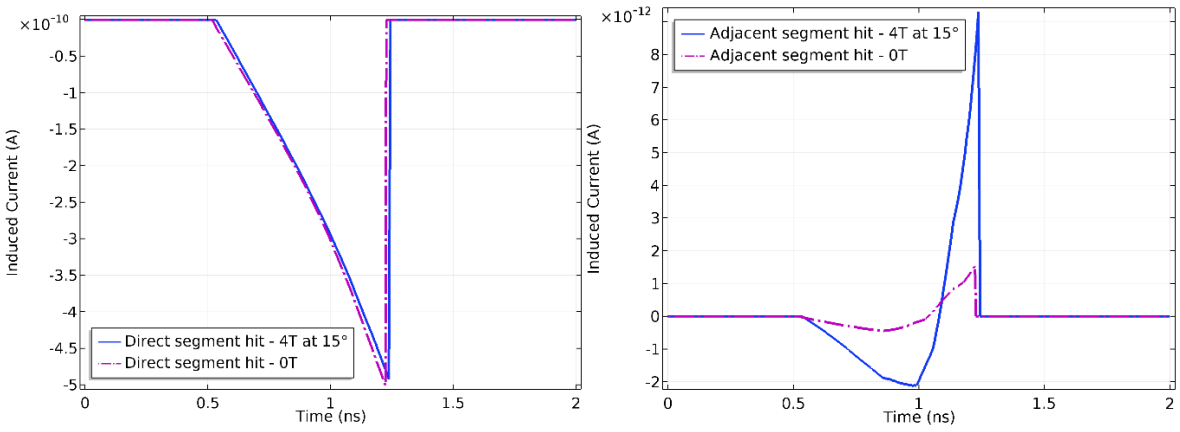

Figure 6-19 - Simulation of the induced current of a single secondary electron for a VPT at 0 T and at 15° to a 4 T field. Left, the current arising from a direct hit on an anode segment. Right, the cross-talk induced current arising from a hit on an adjacent segment.

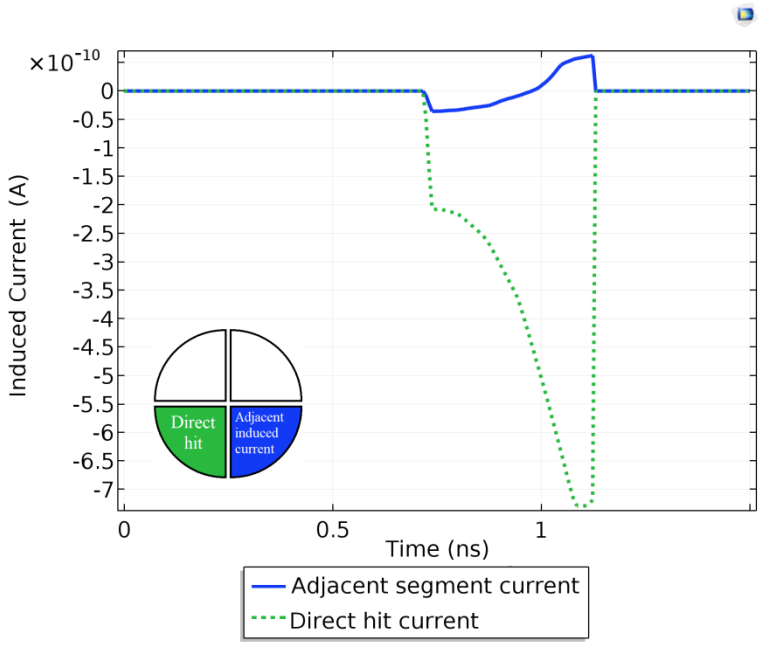

Figure 6-20 – The induced current of a single particle within the VPT. The blue line shows the induced current on the adjacent segment and the dotted green line shows the current due to a direct hit on the segment.

6.3.6.2 Induced Current within Segment Positions

Most of the testing carried out was taking readings from a whole segment. However, there could be some position sensitivity within each segment of the anode. The following test was carried out to test this. A photoelectron was made to hit certain positions of a chosen segment and the output was taken from the adjacent segment. Figure 6-21 shows the induced current from the different positions A, B, C and D on the adjacent segment. The points closest to the adjacent segment produced a higher crosstalk current of ~50 pA. Point C induced a higher current compared to points A and B, as this point was closer to the outer shell of the VPT wall, the electrostatics of the VPT create a grounded effect and the particles were focused towards the centre of the tube. This means the particle had a longer path to travel within the tube and generated a higher current. The 3 points closest to the adjacent segment correspond to ~10% of the current in the hit segment. The last point D was 5 mm from the inter-anode gap, induced a peak crosstalk current of < 2 pA (< 0.3%). The results demonstrated how the Shashlik configuration can benefit from this, each of its four fibres that contain individual sources of light can be positioned in the middle of a segment to minimise the crosstalk between the segments.

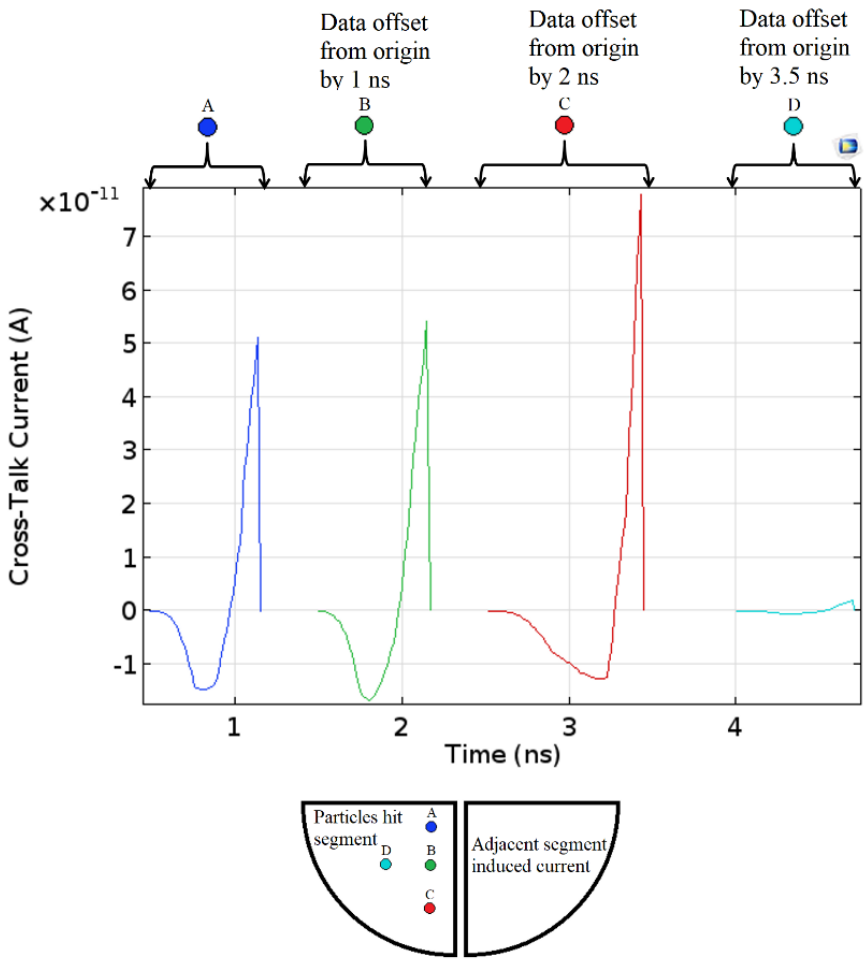

Figure 6-21 - Simulation of the cross-talk current in a prototype at 0 T. Hamamatsu segmented anode VPT due to a single electron within the lower left segment. The response at points A, B, C and D was studied. The cross-talk current is read from the adjacent segment lower right.

6.4 Summary

This chapter has introduced the new prototype for a segmented anode VPT that has four independent channels. The physical device has been characterised. and the results indicate that the VPT performs as expected at 0 T at 0°, but when placed in a 4 T at 0° magnetic field, the output current of the device degrades 6-fold. The crosstalk between segments is small (1%-2%) and the uniformity of the photocathode response was consistently based on the full faceplate scan and the fine scan that was carried out.

The VPT was also designed and modelled in COMSOL to simulate it under varying conditions. The simulation of the VPT prototype showed how it would perform under similar conditions to the physical VPT prototype experiments. The crosstalk induced in the position sensitivity testing in COMSOL, shows similar outcomes for the photocathode sweep carried out on the

physical VPT when tested for crosstalk. The distribution of particles across the segments is uniform which is good for using a single VPT as 4 individual channels.

The varying release angles of the PEs from the cathode showed a higher induced current at the anode segment that the angle is heading towards. This could have a negative effect if each segment was used as an individual device. With a bigger angle, there was less electron loss through the gaps of the segments, but there was more lost from hitting the side walls of the VPT.

The similarities and differences with the experimental results and simulated results are as follows:

- The cross-talk is insignificant moving near the centre of the adjacent segment, similar to the simulation outcome shown in Figure 6-21.
- The experiment showed more cross-talk in the top right region than the simulation. This can be caused by the reflectiveness of the segment boundaries.
- The elevated crosstalk in regions A, B and C in the simulation is also visible in the experiment (Figure 6-4). These are the regions close to the boundary that separates the two segments.
- The middle region of the segments has shown consistent readings and minimal crosstalk, in both experiment and simulation.

The overall indication from simulation and experiment have shown there is similarities in trend of the output and crosstalk between segments. There is a region of approximately 3 mm x 3 mm within each segment which has a uniform response. The results indicate the ideal range of the VPT operation sits between 0 – 3 T. However, the actual response varies in magnitude between the simulation and experiment. This is due to limited specifications provided by Hamamatsu, as the nature of the dynode is unknown. Therefore, the exact properties have not been replicated within the COMSOL model. The entirety of this chapter has been a contribution to this thesis.

Chapter 7. Conclusion & Future Works

This works describes the modelling and experimental testing of two configurations of VPT. The models were created using the Multiphysics software COMSOL Multiphysics software package, where approximations have been created to be able to simulate the model without memory error or the computer crashing. The anode mesh has been modelled with the real VPT dimensions in terms of the pitch of the mesh and the depth of the mesh.

The contributions of this thesis have been demonstrated throughout each chapter. Chapter 2 and Chapter 3 have given an insight into the LHC and the components within it, specifically the CMS detector and its structure. The VPTs within the ECAL subdetector are discussed in detail in their structure and how they operate.

Chapter 4 introduced a Multiphysics simulation package called COMSOL, that is used to model and simulate the current VPT used in CMS. A detailed process for creating the VPT model was provided, along with several simulations that show how it performs under varying environments and conditions.

The time development phase of the signal showed a similar trend to the works by Yaselli [1]. However, when it comes to measuring the magnitude of the total charge, there was a significant difference of 10×. Upon verifying the simulation model several times and using a charge conservation test, it may be possible that the works by Yaselli was inaccurate. This is further supported by the fact that Yasseli had not known the true dimensions of the critical anode mesh (this is not the case for the simulations in this work), which can have an impact on the collision rate and in turn effects the induced current. The simulations have also analysed backscatter which can occur upon electron collisions and is also an advance on Yaselli's works.

A development that has been understood is that when working a device with this geometry, a certain time-step is required to accurately simulate the occurrences that may happen within a small geometry. If the time-step using the VPT is larger than 2 ps, the electrons may not be simulated at the point of interaction with the anode mesh. The limitation of using COMSOL version 5.3 to create the model is that the correct anode mesh pitch and depth is used, however, the maximum array of holes was only achievable to 100×100 with the workstation available. The actual VPT contains a circle array containing approximately 3.2 million holes.

Overall, the simulated model has provided a good visual representation of what occurs within a VPT with a fine anode mesh, which include electron trajectories and their interactions with the electrodes. When the model is placed inside a 4 T simulated magnetic field, the induced current is nearly doubled. Adding a 15° angle to the 4 T had the opposite effect, reducing the induced current by ~ 3 times when compared to 0 T.

Chapter 5 investigated how the CMS detector will be upgraded in 2026 to be improved for the HL-LHC, which includes a higher radiation environment and more data flow from higher luminosity. The upgrade options for the CMS detector include the HG-CAL and the Shashlik Configuration. Another solution that required fewer costs was tested called the DRO. Here was a possibility to partially recover the loss of information caused by radiation damage that has occurred to the CMS detector components. The DRO concept does help mitigate the lost performance caused by the high radiation damage on the inner crystals.

The experiment required retesting the VPTs as a part of checking if the DRO concept is viable. It can in-fact be fully implemented as there are enough VPTs available. For the VPTs, a batch 23 were chosen from a collection of 1000 VPTs that were manufactured during the initial construction of the CMS detector. These were stored in nitrogen purged refrigerators and have been re-characterised to see if they function similar to when they were characterised initially by the manufacturer RIE.

The re-characterisation demonstrated a small loss in performance of approximately 5%. However, it is unknown if the performance is a systematic error or the actual degradation of the VPT as the testing conditions are not identical to the initial testing by the manufacturer.

Chapter 6 introduces a possible prototype for the Shashlik configuration, which is a VPT designed with a segmented anode. This prototype has provided a 4 channel VPT that can be used as a single output or as 4 individual outputs. The experiments undertaken were the first published characterisation of the unique VPT prototype that has also been modelled within COMSOL. Overall, the experiments indicate that the prototype is not successful for a magnetic field strength beyond 3 T. At 4 T, there is a huge drop in performance when compared to 3 T, compared to a small degradation going from 0 T to 3 T.

The modelling of the prototype demonstrated that if the illumination source is projected near the centre of the segment, the crosstalk is minimised. This device would be suitable for an application where you can optimise the illumination to the centre of the segments, i.e. Shashlik configuration, which can be positioned using optical wavelength shifting fibres on the

photocathode to minimise crosstalk. This effect has been validated by the experiment on the physical prototype.

There is a good output response and low crosstalk for up-to an area of 3×3 mm^2. This allows some flexibility on the illumination of a segment whilst providing a good response. If the whole photocathode was used for illumination, this device will not be suitable unless it is placed in an axial magnetic field.

Throughout this thesis the following contributions have been made:

- Chapter 4 – Created a 3D model on COMSOL of the existing VPT used in the CMS detector. The model has been accurately reconstructed with as an improvement to the prior works by Yaselli [1]. The simulations involved varying conditions such as magnetic field strength and angle. The induced current; backscatter; and particle trajectory information has been captured and analysed.
- Chapter 5 – Re-characterisation of stored VPTs to find the least degraded to be used for the beam test experimentation. Physically taking part in the beam test experiment to test the DRO concept.
- Chapter 6 – Developing a new VPT prototype for Hamamatsu to build, that consists of a segmented anode that provides 4 independent outputs. The prototype is then characterised in a physical experiment. A 3D model is also created within COMSOL to replicate the prototype. Simulations are done of the prototype 3D model and the outcome is compared to the physical experiment using similar conditions.

7.1 Future works

Throughout the works from each chapter, there are further works that can be done to achieve more information and higher accuracy. For the modelling of the RIE FEU-188 VPT, achieving the fine mesh across all the anode had been a struggle due to memory and time limitations. This can be possible if modelled with enough computational resources available.

The simulation model can also be set to analyse radiation damage that can occur, in such an environment as in the CMS detector. The lifetime and the output of the device can be better understood, and how it would behave when coupled with a scintillator to get an accurate representation of particle flow from the scintillator through to the device.

Further simulations can be done it different environments for the VPT, to get a better understanding of where the VPT can work best. A more accurate representation of the physics involved can be implemented. The flexibility of using a simulation environment opens the door to many avenues, whether it is to work on the VPT structure and material or to find the best conditions for the VPT to work efficiently.

The secondary emission detail can be made more accurate and sophisticated for the segmented anode VPT. This would include the backscatter emission to be as detailed as that done for the RIE FEU-188 VPT model in Chapter 4.

References

[1] I. Yaselli, “Studying the time response of a vacuum phototriode and measurement of gamma radiation damage to high voltage capacitors and resistors,” 2008. [Online]. Available: http://bura.brunel.ac.uk/handle/2438/3018.

[2] D. E. Leslie, I. Yaselli, and P. R. Hobson, “Timing performance of a vacuum phototriode,” in *Astroparticle, Particle And Space Physics, Detectors And Medical Physics Applications*, World Scientific, 2008, pp. 90–94.

[3] S. Zahid and P. R. Hobson, “Meshing Challenges in Simulating the Induced Currents in Vacuum Phototriode,” 2017. [Online]. Available: https://uk.comsol.com/paper/meshing-challenges-in-simulating-the-induced-currents-in-vacuum-phototriode-50891.

[4] T. Adams *et al.*, “Beam test evaluation of electromagnetic calorimeter modules made from proton-damaged $PbWO_4$ crystals,” *J. Instrum.*, vol. 11, no. 04, pp. P04012–P04012, 2016.

[5] M. T. Lucchini *et al.*, “Double side read-out technique for mitigation of radiation damage effects in PbWO4 crystals,” *J. Instrum.*, vol. 11, no. 04, pp. P04021–P04021, 2016.

[6] S. Zahid, P. R. Hobson, and D. J. A. Cockerill, “A segmented anode vacuum phototriode with position sensitivity,” *J. Instrum.*, vol. 13, no. 1, 2018.

[7] S. Zahid, P. . Hobson, and D. J. A. Cockerill, “Simulating multi-channel vacuum phototriodes using COMSOL,” *Nucl. Instruments Methods Phys. Res. Sect. A Accel. Spectrometers, Detect. Assoc. Equip.*, Nov. 2017.

[8] C. Lefèvre, “The CERN accelerator complex. Complexe des accélérateurs du CERN,” Jul-2008. [Online]. Available: https://cds.cern.ch/record/1260465.

[9] “CMS Luminosity - Public Results (2013).” [Online]. Available: https://twiki.cern.ch/twiki/bin/view/CMSPublic/LumiPublicResults.

[10] T. Speer, W. Adam, R. Frühwirth, A. Strandlie, T. Todorov, and M. Winkler, “Track reconstruction in the CMS tracker,” *Nucl. Instruments Methods Phys. Res. Sect. A Accel. Spectrometers, Detect. Assoc. Equip.*, vol. 559, no. 1, pp. 143–147, 2006.

[11] S. I. Cooper, “Phase I Upgrade of the CMS Hadron Calorimeter,” *Nucl. Part. Phys. Proc.*, vol. 273–275, pp. 1002–1007, 2016.

[12] F. De Guio, “Performance of the CMS Detector During the LHC Run 2,” *Acta Phys. Pol.*, vol. B47, pp. 1451–1457, 2016.

[13] M. Mangano, “Weighing up the LHC’s future,” *Newsletter if the EP department*, 2018. [Online]. Available: https://ep-news.web.cern.ch/content/weighing-lhc’s-future.

[14] “SketchUpCMS,” 2017. [Online]. Available: https://twiki.cern.ch/twiki/bin/view/CMSPublic/SketchUpCMS. [Accessed: 15-Jul-2018].

[15] CMS Collaboration, “CMS Physics: Technical Design Report - Volume 1: Detector Performance and Software,” 2006. [Online]. Available: https://cds.cern.ch/record/922757/files/lhcc-2006-001.pdf.

[16] “CMS-doc-4172-v2: Interactive Slice of the CMS detector,” 2010. [Online]. Available: https://cms-docdb.cern.ch/cgi-bin/PublicDocDB/ShowDocument?docid=4172. [Accessed: 27-Feb-2018].

[17] H.Delonnoy, “Performance of the silicon tracker of the CMS experiment during 2016 LHC data taking.” [Online]. Available: https://indico.ihep.ac.cn/event/6387/session/33/contribution/35/material/slides/0.pdf. [Accessed: 10-Jul-2018].

[18] V. Veszpremi, “Operation and performance of the CMS tracker,” *J. Instrum.*, vol. 9, no. 03, p. C03005, 2014.

[19] The CMS Collaboration, “Description and performance of track and primary-vertex reconstruction with the CMS tracker,” *J. Instrum.*, vol. 9, no. 10, p. P10009, 2014.

[20] 1997. Karimaki, V[1] V. Karimaki et al., The CMS tracker system project: Technical Design Report. Geneva: CERN *et al., The CMS tracker system project: Technical Design Report*. Geneva: CERN, 1997.

[21] CMS, *The CMS Electromagnetic Calorimeter Technical Design Report*, no. December. Geneva: CERN, 1997.

[22] R. M. Brown, “The variation in response of the CMS ECAL vacuum phototriodes as a function of orientation in a strong magnetic field,” no. CMS-NOTE-2009-014, https://cds.cern.ch/record/1291195, 2009.

[23] K. W. Bell *et al.*, “The development of vacuum phototriodes for the CMS electromagnetic calorimeter,” *Nucl. Instruments Methods Phys. Res. Sect. A Accel. Spectrometers Detect. Assoc. Equip.*, vol. 469, pp. 29–46, 2001.

[24] K. W. Bell *et al.*, “Vacuum phototriodes for the CMS electromagnetic calorimeter endcap,” in *Proceedings of the 21st IEEE Instrumentation and Measurement Technology Conference (IEEE Cat. No.04CH37510)*, 2004, vol. 3, p. 1866–1869 Vol.3.

[25] The CMS Electromagnetic Calorimeter Group, “Radiation hardness qualification of $PbWO_4$ scintillation crystals for the CMS Electromagnetic Calorimeter,” *J. Instrum.*, vol. 5, no. 03, pp. P03010–P03010, 2010.

[26] A. . Annenkov, M. . Korzhik, and P. Lecoq, “Lead tungstate scintillation material,” *Nucl. Instruments Methods Phys. Res. Sect. A Accel. Spectrometers, Detect. Assoc. Equip.*, vol. 490, no. 1–2, pp. 30–50, Sep. 2002.

[27] M. Anfreville *et al.*, “Laser monitoring system for the CMS lead tungstate crystal calorimeter,” *Nucl. Instruments Methods Phys. Res. Sect. A Accel. Spectrometers, Detect. Assoc. Equip.*, vol. 594, no. 2, pp. 292–320, 2008.

[28] F. Ferri, “Monitoring and Correcting for Response Changes in the CMS Lead-tungstate Electromagnetic Calorimeter,” *J. Phys. Conf. Ser.*, vol. 404, no. 1, p. 12041, 2012.

[29] A. Jofrehei, “The CMS ECAL Upgrade for Precision Crystal Calorimetry at the HL-LHC,” *IEEE Trans. Nucl. Sci.*, p. 1, 2018.

[30] P. Lecomte, D. Luckey, F. Nessi-Tedaldi, and F. Pauss, “High-energy proton induced damage study of scintillation light output from $PbWO_4$ calorimeter crystals,” *Nucl. Instruments Methods Phys. Res. Sect. A Accel. Spectrometers, Detect. Assoc. Equip.*, vol. 564, no. 1, pp. 164–168, 2006.

[31] “CMS ECAL with 2017 data,” May-2018. [Online]. Available: https://cds.cern.ch/record/2319285.

[32] The CMS Collaboration, “Performance and operation of the CMS electromagnetic calorimeter,” 2011. [Online]. Available: http://cds.cern.ch/record/1345319/?ln=en.

[33] D. Renker, “Properties of avalanche photodiodes for applications in high energy physics, astrophysics and medical imaging.,” *Nucl. Instrum. Method*, vol. A486, no. 1, p. 164{\textendash}169, 2002.

[34] N. Bajanov, “Fine–Mesh Photodetectors for CMS Endcap Electromagnetic Calorimeter,” *Interpret. A J. Bible Theol.*, pp. 1–17, 1998.

[35] “Hadron Calorimeter.” [Online]. Available: http://cms.web.cern.ch/news/hadron-calorimeter.

[36] CMS Collaboration, “Performance of the CMS hadron calorimeter with cosmic ray muons and LHC beam data,” *J. Instrum.*, vol. 5, no. 03, p. T03012, 2010.

[37] A. Hervé *et al.*, “Status of the CMS magnet (MT17),” *IEEE Trans. Appl. Supercond.*, vol. 12, no. 1, pp. 385–390, 2002.

[38] T. C. Collaboration, “Status of the Construction of the CMS Magnet,” *IEEE Trans. Appiled Supercond.*, vol. 14, no. 2, pp. 542–547, 2004.

[39] M. C. Fouz, “The CMS Muon detectors,” in *2007 IEEE Nuclear Science Symposium Conference Record*, 2007, vol. 3, pp. 1885–1890.

[40] “Performance of CMS muon detectors in 2018 Collision Runs,” Jul-2018. [Online]. Available: https://cds.cern.ch/record/2630439.

[41] S. Flyckt and C. Marmonier, “Photomultiplier tubes: Principles and applications,” *Photonis, Brive, Fr.*, no. September, pp. 265–304, 2002.

[42] K. Makónyi *et al.*, “Evaluating vacuum phototriodes designed for the PANDA electromagnetic calorimeter,” *Nucl. Instruments Methods Phys. Res. Sect. A Accel. Spectrometers, Detect. Assoc. Equip.*, vol. 763, pp. 36–43, 2014.

[43] A. G. Wright, *The photomultiplier handbook*. Oxford University Press, 2017.

[44] J. E. Bateman, “The Operation of Vacuum Phototriodes in an Axial Magnetic Field - A Monte-Carlo Study,” *Rutherford Applet. Lab. Tech. Reports*, no. RAL-TR-1998-059, 1998.

[45] D. Contardo, M. Klute, J. Mans, L. Silvestris, and J. Butler, “Technical Proposal for the Phase-II Upgrade of the CMS Detector,” Geneva, Jun. 2015.

[46] G. Negro, “Performance of the CMS precision electromagnetic calorimeter at the LHC Run II and prospects for high-luminosity LHC,” *Nucl. Instruments Methods Phys. Res. Sect. A Accel. Spectrometers, Detect. Assoc. Equip.*, no. September, 2017.

[47] CMS Collaboration, “FLUKA particle flux maps for CMS Detector,” *CMS Performance*

Note, 2013. [Online]. Available: http://cds.cern.ch/record/1612355/files/DP2013_028.pdf. [Accessed: 20-Jul-2018].

[48] A. B. COMSOL, "COMSOL Multiphysics® v. 5.3." Stockholm, Sweden.

[49] A. B. COMSOL, *AC/DC Module User's Guide*. Stockholm, Sweden: COMSOL Multiphysics® v. 5.3, 2015.

[50] A. B. COMSOL, *Particle Tracing Module User's Guide*. Stockholm, Sweden: COMSOL Multiphysics® v. 4.3, 2012.

[51] W. Shockley, "Currents to conductors induced by a moving point charge," *J. Appl. Phys.*, vol. 9, no. 10, pp. 635–636, 1938.

[52] COMSOL, "Finite Element Mesh Refinement," 2016. [Online]. Available: https://uk.comsol.com/multiphysics/mesh-refinement. [Accessed: 02-Apr-2018].

[53] M. Furman and M. Pivi, "Probabilistic model for the simulation of secondary electron emission," *Phys. Rev. Spec. Top. - Accel. Beams*, vol. 5, no. 12, p. 124404, 2002.

[54] R. W. Dressel, "Retrofugal Electron Flux from Massive Targets Irradiated with a Monoenergetic Primary Beam," *Phys. Rev.*, vol. 144, no. 1, pp. 332–343, Apr. 1966.

[55] D. J. A. Bateman, J. E. and Cockerill, "The operation of vacuum phototriodes in a non-axial magnetic field," no. CERN-CMS-NOTE-1999-032, 1999.

[56] COMSOL, "Ray Optics Module Updates," 2017. [Online]. Available: https://uk.comsol.com/release/5.3/ray-optics-module. [Accessed: 27-Feb-2019].

[57] Analog Devices, "LTspice." [Online]. Available: http://www.analog.com/en/design-center/design-tools-and-calculators/ltspice-simulator.html.

[58] L. Cadamuro, "The CMS Level-1 trigger system for LHC Run II," *J. Instrum.*, vol. 12, no. 03, p. C03021, 2017.

[59] F. Pitters, "The CMS High-Granularity Calorimeter for Operation at the High-Luminosity LHC," *arXiv Prepr. arXiv1802.05987*, 2018.

[60] R. Paramatti, "Design options for the upgrade of the CMS electromagnetic calorimeter," *Nucl. Part. Phys. Proc.*, vol. 273–275, pp. 995–1001, 2016.

[61] A. Apresyan *et al.*, "Test beam studies of silicon timing for use in calorimetry," *Nucl. Instruments Methods Phys. Res. Sect. A Accel. Spectrometers, Detect. Assoc. Equip.*, vol. 825, pp. 62–68, 2016.

[62] S. Terzo, "Radiation hard silicon particle detectors for HL-LHC—RD50 status report," *Nucl. Instruments Methods Phys. Res. Sect. A Accel. Spectrometers, Detect. Assoc. Equip.*, vol. 845, pp. 177–180, 2017.

[63] A.-M. Magnan, "HGCAL: a High-Granularity Calorimeter for the endcaps of CMS at HL-LHC," *J. Instrum.*, vol. 12, no. 01, pp. C01042–C01042, 2017.

[64] C. Adloff *et al.*, "Response of the CALICE Si-W electromagnetic calorimeter physics prototype to electrons," *Nucl. Instruments Methods Phys. Res. Sect. A Accel. Spectrometers, Detect. Assoc. Equip.*, vol. 608, no. 3, pp. 372–383, Sep. 2009.

[65] E. Currás *et al.*, "Radiation hardness and precision timing study of silicon detectors for the CMS High Granularity Calorimeter (HGC)," *Nucl. Instruments Methods Phys. Res.*

Sect. A Accel. Spectrometers, Detect. Assoc. Equip., vol. 845, pp. 60–63, 2017.

[66] S. Kuehn, "RD50 Collaboration overview: Development of new radiation hard detectors," *Nucl. Instruments Methods Phys. Res. Sect. A Accel. Spectrometers, Detect. Assoc. Equip.*, vol. 824, pp. 422–425, 2016.

[67] E. Auffray, M. Korjik, and A. Singovski, "Experimental Study of Lead Tungstate Scintillator Proton-Induced Damage and Recovery," *IEEE Trans. Nucl. Sci.*, vol. 59, no. 5, pp. 2219–2223, Oct. 2012.

[68] M. Huhtinen, P. Lecomte, D. Luckey, F. Nessi-Tedaldi, and F. Pauss, "High-energy proton induced damage in PbWO4 calorimeter crystals," *Nucl. Instruments Methods Phys. Res. Sect. A Accel. Spectrometers, Detect. Assoc. Equip.*, vol. 545, no. 1, pp. 63–87, 2005.

[69] S. Agostinelli and Et Al, "Geant4 - a simulation toolkit," *Nucl. Instruments Methods Phys. Res. Sect. A Accel. Spectrometers, Detect. Assoc. Equip.*, vol. 506, no. 3, pp. 250–303, 2003.

[70] HAMAMATSU Photonics K.K. Electron tube division, "Photomultiplier tubes and assemblies for scintillating counters and high energy physics," 2004. [Online]. Available: http://neutron.physics.ucsb.edu/docs/High_energy_PMT_TPMO0007E01.pdf.

[71] S. Chatrchyan *et al.*, "Energy calibration and resolution of the CMS electromagnetic calorimeter in pp collisions at $\sqrt{s}$ = 7 TeV," *J. Instrum.*, vol. 8, no. 9, p. P09009, 2013.

[72] H. Kume, S. Suzuki, J. Takeuchi, and K. Oba, "Newly developed photomultiplier tubes with position sensitivity capability," *IEEE Trans. Nucl. Sci.*, vol. 32, no. 1, pp. 448–452, 1985.

[73] M. Salomon and S. S. A. Williams, "A multi-anode photomultiplier with position sensitivity," *Nucl. Instruments Methods Phys. Res. Sect. A Accel. Spectrometers, Detect. Assoc. Equip.*, vol. 241, no. 1, pp. 210–214, 1985.

[74] M. Salomon, V. Li, G. Smith, and Y. S. Wu, "Fast tracking detector with fiber scintillators and a position sensitive photomultiplier," *IEEE Trans. Nucl. Sci.*, vol. 36, no. 1, pp. 94–97, Feb. 1989.

[75] H. Uchida, T. Yamashita, M. Iida, and S. Muranatsu, "Design of a Mosaic BGO Detector System for Positron CT," *IEEE Trans. Nucl. Sci.*, vol. 33, no. 1, pp. 464–467, Feb. 1986.

[76] S. Suzuki, T. Suzuki, T. Matsushita, and H. Kume, "New mesh PMTs for high magnetic environments," *IEEE Trans. Nucl. Sci.*, vol. 33, no. 1, pp. 377–380, 1986.

[77] "4192A LF Impedance Analyzer," *Keysight technologies*. [Online]. Available: https://www.keysight.com/main/techSupport.jspx?cc=IN&lc=eng&nid=-32775.536883581&pid=330690&pageMode=PL.

[78] Thinksrs, "Digital Lock-In Amplifiers." [Online]. Available: http://www.thinksrs.com/downloads/pdfs/catalog/SR810830c.pdf.

Appendix A – Examples of COMSOL Parameters Screenshots

Some examples of the parameters used within the COMSOL model are shown below:

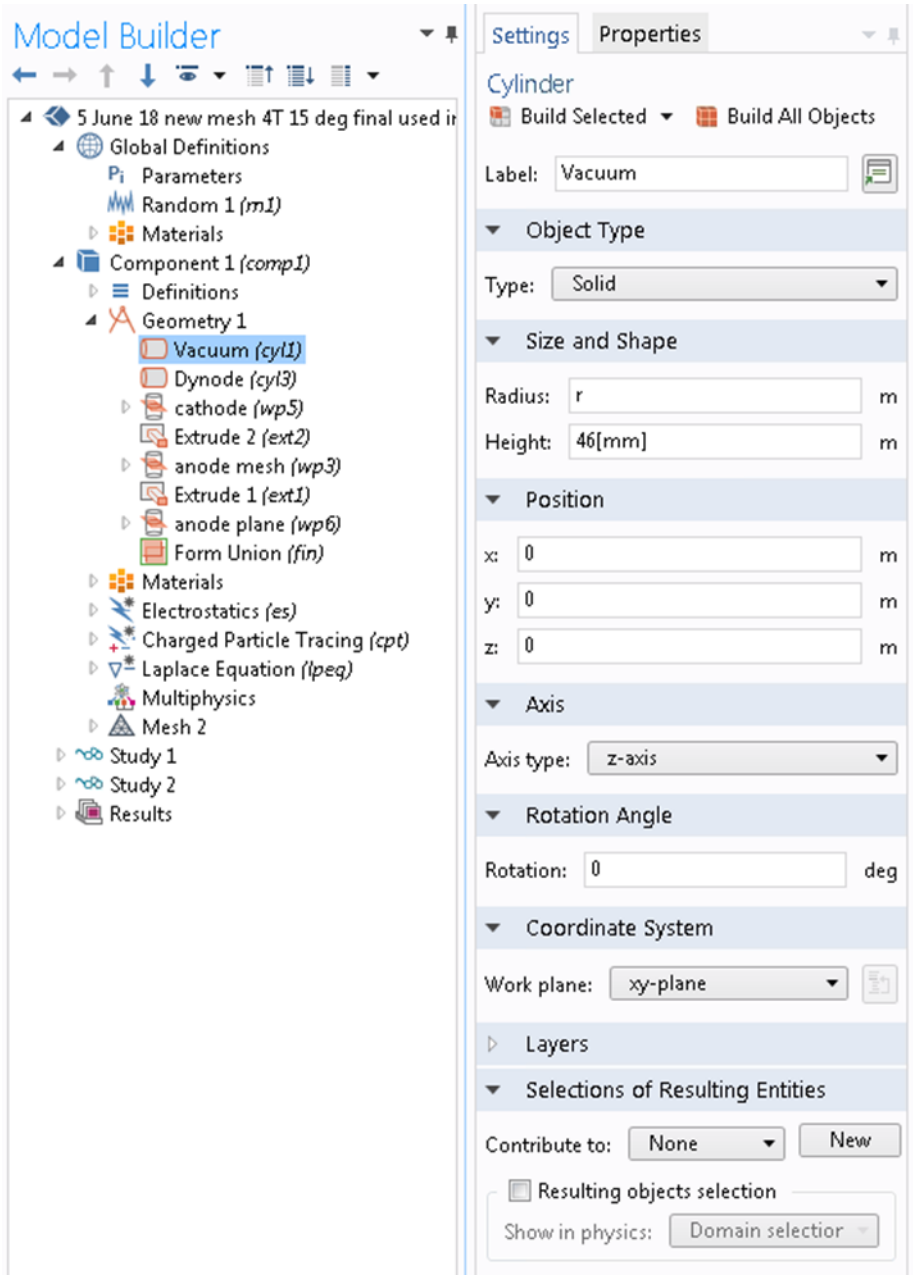

Figure a – This screenshot shows geometry node within COMSOL, specifically the VPT housing and its dimensions, the height is set to 46 mm and the radius is set to 26.5 mm.

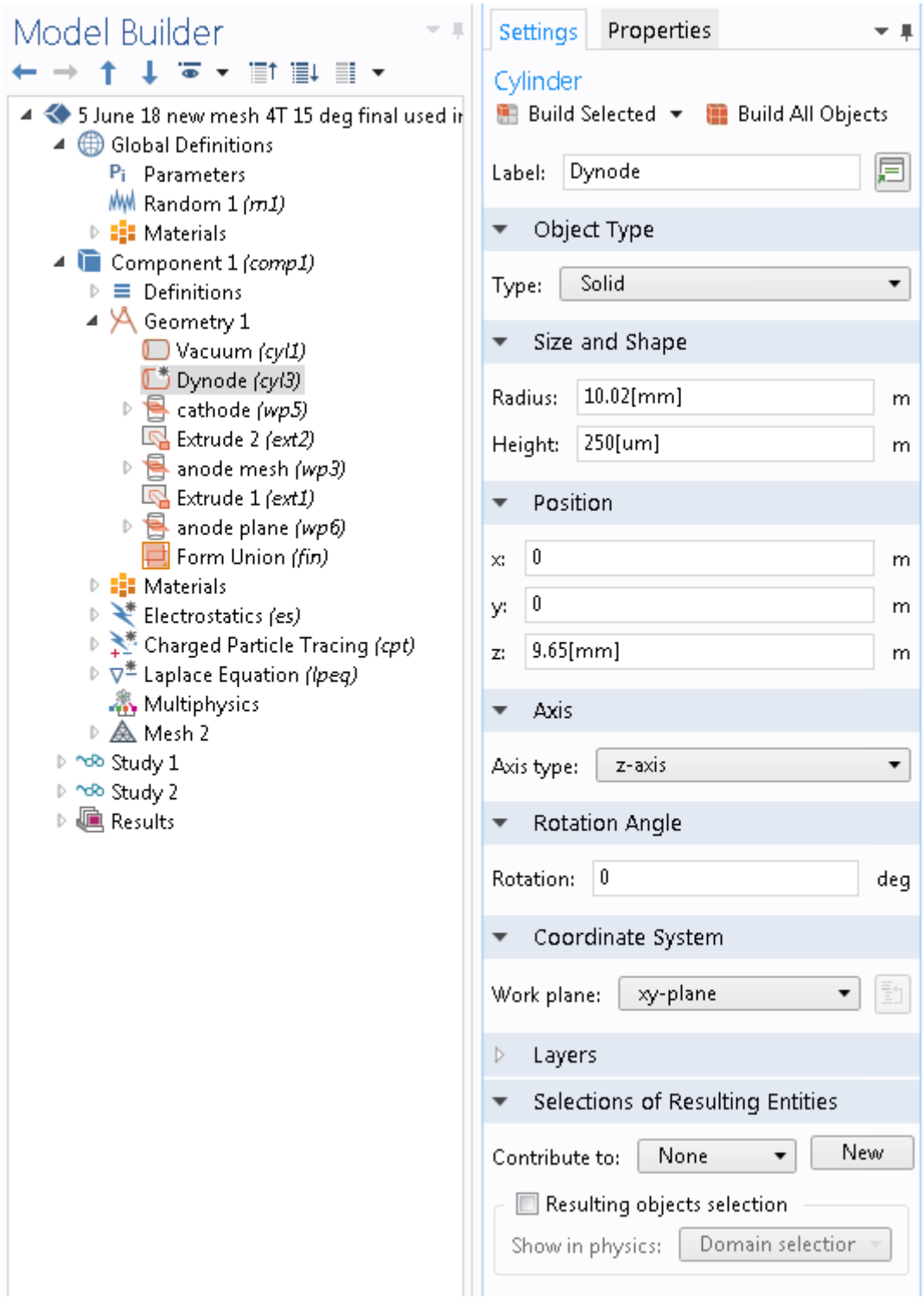

Figure b – This screenshot shows another example in the geometry node within COMSOL, of the dynode dimensions. These are set to a radius of 10.02 mm and with a depth of 250 µm.

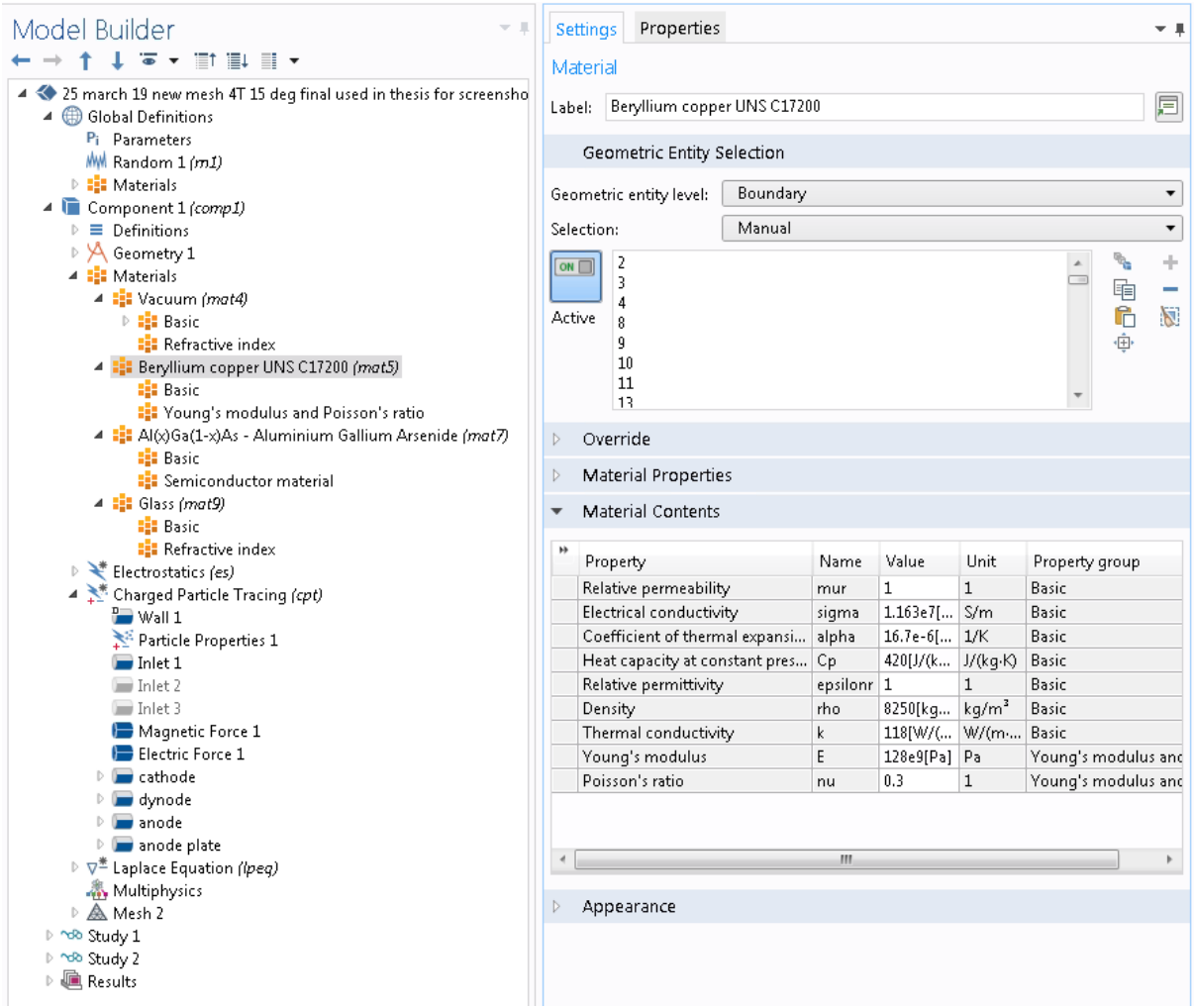

Figure c – This screenshot shows the Materials node within COMSOL, you can see all the materials that are selected for the various components of the VPT. Specifically, the Beryllium copper is shown with the properties which is used for the anode mesh.

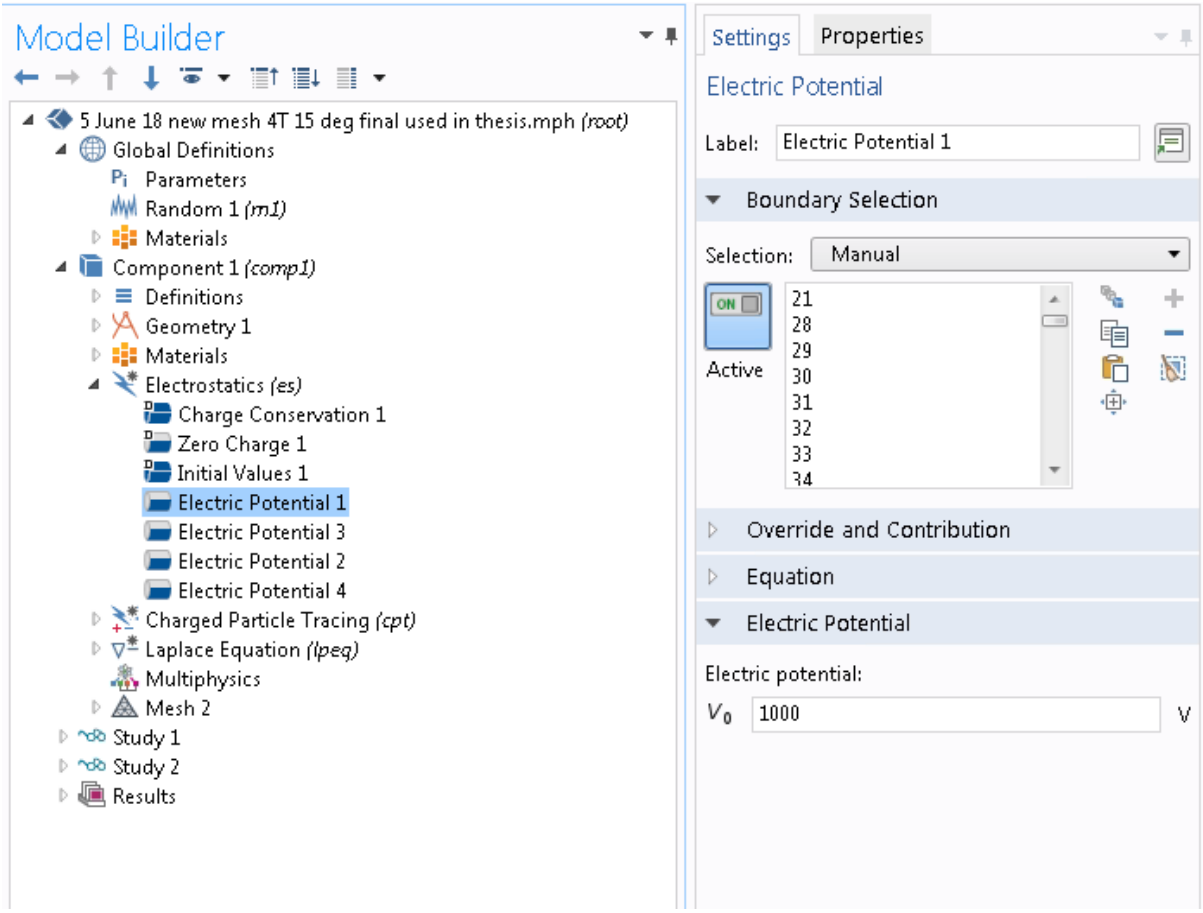

Figure d – This screenshot shows the Electrostatics node of the COMSOL model. An example of setting the anode voltage at 1000 V is shown.

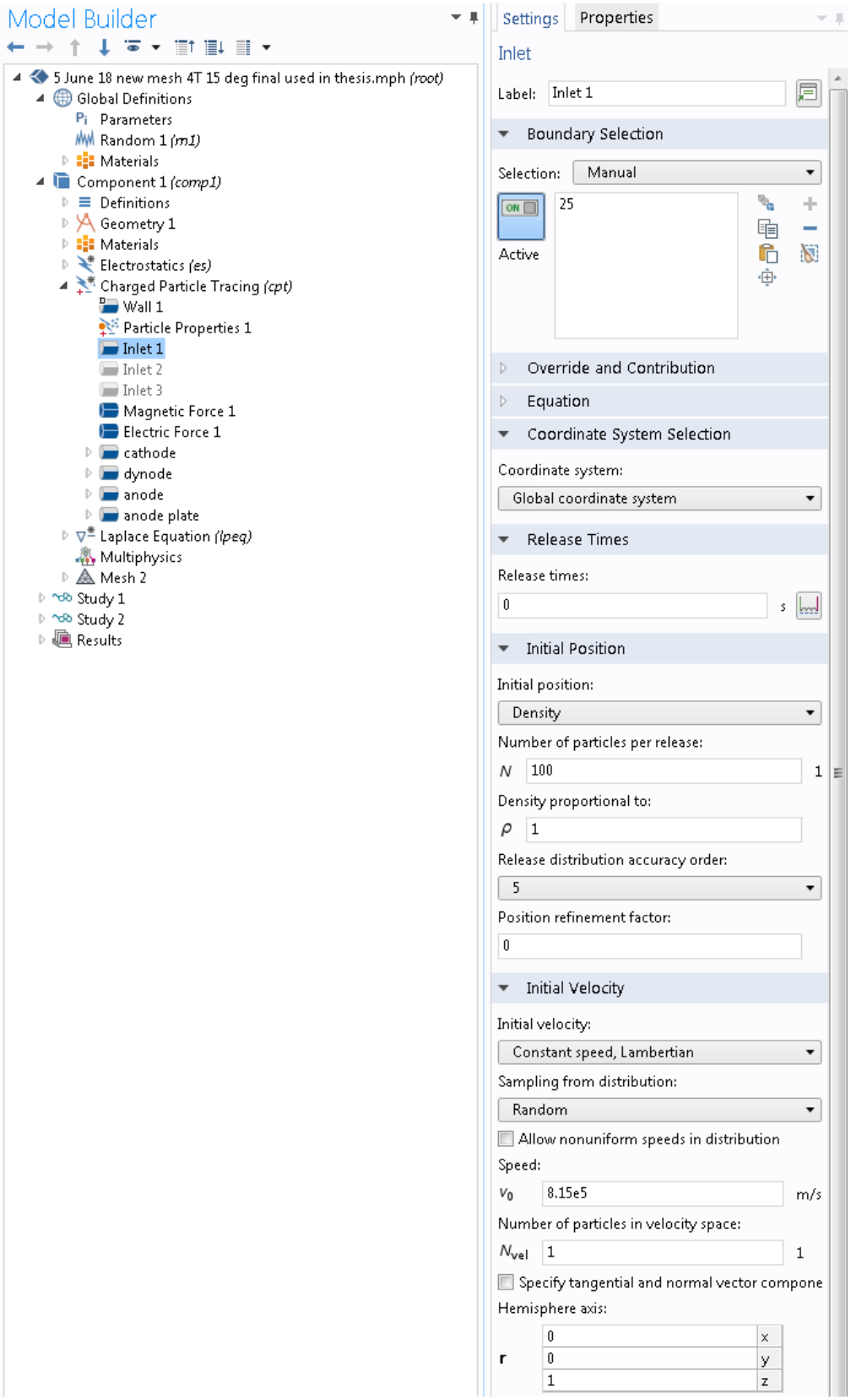

Figure e – This screenshot shows the Charged Particle Tracing node within the COMSOL model, the inlet option has been selected to show the PE release properties. The PE are released at 0 ns, within the runtime of the simulation. With 100 particles being released at a speed of 2 eV (which is converted to in m/s approximately), with a Lambertian distribution directions in the Z domain.

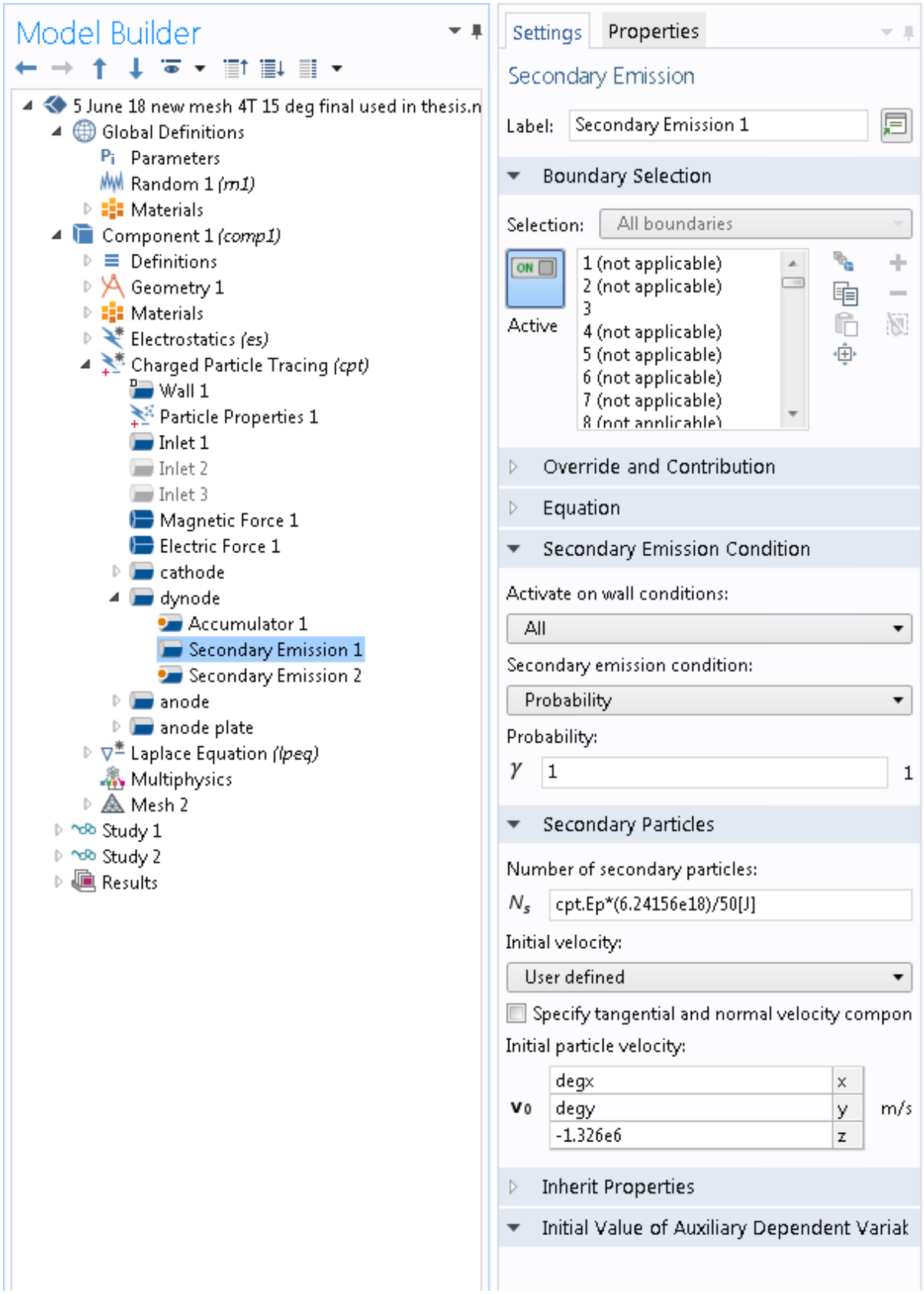

Figure f – This screenshot shows again the Charged Particle Tracing node within the COMSOL model, this time showing the options set for the dynode electrode. This Secondary Emission node shows the number of secondary particles are dependent on the incoming energy of the particle that collides with the dynode.

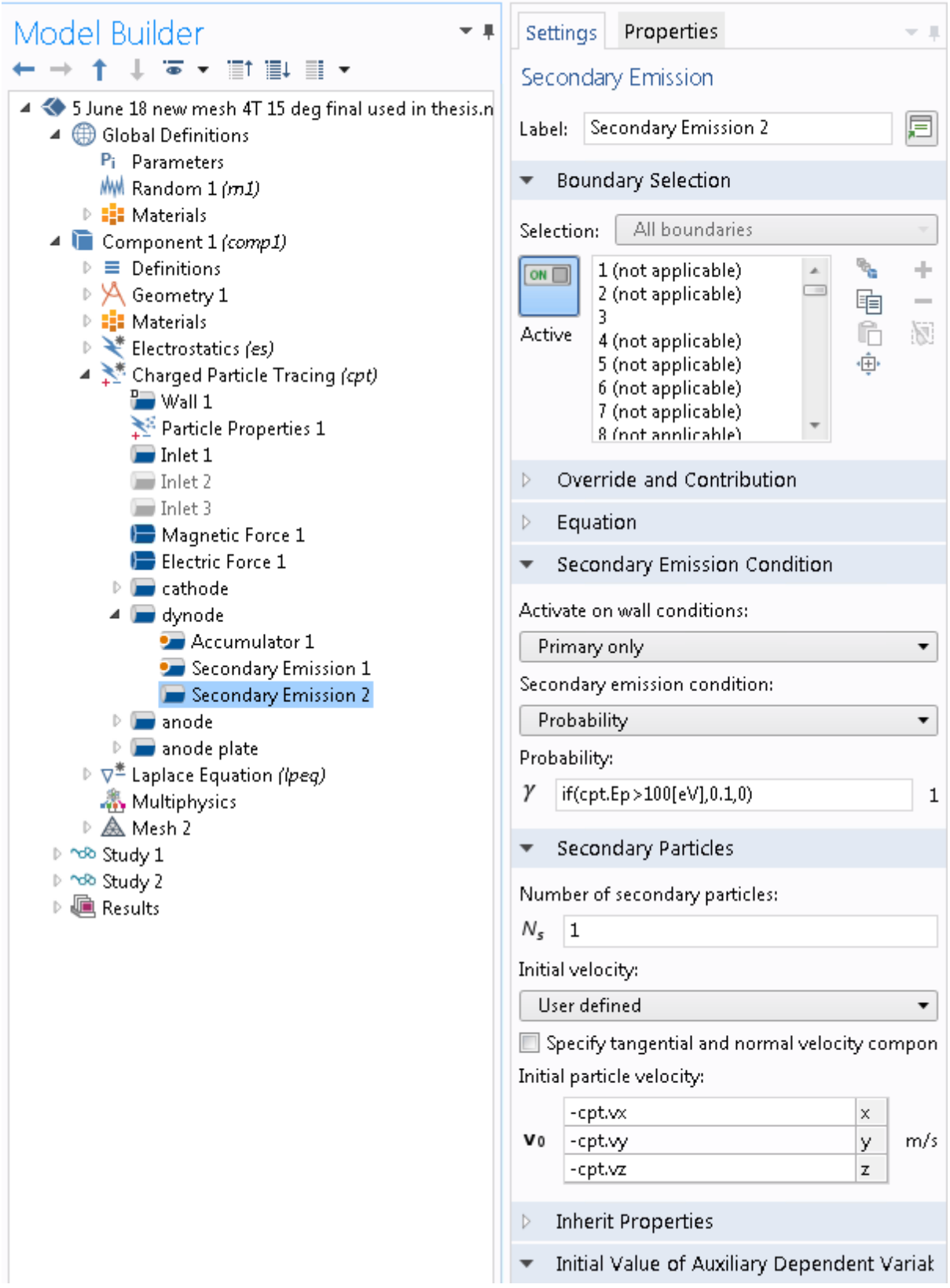

Figure g – This screenshot shows the second 'Secondary Emission' within the dynode electrode – this is actually the backscatter. This is set to a release a single electron with a 10 % chance, if the incoming energy of the electron is above 100 eV. The backscattered (secondary within COMSOL environment) electron as the same speed as the incoming electron and is the direction it came from.

Appendix B – Stored VPT Pulsed Measurements

The full set of results is shown below, from section 5.7.2. The anode voltage is Va and dynode Vd. The peak FWHM and Peak/FWHM are all shown in the ACD counts.

VPT 16294				
Va (V)	Vd (V)	Peak	FWHM	Peak/FWHM
300	100	67.73	2.17	31.21
800	600	180.09	4.49	40.11
1000	800	199.45	5.14	38.8
VPT 16296				
Va (V)	Vd (V)	Peak	FWHM	Peak/FWHM
300	100	91.94	2.21	41.6
800	600	212.25	3.85	55.13
1000	800	229.32	4.14	55.39
VPT 16297				
Va (V)	Vd (V)	Peak	FWHM	Peak/FWHM
300	100	63.61	2.11	30.15
800	600	162.29	4.18	38.83
1000	800	178.7	4.82	37.07
VPT 16302				
Va (V)	Vd (V)	Peak	FWHM	Peak/FWHM
300	100	87.5	2.28	38.38
800	600	236.19	5.39	43.82
1000	800	262.4	6.27	41.85
VPT 16319				
Va (V)	Vd (V)	Peak	FWHM	Peak/FWHM
300	100	83.03	2.16	38.44
800	600	187.64	4.15	45.21
1000	800	202.34	4.61	43.89
VPT 16308				
Va (V)	Vd (V)	Peak	FWHM	Peak/FWHM
300	100	103.79	2.36	43.98
800	600	244.49	4.73	51.69
1000	800	261.26	5.26	49.67

VPT 16324				
Va (V)	Vd (V)	Peak	FWHM	Peak/FWHM
300	100	94.58	2.22	42.6
800	600	209.14	4.33	48.3
1000	800	220.75	4.75	46.47
VPT 16291				
Va (V)	Vd (V)	Peak	FWHM	Peak/FWHM
300	100	126.53	2.54	49.81
800	600	314.08	6.71	46.81
1000	800	342.79	7.83	43.78
VPT 16292				
Va (V)	Vd (V)	Peak	FWHM	Peak/FWHM
300	100	104.26	2.45	42.56
800	600	267.28	6.07	44.03
1000	800	293.52	7.03	41.75
VPT 16311				
Va (V)	Vd (V)	Peak	FWHM	Peak/FWHM
300	100	103.69	2.39	43.38
800	600	262.8	5.61	46.84
1000	800	285.95	6.41	44.61
VPT 16303				
Va (V)	Vd (V)	Peak	FWHM	Peak/FWHM
300	100	126.92	2.53	50.17
800	600	316.87	6.18	51.27
1000	800	350.47	7.18	48.81
VPT 16329				
Va (V)	Vd (V)	Peak	FWHM	Peak/FWHM
300	100	96.19	2.33	41.28
800	600	214.77	4.75	45.21
1000	800	229.75	5.19	44.27
VPT 16354				
Va (V)	Vd (V)	Peak	FWHM	Peak/FWHM
300	100	105.39	2.32	45.43
800	600	233.79	4.33	53.99

1000	800	247.4	4.71	52.53
VPT 16307				
Va (V)	Vd (V)	Peak	FWHM	Peak/FWHM
300	100	98.43	2.34	42.06
800	600	235.69	5.05	46.67
1000	800	249.28	5.58	44.67
VPT 16327				
Va (V)	Vd (V)	Peak	FWHM	Peak/FWHM
300	100	117.98	2.42	48.75
800	600	236.62	4.52	52.35
1000	800	244.13	4.62	52.84
VPT 16466				
Va (V)	Vd (V)	Peak	FWHM	Peak/FWHM
300	100	101.56	2.27	44.74
800	600	232.04	4.44	52.26
1000	800	250.61	4.92	50.94
VPT 16314				
Va (V)	Vd (V)	Peak	FWHM	Peak/FWHM
300	100	94.44	2.28	41.42
800	600	238.17	4.95	48.12
1000	800	258.55	5.51	46.92
VPT 16312				
Va (V)	Vd (V)	Peak	FWHM	Peak/FWHM
300	100	103.39	2.34	44.18
800	600	246.98	4.88	50.61
1000	800	266.56	5.42	49.18
VPT 16488				
Va (V)	Vd (V)	Peak	FWHM	Peak/FWHM
300	100	59.24	2.14	27.68
800	600	179.22	4.6	38.96
1000	800	203.65	5.36	37.99
VPT 16465				
Va (V)	Vd (V)	Peak	FWHM	Peak/FWHM

300	100	93.62	2.16	43.34
800	600	213	3.61	59
1000	800	232.25	3.94	58.95
VPT 16357				
Va (V)	Vd (V)	Peak	FWHM	Peak/FWHM
300	100	71.16	2.08	34.21
800	600	157.47	3.35	47.01
1000	800	168.32	3.61	46.63
VPT 16462				
Va (V)	Vd (V)	Peak	FWHM	Peak/FWHM
300	100	80.91	2.35	34.43
800	600	200.81	4.72	42.54
1000	800	220.94	5.29	41.77
VPT 16330				
Va (V)	Vd (V)	Peak	FWHM	Peak/FWHM
300	100	104.46	2.34	44.64
800	600	220.57	4.63	47.64
1000	800	229.15	4.99	45.92

Appendix C – Brunel Magnet Mechanical Cross section